Sources and Evolution in Space and Time of Hydrothermal Fluids at the Cerro de Pasco Cordilleran Base Metal Deposit, Central Peru

Baumgartner Bendezu, Regina Monika

Regina BAUMGARTNER

Sources and Evolution in Space and Time of Hydrothermal Fluids at the Cerro de Pasco Cordilleran Base Metal Deposit, Central Peru.

2007

Volume 66

Déjà paru /already published :

Previous volumes are listed under

http://www.unige.ch/sciences/terre/mineral/publications/ter_env.html

Vol. 30 (2001) F. Parat: Contemporaneous magmatic differentiation of S-rich trachyandesitic and high-K calc-alkaline andesite in an intracontinental setting, San Juan Volcanic Field, Colorado, U.S.A. (121 pages). ISBN 2-940153-29-9
Commande à : Département de Minéralogie, 13 rue des Maraîchers, 1211 Genève 4; 30.- CHF

Vol. 31 (2001) J. Viszkok: Subsurface fluid flow simulation with finite element method in the East Pannonian Basin. (232 pages). ISBN 2-940153-30-2
Commande à : Institut F.-A. Forel, 10 route de Suisse, 1290 Versoix (Suisse); 30.- CHF

Vol. 32 (2001) T. Ton-That: $^{40}Ar/^{39}Ar$ dating of late Pleistocene marine and terrestrial tephra from the Tyrrhenian and Ionian Seas, Mediterranea; some implications for global climate changes. (99 pages). ISBN 2-940153-31-0
Commande à : Département de Minéralogie, 13 rue des Maraîchers, 1211 Genève 4; 30.- CHF

Vol. 33 (2001) S. Girardclos: Sismostratigraphie et structure sédimentaire en 3D d'un bassin lacustre, du retrait glaciaire à nos jours (Lac Léman, Suisse). (182 pages). ISBN 2-940153-32-9
Commande à : Institut F.-A. Forel, 10 route de Suisse, 1290 Versoix (Suisse); 30.- CHF

Vol. 34 (2001) P. Rosset: Evaluation de l'aléa sismique dans les vallées alpines par des méthodes détermi-nistes. (133 pages). ISBN 2-940153-33-7
Commande à : Département de Minéralogie, 13 rue des Maraîchers, 1211 Genève 4; 30.- CHF

Vol. 35 (2002) R. Gilbin: Caractérisation de l'exposition des écosystèmes aquatiques à des produits phytosanitaires: spéciation, biodisponibilité et toxicité. (192 pages). ISBN 2-940153-34-5
Commande à : Institut F.-A. Forel, 10 route de Suisse, 1290 Versoix (Suisse); 30.- CHF

Vol. 36 (2002) Y. Haeberlin: Geological and structural setting, age, and geochemistry of the orogenic gold deposits at the Pataz Province, eastern Andean Cordillera, Peru. (182 pages). ISBN 2-940153-35-3
Commande à : Département de Minéralogie, 13 rue des Maraîchers, 1211 Genève 4; 50.- CHF

Vol. 37 (2002) S. Mosquera Machado: Analyse multi-aléas et risques naturels dans le département du Chocó, nord-ouest de la Colombie. (159 pages). ISBN 2-940153-36-1
Commande à : Département de Minéralogie, 13 rue des Maraîchers, 1205 Genève; 30.- CHF

Vol. 38 (2002) I. Baster: Holocene delta in western Lake Geneva and its palaeoenvironmental implications: seismic and sedimentological approach. (159 pages). ISBN 2-940153-37-X
Commande à : Institut F.-A. Forel, 10 route de Suisse, 1290 Versoix (Suisse); 30.- CHF

Vol. 39 (2002) Ö. F. Çelik: Geochemical, petrological and geochronological observations on the meta-morphic rocks of the Tauride Belt Ophiolites (S. Turkey). (257 pages). ISBN 2-940153-38-8
Commande à : Département de Minéralogie, 13 rue des Maraîchers, 1205 Genève; 50.- CHF

Vol. 40 (2002) A. Carnelli: Long term dynamics of the vegetation at the subalpine-alpine ecocline during the Holocene: comparative study in the Aletsch region, Val d'Arpette, and Furka Pass (Valais, Switzerland). (324 pages). ISBN 2-940153-39-6
Commande à : Institut F.-A. Forel, 10 route de Suisse, 1290 Versoix (Suisse); 30.- CHF

Vol. 41 (2003) S. Beuchat: Geochronological, structural, isotopes and fluid inclusion constrains of the polymetallic Domo de Yauli district, Peru. (130 pages). ISBN 2-940153-40-X
Commande à : Département de Minéralogie, 13 rue des Maraîchers, 1205 Genève; 50.- CHF

Vol. 42 (2003) Z. El Morjani: Conception d'un système d'information à référence spatiale pour la gestion environnementale; application à la sélection de sites potentiels de stockage de déchets ménagers et industriels en région semi-aride (Souss, Maroc). (300 pages). ISBN 2-940153-41-8
Commande à : Institut F.-A. Forel, 10 route de Suisse, 1290 Versoix (Suisse); 30.- CHF

Vol. 43 (2003) C. Pellaton: Distribution of sedimentary organic matter (palynofacies) with respect to palaeoenvironmental conditions: two case histories from the Miocene of the USA. (185 pages). ISBN 2-940153-42-6
Commande à : Département de Géologie, 13 rue des Maraîchers, 1205 Genève; 30.- CHF

→ suite page III de couverture

UNIVERSITÉ DE GENÈVE
Département de minéralogie

FACULTÉ DES SCIENCES
Professeur Lluís Fontboté

Sources and Evolution in Space and Time of Hydrothermal Fluids at the Cerro de Pasco Cordilleran Base Metal Deposit, Central Peru.

THÈSE

présentée à la Faculté des sciences de l'Université de Genève
pour obtenir le grade de Docteur ès sciences, mention Sciences de la Terre

par

Regina BAUMGARTNER

de St-Gall

Thèse N°3804

GENÈVE
Atelier de reproduction de la Section de Physique
2007

Table of Contents

PART II

Abstract

The Cerro de Pasco epithermal Cordilleran deposit is located in central Peru and is related to a Mid-Miocene diatreme-dome complex. Cerro de Pasco constitutes a large polymetallic resource with past production plus known resources of more than ~175 Mt @ 7 percent Zn and 2 percent Pb and 3 oz/t Ag. In addition, prior to 1950 mining produced 1200 Moz Ag, 2 Moz of Au and around 50 Mt @ 2 percent Cu.

The Cerro de Pasco deposit comprises two mineralization stages with contrasting mineralogy and deposition environments. The first mineralization stage (IA) occurs on the eastern edge of the diatreme-dome complex and consists of a large pyrite-quartz body replacing mainly adjacent carbonate rocks of the Upper Triassic-Lower Jurassic Pucará Group and to a lesser extent the diatreme breccia. This body is composed of pyrite with pyrrhotite inclusions, quartz, and black and red chalcedony (containing hypogene hematite). At the contact of the pyrite-quartz body, the diatreme breccia is altered to sericite-pyrite-quartz. Pipe-like pyrrhotite bodies zoned outwards to Zn-Pb mineralization bearing Fe-rich sphalerite, containing up to 25 mol% FeS (stage IB), were subsequently emplaced within the pyrite-quartz body, mainly replacing Pucará carbonate rocks.

Recent mine developments have allowed to study in detail the mineralogy and spatial distribution of the second mineralization stage which superimposes partially the first one and includes zoned veins and replacement bodies. E-W trending fractures cutting the diatreme breccia, the pyrite-quartz body, and the Excelsior Group focused hydrothermal fluids which altered the rock and deposited enargite-pyrite forming relatively irregular (Cu-Ag-Au-(Zn-Pb) veins. These veins, located in the western part of the deposit, display mineral zoning with, from the center outwards, a core of enargite-pyrite and Au traces; an intermediate zone of tennantite, chalcopyrite and Bi-minerals; and a poorly developed outer zone bearing sphalerite-galena. The replacement ores are hosted by Lower Mesozoic carbonate rocks and are controlled along N35°E, N90°E, N120°E and N170°E faults. They form upward-flaring pipe-like well zoned orebodies with a core of famatinite-pyrite and alunite; an intermediate zone with tetrahedrite-pyrite, chalcopyrite, matildite, cuprobismutite, emplectite, and other Bi-minerals (Ag and Bi contents may reach up to more than 1000 ppm) accompanied by APS minerals, kaolinite, and dickite; and an outer zone composed of Fe-poor sphalerite (in the range of 0.05 to 3.5 mole % FeS) and galena. The outermost zone consists of hematite, magnetite and Fe-Mn-Zn carbonates.

Most of the second stage carbonate replacement bodies display an inclined plunge (between 25 and 60°) to the West, i.e., in the direction of the diatreme-dome complex, suggesting that the hydrothermal fluids ascended from deeper levels and that no lateral feeding from the veins to the carbonate replacement bodies took place. Rather, both veins in the diatreme breccia and carbonate replacement bodies may be the result of parallel and divergent ascending fluid paths within the same hydrothermal system. This is also reflected by the different mineral compositions recognized in the cores of the western enargite-pyrite veins (Cu, As, and Au rich) and of the carbonate replacement deposits (Cu and As poor, Sb>As, virtually Au free).

The mineral zoning and the observed mineral assemblages and associations indicate that, during the second mineralization stage, the fluid evolution reflects fluid advances and retreats controlled by the hydrothermal activity and host rock type. The inner zone assemblages encroach on those of the outer zone during fluid advance and the outer zone assemblages encroach on those of the inner zones during fluid retreat.

Taking in account the deposition temperatures derived from fluid inclusion data (see below), the mineral assemblages of the first stage are characterized predominantly by low sulfidation states as indicated by pyrrhotite inclusions in pyrite and by the deposition of pyrrhotite pipes and related Zn-Pb ores bearing Fe-rich sphalerite. However, the presence of hematite within quartz from the pyrite-quartz body suggests that the fluids were locally oxidizing which is typical of exsolving magmatic fluids. The observed mineral assemblages are consistent with precipitation from magmatic fluids reduced by interaction with host rocks, probably Excelsior Group rocks. The quartz-sericite alteration halo at the margin of the pyrite-quartz body suggests moderate acidic conditions for the first mineralization stage. The second mineralization stage contains high to intermediate sulfidation state mineral assemblages bearing Fe-poor sphalerite. The recognized alteration assemblages with development of vuggy quartz in the diatreme and deposition of alunite both in the enargite-pyrite veins and carbonate replacement bodies, indicate very acidic fluids. Limited interaction with the host rock, owing to fluid channeling along fractures and because the buffering capacity of the host rock had been lowered by alteration during the first mineralization stage, may explain the prevailing high sulfidation conditions during the second mineralization stage.

In order to gain information on the absolute duration of the magmatic-hydrothermal system at Cerro de Pasco,

a single zircon U-Pb survey and Hf isotopes on magmatic products and a step-wise IR-CO_2 laser $^{40}Ar/^{39}Ar$ study on biotite from intrusive rocks as well as sericite and alunite related to the first and second mineralization stage, respectively, have been conducted. This study has been complemented by Rb-Sr and Pb isotope analyses of sericite and associated pyrite.

The single zircon U-Pb survey reveals that the ages of an accretionary lapilli tuff from a collapsed block within the diatreme (15.36 ± 0.03 Ma), a dacitic porphyry dome in the diatreme (15.40 ± 0.07 Ma), and two quartz-monzonite porphyritic dykes emplaced into the diatreme-dome complex (15.35 ± 0.35 Ma and 15.16 ± 0.03 Ma) are comprised within a time span of 350'000 yr. No field evidence has been found so far that magmatic activity at the surface could have started earlier than the formation of the diatreme-dome complex.

Step-wise IR-CO_2 laser $^{40}Ar/^{39}Ar$ ages have been obtained on second mineralization stage alunite from advanced argillic altered domes and from halos of oxidized enargite-pyrite veins in the Venencocha and Santa Rosa areas, located on the northwestern margin of the diatreme-dome complex and on the southern part of the Cerro de Pasco open pit, respectively. $^{40}Ar/^{39}Ar$ alunite ages cluster between 14.54 ± 0.08 and 14.41 ± 0.07 Ma. The age consistency suggests that advanced argillic alteration related to the second mineralization stage at Cerro de Pasco has been produced during a short period of around 100'000 yr. Three alunite ages at 12.39 ± 0.06, 12.13 ± 0.07 Ma, and 10.94 ± 0.1 Ma, outliers of the main age cluster (14.5 - 14.4 Ma), are interpreted to have probably experienced resetting by late circulating fluids. Therefore, magmatic-hydrothermal activity at Cerro de Pasco appears to have lasted for around 1 My, from 15.4 to 14.5 Ma, a relatively short time span for such a large mineralized system but in the same range as at the nearby Mid Miocene Colquijirca District.

An attempt to date more precisely the first mineralization stage, bracketed in time between the quartz-monzonite dykes and the second mineralization stage, i.e. between 15.1 and 14.5 Ma, has failed because $^{40}Ar/^{39}Ar$ ages obtained on sericite occurring in the alteration halo of the pyrite-quartz body are not reliable probably due to inherited argon derived from micas contained in Paleozoic clasts within the diatreme breccia.

Sericite Rb-Sr data sericite indicate binary geochemical mixing between Miocene magmatic and Paleozoic basement sources. Lead isotopic compositions of pyrite and sericite ($^{206}Pb/^{204}Pb$ = 18.743 - 18.922, $^{207}Pb/^{204}Pb$ = 15.629 - 15.660, $^{208}Pb/^{204}Pb$ = 38.789 - 38.958) are comparable to those published previously of galena at Cerro de Pasco, Colquijirca, San Cristobal, and Morococha, and are explained by magmatic mixing of enriched upper mantle-derived lead and radiogenic upper crustal rocks lead

Microthermometric data on fluid inclusions in quartz indicate that the different ores of the first mineralization stage formed at similar temperatures and moderate salinities (pyrite-quartz body: 200 – 275°C and 0.2 – 6.8 wt % NaCl equiv, pyrrhotite bodies: 192 – 250°C and 1.1 – 4.3 wt % NaCl equiv., and Zn-Pb ores: 183 – 212°C and 3.2 – 4.0 wt % NaCl equiv.). These values are in the same range as those obtained for fluid inclusions of second stage quartz and sphalerite (enargite-pyrite veins: 187–293°C and 0.2–5.2 wt % NaCl equiv., carbonate replacement bodies quartz: 178–265°C and 0.2–7.5 wt % NaCl equiv., carbonate replacement bodies sphalerite: 168–222°C, and Venencocha: 245–261 and 3.2–7.7 wt % NaCl equiv.). Oxygen and hydrogen isotope compositions have been measured for kaolinite from carbonate replacement bodies ($\delta^{18}O$ = 5.3 to 11.5 ‰, δD = –82 to –114 ‰) and in alunite from the Venencocha and Santa Rosa areas ($\delta^{18}O$ = 1.9 to 6.9 ‰, δD = –56 to –73 ‰). Oxygen isotope compositions of quartz from the first and second mineralization stages have $\delta^{18}O$ values from 9.1 to 17.8 permil. Calculated fluids in equilibrium with kaolinite and alunite have $\delta^{18}O$ values of 2.0 to 8.2 permil and δD values of –69.4 to –96.8 permil, l and –1.4 to –6.4 ‰ and –62 to –79 ‰, respectively. Sulfur isotope compositions of sulfides from both stages have a narrow range of $\delta^{34}S$ values between –3.7 and 4.2 permil, and sulfates from the second stage between 4.2 to 31.2 permil. The microthermometric data and the stable isotope studies define two mixing trends of the ore-forming fluids.. The first trend reflects mixing between a saline magmatic end-member and an isotopically exchanged hydrothermal end-member of meteoric origin. According to the available data, for all ore types, except perhaps for the enargite-pyrite veins from the western part of the open pit, the saline end-member should correspond to a hypersaline magmatic fluid. According to the data concerning the enargite-pyrite veins, the saline magmatic end-member could also correspond to a contracted vapor separated at great depth or a single phase fluid. The second mixing trend is revealed by the stable isotope results of alunite and points toward mixing of volcanic SO_2 vapor plumes and unexchanged meteoric water.

The hydrothermal system at Cerro de Pasco was emplaced at shallow levels (in the order of 500 m) in the epithermal part of a porphyry environment. The similar temperatures and salinities obtained for the first (pyrite-quartz body, pyrrhotite pipes and related Zn-Pb ores) and second mineralization stages (enargite-pyrite veins and carbonate replacement bodies) jointly with the stable isotope study has permitted to conclude that they are linked and represent successive mineralizing stages of a Cordilleran base metal deposit.

RÉSUMÉ ÉTENDU

Introduction

Cette thèse de doctorat a été consacrée au gisement polymétallique de Cerro de Pasco, situé à 180 km au nord-est de Lima, dans le Pérou central. Les ressources, incluant la production passée, correspondent à un total de 175 Mt @ 7 % Zn, 2 % Pb et 3 oz/t Ag. De plus, avant 1950, l'activité minière a produit plus de 1200 Moz d'Ag, 2 Moz d'Au et environ de 50 Mt @ 2 % Cu. Ce gisement est exploité depuis le milieu du 17 siècle (1630) mais il fut probablement connu depuis plus longtemps. Il a d'abord été exploité pour ses ressources en argent présentes dans des parties oxydées du gisement, puis pour le cuivre dans les veines d'énargite et pyrite et jusqu'à nos jours, le zinc, l'argent et le plomb sont exploités avec le cuivre, le bismuth et l'or comme sous-produit.

Le district de Cerro de Pasco, situé sur les hauts plateaux andins, est composé d'une mine à ciel ouvert et de galeries souterraines. Dans la mine à ciel ouvert, les conditions d'affleurement sont très bonnes, mis à part du fait que certaines parties sont actuellement inaccessibles. Dans la mine souterraine, nombreuses sont les parties anciennes inaccessibles. Cette étude a principalement été effectuée à l'aide d'une cartographie à l'échelle régionale, à l'échelle locale de zones clés au sein de la mine à ciel ouvert et d'échantillons provenant de forages et de certaines galeries de la mine souterraine.

Cadre géologique

Le gisement de Cerro de Pasco est encaissé, en bordure d'un complexe dôme-diatrème, principalement dans des séries carbonatées du Trias Supérieur - Jurassique Inférieur appartenant au Group du Pucará. Ces séries sont composées, dans le voisinage de la mine, de successions de carbonates sableux, de carbonates foncé bitumineux, de niveaux à nodules de chert, de niveaux massifs fossilifères ainsi que de niveaux à carbonates massifs (Jenks, 1951; Angeles, 1999). Le volcanisme dans la région de Cerro de Pasco est constitué par l'emplacement d'un diatrème et de dômes dacitiques en bordure du complexe. Des dykes plus tardifs de composition quartzo-monzonitique recoupent le diatrème. Le diatrème et ses environs ont été érodé depuis le Miocène Moyen, éliminant les faciès de surface en laissant affleurer les roches encaissantes plus profondes qui sont principalement des phyllites, des shales et quartzites appartenant au Groupe de l'Excelsior. Une partie du gisement de Cerro de Pasco est encaissé dans la brèche de diatrème, le complexe dôme-diatrème ayant été mis en place durant le Miocène Moyen (voir section geochronologie) aux abords d'une faille de direction N-S.

Minéralisation et altération

Cette étude confirme que le gisement de Cerro de Pasco appartient à la classe des gisements épithermaux de type polymétallique Cordilleran. Ces gisements se situent spatialement à l'aplomb d'un environnement porphyrique. Deux stades de minéralisations, possédant une minéralogie contrastée, sont présents à Cerro de Pasco (Fig. 1). Le premier stade (IA), qui se situe en bordure Est du complexe de diatrème-dôme, consiste en un large corps de pyrite-quartz qui remplace essentiellement les roches carbonatées du Groupe du Pucará, d'âge Trias Supérieur- Jurassique Inférieur et, dans une moindre mesure, la brèche de diatrème. Ce corps est composé de pyrite avec des inclusions de pyrrhotine, du quartz, et de la calcédoine noir et rouge (contenant de l'hématite hypogène). La brèche de diatrème, au contact avec le corps de pyrite-quartz, est altérée en sericite-pyrite-quartz, typique de l'altération phyllique. Par la suite (stade IB), des corps de pyrrhotine, en forme de conduits verticaux allongés, ont été mis en place au sein du corps de pyrite-quartz. Ces corps verticaux sont zonés à des minerais à Zn-Pb (contenant de la sphalerite riche en fer) qui se sont mis en place en remplacement dans les roches carbonatées du Pucará. Les corps verticaux

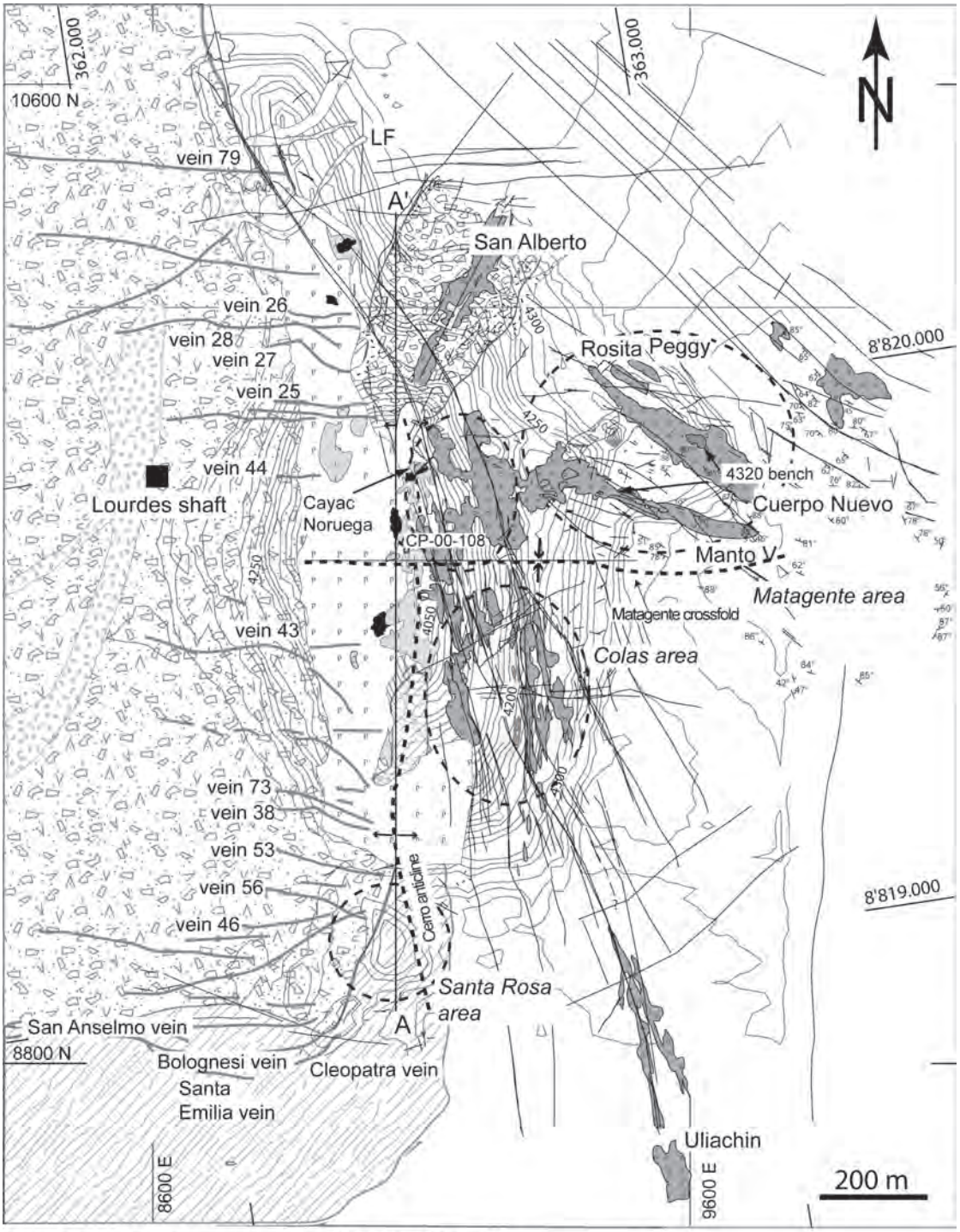

Fig. 1: *Carte géologique du gisement de Cerro de Pasco indiquant les unités lithologiques, les failles et la localisation des deux stades de minéralisations. Cette carte basée sur des archives du groupe de géologie de la mine de Cerro de Pasco. Il est à noter que les coordonnées UTM ainsi que les coordonnées locales sont indiquées.*

de pyrrhotine, présentent une zonation vers l'extérieur et vers le haut défini par Einaudi (1977) et comprend les associations minérales suivantes : 1) pyrrhotine + quartz + wolframite (parties profondes), 2) pyrrhotine + sphalerite + chalcopyrite + stannite + (parties profondes à intermédiaires) et 3) pyrrhotine + sphalerite + arsenopyrite (présent dans toute l'extension verticale des corps de pyrrhotine). Cette dernière association minérale persiste horizontalement dans les minerais à Zn-Pb qui sont caractérisés par de la sphalérite riche en fer (FeS jusqu'à 25 % mole), formant des corps de remplacement qui sont structuralement contrôlés par le synclinal de Matagente (Fig. 1).

Les développements récents de la mine ont permis une étude minéralogique et distribution spatiale détaillée du second stade de minéralisation (II) qui télescope partiellement le premier stade. Le deuxième stade de minéralisation est caractérisé par des veines à Cu-Ag-(Au-Zn-Pb) encaissées dans la brèche de diatrème et des corps de remplacement à Zn-Pb-(Bi-Ag-Cu) encaissés dans les carbonates du Pucará, tous deux essentiellement contrôlés par des failles ayant pour direction N35°E, N90°E, N120°E et N170°E (Fig. 1). Les veines à Cu-Ag-(Au-Zn-Pb), situées dans la partie Ouest du gisement, possèdent un cœur bien développé à énargite-pyrite accompagné d'alunite-zunyite et de diaspore. La zone intermédiaire est constituée de tennantite, chalcopyrite et minéraux de Bi ainsi que de la kaolinite. La zone externe, faiblement développée, est composée de sphalerite pauvre en fer (moins de 3.5 mole % FeS) et de galène. Les corps de remplacement à Cu-Ag-(Au-Zn-Pb) dans les roches carbonatées, situés principalement dans la partie Est en centrale du gisement, forment des corps en forme de tubes verticaux avec une zonation bien développée. Le centre du corps est composé de famatinite-pyrite avec de l'alunite. La zone intermédiaire est composée de tétrahedrite-pyrite, de la chalcopyrite, des minéraux de Bi ainsi que de la hinsdalite (minéral appartenant à la famille des alumino-phosphates-sulfates) et de la kaolinite alors que la zone externe est composée de sphalérite pauvre en fer (0.05 - 3.5 % mole de FeS), de galène ainsi que de hinsdalite et kaolinite. La zone la plus externe consiste en hématite, magnétite ainsi que des carbonates de Fe-Mn-Zn. Contrairement aux veines encaissées dans la brèche de diatrème, les zones intermédiaires et externes des corps de remplacements sont les mieux développées.

Dans l'aire de Venencocha, qui est située à 2.5 km au Nord-Ouest du diatrème, ainsi que dans l'aire de Santa Rosa (Sud de la mine à ciel ouvert), on observe des dômes dacitiques qui ont été affectés par une altération argillique avancée ainsi que des veines oxydées possédant des halos d'altération argillique avancée. Ces dernières sont l'équivalent oxydé des veines de pyrite-énargite.

La plupart des corps de remplacement dans les roches carbonatées plongent entre 25 et 60° en direction du diatrème, ce qui suggère que les fluides hydrothermaux sont issus de niveaux plus profonds et n'ont donc pas été alimenté latéralement les veines d'énargite-pyrite, comme suggéré auparavant par Einaudi (1977). Par contre, aussi bien les veines à énargite-pyrite que les corps de remplacements dans les roches carbonatées sont probablement le résultat de fluides émanent du même système hydrothermal et qui ont emprunté des parcours distincts. Les données des inclusions fluides et des isotopes stables soutiennent cette hypothèse (cf. section inclusions fluides). Cette observation est également reflétée par une composition minéralogique différente des coeurs des veines d'énargite (riche en Cu, As et Au) et ceux dans les corps de remplacement dans les roches carbonatées (pauvre en Cu et As et Au virtuellement absent).

La zonation minérale présente dans le second stade de minéralisation peut être expliqué en termes d'avancements et de retraits de fluides, qui sont contrôlés par l'activité hydrothermale et la nature de la roche encaissante. Pendant l'avancement de fluides, les assemblages de la zone interne empiètent sur ceux des zones externes. Lors du retrait de fluides, les assemblages des zones externes empiètent sur ceux des zones internes. La brèche de diatrème qui est une roche peu réactive, gêne l'infiltration des fluides dans les épontes de la veine dans la roche encaissante. Dans les carbonates plus poreux et réactifs du Pucará, des corps plus étendus ont été formés.

D'après les températures de déposition dérivées de l'étude des inclusions fluides, les assemblages minéralogiques d'état de sulfidation bas sont prédominants dans le premier stade de minéralisation, comme le suggère la présence d'inclusions de pyrrhotine dans la pyrite et la précipitation de corps verticaux de pyrrhotine zonés à des minerais de Zn-Pb contenant de la sphalérite riche en Fe. Cependant, la présence d'hématite hypogène dans le quartz appartenant au corps de pyrite-quartz suggère que les fluides étaient localement oxydants, ce qui typique des fluides magmatiques exsolvant d'un magma. Il est conclut que ces fluides magmatiques ont été réduits par leur interaction avec les phyllites de la Formation Excelsior. Le halo d'altération quartz-sericite dans la brèche de diatrème aux abords du corps de pyrite-quartz suggère des conditions acides modérées pour le premier stade de minéralisation.

Le deuxième stade de minéralisation est caractérisé par des assemblages minéralogiques d'états de sulfidation hauts à intermédiaires contenant de la sphalérite pauvre en Fe. Les assemblages d'altération avec développement de vuggy quartz dans le diatrème et de la déposition d'alunite aussi bien dans les veines d'énargite-pyrite que dans le centre des corps de replacements au sein des roches carbonatées indiquent des fluides très acides. Les fluides minéralisateurs du second stade ont été structuralement contrôlés par des fractures, probablement avec un rapport fluide/roche élevé, en raison d'une interaction

avec la roche encaissante limitée, dont la capacité de tamponnage a été réduite lors du premier stade de minéralisation, ce qui expliquerait les conditions prédominantes high sulfidation durant le second stade de minéralisation.

Géochronologie

Dans le but d'obtenir des informations sur la durée absolue du système magmato-hydrothermal, une étude U-Pb ainsi que les isotopes de Hf sur zircon provenant des roches magmatiques a été conduite. De plus, une étude $^{40}Ar/^{39}Ar$ à l'aide de la méthode par paliers avec laser IR-CO_2 sur biotite des roches intrusives, sur sericite et alunite liés au premier et deuxième stade de minéralisation, respectivement, a été effectuée (Fig. 2). En outre, des analyses isotopiques de Rb-Sr et Pb ont été réalisés sur la pyrite et la sericite.

Les ages U-Pb sur zircon révèlent que les ages de lapilli accrétionnés d'un bloc collapsé au sein du diatrème (15.36 ± 0.03 Ma), des dômes porphyriques de composition dacitique dans le diatrème (15.40 ± 0.07 Ma, daté sur un dôme), et des dykes porphyriques de composition quartzo-monzonitique, mis en place au sein du complexe de diatrème-dôme (15.35 ± 0.35 Ma et 15.16 ± 0.03 Ma) sont compris dans un laps de temps de 350'000 ans. Aucune évidence de terrain ne suggère que l'activité magmatique ait commencé avant le complexe de dôme-diatrème.

La géochronologie $^{40}Ar/^{39}Ar$ avec laser IR a été effectuée sur des alunites provenant de l'altération argillique avancée de dôme et des halos d'altération des veines d'énargite-pyrite du second stade de minéralisation ainsi que sur sericite du premier stade. La plupart des âges d'alunite forment un groupe entre 14.5 ± 0.08 et 14.4 ± 0.07 Ma. Cette constance dans les âges indique que l'altération argillique avancée affectant les dômes et les veines oxydées est le résultat d'une activité hydrothermale qui a duré environ 100'000 ans. Trois âges sur alunite à 12.39 ± 0.06, 12.13 ± 0.07 Ma, et 10.94 ± 0.1 Ma ne font pas partie du groupe principal à 14.5-14.4 Ma et sont interprétés comme ayant subit une perturbation lors de circulations de fluides tardifs. De ce fait, le système magmatique-hydrothermal de Cerro de Pasco a probablement duré environ 1 Ma, de 15.4 à 14.5 Ma, ce qui correspond à une durée relativement courte pour un système aussi grand, mais dans la même mesure que le district voisin Miocène Moyen de Colquijirca. Un essai pour dater plus précisément le premier stade de minéralisation, délimité en temps entre la formation des dykes quartzo-monzonitiques et le second stade de minéralisation, c'est-à-dire. entre 15.1 et 14.5 Ma, a échoué car les âges $^{40}Ar/^{39}Ar$ sur séricite présente dans le halo d'altération du corps de pyrite-quartz ne sont pas fiables, probablement à cause de la présence d'argon hérité dérivé de micas provenant de clastes paléozoïques présents dans le brèche de diatrème.

Les données de Rb-Sr sur séricite indiquent un mélange géochimique binaire entre une source magmatique Miocène et un socle paléozoïque. Les compositions isotopiques de Pb de la pyrite et de la séricite ($^{206}Pb/^{204}Pb$ = 18.743 - 18.922, $^{207}Pb/^{204}Pb$ = 15.629 - 15.660, $^{208}Pb/^{204}Pb$ = 38.789 - 38.958) sont compatibles avec celles de galène de Cerro de Pasco, Colquijirca, San Cristobal et Morococha publiées précédemment, qui sont expliquées par un mélange magmatique de plomb dérivé d'un manteau supérieur enrichit et du plomb radiogénique provenant de roches de la croûte supérieure.

Inclusions fluides et isotopes stables

Une étude microthermométrique menée sur des monograins de quartz du premier stade de minéralisation ainsi que sur des monograins de quartz et de sphalérite du second stade indique que les deux stades ont été formés à des températures similaires et des salinités faibles à modérées (Fig. 3). Les inclusions dans le quartz du corps de pyrite-quartz indiquent des températures entre 200 et 275°C et des salinités allant de 0.2 à 6.8 % poids NaCl équiv. Les températures d'homogénisation des inclusions dans quartz des corps verticaux de pyrrhotine varient entre 192 et 250°C et la salinité varie entre 1.1 et 4.3 % poids NaCl équiv., alors que les inclusions dans le quartz des corps de Zn-Pb (liés au corps verticaux de pyrrhotine) indiquent des températures allant de 183 à 212°C et des salinités variant de 3.2 à 4.0 % poids NaCl équiv. Les valeurs de températures d'homogénisation et salinités du premier stade de minéralisation sont du même ordre que ceux obtenus dans les inclusions fluides piégés dans le quartz et la sphalérite du second stade de minéralisation (veines d'énargite-pyrite = 187–293°C et 0.2–5.2 % poids NaCl équiv., quartz des corps de remplacement encaissés dans les roches carbonatées = 178–265°C et 0.2–7.5 % poids NaCl équiv., sphalérite des corps de remplacement encaissés dans les roches carbonatées = 168 – 222°C, et Venencocha = 245–261 et 3.2–7.7 poids % NaCl équiv., Fig. 3).

Les isotopes d'oxygène et d'hydrogène ont été mesurés sur des échantillons d'alunite provenant des zones d'altération argillique avancée à Venencocha et Santa Rosa. $\delta^{18}O$ varie entre 1.9 et 6.9 ‰ alors que δD varie entre –56 et –73 ‰. Les rapports isotopiques calculées des fluides en équilibre avec l'alunite

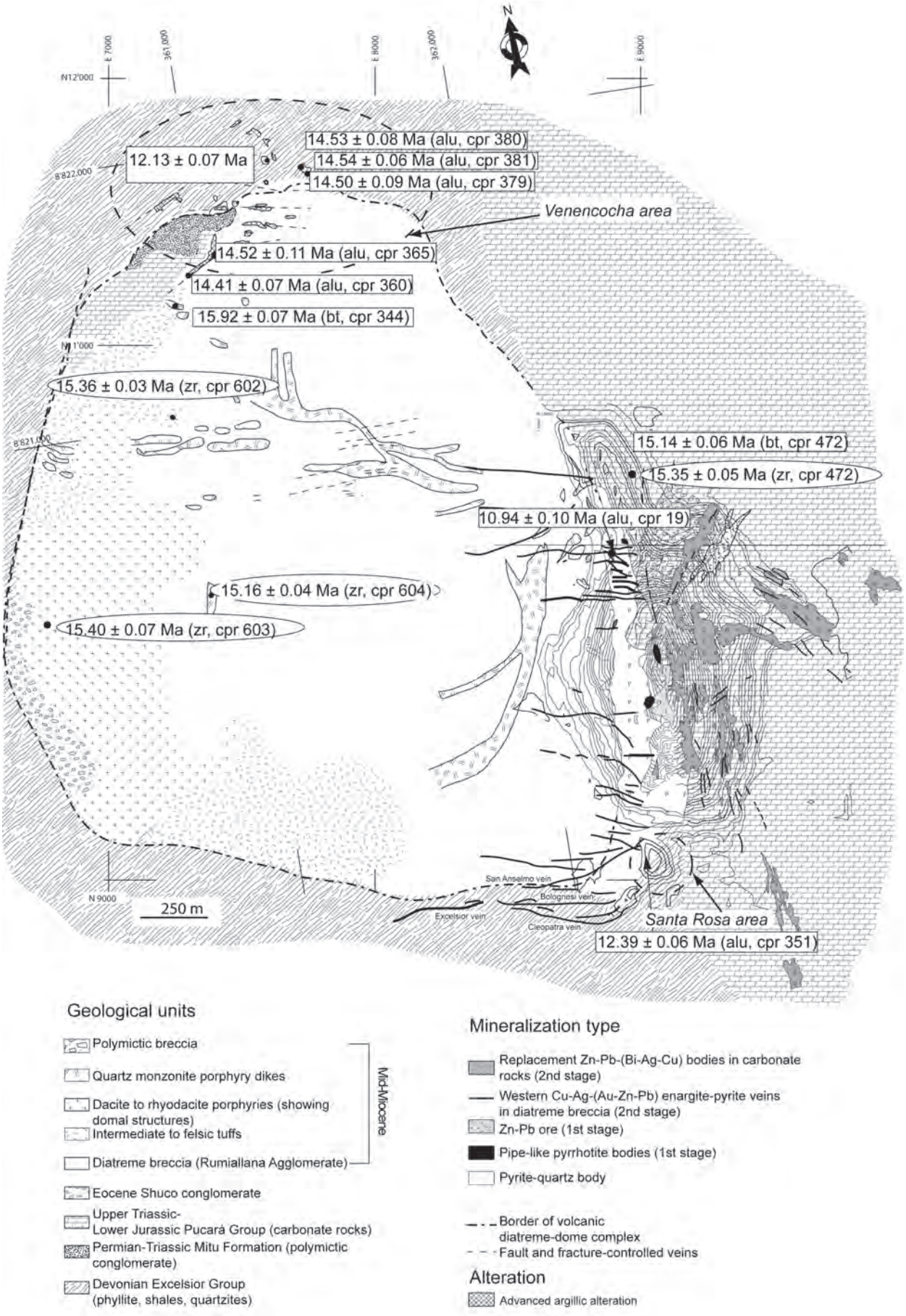

Fig. 2 : Carte géologique du complexe de dôme-diatrème à Cerro de Pasco, compilée de Rogers, (1983) et Huanqui (1994) ainsi que de la géologie de la mine à ciel ouvert. Les âges U-Pb sur zircon et U-Pb et les âges $^{40}Ar/^{39}Ar$ sur biotite et alunite sont indiqués. Les abbreviations sont: alu = alunite, bt = biotite, and zr = zircon.

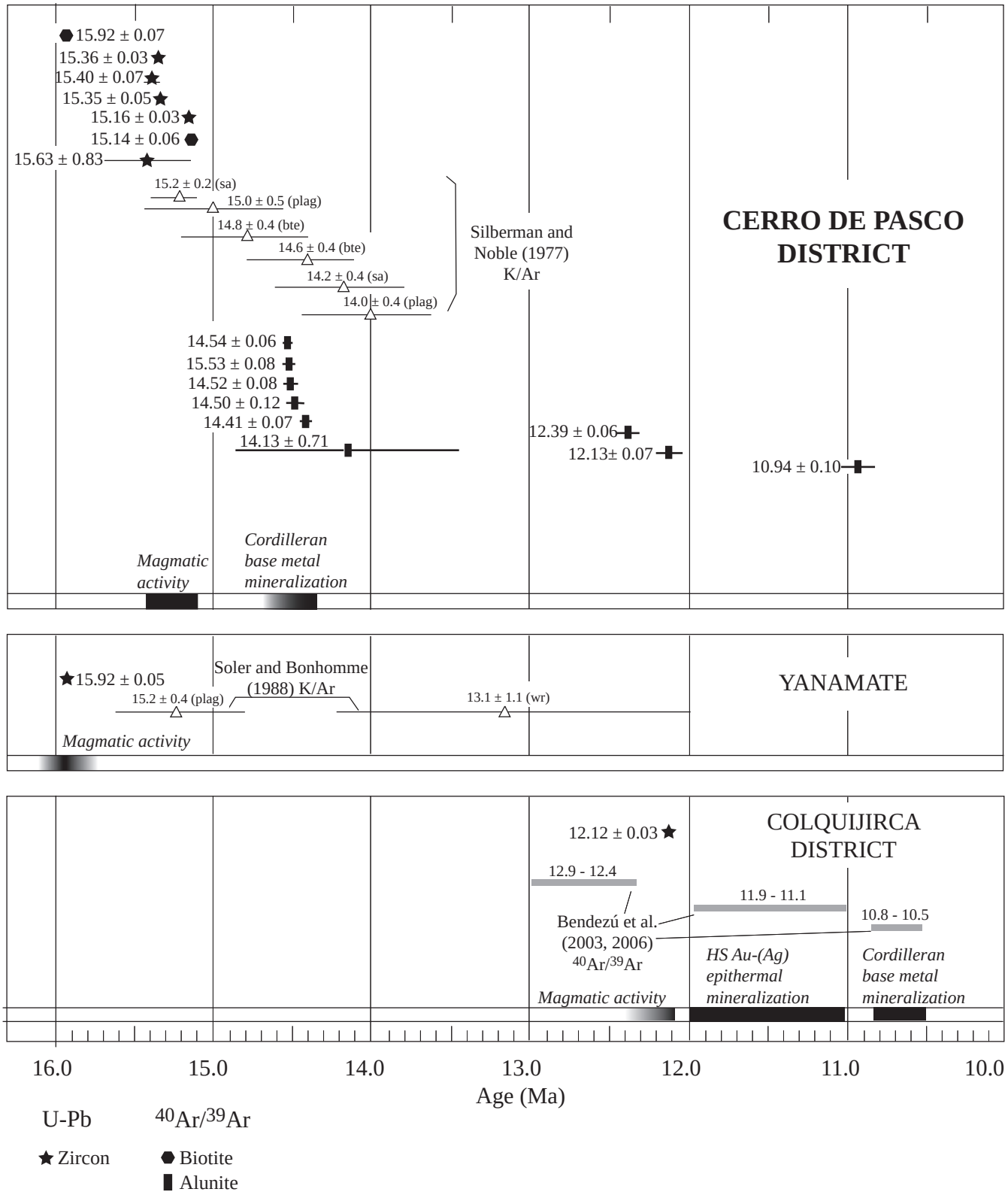

Fig. 3: *Diagramme résumant les données U-Pb and 40Ar/39Ar de cette étude et incluant les données géochronologiques préexistantes. Les barres d'erreurs sont ± 2σ. Les abbreviations sont: sa = sanidine, plag = plagioclase, wr = whole rock (roche totale).*

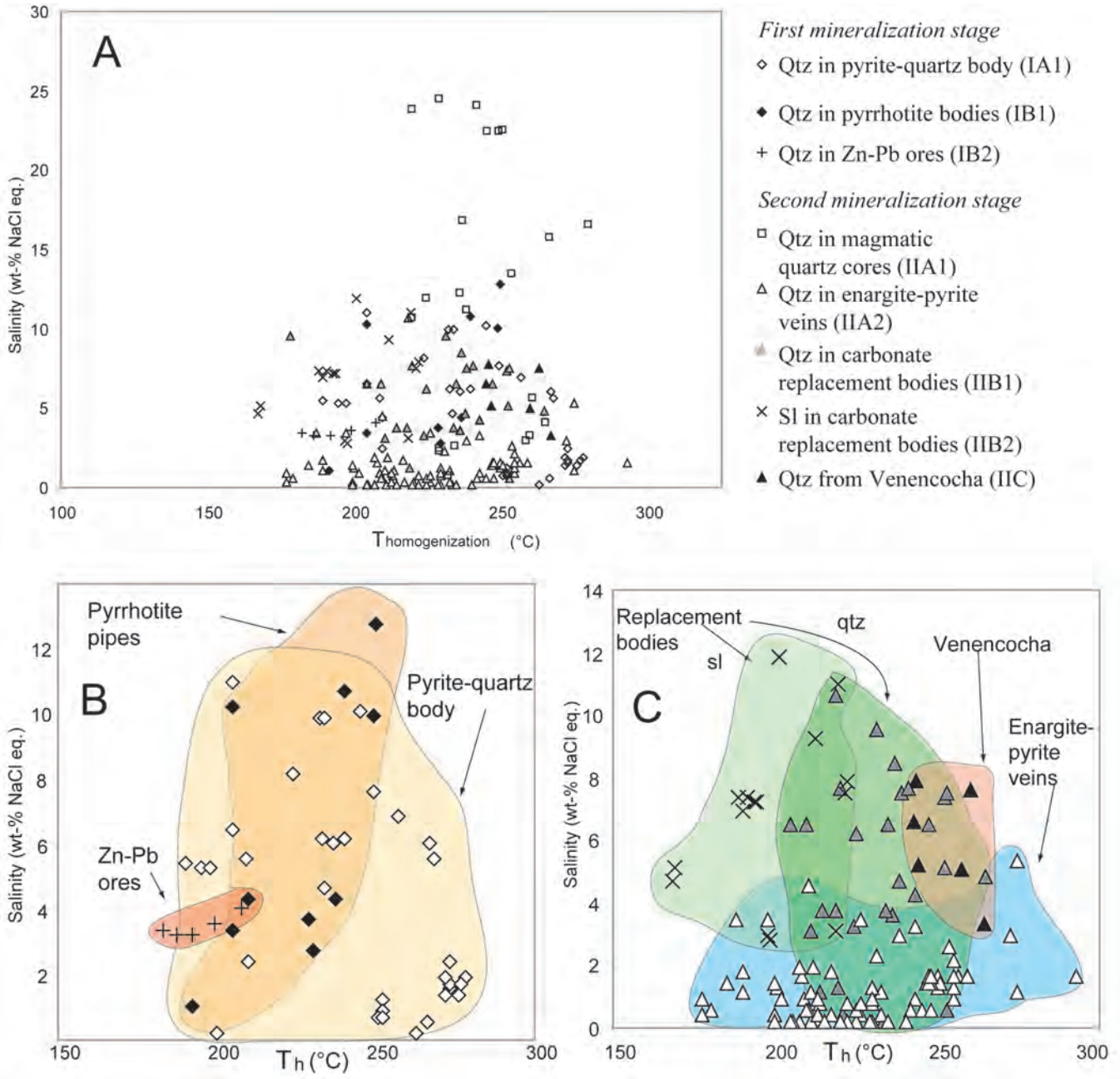

Fig. 4: *A) Température d'homogénisation (Th) vs. salinité (% poids NaCl equivalent) d'inclusions fluides dans le quartz du premier et second stade de minéralisation et dans la sphalérite des corps de remplacements dans les roches carbonatées (second stade). B) Détail de A, Th vs. salinité d'inclusions fluides dans le quartz du premier stade de minéralisation incluant le corps de pyrite-quartz, les pipes de pyrrhotine et les minerais à Zn-Pb liés à ceux-ci. C) Détail de A) Th vs. salinité des inclusions fluides dans du quartz du second stade de minéralisation incluant les veines d'énargite-pyrite, les corps de remplacement dans les roches carbonatées (aussi avec les inclusions fluides dans la sphalérite) et les veines d'énargite-pyrite oxydées de Venencocha.*

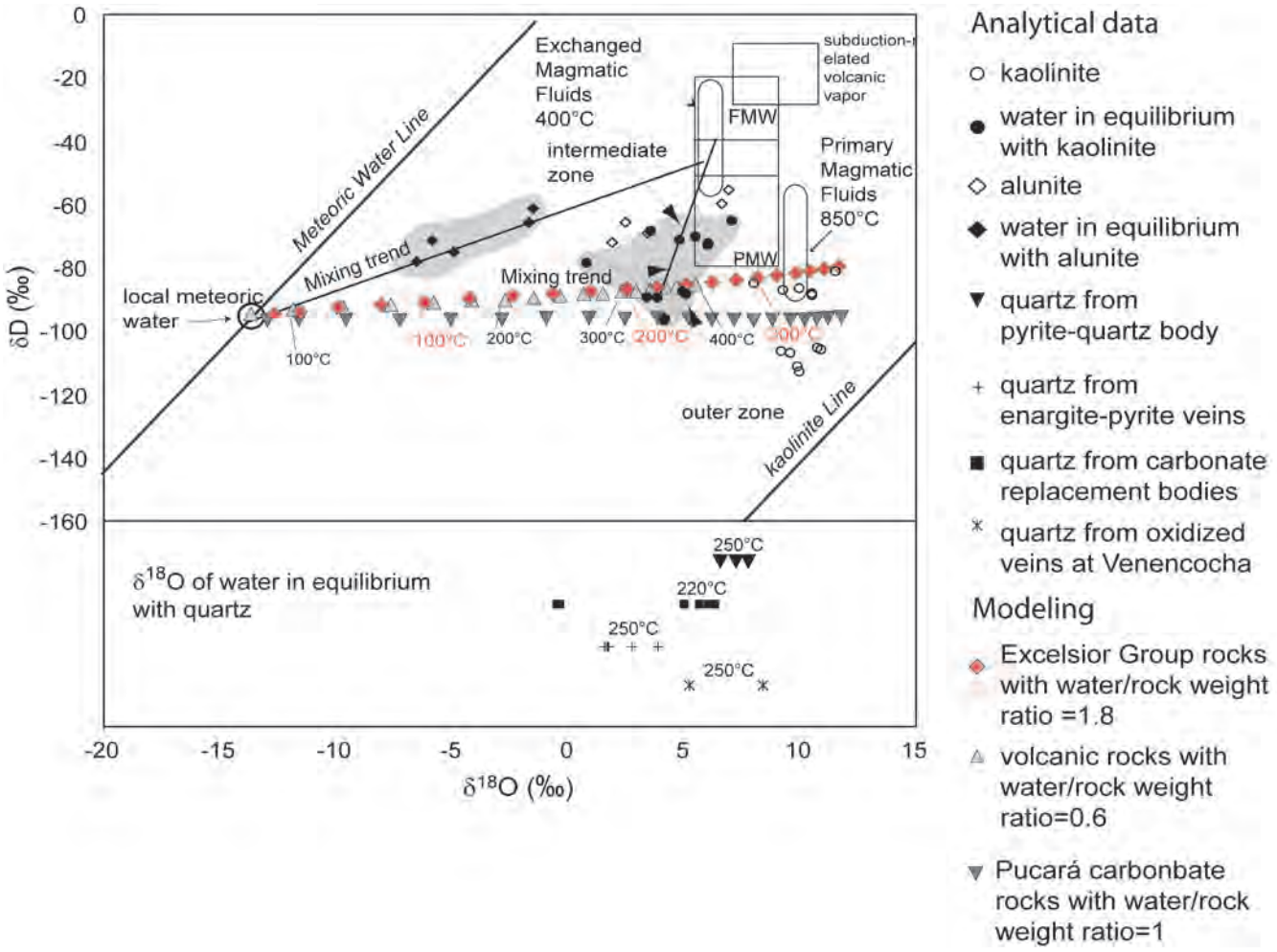

Fig. 5: Diagramme δD vs. $\delta^{18}O$ plot d'alunite et kaolinite et des fluides correspondant en équilibre avec ces minéraux. Les valeurs de δD et $\delta^{18}O$ des fluides en équilibre avec l'alunite (des veines d'énargite-pyrite oxydées de Venencocha) on été calculées à l'aide de l'équation de Stoffregen et al. (1994) à 250°C. Une ligne de mélange montre les deux pôles formant les fluides ayant formés l'alunite. Cette ligne de mélange recoupe la ligne de l'eau météorique de Craig (1961) à des valeurs de δD et $\delta^{18}O$ pour les fluides météoriques au Miocène Moyen à Cerro de Pasco (δD = ~95 ± 10 ‰ and $\delta^{18}O$ close to 13 ± 1 ‰. Les valeurs de δD et $\delta^{18}O$ des fluides en équilibre avec la kaolinite ont été calculées à l'aide de l'équation de Sheppard and Gilg (1996) pour O et Gilg and Sheppard (1996) pour H, à 220°C pour la kaolinite de la zone intermédiaire et à 200°C pour la zone externe des corps de remplacements dans les roches carbonatées. Le champs de la kaolinite se situe sur une courbe de mélange entre les fluides magmatiques de Deen et al. (1994) et un pôle composé d'eau météorique isotopiquement échangée à des températures de 200-250°C. Les valeurs de δD et $\delta^{18}O$ de l'eau météorique échangée avec des roches volcaniques et du Groupe de l'Excelsior ont été modélisées. Le modèle montre que le pôle composé d'eau météorique isotopiquement échangée en profondeur à des températures de 200-250°C. Dans la partie inférieure du diagramme, les valeurs de $\delta^{18}O$ des fluides en équilibre avec le quartz sont présentés et ont été calculés à l'aide de l'équation de Zhang et al. (1989) à 250°C pour le quartz du corps de pyrite-quartz, à 220°C pour le quartz présent dans le centre des corps de remplacements, à 250°C pour le quartz des veines d'énargite-pyrite dans la mine et celles oxydées à Venencocha. Zhang et al. (1989) at 250°C. Les autres champs et lignes présents sont la ligne de la kaolinite de Sheppard et al. (1969), les fluides magmatiques primaires de Deen et al. (1994), l'eau magmatique felsique (FMW) de Taylor (1992), l'eau magmatique primaire (PMW) de Taylor (1979) et les vapeurs volcaniques liées aux zones de subductions de Giggenbach (1997).

ont des valeurs de $\delta^{18}O$ entre l et −1.4 ‰ et des valeurs de δD entre −62 et −79‰ et se situent, dans un diagramme $\delta^{18}O$ sur δD, sur une ligne de mélange entre un pôle d'eau météorique et un pôle d'eau magmatique. Par contre, les résultats des compositions isotopiques calculées d'oxygène et d'hydrogène de kaolinite provenant de la zone intermédiaire et externe des corps de remplacement dans les roches carbonatées ($\delta^{18}O$ = 2.0 à 8.2 ‰ et δD = −69.4 à −96.8 ‰) donnent des valeurs de $\delta^{18}O$ entre 5.3 et 11.5 ‰ et δD entre – 82 et −114 ‰, se situant en dessous de cette ligne de mélange (Fig. 4). En compilant ces résultats avec ceux obtenus à l'aide des inclusions fluides, deux tendances de mélange peuvent être mises en évidence. La première tendance, mise en évidence par les mesures effectuées sur les kaolinites, reflète un mélange entre un pôle de d'eau magmatique saline et un pôle d'eau météorique qui a subi un échange isotopique avec les roches encaissantes (phyllite et shale du Groupe Excelsior). D'après les données disponibles pour les deux stades de minéralisation, peut être mis à part les veines d'énargite-pyrite situées dans la partie ouest du gisement, le pôle magmatique salé pourrait représenter un fluide magmatique hypersalin. En ce qui concerne les veines d'énargite-pyrite, le pôle d'eau magmatique salée pourrait aussi correspondre à une vapeur contractée qui a été séparée à grande profondeur (selon Heinrich, 2005) ou à un fluide à une phase (selon Hedenquist et al., 1998). La deuxième tendance de mélange, mise en évidence par les résultats des isotopes stables sur alunite, montre un mélange entre des vapeurs volcaniques de SO_2 et des eaux météoriques isotopiquement non-échangées.

Au terme de cette étude, il a été montré que le système hydrothermal de Cerro de Pasco a été mis en place à de faibles profondeurs (dans l'ordre de 500-800 m) dans la partie épithermale d'un système porphyrique. Les températures et les salinités qui ont été obtenues lors de cette étude pour le premier stade de minéralisation (corps de pyrite-quartz, corps verticaux de pyrrhotine et minerais de Zn-Pb associés) ainsi que pour le second stade de minéralisation (veines à énargite-pyrite et corps de remplacement) sont similaires et, conjointement avec les données d'isotopes stables, il a été possible de conclure que les deux stades sont issus du même système hydrothermal et représentent des stades de minéralisations successifs de type Cordilleran.

Références

Angeles, C., 1999, Los sedimentos Cenozoicos de Cerro de Pasco; estratigrafia, sedimentacion y tectonica, *in* Machare, J., Benavides-Caceres, V., and Rosas, S., eds., Sociedad Geológica del Perú, Volúmen Jubilar, 5, p. 103-118.

Einaudi, M. T., 1977, Environment of ore deposition at Cerro de Pasco, Peru: Economic Geology, v. 72, p. 893-924.

Hedenquist, J. W., Arribas, A., and Reynolds, T. J., 1998, Evolution of an intrusion-centered hydrothermal system; Far Southeast-Lepanto porphyry and epithermal Cu-Au deposits, Philippines: Economic Geology, v. 93, p. 373-404.

Huanqui, F., 1994, Ocurrencias de mineralización en la chimenea volcanica de Cerro de Pasco, Unpublished internal memorandum to A. Alvarez, Empresa Minera del Centro del Perú, p. 15.

Heinrich, C. A., 2005, The physical and chemical evolution of low-salinity magmatic fluids at the porphyry to epithermal transition: a thermodynamic study: Mineralium Deposita, v. 39, p. 864-889.

Jenks, W. F., 1951, Triassic to Tertiary stratigraphy near Cerro de Pasco, Peru: The Geological Society of America Bulletin, v. 62, p. 203-219.

Rogers, R., 1983, Structural and geochemical evolution of a mineralized volcanic vent at Cerro de Pasco, Peru, Unpublished PhD Thesis, University of Arizona, 116 p.

Stoffregen, R. E., Rye, R. O., and Wasserman, M. D., 1994, Experimental studies of alunite: I. 18O-16O and D-H fractionation factors between alunite and water at 250-450°C: Geochimica et Cosmochimica Acta, v. 58, p. 903-916.

Craig, H., 1961, Isotopic variations in meteoric waters: Science, v. 133, p. 1702-1703.

Gilg, H. A., and Sheppard, S. M. F., 1996, Hydrogen isotope fractionation between kaolinite and water revisited: Geochimica et Cosmochimica Acta, v. 60, p. 529-533.

Sheppard, S. M. F., and Gilg, H. A., 1996, Stable isotope geochemistry of clay minerals; The story of sloppy, sticky, lumpy and tough, Cairns-Smith (1971): Clay Minerals, v. 31, p. 1-24.

Deen, J. A., Rye, R. O., Munoz, J. L., and Drexler, J. W., 1994, The magmatic hydrothermal system at Julcani, Peru; evidence from fluid inclusions and hydrogen and oxygen isotopes: Economic Geology, v. 89, p. 1924-1938.

Zhang, X., Nesbitt, B. E., and Muehlenbachs, K., 1989, Gold mineralization in the Okanagan Valley, southern British Columbia; fluid inclusion and stable isotope studies: Economic Geology, v. 84, p. 410-424.

Sheppard, S. M. F., Nielsen, R. L., and Taylor, H. P., 1969, Oxygen and hydrogen isotope ratios of clay minerals

from porphyry copper deposits: Economic Geology, v. 64, p. 755-777.
Taylor, H. P., 1979, Oxygen and hydrogen isotope relationships in hydrothermal deposits, *in* Barnes, H. L., ed., Geochemistry of hydrothermal ore deposits, Wiley and Sons, p. 236-277.
Giggenbach, W. F., 1997, The origin and evolution of fluids in magmatic-hydrothermal systems, *in* Barnes, H. L., ed., Geochemistry of Hydrothermal Ore Deposits: N. Y., Wiley and Sons, Inc., p. 737-796.

INTRODUCTION

THE CERRO DE PASCO DISTRICT

Geographic setting

The Cerro de Pasco district (10°40', 76°20') is located in the Eastern Cordillera of central Peru, 180 km northeast of Lima, at an elevation of 4380 m above sea level. The deposit is one of the most extensively-worked mining districts in Peru. Cerro de Pasco is part of the Miocene Metallogenic Belt of Noble and McKee (1999).

Tectonic evolution and regional geologic setting

The oldest rocks exposed in the Cerro de Pasco district consist of Devonian (400-360 Ma) shale and phyllite with interbedded quartzite of the Excelsior Group (Jenks, 1951). These basement rocks formed in the evolution of the proto-Andean margin of western Gondwana. At the end of the Paleozoic (~250 Ma), the Andean region was situated on the western margin of Pangea (Benavides-Cáceres, 1999). The beginning of subduction along the Pacific margin started at 180Ma along the present trench (Ramos and Aleman, 2000).

Late Permian-Early Triassic extension resulted in intense intra-continental rifting, with horst and grabens displaying an Andean trend (NW-SE), and the deposition of as much as 3000 m of continental red beds, volcaniclastic rocks and alkaline volcanic rocks known as the Mitu Group (Benavides-Cáceres, 1999). This extension was the precursor of Pangean break-up (Ramos and Aleman, 2000). The Mitu red beds overlie the Devonien Excelsior Group with a sharp angular unconformity and consist, in the vicinity of Cerro de Pasco, of conglomerates with pebbles of milky quartz and argillaceous material belonging to the Excelsior Group (Jenks, 1951). Intercalated volcaniclastic and volcanic rocks are prominent within the Excelsior Group 80 km to the south of Cerro de Pasco, do not occur in the Cerro de Pasco district (Jenks, 1951). In the Triassic (230 to 200 Ma), the rifting continued until the opening of the Atlantic Ocean which resulted in intensified extension and the reactivation of the western continental margin subduction (Benavides-Cáceres, 1999). This geodynamic change was marked by the beginning of the Andean cycle as described by Mégard (1984). Carbonate sedimentation occurred, with the deposition of the Pucará Group of the Upper Triassic-Lower Jurassic. On the western side of Cerro de Pasco, the Pucará Group is up to 620 m thick and consists of limestone, dolomite which are locally bituminous. To the east, a 2900 m thick sequence containing limestone and black dolomite (which is commonly bituminous) was deposited (Mégard, 1978). According to Mégard (1978), the thickness difference in the Pucará Group is in part due to a synsedimentary fault which has downthrown the eastern block significantly.

During the Hauterivian-Middle Albian (135-105 Ma), extensional tectonism took place, probably due to an increase in the plate convergence rate at a time of steep-dipping subduction (Soler, 1991). This resulted in the formation of sedimentary basins and the deposition of the Goyllarizquizga Group consisting of terrigenous basal red shaly sandstone and quartz conglomerate with coal lenses at the top of the Group (Jenks, 1951). It usually rests conformably (but is locally slightly discordant) on the Pucará Group (Jenks, 1951). This formation occurs ~5 km to the south and west of Cerro de Pasco but not in the immediate vicinity of the deposit. The Incaic I period of folding (59-55 Ma) produced a major anticline affecting the Excelsior and Pucará Groups in the Cerro de Pasco region. This folding is well developed on the western part of the Cerro de Pasco district, where the Pucará Group is thinner than on the eastern side (Jenks, 1951). During a period of tectonic quiescence, erosion denuded the landscape to moderate relief, close to sea level (Jenks, 1951).

During the Eocene, the Goyllarizquizga Group was succeeded transgressively by marls and limestone (Benavides-Cáceres, 1999) of the Cacuán member, which defines the base of the Pocobamba Formation. It is overlain by the Shuco member, which crops out in the Cerro de Pasco district and consists mainly of alluvial deposits characterized by conglomerate (Angeles, 1999). The Calera Formation sits more or less concordantly on the Shuco member, and consists of shale, siltstone, and sandstone as well as limestone (Jenks, 1951; Angeles, 1999), but is not exposed at Cerro de Pasco. Intense folding and faulting of the Incaic II orogenic pulse (43-42 Ma) ended the period of Pocobamba sedimentation. Several other orogenic pulses occurred subsequently (Incaic III, IV, and Quechua I, II, III, and IV) but are of less importance in the Cerro de Pasco district.

Mid-Miocene (15 Ma), igneous activity formed a diatreme followed by intrusion of dacitic to rhyodacitic porphyritic domes which are presently exposed near the southwestern and northern margins of the diatreme. E-W trending quartz-monzonite porphyry dykes cut the diatreme-dome complex and also extend into the Pucará carbonate rocks. The diatreme breccia, tuffs, and accretionary lapilli crop out on the present-day surface. The ring-dyke tuffs and part of the pyroclastic rocks must have been eroded. Collapsed blocks of Mitu and Pucará Groups in the diatreme-dome complex indicate

that these rock units were once present above the present surface. In the western part of the Cerro de Pasco district, the thickness of the Mitu and Pucará Groups overlying the Excelsior Group is in the order of 400 m (Jenks, 1951). Therefore, erosion is estimated to be in the order of 500 m in the vicinity of the diatreme-dome complex (see Part I). A hydrothermal system related to the diatreme-dome complex produced polymetallic ores mainly on the western border of the diatreme-dome complex, within Pucará carbonate rocks and diatreme breccia, and to a lesser extent within Excelsior phyllite and shale (see Part I).

Mining history

Discovery of the Cerro de Pasco district

While it is quite probable that silver ores were mined before the Spanish conquest at what is now Cerro de Pasco, the first historical record of production from the district dates from 1630 (De Rivero, 1830, 1832; Pickering, 1908; Marsters, 1912). It is reported that the city of Pasco was founded in 1578, and during the year 1567, the first claims were taken (De Rivero, 1830). Numerous ancient works (De Rivero, 1830) report a legend that the mines of Pasco, formerly named the Yauricocha mines, were discovered by a poor shepherd called Huari Capacha. As he was feeding his herd in Santa Rosa one evening, he made a fire to warm himself and at the same time, prepared a scanty meal. The rocks he collected to make a hearth melted and he discovered threads of silver (De Rivero, 1832). He reported his discovery to Don José Ugarte who lived in the town of Pasco. At that time, the inhabitants were mainly employed in the mines at Colquijirca, 10 km to the south of Cerro de Pasco. Convinced by this discovery, he began to work in Santa Rosa with great success. The local prospectors soon discovered numerous orebodies in the extensive iron-stained outcrops (pacos) and active production of silver started, which was maintained with few interruptions for nearly two hundred years (De Rivero, 1832). In 1816, at the onset of the industrial revolution and steam engines, a group headed by Pedro Abadia began deeper excavation and native silver were encountered, named at that time pavonados and polvorillas (De Rivero, 1830). Drainage tunnels were built to pump out water (such as the Quilacocha, the Rumiallana, and the Avellafuerte tunnels). In 1827, more than 558 small mines existed, situated at Yauricocha, Santa Rosa, Caya, Yanacancha, and Matagente (Fig. 1A and B). The Matagente mines were at this period the richest and the most actively exploited. Their exploitation was interrupted by an accident in which three hundred workmen were buried and killed, and the location where this happened has been called ever since the Matagente area.

From the Cerro de Pasco Corporation to Volcán Compañía Minera S.A.

In 1901, the "Cerro de Pasco Investment Company" of New York began the mining workings at Cerro de Pasco (Fig. 2A). In 1904, the Railway between La Oroya and Cerro de Pasco was completed by the "Cerro de Pasco Railway". Also at that time, the old smelter of Tinyahuarco (Fig. 2B), formerly the "Smelter", and subsequently named "La Fundición" was built, along with the opening of the coal mines at Goyllarisquisga, and the installation of a new mining plant permitted modern scale exploitation. In 1915, the merger of the "Cerro de Pasco Mining Corporation", the "Cerro de Pasco Railway", and "Morococha Mining" gave birth to the "Cerro de Pasco Copper Corporation". Between 1630 and the end of the 19th Century, silver was the main metal exploited. From 1904, Cerro de Pasco was mainly a copper producing mine. Narrow and rich copper veins and orebodies (mainly enargite and chalcopyrite) were mined to a depth of 700 m, mainly in the western part of the present open pit. Silver and gold were recovered from the copper concentrate. These were produced by "La Fundición" at Smelter, owned by the "American Smelting and Refining Metal Corporation" (ASARCO). In 1943, the Paragsha mining plant was constructed at Cerro de Pasco and in mid - 1946, lead and zinc were treated and exported. From 1946 onwards, Cerro de Pasco became a Zn-Pb-Ag producer. In 1956, the open pit mining began in the new "MacCune" pit, which is presently the location of the "Rául Rojas" open pit (Fig. 2C and D).

In 1973, the Peruvian government expropriated the Cerro de Pasco Corporation and nationalized most of the Peruvian mines by founding the "Empresa Minera del Centro del Peru" (CENTROMIN). Cerro de Pasco was again privatized in 1999 and Vólcan Compánia Minera S.A. won the tender. This company is the present owner and exploiter of the Cerro de Pasco deposit.

Production estimates

The production has been estimated using several bibliographical sources. The most relevant include Pickering (1908), Marsters (1912), McLaughlin (1924), Jiménez (1924), Bowditch (1935), Geological staff of Cerro de Pasco Corporation (1950), Fischer (1977), Einaudi (1977), Bartos (1989), as well as Bendezú (pers. comm. 2004) and the Cerro de Pasco geology staff (pers. com. 2004). Estimates for the period between 1630 and 1880 are believed to have been underestimated by about 30 to 40% due to smuggling and this has been taken into account in the overall production estimates. The total contained silver at Cerro de Pasco is estimated to amount to at least 1450 Moz, excluding the non-estimated global resources. For zinc, lead and gold, post 1950 production plus known resources amount to more than ~175 Mt @ 7 percent Zn and 2 percent Pb. In addition, prior to 1950, 2 Moz of Au and around 50 Mt @ 2 percent Cu were mined.

Previous work and literature

The earliest works deal mainly with the exten-

sive oxidized "pacos" deposits, while the geology was usually poorly understood and therefore not described. Most of the early accounts are of historical rather than scientific interest. De Rivero (1830), De Rivero (1832), Raimondi (1902), Pickering (1908), and Jiménez (1924) report the beginning of the mining operations. Fuchs (1920) was the first to suggest (in print) that the igneous rocks represent an ancient volcanic edifice. McLaughlin (1924) and later Jenks (1951) and Mégard (1978) made a detailed description of the geology of Cerro de Pasco and its surroundings. Recently, Angeles (1999) published a detailed stratigraphic and tectonic description of the Cenozoic sedimentary rocks in the Cerro de Pasco district.

From a metallogenic point of view, the first descriptions of the Cerro de Pasco deposit deal with the oxidized Ag-rich ores, the pacos (De Rivero, 1830, 1832; Bowditch, 1935; Lacy, 1949; Amstutz and Ward, 1956). As soon as exploitation of deeper hypogene ores began (at the beginning of the 20th Century), studies shifted to the detailed mineralogy of the copper veins and orebodies located in the western part of the present open pit (Bowditch, 1935; Graton and Bowditch, 1936; Lacy, 1949; Geological staff of Cerro de Pasco Corporation, 1950; Ward, 1961). A structural study on the deposited is outlined by Ward (1961). Graton and Bowditch (1936) emphasized the role of mineralizing fluids and concluded that the ore-forming fluids for copper veins and orebodies were acidic and oxidizing. Petersen (1965) described several major ore deposits in Peru and reviewed the general features of Cerro de Pasco including the structure and ore control, mineralogy, and alteration. The last major work on the metallogeny of Cerro de Pasco was undertaken by Einaudi (1968; 1977) where the first mineralization stage and enargite-pyrite veins (named copper veins) from the second mineralization stage were studied in detail. Since then, no major research has been performed at Cerro de Pasco, particularly on the second mineralization stage base metal carbonate replacement ores situated on the eastern part of the present open pit (Matagente area). This was described only briefly by Petersen (1965).

Aims of the project

When this project started in 2002, the geology of the Matagente area (second stage polymetallic carbonate replacement ores) was poorly known and the geological staff did not consider the deposit as an entity, although the location of the ore was well known. Recent studies at nearby Colquijirca (Fontboté and Bendezú, 1999, 2001; Bendezú and Fontboté, 2002; Bendezú et al., 2003; Bendezú, 2006) helped the inception of this project at Cerro de Pasco. The project began with a detailed description of the mineralogy of the orebodies in the Matagente area (including the Cuerpo Nuevo and the Manto V orebodies). The Cerro de Pasco district is large, and it was felt that a focused study was warranted. However, while the project became more advanced, and due to the collaboration of the Cerro de Pasco Geology staff, we enlarged our study to the entire deposit in order to be able to address the different hydrothermal events in detail.

The present study includes the characterization of the mineralogy in the carbonate replacement ores at Matagente and a complementary mineralogical study of the first mineralization stage as well as of the enargite-pyrite veins from the second mineralization stage (see Part I). In addition, a geochronological survey has been undertaken in order to resolve the timing and duration of the Mid-Miocene magmatic-hydrothermal system at Cerro de Pasco, integrating U-Pb, $^{40}Ar/^{39}Ar$, Rb-Sr, and Pb isotopes (see Part II). Moreover, a fluid inclusion and stable isotope study on both mineralization stages permits us to draw implications on the environment of deposition of the polymetallic mineralization and the characterization of the ore-forming fluids (Part III).

In the light of the obtained results, a clear view and understanding of the deposit is now available and it will serve as a useful exploration guide when investigating analogous ore deposits (e.g. Cordilleran base metal type). Moreover, the numerous reports undertaken for the Volcán Compania Minera S.A. has been very useful for the Cerro de Pasco geology staff, which followed our nomenclature and suggestions. We are therefore pleased by this collaboration.

Future work at Cerro de Pasco should include a detailed regional structural study and emphasis should be given to the pyrite-quartz body and its metal content, particularly silver and gold. Furthermore, a report on the presence of anomalous high contents of rare earth elements associated with the second stage carbonate replacement ores (Baumgartner and Fontboté, 2005) suggests that this topic warrants further investigation.

References

Amstutz, C., and Ward, H., J, 1956, Geología y mineralización del depósito de plomo de Matagente, Cerro de Pasco: Boletín de la Sociedad Geológica del Perú, v. 30, p. 13-31.

Angeles, C., 1999, Los sedimentos Cenozoicos de Cerro de Pasco; estratigrafia, sedimentacion y tectonica, *in* Machare, J., Benavides-Caceres, V., and Rosas, S., eds., Sociedad Geológica del Perú, Volúmen Jubilar, 5, p. 103-118.

Bartos, P. J., 1989, Prograde and retrograde base metal lode deposits and their relationship to underlying porphyry copper deposits: Economic Geology, v. 84, p. 1671-1683.

Baumgartner, R., and Fontboté, L., 2005, Anomalous rare earth, Sc, Y, Ga, In, Tl contents associated to Zn-Pb-(Bi-Ag-Cu) Cordilleran ores at Cerro de Pasco: Private report to Volcán Compania Minera, S.A., Peru, p. 1-10.

Benavides-Cáceres, V., 1999, Orogenic evolution of the Peruvian Andes: The Andean Cycle: Society of Economic Geologists, Special publication, v. 7, p. 61-107.

Bendezú, R., 2006, Shallow polymetallic and precious metal mineralization associated to a Miocene diatreme-dome complex of the Peruvian Andes. The Colquijirca District., Unpublished PhD Thesis, University of Geneva, Switzerland.

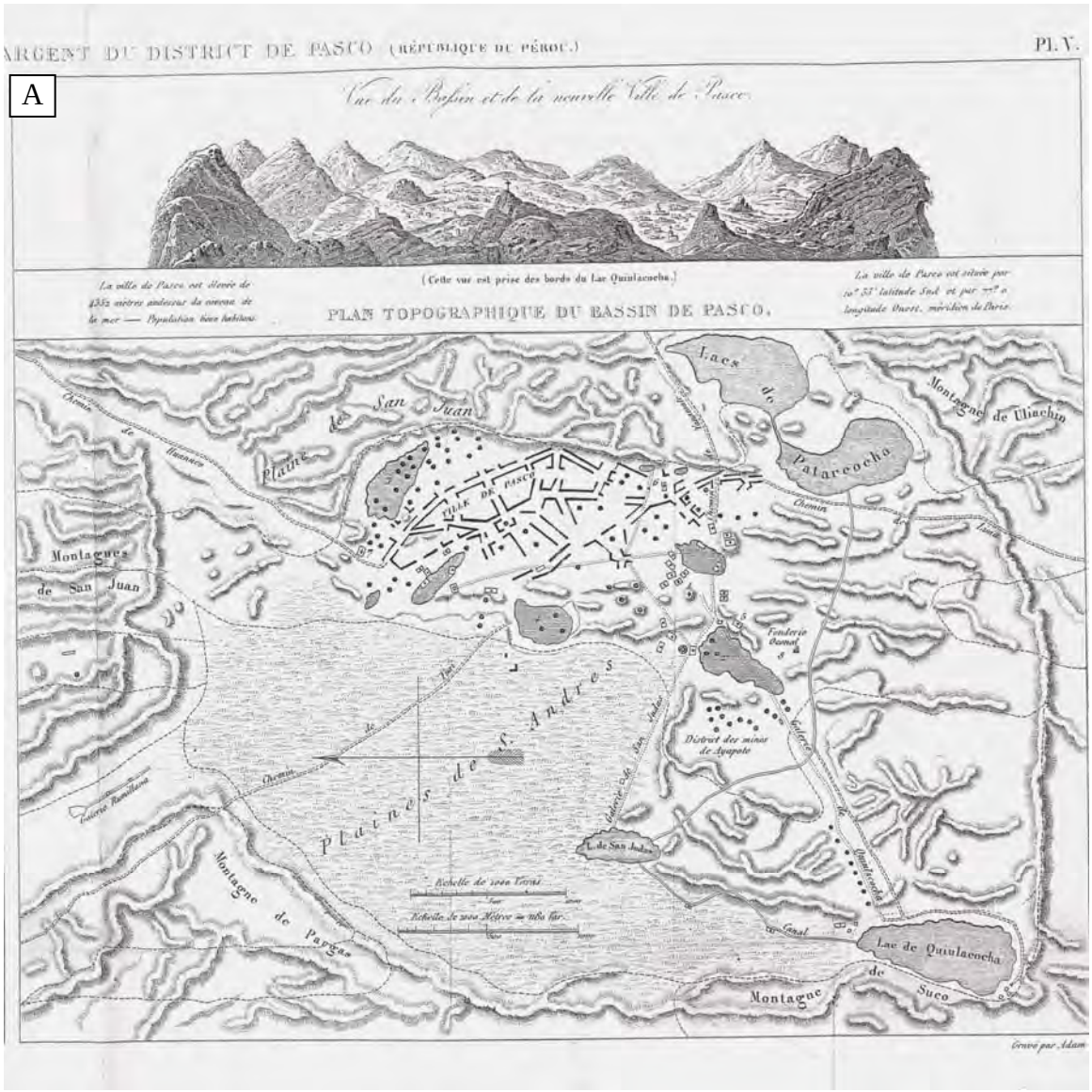

Figure 78. Silver mines of Cerro de Pasco (Simonin, 1869).

Fig. 1: *A) Topographic map of the Cerro de Pasco district around 1820 (from De Rivero, 1832). All mines were underground workings and are represented by black dots. B) View of the Cerro de Pasco district in 1869. The town of Cerro de Pasco is visible on the left side of the picture (from Simonin, 1869)*

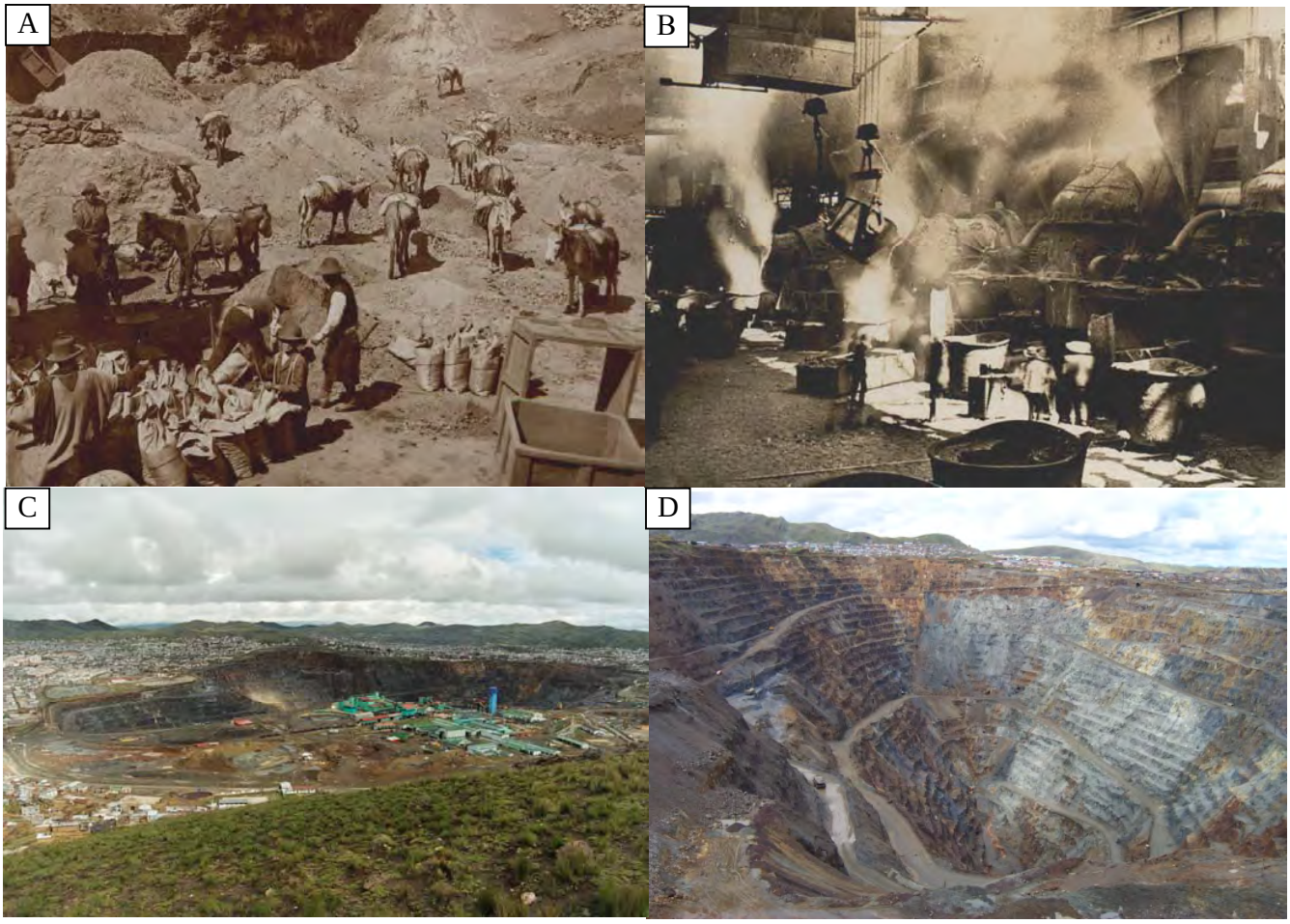

Fig. 2: *A) Mines at Cerro de Pasco (around 1905) where the ore was transported by donkey back. B) Smelter of Tinyahuarco (around 1910). C) Cerro de Pasco open pit (2002). Note the presence of the shaft on the right hand side of the picture (blue building). North is on the left. D) Open pit view from the north looking south (2002, M. Mount). The grey part of the open pit is the pyrite-quartz body (right hand side of the picture) with its phyllic alteration halo (on the top and side of it).*

Bendezú, R., and Fontboté, L., 2002, Late timing for high sulfidation Cordilleran base metal lode and replacement deposits in porphyry-related districts: the case of Colquijirca, central Peru: SGA News, v. 13, p. 9-13.

Bendezú, R., Fontboté, L., and Cosca, M., 2003, Relative age of Cordilleran base metal lode and replacement deposits, and high sulfidation Au-(Ag) epithermal mineralization in the Colquijirca mining district, central Peru: Mineralium Deposita, v. 38, p. 683-694.

Bowditch, S. I., 1935, The geology and ore deposits of Cerro de Pasco, Peru, Unpublished PhD thesis, Harvard University, 160 p.

De Rivero, M. M., 1830, Sketch of the rich mine of Pasco: American Journal of Science, v. 17, p. 43-63.

De Rivero, M. M., 1832, Les mines d'argent de Pasco, au Pérou: Anales des Mines, v. 2, p. 169-198.

Einaudi, M. T., 1968, Pyrrhotite-pyrite-sphalerite relations at Cerro de Pasco, Peru, Unpublished PhD Thesis, Harvard University, 381 p.

Einaudi, M. T., 1977, Environment of ore deposition at Cerro de Pasco, Peru: Economic Geology, v. 72, p. 893-924.

Fischer, J., 1977, Silver mines and silver miners in colonial Peru 1776-1824. Centre for Latin-American studies: University of Liverpool, Monograph 7, p. 150p.

Fontboté, L., and Bendezú, R., 1999, The carbonate hosted Zn-Pb San Gregorio deposit, Colquijirca District, central Peru, as a high sulfidation epithermal system, in (eds.), v. 1, p.: Fifth Biennial SGA Meeting, Mineral Deposits: Processes to Processing, 1999, p. 495-498.

Fontboté, L., and Bendezú, R., 2001, The carbonate-hosted San Gregorio and Colquijirca (Zn-Pb-Ag) deposits (central Peru) as products of an epithermal high sulfidation system: Proexplo 2001 CD-ROM, Lima, Perú,, 2001, p. 19 p.

Fuchs, F. G., 1920, La Región mineral del Cerro de Pasco: Anales del Congreso Nacional de la Industria Minera, Lima, Perú.

Geological staff of Cerro de Pasco Corporation, 1950, Lead and zinc deposits of the Cerro de Pasco Corporation in Central Peru: 18th International Geological Congress, Great Britain 1948, 1950, p. 154-186.

Graton, L. C., and Bowditch, S. I., 1936, Alkaline and acid solutions in hypogene zoning at Cerro de Pasco, Peru: Economic Geology, v. 31, p. 651-698.

Jenks, W. F., 1951, Triassic to Tertiary stratigraphy near Cerro de Pasco, Peru: The Geological Society of America Bulletin, v. 62, p. 203-219.

Jiménez, C., 1924, Síntesis de la minería peruana en el centenario de Ayacucho, Ministerio de fomento, Minas y Petróleo, p. 3-71.

Lacy, W. C., 1949, Types of pyrite and their relations to mineralization at Cerro de Pasco, Peru, Unpublished PhD Thesis, Harvard University, 193 p.

Marsters, V. F., 1912, The physiography of the Peruvian Andes with notes on early mining in Peru: Annals New York Academy of Sciences, v. 22, p. 225-258.

McLaughlin, D. H., 1924, Geology and physiography of the Peruvian Cordillera, Department of Junin and Lima: Geological Society of America Bulletin, v. 35, p. 591-632.

Mégard, F., 1978, Etude géologique des Andes du Pérou central-Contribution à l'étude écologique des Andes, Mémoire ORSTOM no. 86, Office de la Recherche Scientifique et Technique Outre-Mer, Paris,, 310 p.

Mégard, F., 1984, The Andean orogenic period and its major structures in central and northern Peru: Journal of the Geological Society of London, v. 141, p. 893-900.

Noble, D. C., and McKee, E. H., 1999, The Miocene metallogenic belt of central and northern Peru: Society of Economic Geologists Special Publication, v. 7, p. 155-193.

Petersen, U., 1965, Regional geology and major ore deposits of central Peru: Economic Geology, v. 60, p. 407-476.

Pickering, J. C., 1908, Recent development at Cerro de Pasco, Peru: The engineering Mining Journal, v. April 11, p. 760-763.

Raimondi, A., 1902, Memoria sobre el Cerro de Pasco y la Montaña de Chamchamayo, el Perú: Estudios mineralógicos y Geológicos, v. 4, p. 444-488.

Ramos, V. A., and Aleman, A., 2000, Tectonic evolution of the Andes., *in* Cordani, U., E., M., Thomaz Filho, A., and Campos, D., eds., Tectonic evolution of South America, p. 635-685.

Simonin, L., 1869, Underground Life of Mines and Miners: London, p. 522.

Soler, P., 1991, Contribution à l'étude du magmatisme associé aux marges actives. Pétrographie, géochimie et géochimie isotopique du magmatisme Crétacé à Pliocene le long d'une transversale des Andes du Pérou central. Implications géodynamques et métallogéniques., Unpublished PhD thesis, Université Pierre et Marie Curie, Paris VI, 777 p.

Ward, H. J., 1961, The pyrite body and copper orebodies, Cerro de Pasco Mine, central Peru: Economic Geology, v. 56, p. 402-422.

Part I

Mineralogical zoning of Cordilleran base metal mineralization related to a Mid-Miocene diatreme-dome complex: The Cerro de Pasco deposit, Peru.

Regina Baumgartner, Lluís Fontboté

Department of Mineralogy, University of Geneva, 13 Rue des Maraichers, Switzerland

Abstract

The Cerro de Pasco epithermal polymetallic Cordilleran deposit (central Peru) is located in the upper part of a porphyry environment related to a Mid-Miocene dacitic diatreme-dome complex (15.4 ± 0.07-15.1 ± 0.3Ma). Cerro de Pasco constitutes a large polymetallic resource with past production (from 1950 to present) plus known resources of more than ~175 Mt @ 7 percent Zn and 2 percent Pb and 3 oz/t Ag. In addition, prior to 1950 mining produced 1200 Moz Ag, 2 Moz of Au and around 50 Mt @ 2 percent Cu.

The present study confirms that at Cerro de Pasco, two mineralization stages with contrasting mineral assemblages took place. The first mineralization stage (IA) occurs on the eastern edge of the diatreme-dome complex and consists of a large pyrite-quartz body replacing mainly adjacent carbonate rocks of the Upper Triassic-Lower Jurassic Pucará Group and to a lesser extent the diatreme breccia. This body is composed of pyrite with pyrrhotite inclusions, quartz, and black, and red chalcedony (containing hypogene hematite). At the contact of the pyrite-quartz body, the diatreme breccia is altered to sericite-pyrite-quartz. Pipe-like pyrrhotite bodies zoned outwards to Zn-Pb mineralization bearing Fe-rich sphalerite, containing up to 25 mol% FeS (stage IB), were subsequently emplaced within the pyrite-quartz body, replacing Pucará carbonate rocks.

Recent mine developments have allowed to study in detail the mineralogy and spatial distribution of the second mineralization stage which superimposes partially the first one and includes zoned veins and replacement bodies. E-W trending fractures cutting the diatreme breccia, the pyrite-quartz body, and the Excelsior Group focused hydrothermal fluids which altered the rock and deposited enargite-pyrite forming relatively irregular (Cu-Ag-Au-(Zn-Pb) veins. These veins, located in the western part of the deposit, display mineral zoning with, from the center outwards, a core of enargite-pyrite and Au traces; an intermediate zone of tennantite, chalcopyrite and Bi-minerals; and a poorly developed outer zone bearing Fe-poor sphalerite and galena. The replacement ores are hosted by Lower Mesozoic Pucará carbonate rocks and are controlled along N35°E, N120°E and N170°E faults. They form upward-flaring pipe-like well zoned orebodies with a core of famatinite-pyrite and alunite; an intermediate zone with tetrahedrite-pyrite, chalcopyrite, matildite, cuprobismutite, emplectite and other Bi-minerals (Ag and Bi contents may reach up to more than 1000 ppm) accompanied by APS minerals, kaolinite and dickite; and the outer zone composed of Fe-poor sphalerite (in the range of 0.05 to 3.5 mole % FeS) and galena. The outermost zone consists of hematite, magnetite and Fe-Mn-Zn carbonates.

Most of the second stage carbonate replacement bodies display an inclined plunge (between 25 and 60°) to the west, i.e., in the direction of the diatreme-dome complex, suggesting that the hydrothermal fluids ascended from deeper levels and that no lateral feeding from the veins to the carbonate replacement bodies took place. Rather, both veins in the diatreme breccia and carbonate replacement bodies may be the result of parallel and divergent ascending fluid paths within the same hydrothermal system. This is also reflected by the different mineral compositions recognized in the cores of the western enargite-pyrite veins (Cu, As, and Au rich) and of the carbonate replacement deposits (Cu and As poor, Sb>As, virtually Au free).

The mineral zoning and the observed mineral assemblages and associations indicate that, during the second mineralization stage, the fluid evolution reflects fluid advances and retreats controlled by the hydrothermal activity and host rock type. The inner zone assemblages encroach on those of the outer zone during fluid advance and the outer zone assemblages encroach on those of the inner zones during fluid retreat.

Taking in account the deposition temperatures derived from fluid inclusion data, the mineral assemblages of the first stage are characterized predominantly by low sulfidation states as indicated by pyrrhotite inclusions in pyrite and by the deposition of pyrrhotite pipes and related Zn-Pb ores bearing Fe-rich sphalerite. However, the

presence of hematite within quartz from the pyrite-quartz body suggests that the fluids were locally oxidizing which is typical of exsolving magmatic fluids. The observed mineral assemblages are consistent with precipitation from magmatic fluids reduced by interaction with host rocks, probably Excelsior Group rocks. The quartz-sericite alteration halo at the margin of the pyrite-quartz body suggests moderate acidic conditions for the first mineralization stage. The second mineralization stage contains high to intermediate sulfidation state mineral assemblages bearing Fe-poor sphalerite. The recognized alteration assemblages with development of vuggy quartz in the diatreme and deposition of alunite both in the enargite-pyrite veins and carbonate replacement bodies, indicate very acidic fluids. Limited interaction with the host rock, owing to fluid channeling along fractures and because the buffering capacity of the host rock had been lowered by alteration during the first mineralization stage, may explain the prevailing high sulfidation conditions during the second mineralization stage.

Introduction

Epithermal polymetallic deposits in the upper part of a porphyry environment are known in numerous districts (Butte, Magma, Superior, Bisbee and Tintic, USA; Yauricocha, Morococha, Julcani, Quiruvilca, Huarón, Hualgayoc, Colquijirca and Cerro de Pasco, Peru; Bor, Serbia; Chuquicamata, La Escondida, Collahuasi, Chile, and elsewhere) where they occur as veins, massive replacement bodies, and sulfide-cemented breccia bodies. Several of these deposits are superimposed on a porphyry-copper deposit while some are spatially separated from it and even others have no known link to mineralized porphyries such as Cerro de Pasco (Einaudi, 1982; Einaudi et al., 2003). These polymetallic deposits can be classified as Cordilleran base metal deposits, a term introduced by Sawkins (1972) to replace the former nonspecific *post-magmatic* or *magmatic hydrothermal* deposit class. The expression "Cordilleran base metal" veins/deposits was subsequently used by Einaudi (1982), Gilbert and Park (1986), Bartos (1987), Macfarlane and Petersen (1990), Bendezú and Fontboté (2002), Bendezú et al. (2003), and Bendezú (2006). According to Sawkins (1972), the main features of Cordilleran base metal deposits are: (1) close association in time and space with calc-alkaline igneous activity, (2) occurrence of open-space fillings in silicate host rocks and as replacement bodies in carbonate rocks, (3) well-developed metal zonation in veins or bodies, (4) deposition at shallow levels beneath the paleo-surface. An additional characteristic pointed out by Bendezú (2006) is high Ag/Au ratios. We add a new feature, common of several of the largest deposits (Table 1), which is the existence of an early pyrite-quartz assemblage that can be extensive and form large orebodies. Cordilleran deposits have also been termed as Butte-type vein deposits (Meyer et al., 1968), Cu veins (Ward, 1961), polymetallic veins, and recently zoned base-metal veins (Einaudi et al., 2003).

Cordilleran base-metal deposits have been historically an important source of Cu and Zn-Pb-Ag in the North American Cordillera and Peru. Today, the main Zn-Pb-Ag production in Peru comes from Cordilleran deposits such as Cerro de Pasco, Huarón, Quiruvilca, Julcani, and Colquijirca (Table 1), all of them belonging to the Miocene Metallogenic Belt of Central and Northern Peru (Noble and McKee, 1999). The Cerro de Pasco deposit is the second largest known Cordilleran base-metal deposits after Butte (Montana), and offers insights as to the relationship between different base-metal mineralization stages in a porphyry environment. Cerro de Pasco constitutes a large polymetallic resource with past production plus known resources of more than ~175 Mt @ 7 percent Zn and 2 percent Pb and 3 oz/t Ag. In addition, prior to 1950 mining produced 1200 Moz Ag, 2 Moz of Au and around 50 Mt @ 2 percent Cu (Jiménez, 1924; Geological staff of Cerro de Pasco Corporation, 1950; Einaudi, 1977; Fischer, 1977 , and Cerro de Pasco Geology staff pers. comm.).

While it is probable that silver was mined at Cerro de Pasco prior to the Spanish conquest, the first historical record of production from the district is in 1630 (Bowditch, 1935 and references therein). In the 19th Century, Ag production declined and most claims at Cerro de Pasco were acquired by the american Cerro de Pasco Corporation (1906-1970). This company started mining narrow and rich copper veins and orebodies (mainly enargite and chalcopyrite) down to a depth of 700 m, in the western part of the present open pit. In the late 40's, the Cerro de Pasco Corporation began mining the Zn-Pb orebodies characterized by marmatitic sphalerite (mainly the Cayac Noruega A, B, and J-337 and K-327A orebodies, see Einaudi, 1977) and also the oxidized part of the Matagente area. In the early 70's, the mine was nationalized and was integrated to the state-owned Centromin. In 1999, Cerro de Pasco was again privatized and Volcán Compañia Minera S.A., the current owner, took the control of the mine.

Early descriptions of the regional geology were published by McLaughlin (1924) and Jenks (1951). Bowditch (1935), Graton and Bowditch (1936), Ward (1961), Petersen (1965), Mégard (1978), and Einaudi (1977) described veins mainly hosted in the diatreme-dome complex as well as a part of the Fe-rich sphalerite-bearing Zn-Pb bodies. Bowditch (1935) and Petersen (1965) characterized diatreme breccia-hosted veins, whereas late carbonate-hosted replacement bodies were briefly described by Petersen (1965). Since the fundamental work of Einaudi (1968, 1977) several unpublished reports of Cerro de Pasco Corporation, Centromin, and Vólcan Compañía Minera S.A., and abstracts, including Rivera (1997), contain additional information

on Cerro de Pasco. Rogers (1983) studied the diatreme-dome complex from a petrological and physical volcanic perspective.

The present work is based on a total of 6 months field work including bench mapping in key areas, core logging and regional geology mapping. Observation of 260 polished and thin sections in reflected and transmitted light has allowed to document the evolution in space and time of two stages of mineralization already recognized by Einaudi (1968, 1977) at Cerro de Pasco. The first one (I) is constituted by a large pyrite-quartz body forming a sericitic halo and pyrrhotite bodies zoned outwards to Zn-Pb ores. The second mineralization stage (II) consists of enargite/famatinite-bearing Zn-Pb- (Bi - Ag-Cu) veins and carbonate replacement bodies accompanied by argillic to advanced argillic alteration. This study is focused on field- and petrographic-based documentation of the second stage well-zoned polymetallic mineralization and also includes minor updates of early descriptions of Ward (1961) and Einaudi (1968, 1977) of the first mineralization stage. This work is complementary to parallel articles devoted to the geochronology of magmatic and hydrothermal events (Baumgartner et al., Part II) and to the fluid inclusion and stable isotope characterization of the ore forming fluids (Baumgartner et al., Part III). The documentation of the second stage polymetallic mineralization has become possible because of recent extensive mine development in the eastern part of the open pit which has allowed a detailed description of the structure, shape, mineralogy, and zoning of the newly exposed orebodies at Cerro de Pasco.

General Geology

Cerro de Pasco is located in the Andean plateau of central Peru, at an elevation of 4320 m. A regional NS "Longitudinal Fault" juxtaposes Paleozoic metamorphic rocks with Mesozoic sedimentary rocks (Fig. 1). In the mine area, the Longitudinal Fault is believed to be represented by high-angle N15°W striking reverse faults dipping steeply east (Fig. 2).The oldest exposed rocks in the district are slightly metamorphosed Devonian shale and phyllite with interbedded fine-grained quartzite, which are part of the Excelsior Group (Jenks, 1951). These rocks are overlain in an angular unconformity by Permo-Triassic red beds of the Mitu Group consisting, in the vicinity of Cerro de Pasco, of sandstone and conglomerate with pebbles of quartz and Excelsior-type argillaceous clasts (McLaughlin, 1924; Jenks, 1951). In the eastern part of the district, the Mitu Group is covered by a thick (up to 3000 m) Upper Triassic-Lower Jurassic carbonate sequence within the Pucará Group (Angeles, 1999). This carbonate sequence is principally composed, in the Cerro de Pasco open pit, of successions of sandy limestone, black bituminous limestone, beds with chert nodules as well as massive fossiliferous horizons and thick sequences of massive limestone. The Pucará Group west of the "Longitudinal Fault" is only about 300 m thick and consists of thin-bedded, light-colored limestone (Jenks, 1951; Angeles, 1999). After multiple Eocene to Lower Miocene folding episodes characterized by a main NE-SW axial direction, late-mid Miocene magmatic activity affected the region (Silberman and Noble, 1977) and formed a diatreme-dome complex located west of the present open pit (Rogers, 1983). Similar diatreme-dome complexes are known at Colquijirca (Bendezú, 2006) and Yanamate (Fig. 1). The Cerro de Pasco diatreme-dome complex was emplaced in a zone of weakness, on the western margin of the Longitudinal Fault (Fig. 1). The diatreme is located west of a northerly trending anticline recognized in the central and southern part of the open pit (Fig. 2).

The diatreme-dome complex is 2.5 km in diameter and formed in two phases (Einaudi, 1968; Rogers, 1983). An early phase of explosive development produced a diatreme breccia (known locally as Rumiallana Agglomerate) which occupies most of the diatreme-dome complex outcrop (Fig. 1). The diatreme breccia fragments are mainly dacitic in composition and include clasts of phyllite from the Excelsior Group, Mitu sandstone, limestone, and chert from the Pucará Group, as well as small amounts of altered porphyric igneous rock. Close to the northwest and southwest diatreme margins, tuffaceous dacitic volcanic rocks occur and contain accretionary lapilli. Rootless Pucará limestone and Mitu sandstone blocks are observed in the north-western part of the complex, indicating that these blocks collapsed into the diatreme. The second phase of the diatreme-dome complex formation is characterized by dacitic to rhyodacitic porphyry dome intrusions which occur along the NW and N margins of the diatreme (Rogers, 1983); these have been dated at 15.4 Ma (Baumgartner et al., Part II). East-west trending dykes of quartz-monzonite porphyry (Bowditch, 1935) cut the diatreme and locally pass into the carbonate wall-rocks (Fig. 2). They have been dated at 15.35 and 15.16 Ma (Baumgartner et al. Part II).

Field evidences allow an estimation on erosion since the Mid-Miocene times. At the Santa Rosa area, the Mid-Miocene paleorelief in which pyroclastic dacitic rocks related to the diatreme-dome complex is located less than 100 m below the present surface (Fig. 3). This implies that at the southeastern part of the diatreme, only rocks of the diatreme-dome complex were eroded. Taking into account the size of the diatreme and the lack of external volcanic deposits (except et Santa Rosa), this erosion was not more than in the order of hundreds of meters. Our estimate is in agreement with the estimates from Rogers (1983) of less than 1 km based on the geometry and texture of the porphyry dikes and domes. The cross sections in Figures 1 and 3 illustrate the post-volcanic surface with the indication of the present erosion surface.

The structural geology at Cerro de Pasco has been described by Amstutz and Ward (1956) and Ward (1961) and is summarized here. The E-W striking Matagente syncline (Fig. 2) plunges 30°E. The Cerro anticline is a broad, north-plunging anticline composed of Excelsior Group rocks (Fig. 2). The Longitudinal Fault mentioned

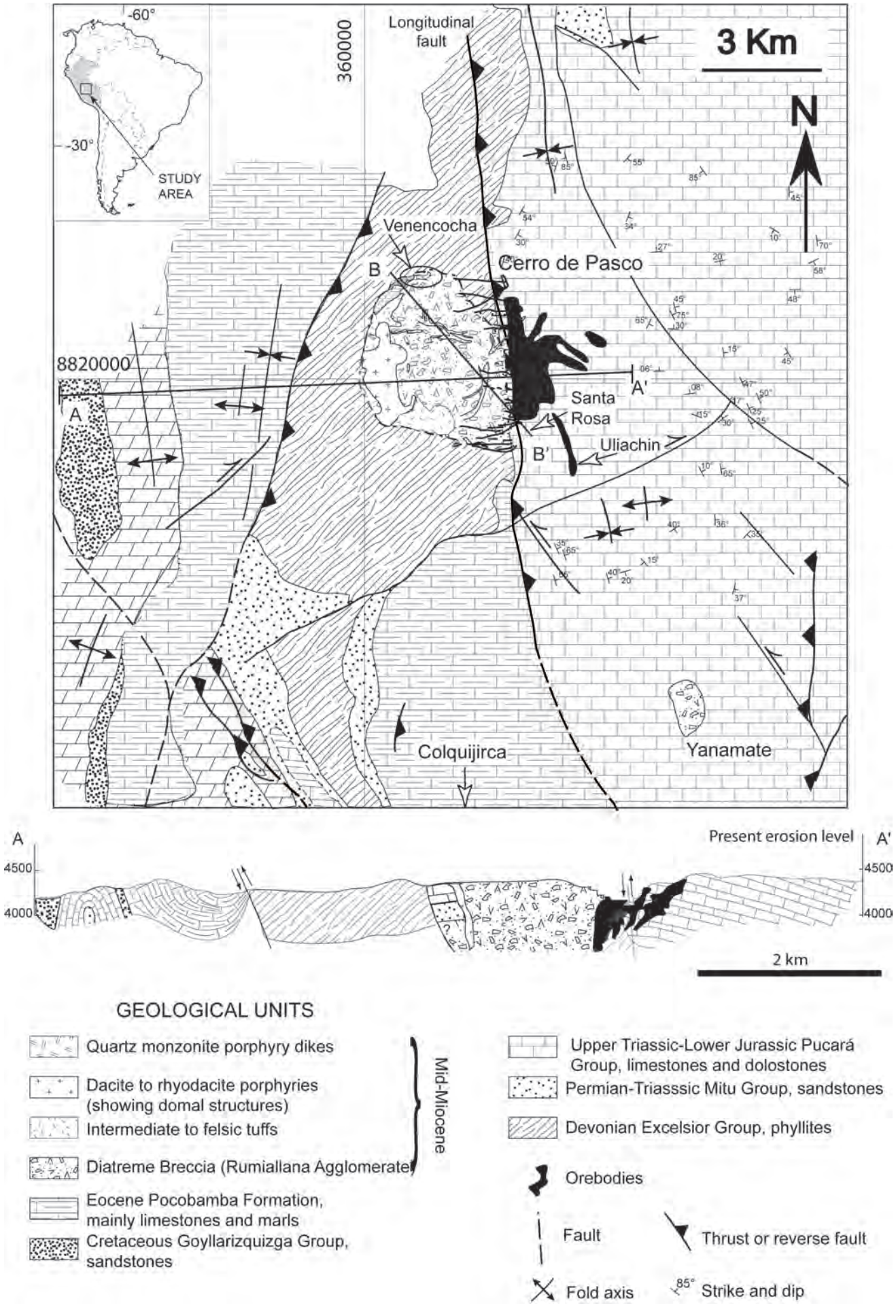
-60°
-30°
STUDY AREA
360000
Longitudinal fault
3 Km
N
Venencocha
B
Cerro de Pasco
8820000
A
A'
Santa Rosa
B'
Uliachin
Colquijirca
Yanamate
A
A'
Present erosion level
4500
4000
2 km
GEOLOGICAL UNITS
Quartz monzonite porphyry dikes
Dacite to rhyodacite porphyries (showing domal structures)
Intermediate to felsic tuffs
Diatreme Breccia (Rumiallana Agglomerate)
Mid-Miocene
Eocene Pocobamba Formation, mainly limestones and marls
Cretaceous Goyllarizquizga Group, sandstones
Upper Triassic-Lower Jurassic Pucará Group, limestones and dolostones
Permian-Triasssic Mitu Group, sandstones
Devonian Excelsior Group, phyllites
Orebodies
Fault
Thrust or reverse fault
Fold axis
85° Strike and dip

above was probably already active during the Triassic-Jurassic, at the time of the Pucará Group deposition, as supported by the fact that its thickness is different on both sides of the Longitudinal Fault. The occurrence of the Upper Cretaceous-Eocene Shuco breccia and conglomerate (belonging to the Pocobamba Formation) consisting of Pucará clasts along the Longitudinal Fault is an additional evidence for the protracted tectonic activity of the longitudinal fault. A complex set of faults is prominent in the Pucará carbonate rocks in the Cerro de Pasco open pit. The first set strikes N120°E, dips 70-80°S south, and is present in the eastern part of the open pit (Fig. 2). The second set strikes N170°E, dips vertically and is mainly present in the southern part of the deposit while the third fault set strikes N35°E, dips 80°E and is present in the northern open pit. The three faults sets are dextral and/or sinistral strike-slip faults and formed by compression in the later stages of folding.

Mineralization

Einaudi (1977) divided mineralization at Cerro de Pasco into a "first" and "second" stage of ore deposition based on the different mineralization styles. In the present work, this subdivision has been maintained and in addition, substages IA and IB have been distinguished on the basis of crosscutting relationships among them. It must be underlined that only stage II is geochronologically constrained and that stages IA, IB, and II could be all part of the same mineralization process.

Sampling and terminology used for mineralogical descriptions

Most part of the studied samples was devoted to stage II which had been lees studied in the past. This includes selected sampling from the main enargite-pyrite veins and carbonate replacement bodies and a detailed bench sampling of a particularly well zoned carbonate replacement body at Cuerpo Nuevo (Fig. 2). Furthermore, core logging and detailed sampling on a representative drill core of the Cayac Noruega body (CP-00-108, Fig. 2) was performed. Additional key samples were collected from the Manto V and the Colas orebodies (Fig. 2). The western enargite-pyrite veins n°25, 43, 44, and 79 were sampled and detailed sampling and logging in the Santa Rosa area was undertaken in cooperation with Y. Jobin and M. Henry (Jobin, 2004; Henry, 2006). For the first stage, only selective sampling in representative areas from the pyrite-quartz body in the open pit (mainly bench 4190) and the pyrrhotite pipes in the underground mine (level 1200) was performed.

A detailed bench mapping (two traverses) and sampling was undertaken at Cuerpo Nuevo (4320 bench), where a clear zoning can be observed. In addition, core logging was performed at Cayac Noruega (drill core CP-00-108, Fig. 2). Mapping and sampling of the western enargite-pyrite veins, the pyrite quartz-body as well as mapping, sampling and logging in the Santa Rosa area was undertaken. Minerals were identified by reflected- and transmitted-light microscopy. Selected minerals were analyzed by electron microprobe (University of Lausanne), with wavelength dispersive x-ray spectrometry and energy dispersive spectroscopy. X-ray powder diffraction was performed for alteration minerals. FeS content of sphalerite was determined by electron microprobe analyses (EMPA) at the University of Lausanne, Switzerland (Appendix 1). Minor elements such as Cu, Cd, and Mn were analyzed. Copper and Mn contents were always below detection limits (<0.01 wt %) while Cd contents range from 0.01 to 0.6 percent (rarely up to 1%) and average 0.2 percent. Microscopic studies under transmitted light coupled with EMPA reveal that the FeS content can be roughly estimated using a color scale.

First mineralization stage (IA and IB)

The replacement of Pucará Group rocks and to a lesser extent of the eastern part of the diatreme breccia (Fig. 2) by a large pyrite-quartz body constitutes mineralization stage IA. The pyrite-quartz body is 1800 m long and 150 m wide (in places up to 300 m). It has an elongated vertical, funnel-shape (Fig. 4 and 5). Below the 1800 level (~550 m), the pyrite-quartz body is narrower and becomes a discontinuous sheath along the diatreme breccia-Excelsior shale contact and, according to Lacy (1949), at greater depth (below 750 m) it passes into the diatreme breccia and lies near the contact of a stock of quartz-monzonite porphyry. The western contact of the pyrite-quartz body with the diatreme breccia is sharp (Fig. 2), while the eastern portion against the Pucará carbonate rocks is irregular, apparently reflecting different facies of the replaced carbonate rocks. Relics of both Pucará carbonate and diatreme breccia rocks are observed within the pyrite-quartz body. Pyrite constitutes more than 90 percent of the body and black- and red-chalcedonic silica and quartz account for the remaining 10 percent. The red color of the chalcedonic silica is due to the presence of hematite. The elongated shape of the pyrite-quartz body (IA) and the replacement bodies constituted by Fe-rich sphalerite (IB) suggest that the first mineralization stage is controlled by

Fig. 1: *Regional geological map of the Cerro de Pasco district, central Peru, showing location of the major base-metal deposits. The Colquijirca district is located south of Cerro de Pasco. Note that the Cerro de Pasco deposit is located on the eastern edge of the diatreme-dome complex. Compiled from Rogers (1983), Angeles (1999) and Cerro de Pasco Geology staff. E-W cross sections A-A' (modified from Jenks, 1951) with present erosion level and speculative reconstruction of the Mid-Miocene topography (modified from Jenks, 1951). Note that the collapsed blocks at the northwestern margin of the diatreme-dome complex are projected from 1km to the north.*

Table 1: Occurrences of Cordilleran base metal deposits.

Location	Age	First stage main ore minerals described	Second stage main ore minerals[d,e]	Host rock	Vein orientation or main structure controlling ore	Type of orebodies	References
Cerro de Pasco, Peru[a]	15-11 Ma	py-qtz body, po, asp, sl	enr, lz, fm, tt-tn, sl, gn	Mainly carbonate rocks (Pucará Grp.) but also diatreme breccia and siliciclastic rocks (Excelsior Fm.)	N45°, N90°, N120°, N170	Veins and replacement bodies	Baumgartner et al. (2003), this study, Einaudi (1977), Petersen (1965)
Colquijirca, Peru[a]	10.6-12.4 Ma		enr, cpy, tn-tt, bn, sl, gn	Mainly carbonate Pocobamba Fm. but also in diatreme breccia and dacitic volcanic rocks	N-S	Veins and replacement bodies	Bendezú et al. (2003), Fontboté and Bendezú (1999, 2001), Bendezú (2006)
Huanzala, Peru[a]	7.7 ± 0.4 Ma	po, asp, sl	tn, enr	Santa Formation limestone	N40°W	Replacement bodies	Imai et al. (1985), Soler et al. (1986), Imai (1986)
Hualgayoc, Peru[a]	~11 Ma		replacement bodies: po, asp, sl, veins: enr, tn, cp, pyrg, sl, gn	Limestones from the Chulec Fm. and sandstone from the Goyllarisquizga Group and the Inca Fm.	N45°W, N80°E and N45°E	Veins and replacement bodies	MacFarlane and Petersen (1990)
Julcani, Peru[a]	10.1-7.0 Ma		enr, cp, sl, gn	Dacite-rhyolite domes	N45°W	Veins	Deen et al. (1994)
Morococha, Peru[a]	9.1 and 6.4 Ma	py-qtz body, po, mt, sl, gn	enr, tn-tt, cp, sl, gn	Quartz-monzonite porphyry stocks and limestones (Pucará Grp.)	W-NW and E-NE	Replacement bodies and veins	Barrentes (1970), Petersen (1965), Beuchat (2003)
San Cristobal[a]	~5-6 My	py-qtz body, py, wf, asp, sl	tt, sl-gn	Pucará Group limestone, Mitu Group volcanics	N120°E-N150°E	Veins and replacement bodies	Beuchat (2003), Campbell (1983), Bartlett (1984)
Quiruvilca, Peru[a]	Miocene		enr, tn-tt, cp, sl, sn	Andesitic lavas and quartz-monzonite porphyry	N 60-70°, N85-120°	Veins	Bartos (1987)
Yauricocha, Peru[a]	late Miocene	py-qtz body	enr, cp, bn, cv, sl, gn	Mainly limestones (Machay Fm.) but also granodiorite stocks	E-W and NNW	Replacement bodies and veins	Petersen (1965), Thomson (1960), Alvarez and Noble (1988)
Pasto Buena, Peru[a]	~9 Ma	wf, po, asp, mo	late stage: enr, tt, sl, gn	Quartz-monzonite Consuzo stock	N	Veins	Landis and Rye (1974)
Huarón, Peru[a]	~15 Ma	po, wf, cst, asp, cp, sl	Late stage: enr, lz, cp, tn-tt, sl, gn	Eocene to Oligocene sandstone and conglomerate and quartz-monzonite porphyric dykes (Callipuy volcanism)	E-W	Veins and replacement bodies	Thouvenin (1984)

Table 1: (cont.)

Bor (Serbia)[a]	65 ± 4 Ma	enr, cp, bn, tn-tt, sl, gn	Andesite, volcaniclastic rocks, pyroclastic rocks	NNW-SSE	Veins and replacement bodies	Sillitoe (1983), Jankovic et al. (1980)
Main and East Tintic, Utah, USA[a]	Late Eocene	enr, tn-tt, Ag-gn, sl	Paleozoic limestones (Ophir Fm.)	NE-SW, NNW	Replacement bodies and veins	Shepard et al. (1968), Morris (1968), Hildreth and Hannah (1996)
Magma, Arizona, USA[b]	Paleocene	cp, bn, sl, tn, enr, cc, dg, gn	Devonian Martin limestones	E-W trending veins	Replacement bodies and veins	Ransome (1912), Short and Ettlinger (1926), Short et al. (1943), Gustafson (1961), Hammer and Peterson (1968), Paul and Knight (1995)
Butte Main stage, Montana, USA[b]	66-63 Ma	enr, cc, bn, cv, dg, tn, cp, sl, gn	Butte quartz-monzonite	E-W, N60°-70°E and N-E	Veins	Sales and Meyer (1949), Profett (1979), Meyer et al. (1968), Brimhall, (1979)
Bisbee, Arizona, USA[b]	late Jurassic	enr, bn	Argillaceous limestone		Replacement bodies	Bryant (1964), Friehauf (1998), Schwartz and Park (1932)
Cananea, Mexico[b]		lz, cv, cp, sl, gn	Limestone (Puertecitos Lm.)	E-W and NE-SW	Replacement bodies	Emmons (1910), Kelley (1935), Perry (1961)
Bingham, “non-porphyry ores”, Utah	37.0-38.5 Ma	py, cc, nk, bn cp, sl, gn, tn	Sandstone and limestone	NE-SW	Veins and replacement bodies	Rubright and Hart (1968); ages compiled in Landtwing (2004); Inan and Einaudi (2002)
Chuquicamata, Main stage veins (superimposed on early porphyry), Chile[c]	31-33 Ma	py, enr, cp, bn, tt-tn supergene cc and cv	Chuqui porphyry Complex	N-S, N10°E	Veins	Sillitoe (2000), Ossandón et al. (2001)
La Escondida, Late stage, Chile[c]	38-36 Ma	enr, cv, cp, bn, tn, sl, gn	Paleocene andesite, and quartz-monzonite porphyry	N10°W	Veins	Padilla (2001)
Collahuasi, Rosario vein, Chile[c]	32.9 Ma (porphyry stage)	py-cp-(tn), py-bn-(enr), cc-dg-cv	Porphyry stock and volcano-sedimentary rocks	N-W	Veins	Hunt (1985), Dick et al. (1994), Clark et al. (1998), Masterman et al. (2005)

[a] Main ore in the district
Subordinate ore in the district
Cordilleran ores are not mined
Pyrite accompanies ore minerals
[e] Mineral abbreviations: asp = arsenopyrite; bn = bornite; cc = chalcocite; cp = chalcopyrite; cst = cassiterite, cv = covellite; dg = digenite; enr = enargite; fm = famatinite; gn = galena; lz = luzonite; mt = magnetite; mo = molybdenite; nk = nukundamite; po = pyrrhotite; pyrg = pyrargyrite; py = pyrite; sl = sphalerite; tn = tennantite; tt = tetrahedrite; wf = wolframite

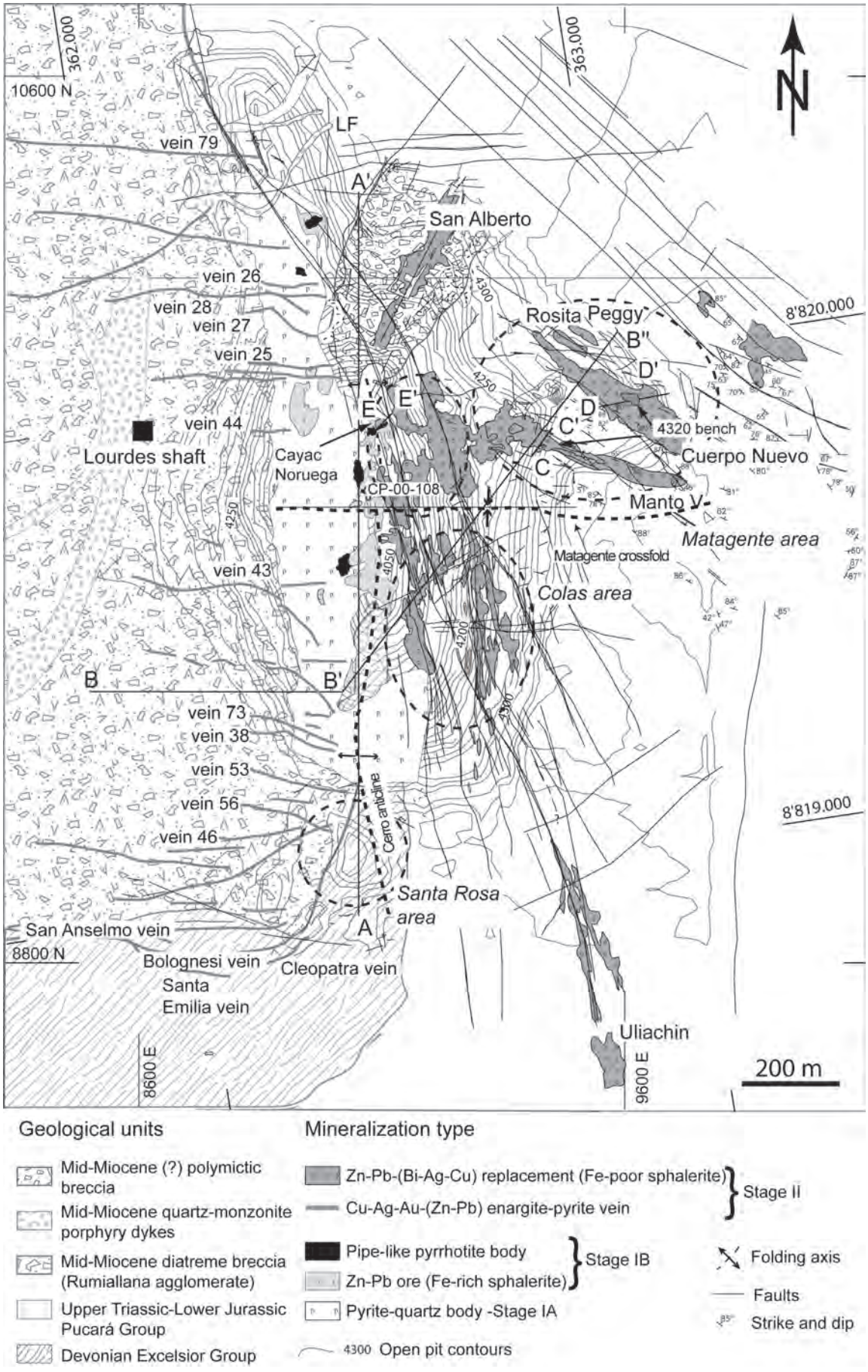

Fig. 2: *Geological map of the Cerro de Pasco open pit showing rock units, faults and the location stages of mineralization. Based on maps of the Cerro de Pasco Geology staff. Note that UTM and local coordinates are shown.*

major structures such as the Matagente cross fold and the Longitudinal Fault. Following the contour of the pyrite-quartz body and up to a distance of 50 m, an alteration halo occurs and is characterized by the assemblage sericite-pyrite-quartz, typical of phyllic alteration (Fig 6A).

A paragenetic sequence for the first stage of mineralization is presented in Figure 7, which integrates the data of Einaudi (1968; 1977), Lacy (1949), and Bowditch (1935). In the present study, the pyrite in the pyrite-quartz body is termed, according to Lacy (1949), pyrite I. It has a grain size of 500 μm to 1 mm and is anhedral and subordinately octahedral or cubic. Non through-going minute cracks have been observed within the pyrite grains (Fig. 6C). Quartz occurs as black- and red- chalcedony as well as euhedral grains up to 1 cm in size. In addition, pyrite I is characterized by the presence of pyrrhotite inclusions (Fig. 6B). Trace amounts of chalcopyrite and arsenopyrite are present in inclusions in pyrite I. Lacy (1949) reports stannite inclusions in pyrite I.

Vertical pyrrhotite pipes pyrrhotite replaced the pyrite-quartz body. They grade outwards to Zn-Pb ore characterized by Fe-rich sphalerite mainly replacing adjacent Pucará carbonate rocks, and to a lesser extent, Excelsior Group phyllite. In the northern part of the open pit, the pyrrhotite pipes dip to the south and in the southern portion of the pit, they dip to the north (Einaudi, 1977). This symmetry reflects structural control, being the most important control the Matagente cross fold, a syncline whose axis trends E-W (Fig. 2). According to Einaudi (1968; 1977), three mineral associations of the pyrrhotite stage define an upward and outward zoning pattern relative to the centrally located pipe-like pyrrhotite bodies (Fig. 8). A deep-level assemblage composed of pyrrhotite-pyrite-quartz with trace amounts of wolframite, cassiterite, and ilmenite. A deep- to intermediate-level association of pyrrhotite + sphalerite + chalcopyrite + stannite which occurs locally as an assemblage (Einaudi, 1977) (Fig. 6D). An association of pyrrhotite + sphalerite + arsenopyrite (Fig. 6E) is present throughout the whole vertical extent of the pipe-like pyrrhotite bodies. The latter association extends horizontally into Zn-Pb ore up to 600 m from the pipe-like pyrrhotite bodies, where pyrrhotite disappears and galena becomes increasingly abundant (Einaudi, 1977). Fe-rich sphalerite (up to 25 mole % FeS, Fig. 9) shows large variations in FeS content along crystallographic growth zones, as a feature also described by Einaudi (1977). Generally, the overall zoning is characterized by decreasing FeS content from core to rim but, in detail, numerous oscillations in the Fe content are recognized. In addition, galena, quartz with minor pyrrhotite, arsenopyrite, marcasite, tennantite, chalcopyrite, chlorite, sericite, siderite, and calcite occur in the Zn-Pb ores. Fine-grained (average size 50 μm) pyrite intergrown with Fe-rich sphalerite is named pyrite II, maintaining the terminology of Lacy (1949). Late replacement of pyrrhotite by pyrite and marcasite occurs and displays a typical bird's eye texture (Fig. 6F).

Second mineralization stage

Introduction

The second mineralization stage comprises (i) enargite-pyrite veins (Cu-Ag-Au-(Zn-Pb)) hosted in the diatreme breccia and the pyrite-quartz body and located on the western side of the deposit, and (ii) Zn-Pb-(Bi-Ag-Cu) bodies replacing Pucará carbonate rocks, mainly in the eastern side of the open pit as well as in the center of the deposit, where they crosscut the pyrite-quartz body and the Fe-rich sphalerite ores related to pyrrhotite pipes (e.g. Fig. 6H, N9940-E9000, underground mine,). Crosscut relationships between enargite-pyrite veins and carbonate replacement bodies could not be observed.

The recent development of the deposit coupled with our descriptions have shown that the second stage ores hosted in carbonate rocks on the eastern side of the open pit, in the Matagente and Diamante areas, are much more abundant than previously documented and presently represent the main mined ressource. Therefore, they will be first described.

Second mineralization stage - Carbonate replacement orebodies

Main orebodies-morphology

The main zoned Zn-Pb-(Bi-Ag-Cu) carbonate replacement orebodies are Cuerpo Nuevo, Manto V, Cayac Noruega C, Rosita, Peggy and Cola C.N.A and Cola C.N.B (Fig. 2). These bodies follow sub-vertical faults trending N35°E, N120°E, and N170°E (Fig. 2 and 10), and locally favorable Pucará beds, mainly dolo-arenite horizons. The carbonate replacement orebodies have an irregular upward-flaring pipe-like shape with a diameter ranging from 50 cm to 50 m (Fig. 10 and 11). Most of these bodies show an inclined plunge (between 25 and 60°) in the direction of the diatreme-dome complex. The Matagente area contains two main orebodies, Cuerpo Nuevo and Manto V as well as two smaller ones, Peggy and Rosita (Fig. 2). The Cuerpo Nuevo orebody has a trend of N120°E, with an average plunge of 25° to the W (Fig. 12A); the plunge follows the plane direction of the main fault set which strikes N120°E with an average dip of 60° S. This orebody has a minimum size of approximately 400 m by 100 m and the down-plunge distance is at least 400m. The Manto V orebody trends east-west in its western part and bends to N60°W (i.e., direction of the main fault set) on its eastern end with a plunge of approximately 30° to the W (Fig. 4 and 11). The body is at least 500 m by 80 m in diameter with a minimum down-dip distance of 160 m. The upper portion of the body is oxidized to an up-dip distance of 250 m.

The Cayac Noruega body is located in the Diamante area and trends N170°E (direction of the main fault set in the southern part of the deposit) with a plunge of approximately 55°S (Fig. 2 and 12B). The size of the

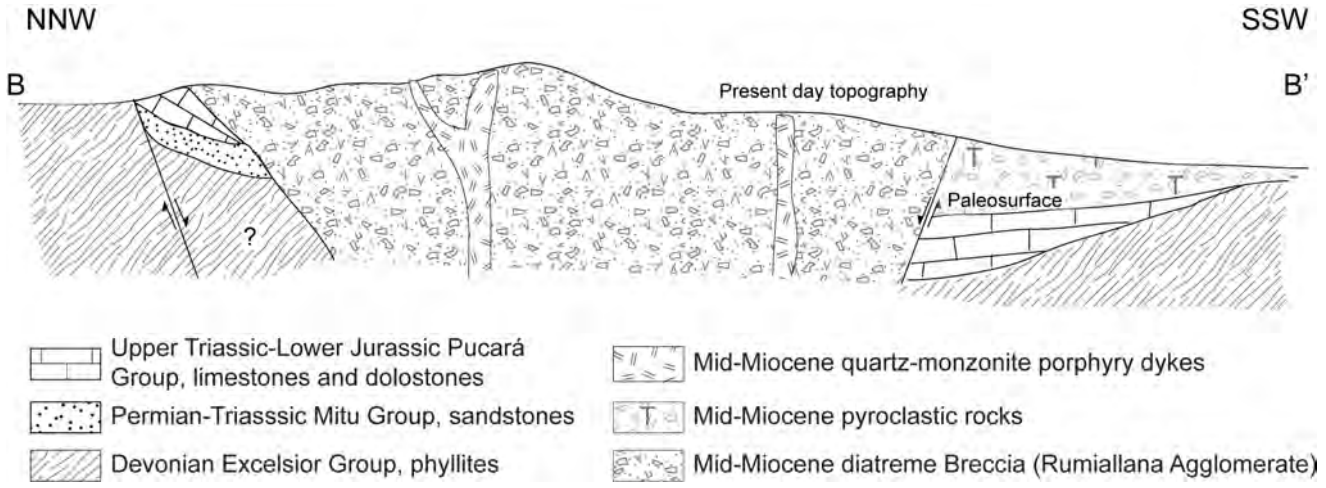

Fig. 3: *Regional cross section (B-B' in Fig. 1) showing present day topography and Mid-Miocene paleorelief.*

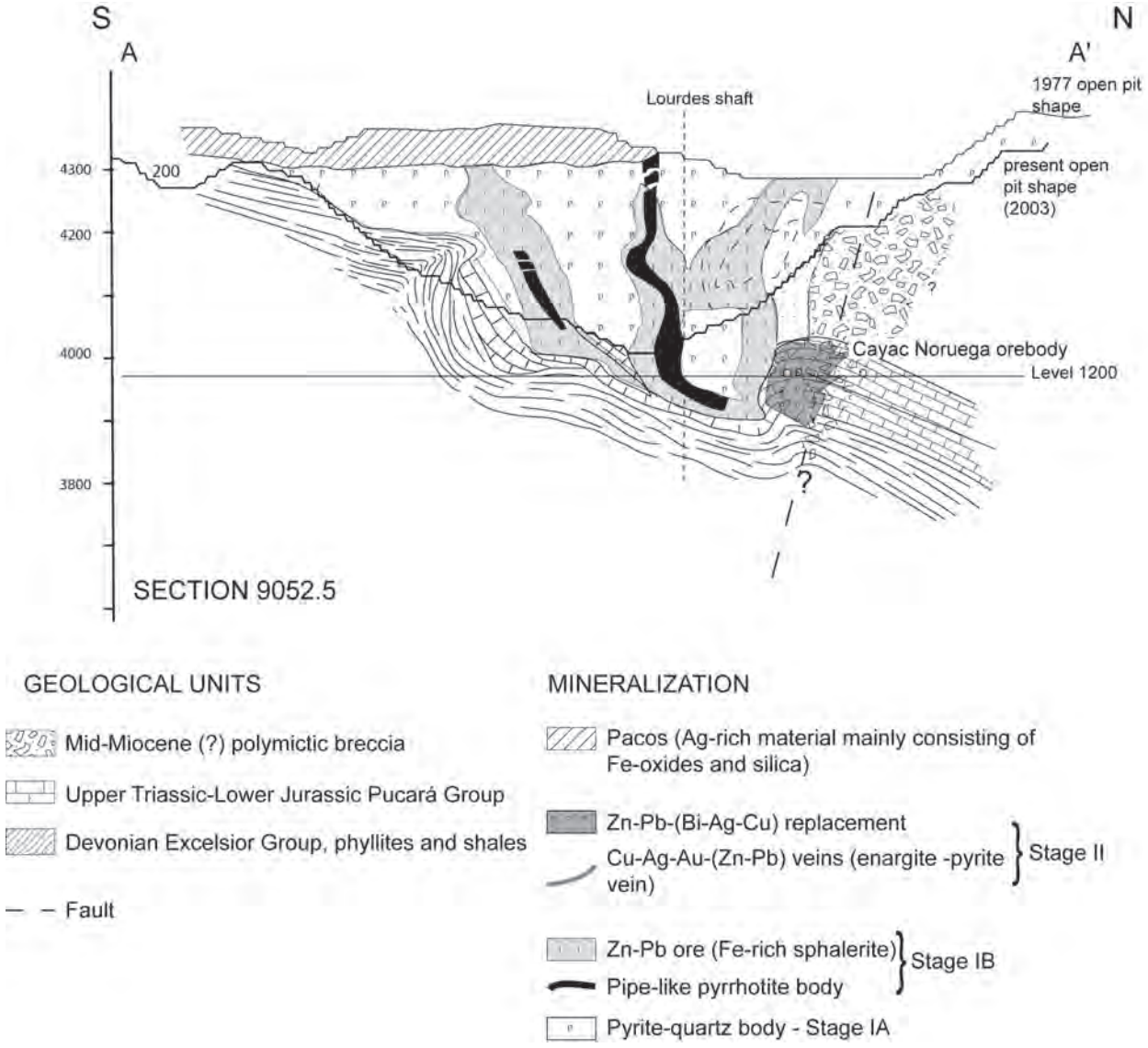

Fig. 4: *N-S cross section (A-A' in Fig. 2) showing pipe-like pyrrhotite bodies and related Zn-Pb mineralization emplaced in the pyrite-quartz body and in the Pucará carbonate rocks. Modified from Einaudi (1977).*

body is 50 x 50 m with a minimum depth of 110 m.

The San Alberto orebody trends N35°E and plunges 50°SW (Fig. 2) with a horizontal section of approximately 30 x 50 m at level 4300 with a minimum depth of 200 m in the direction of its plunge. It does not show clear zonation. This orebody is hosted by a polymictic breccia consisting of angular and sub-angular Pucará Group clasts, up to 5 cm in size, with a rock flour matrix of the same composition (Fig. 6G). The breccia is an elongated NE-SW, subvertical body extending from the bench 4350 to 4100 and crosscuts bedding. In the benches of level 4200 and deeper, the breccia contains, in addition to Pucará carbonate fragments, clasts of Excelsior Group phyllite. This breccia may be related to a diatreme apophyse controlled by faults following a N35°E direction.

The Uliachín and El Pilar orebodies, located 500 m south and 200 m east of the open pit, respectively (Fig. 2) also belong to the second stage carbonate replacement bodies and have been mined since ancient times.

Mineral assemblages and zoning

Sulfide minerals found in contact without showing reaction products are grouped into the term "assemblage" according to Barton et al. (1963). The symbol (-) joins minerals of a single assemblage. The term "association" is used for all minerals appearing in a sample but not necessary in contact or are in contact but show reaction borders. The symbol (+) joins minerals that are present everywhere in the association and the symbol (±) precedes minerals that are not always present or are rare.

The orebodies replacing carbonate rocks ideally show the following zoning (Fig. 13): (1) A core zone comprises the assemblage famatinite-pyrite. It is surrounded by (2) an intermediate zone with the assemblage pyrite-tetrahedrite + Bi_2S_3-Sb_2S_3 ss, and (3) an outer Zn-Pb rich zone with the association pyrite + sphalerite + galena. (4) The outer-most zone is characterized by the association Fe-Mn-Zn carbonates + hematite + magnetite. The best developed zones are the pyrite-tetrahedrite + Bi mineral-bearing intermediate zone and the sphalerite-galena–bearing outer zone, which are economic, whereas the core zone is only weakly developed, and in part absent. This zoning is typical for all orebodies in the Cerro de Pasco pit except San Alberto, where only the outer Zn-Pb and the outer-most zones are recognized. Figure 14 shows a paragenetic sequence for each zone. This sequence must be viewed as the evolution of a fluid in time and space, therefore, minerals precipitating in the outer zones (right part of the diagram), may be contemporaneous with other minerals in the inner zones (left part of the diagram). Table 2 shows the chemical formula of uncommon sulphosalts present at Cerro de

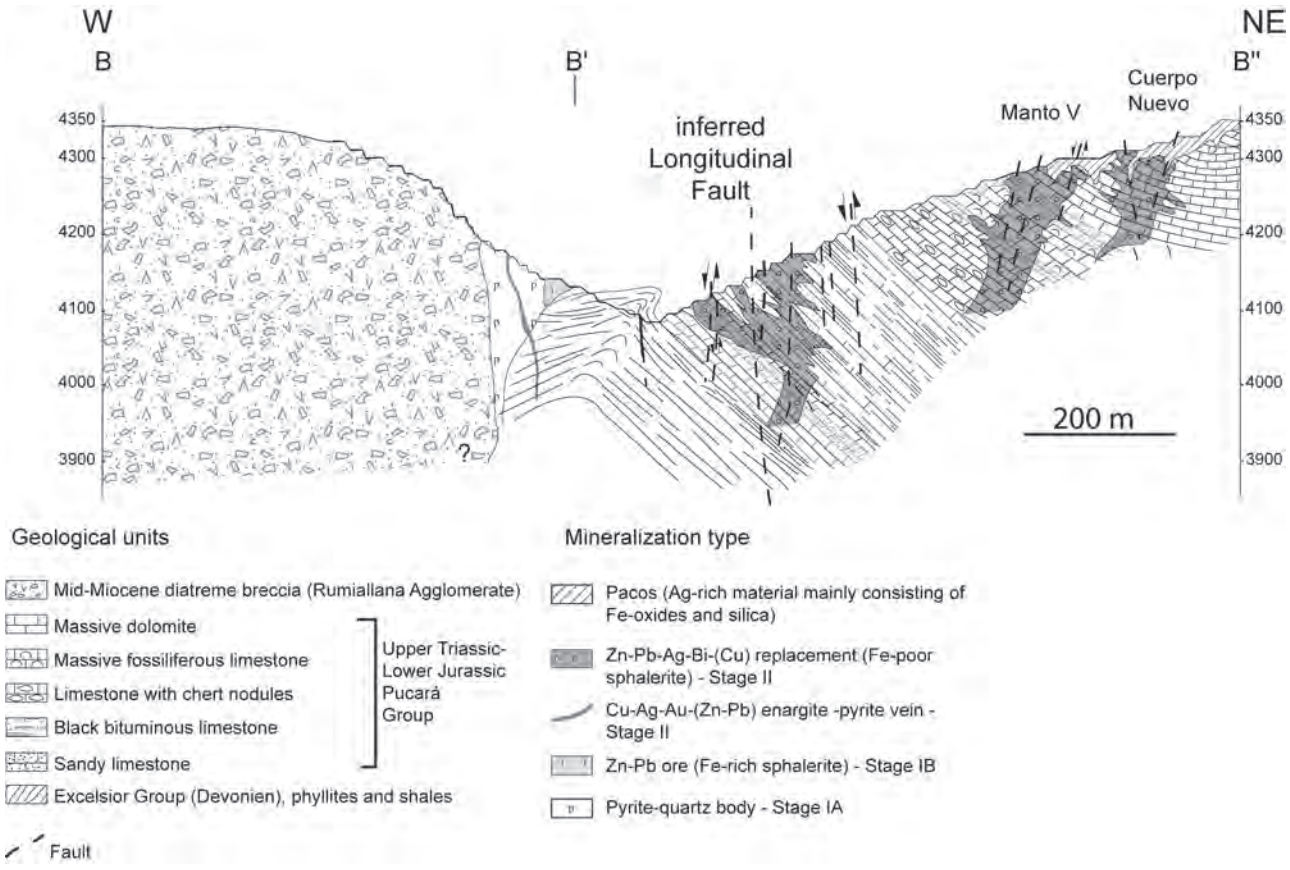

Fig. 5: *B-B'B" cross section (in Fig. 2) through the diatreme and the first mineralization stage (including the pyrite-quartz body and the Zn-Pb ores) and the second stage veins in the diatreme breccia and replacement bodies hosted in Pucará carbonate rocks. These second mineralization stage orebodies are structurally controlled.*

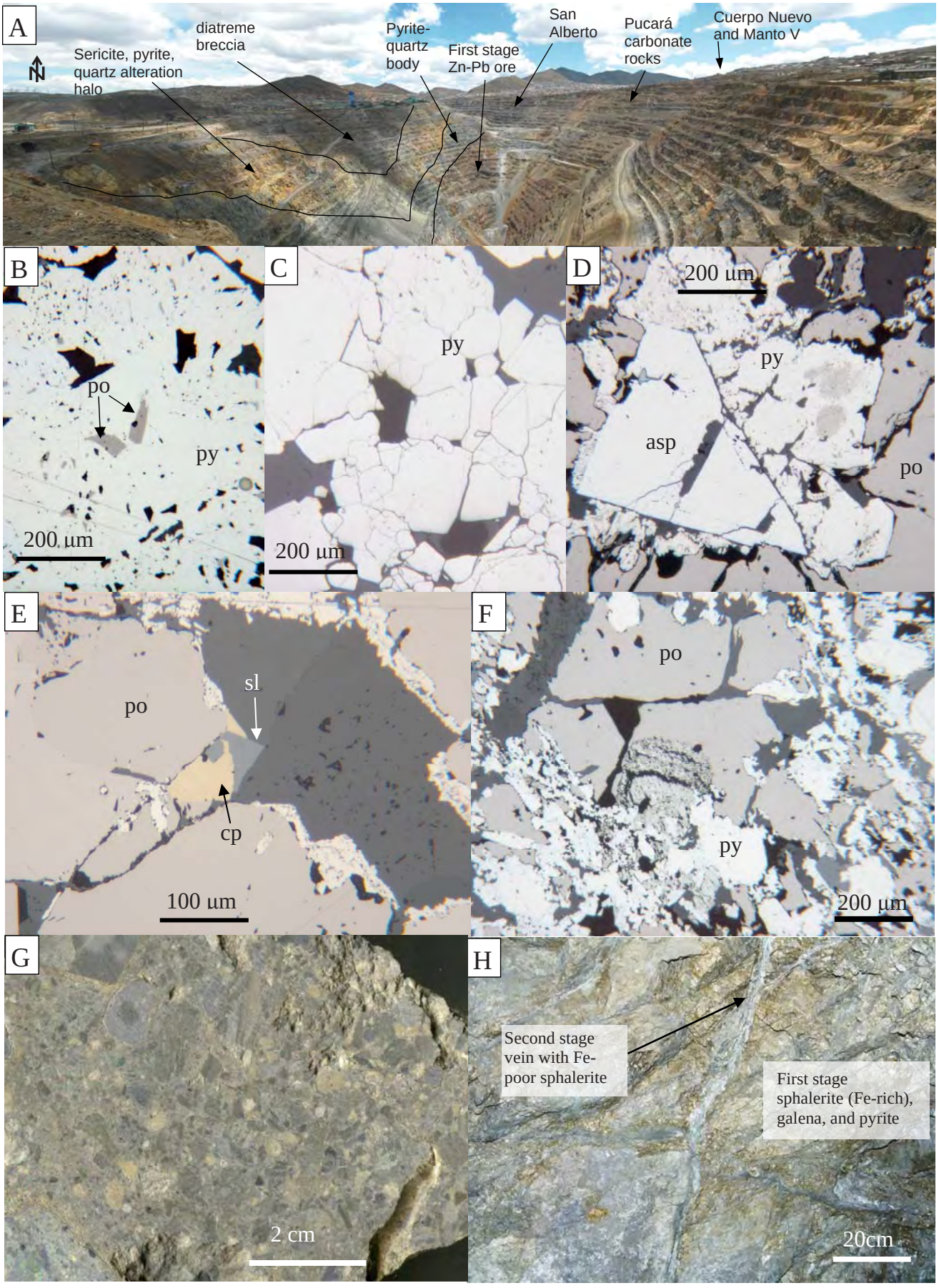
A
Sericite, pyrite, quartz alteration halo
diatreme breccia
Pyrite-quartz body
First stage Zn-Pb ore
San Alberto
Pucará carbonate rocks
Cuerpo Nuevo and Manto V
B
po
py
200 µm
C
py
200 µm
D
200 µm
py
asp
po
E
po
sl
cp
100 µm
F
po
py
200 µm
G
2 cm
H
Second stage vein with Fe-poor sphalerite
First stage sphalerite (Fe-rich), galena, and pyrite
20cm

Fig. 6: *A) View on the Cerro de Pasco open pit looking north. The important features have been outlined. B) Microphotograph showing pyrite I with pyrrhotite blebs (reflected light, // nicols, CPR 433). C) Pyrite I from the pyrite-quartz body showing cracks (reflected light, // nicols, CPR 319). D) Association of pyrrhotite with arsenopyrite and pyrite (reflected light, // nicols, fpe-131-3). E) Deep- to intermediate-level association of pyrrhotite, chalcopyrite, and sphalerite occurring in the pipe-like pyrrhotite bodies (reflected light, // nicols, fpe-131-3). F) Pyrite replacing pyrrhotite in part showing bird eye texture (reflected light, // nicols, fpe-136-9). G) Polymictic breccia consisting of angular and sub-angular clasts of different facies of the Pucará Group rocks with a flour matrix of the same composition (CPR 99). H) Example of a second stage vein crosscutting the first stage Zn-Pb mineralization related to pyrrhotite in the central part of the open pit, 1200 Level, 8920-E, 9860-N. Abbreviations: asp = arsenopyrite; cp = chalcopyrite; sl = sphalerite; po = pyrrhotite; py = pyrite.*

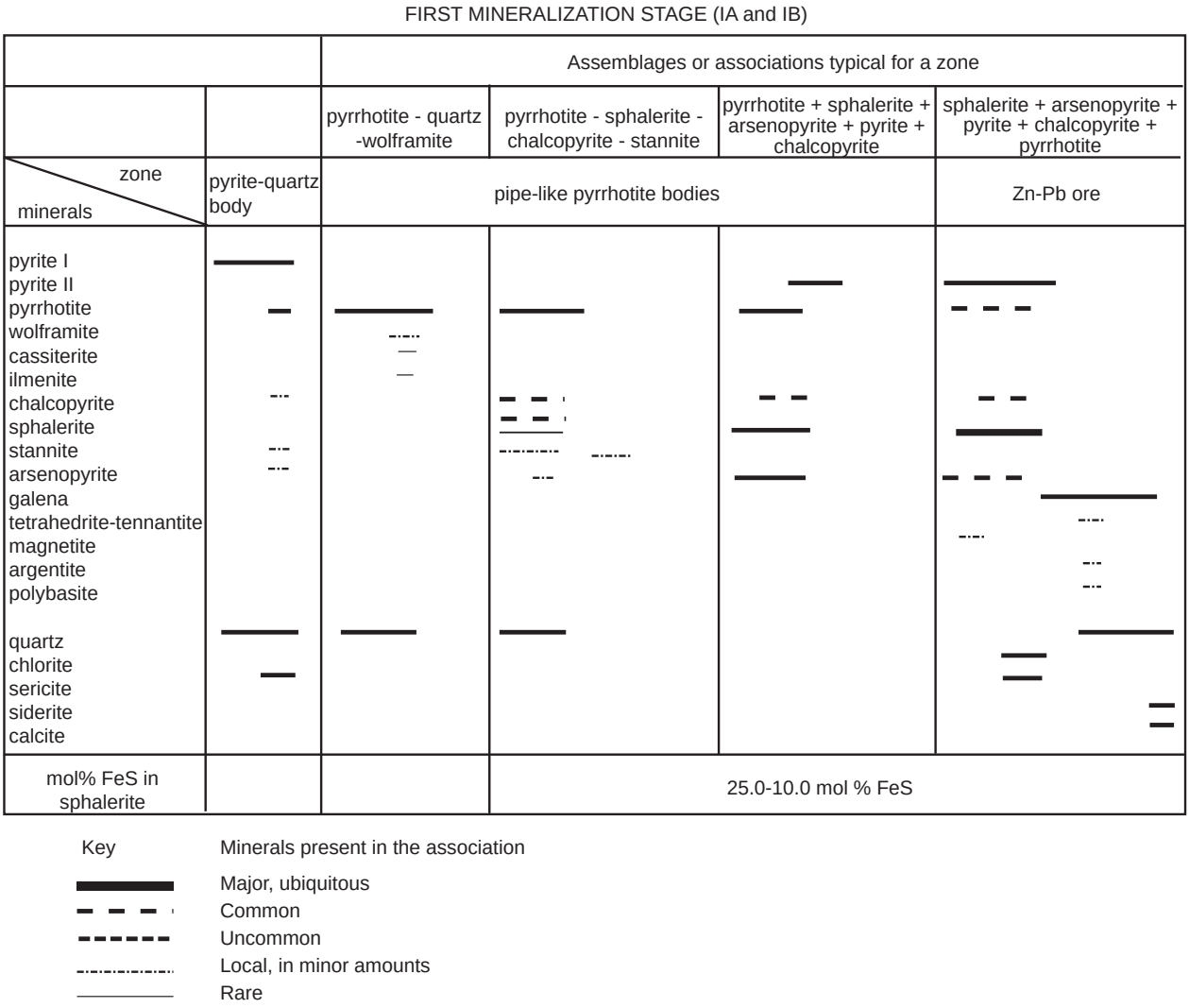

Fig. 7: *Paragenetic sequence for the first stage of mineralization (including observations of Bowditch, 1935, Lacy, 1949, Einaudi, 1968, 1977).*

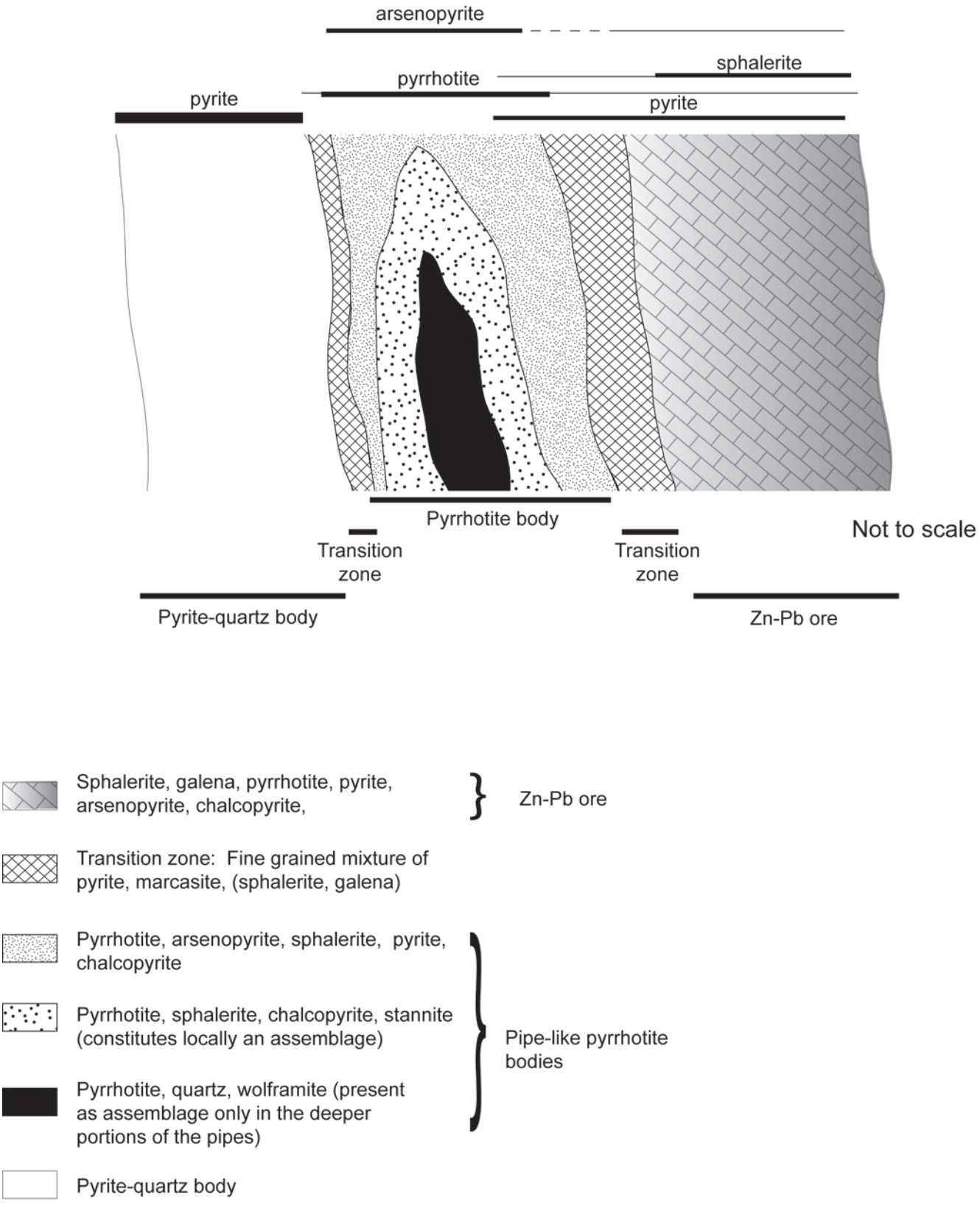

Fig. 8: *Schematic zoning of the first mineralization stage pipe-like pyrrhotite bodies and related Zn-Pb ores bearing Fe-rich sphalerite, based on Einaudi (1977) and this study.*

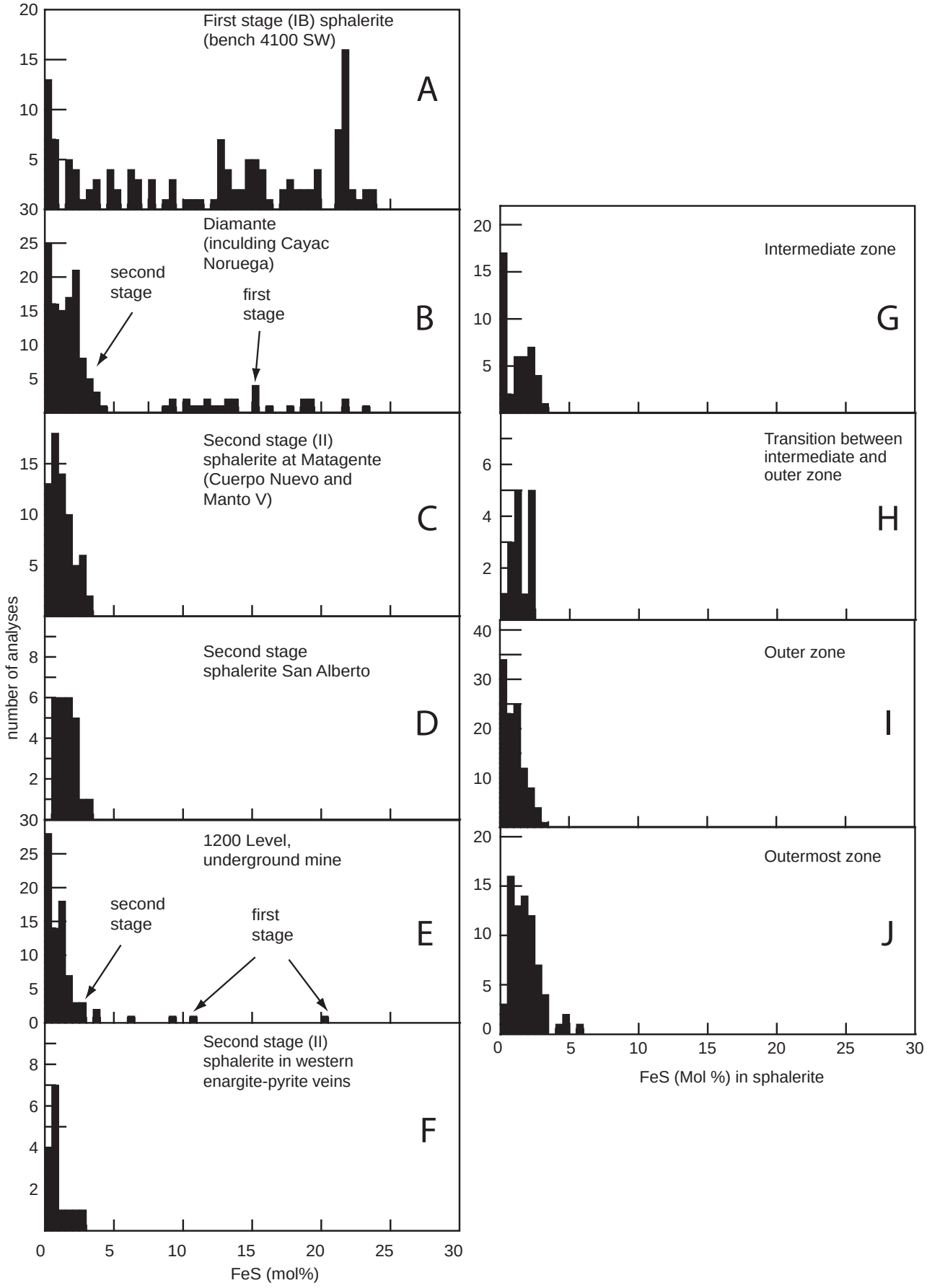

Fig. 9: *A-F) Electron microprobe results of sphalerite from different orebodies. G-J) FeS content of second stage sphalerite ordered according to zones*

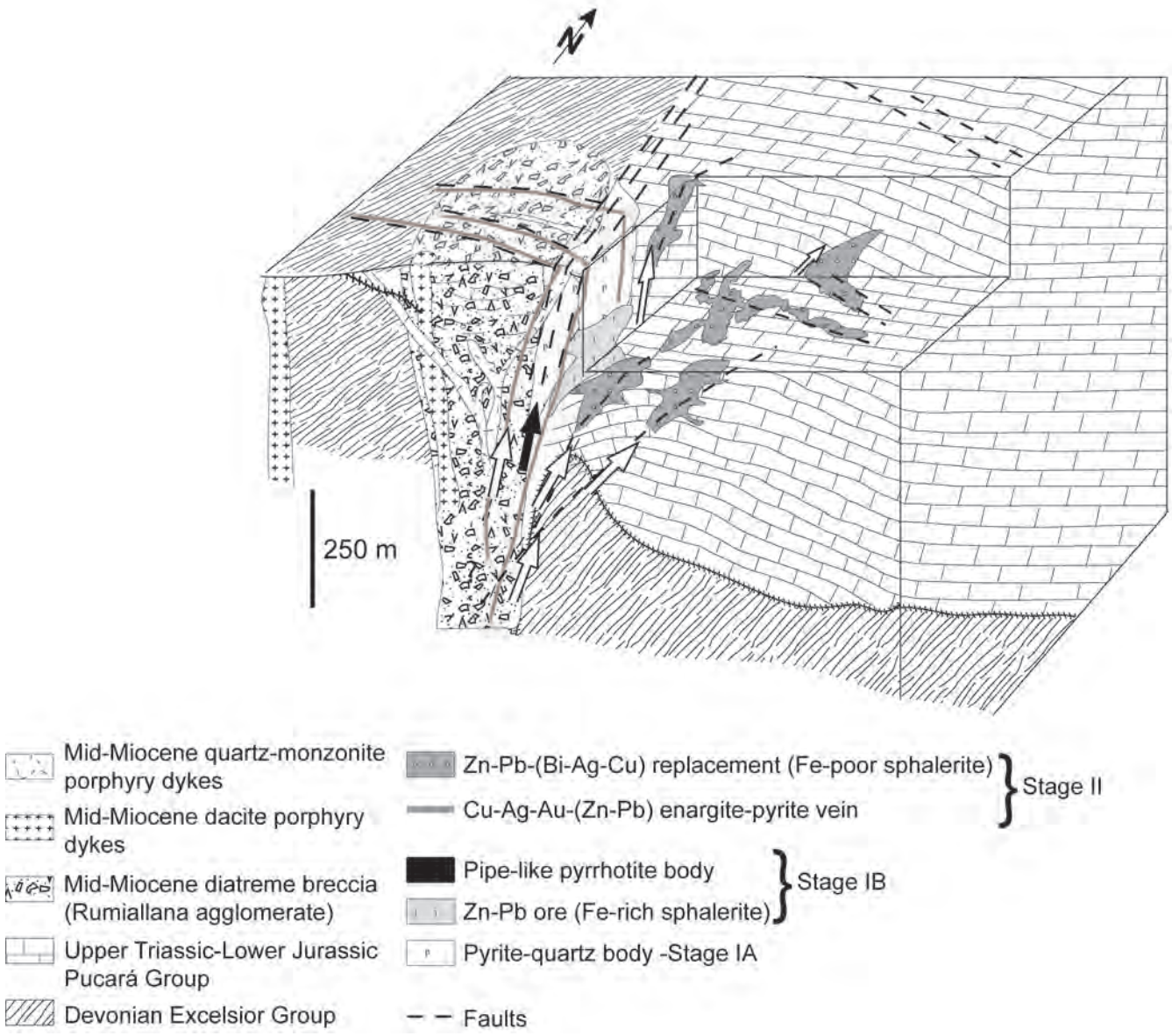

Fig. 10: Three dimensional block diagram showing the Cerro de Pasco deposit with possible fluid path for the two mineralizing stages. The black arrow represents the first mineralization stage (IA and IB), mainly following the N-S structures and the white arrow the second mineralization stage. The fluids for the enargite-pyrite veins followed E-W structures while the fluids responsible for the carbonate replacement bodies followed structures along N35°E, N120°E and N170°E faults

Pasco.

(1) Core zone (famatinite-pyrite)

The core zone is generally less than 5-20 cm wide and has been observed at the 4320 bench outcrop in the Cuerpo Nuevo orebody, in the Cayac Noruega, and Manto V orebodies. Cuerpo Nuevo consists of a well-zoned replacement body. The bulk rock texture is fine grained (150 μm) and friable, showing a grayish color. The sulfide assemblage in the core consists of famatinite (Cu_3SbS_4)-pyrite. Famatinite occurs as subidiomorphic roundish grains (avg. 100 μm in diameter), in part showing crystallographic faces and commonly replaced and overgrown by tetrahedrite-tennantite (Fig. 15D). Locally, tetrahedrite grains contain relics of famatinite suggesting that the replacement of famatinite by tetrahedrite went nearly to completion. Famatinite is close to stoichiometry in composition, with arsenic contents less than 5 percent, (Table 3). Pyrite, named pyrite III, occurs as euhedral grains which average 80 to 200 μm in diameter and is in direct contact with famatinite and does not show any reaction rim. Late fine-grained (<20μm) pyrite is present, generally disseminated within kaolinite. In the core zone, copper grades in hand specimens range up to 1 percent, locally up to 4.8 percent (Table 4).

In the core zone, alunite, quartz, and kaolinite

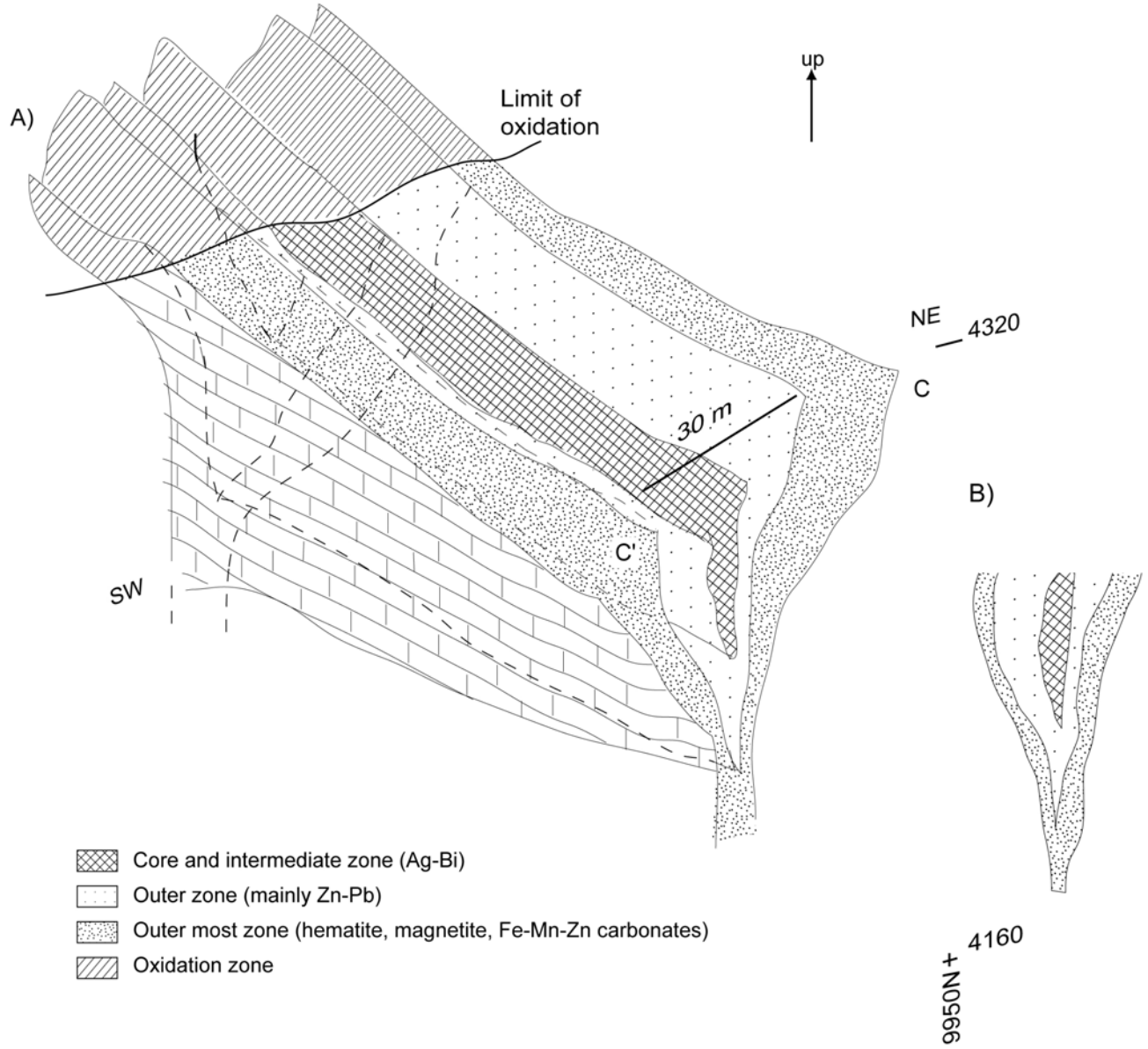

Fig. 11: *3D view of the Manto V orebody. The body has an upward-flaring pipe-like shape as shown in the scheme B. Above 4320 m, the body is oxidized to an Ag-rich material consisting mainly of Fe-oxides and silica (pacos).*

occur, alunite is present as small idiomorphic crystals (10-40 μm) within famatinite and tetrahedrite (Fig. 15B and E). Quartz occurs as idiomorphic crystals frequently within pyrite (20-60 μm, Fig. 15C). The presence of abundant kaolinite (10-30% of the rock) is responsible for the rock being friable

The core zone overprints an early quartz and pyrite assemblage which deposited along the N120°E and N170°E faults present in the open pit (Fig. 2). Quartz occurs as euhedral grains with an average size of up to 100 μm and pyrite occurs as subhdral to euhedral grains (up to 100 μm). Locally, pyrite contains rare inclusions of pyrrhotite (up to 20 μm), which could be attributed to the first stage. This assemblage appears to shield the vein walls and it may be necessary to the development of a high sulfidation assemblage in the core zone.

(2) Intermediate zone (tetrahedrite-pyrite + Bi-minerals)

Transition between the core and the intermediate zone is gradual and is marked by assemblages consisting mainly of pyrite, tetrahedrite and Bi-minerals (Fig. 14). The intermediate zone has been observed in the drillhole CP-00-108 and in the 4320 bench at Cuerpo Nuevo. The ore contains abundant pyrite (5 - 40%) and kaolinite/dickite and has a friable texture. The rock is generally fine-grained (150-200 μm), and pyrite and tet-

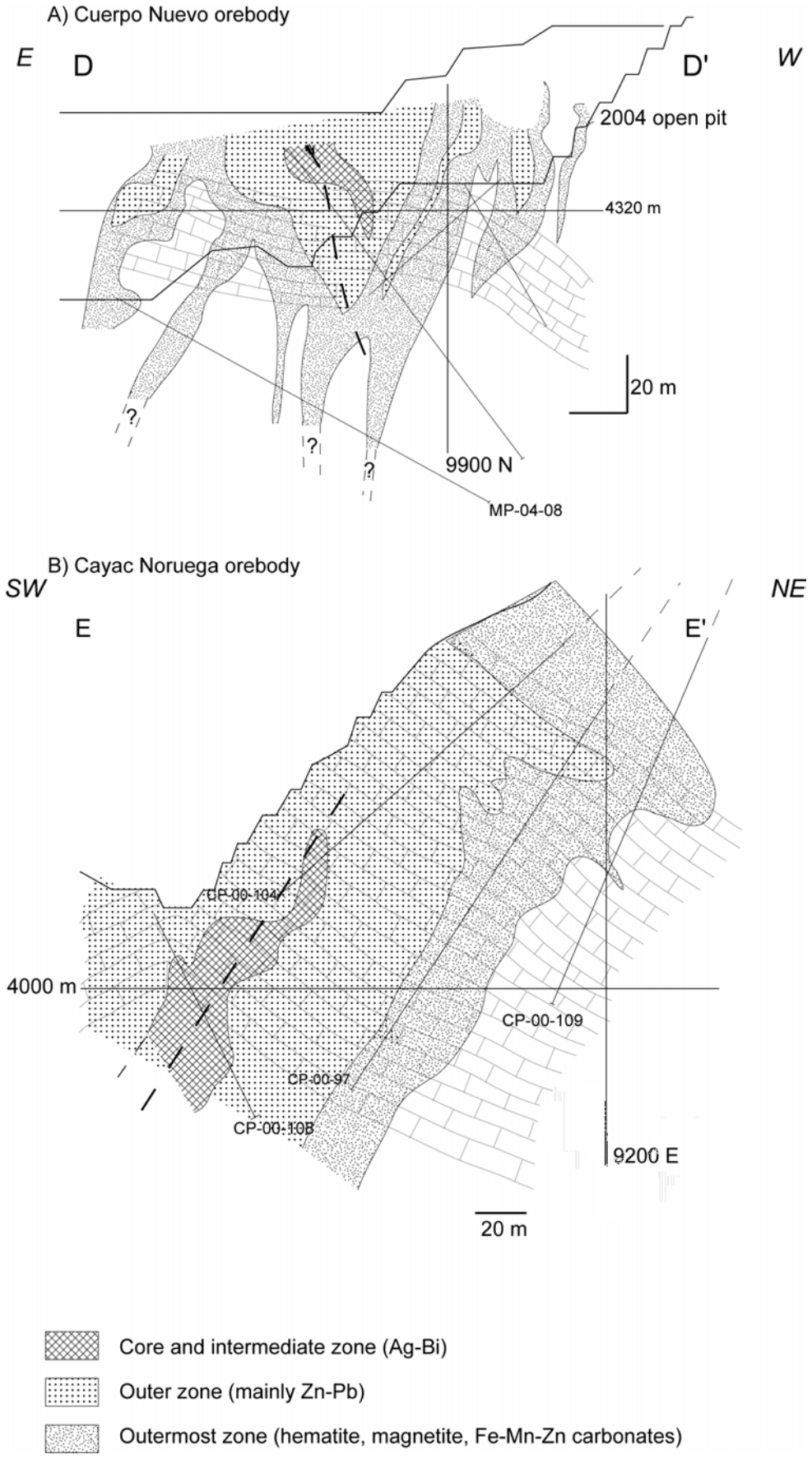

Fig. 12: *A) NE-SW cross section (D-D' in Fig. 2) showing the geometry of zonation in the Cuerpo Nuevo orebody. Note that the lower part is unknown but has a continuation going down dip of the body. Core and intermediate zones have been merged (drawn from surface and drill hole data). B) NE-SW cross section (E-E' in Fig 2) on the Cayac Noruega replacement body in the central part of the open pit (drawn from surface and drill hole data).*

Table 2: Chemical formula of uncommon sulfosalts and gangue minerals present at Cerro de Pasco

Minerals	Chemical formula
Major ore minerals	
Famatinite	Cu_3SbS_4
Tetrahedrite	$(Cu,Fe)_{12}Sb_4S_{13}$
Bi-tetrahedrite-tennantite	$(Cu,Fe,Bi,Zn,Ag)_{12}(Sb,As)_4S_{13}$
Bismutinite-stibnite solid solution series[1]	$(Bi,Sb)S_2$
Cuprobismutite	$Cu_{10}Bi_{12}S_{23}$
Subordinate ore minerals	
Matildite	$AgBiS_2$
Emplectite	$CuBiS_2$
Antimonpearcite	$(Ag,Cu)(Sb,As)_2S_{11}$
Colusite	$Cu_{26}V_2(As,Sn,Sb)S_{32}$
Proustite	Ag_3AsS_3
Jordanite	$Pb_{14}(As, Sb)_6S_{23}$
Gangue minerals	
Alunite	$KAl_3(SO_4)_2(OH)_6$
Hinsdalite	$(Pb,Sr)Al_3(PO_4)(SO_4)(OH)_6$
Svanbergite	$(SrAl_3(PO_4)(SO_4)(OH)_6)$

[1] Bi content: 64.3-69.0%, Bi_2S_2 between 73.6 and 83.2

rahedrite are visible at macroscopic scale (rarely up to 1-2 mm, Fig. 15A). The silver content in the intermediate zone can locally reach up to 2000 g/t, bismuth up to 1 percent, copper up to 7 percent, antimony up to 5 percent, zinc up to 1 percent, and lead up to 0.4 percent (Table 3).

The main Ag-Bi-Cu sulfosalts include tetrahedrite, cuprobismutite ($Cu_{10}Bi_{12}S_{23}$), bismuthinite-stibnite solid solution series (Bi_2S_3-Sb_2S_3), matildite ($AgBiS_2$), emplectite ($CuBiS_2$), and chalcopyrite. Tetrahedrite grains containing relics of famatinite occur suggesting that locally, the replacement of famatinite by tetrahedrite went nearly to completion (Fig. 15E). Electron microprobe analyses show two populations of tetrahedrite grains (Fig. 16). In addition single grains are commonly chemically oscillatory As-Sb zoned, the cores being Sb richer (Fig. 17A). Tetrahedrite replacing famatinite (Fig. 17C) falls in the composition field of tetrahedrite (Nickel, 1992) while the other population falls in the field of tetrahedrite-tennantite and Bi-bearing tetrahedrite. This latter population occurs always in the presence of bismuth minerals. Cu contents in tetrahedrite range from 34 to 43 wt percent, Sb and As contents of 0.36-28.4 wt percent and 0.79-9.8 wt percent respectively (Table 3). Tetrahedrite shows an average Bi content of 8 percent (up to 18%), Zn of 4 wt percent avg, and Fe of 2 wt percent (Table 3). Grains with bismuthinite-stibnite solid solution series occur as laths and are strongly anisotropic in reflected light (crossed polars) with Sb_2S_3 contents between 16 to 26 wt percent. At the margin of grains of bismuthinite-stibnite solid solution series being replaced by tetrahedrite, a thin rim (<4 μm) of an undetermined mineral occurs (Fig. 17B). Emplectite (~100 μm) is greenish in parallel nicols (reflected light) and is generally replaced by cuprobismutite and contains average Bi contents of 61.8 wt percent and Cu contents of 19.9 wt percent (Table 3). Cuprobismutite (up to 200μm) occur as laths and is characterized by a strong bright white color in reflected light. Bi contents in cuprobismutite are 65 wt percent, 12 wt percent Cu and between 2.9 to 4.7 wt percent Ag (Table 3). Matildite forms in places an outer rim (5-10 μm) of bismuthinite-stibnite solid solution series, the whole being surrounded by tetrahedrite. Matildite is also present in xenomorphic grains within tetrahedrite, which averages 50 μm in diameter (Fig. 17D) and is close to stoichiometry with 54.8 wt percent Bi, 28 wt percent Ag, and 16.5 wt percent S (Table 3). Chalcopyrite occurs in the tetrahedrite as small blebs (50-70 μm) and occurs in some places with covellite. Traces of covellite replace along fractures most Cu-bearing minerals.

Additional sulfides that occur in the intermediate zone are minor antimonpearceite ($(Ag,Cu)_{16}(Sb,As)_2S_{11}$), colusite, and sphalerite. Antimonpearceite is present as inclusions (40-50 μm in diameter) in tetrahedrite (Fig. 17D). Antimonpearceite contains between 64.8 and 67 wt percent Ag, 6.6 to 8 wt percent Cu, 5-7 wt percent Sb (one sample as low as 2 wt % Sb, Table 3), and between 1 and 2 wt percent As. Bismuth contents reach up to 4.8 wt percent (one sample up to 7.3 wt % Bi, Table 3). Colusite appears in two samples as small crystals (50 μm) adjacent to tetrahedrite, and shows no replacement textures. A pyrite-tetrahedrite-colusite assemblage occurs locally (Fig. 17E). Late pyrite occurs with kaolinite as small euhedral grains (10 μm) and cements brecciated sphalerite (Fig. 17F). Sphalerite FeS composition ranges from 0.1 to 4 mol %, although the average value is less than 1 mol % (Fig. 9).

Kaolinite, quartz, alunite, and hinsdalite ($(Pb,Sr)Al_3(PO_4)(SO_4)(OH)_6$), an aluminium phosphate sulfate (APS) mineral (Fig. 18A) occur in the intermediate zone. Alunite gives way to hinsdalite from the core to the intermediate zone. Hinsdalite and alunite occur locally as small euhedral grains (10 μm) within colusite. Barite is also present in the intermediate zone. Kaolinite and APS minerals contents vary in this zone from 5 to 50 percent of the total material. APS minerals normally show Sr contents between 5.5 to 7.4 wt percent and Pb contents of 6.4 to 8.4 wt percent. Ca contents vary between 2.4 and 2.7 wt percent. Quartz occurs as euhedral grains in pyrite.

(3) Outer zone (sphalerite + galena + pyrite ± Ag-sulfosalts)

Transitions from core to intermediate zone and to outer zone are gradual on macroscopic and microscop-

ic scale. Macroscopically, the outer zone consists of a friable sphalerite-bearing material and near the outermost zone, it becomes more massive. Sphalerite is light brown or colorless and occurs mainly as small grains (average 50 μm to 1 mm, rarely up to 2mm in size). In the Manto V and Cuerpo Nuevo orebodies (Matagente area), as well at Cayac Noruega (Diamante area), low FeS contents predominate, ranging from 0 to 3.5 mole percent FeS (usually less than 1 mole percent FeS, Fig. 9B-D). Figure 9G-I presents the second stage sphalerite composition according the mineral zones defined above. In general, very low FeS contents (< 1 mole %) predominate over higher FeS contents (between 1 and 3.5 mole %).

Galena is also present (50 μm to 1 mm, up to 5 mm in size) and generally replaces or, less commonly, is replaced by sphalerite. In places, it overgrows sphalerite and pyrite. Whole rock analyses of typical ore show Zn contents up to 45 percent, Pb up to 6 percent, and silver up to 300 ppm (Table 4).

When Ag-sulfosalts are present, they occur near to the contact to the intermediate zone and only in minor amounts (Table 3). Silver and Pb sulfosalts such as proustite (Ag_3AsS_3) and jordanite ($Pb_{14}(As,Sb)_6S_{23}$), are present as ~50 to ~30 μm inclusions in galena replacing pyrite (Fig. 18B). Sphalerite abundance diminishes through the outer to the outermost zone and galena is the main constituent of massive galena-bearing ores on the outer margins of the outer zone. Hinsdalite and svanbergite ($SrAl_3(PO_4)(SO_4)(OH)_6$) abundances decrease from the intermediate to the outer zone. Kaolinite is abundant in the outer zone and is responsible for the friable texture of the Zn-Pb ore.

(4) Outermost zone (magnetite + hematite + Fe-Mn-Zn carbonates)

The outermost zone contains magnetite, hematite

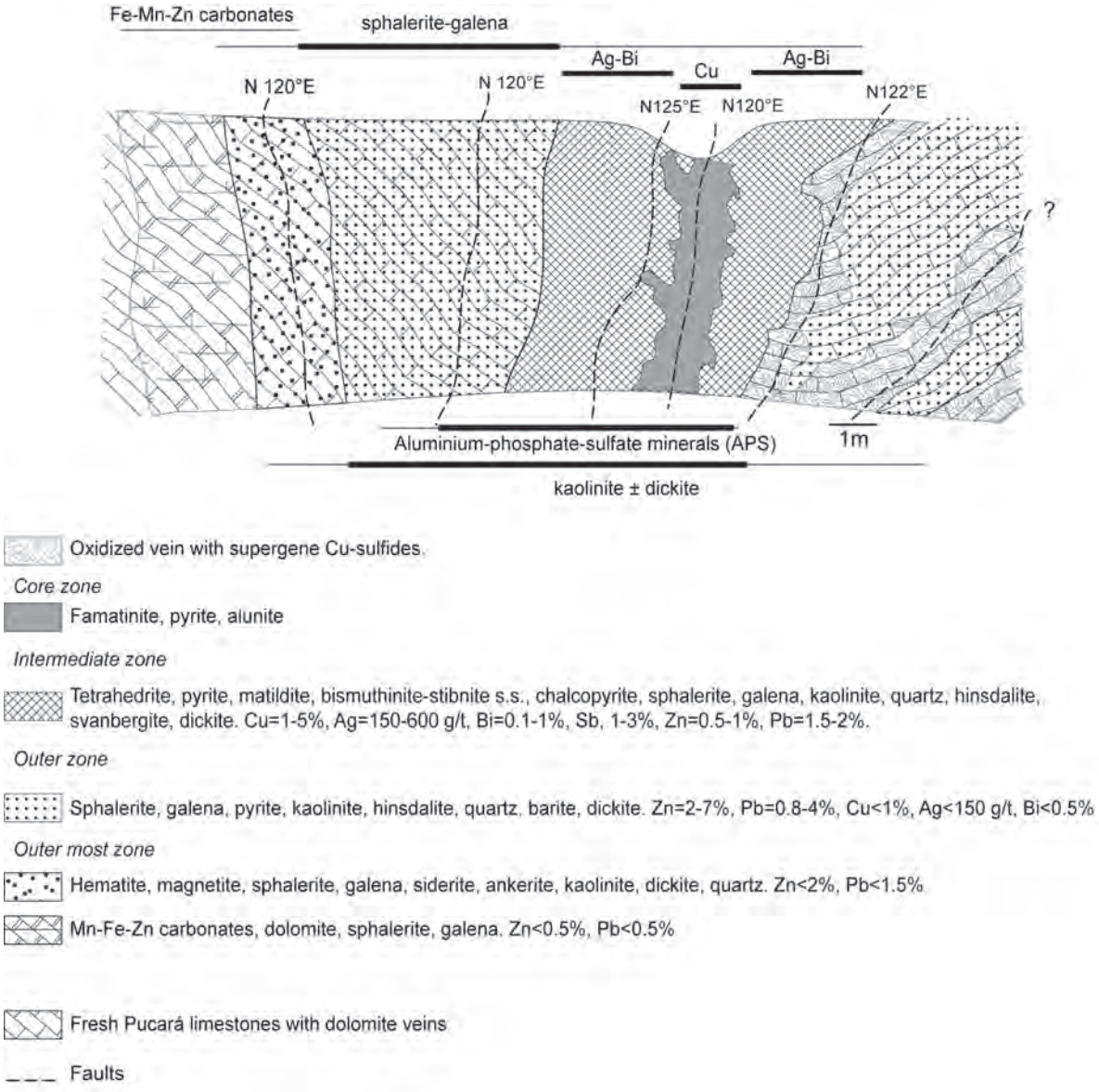

Fig. 13: *Idealized zonation based on mapping of the 4320 bench and drill hole (CP-00-108) descriptions (modified from Baumgartner et al., 2003). For whole rock analyses of typical mineralized samples, see Table 5.*

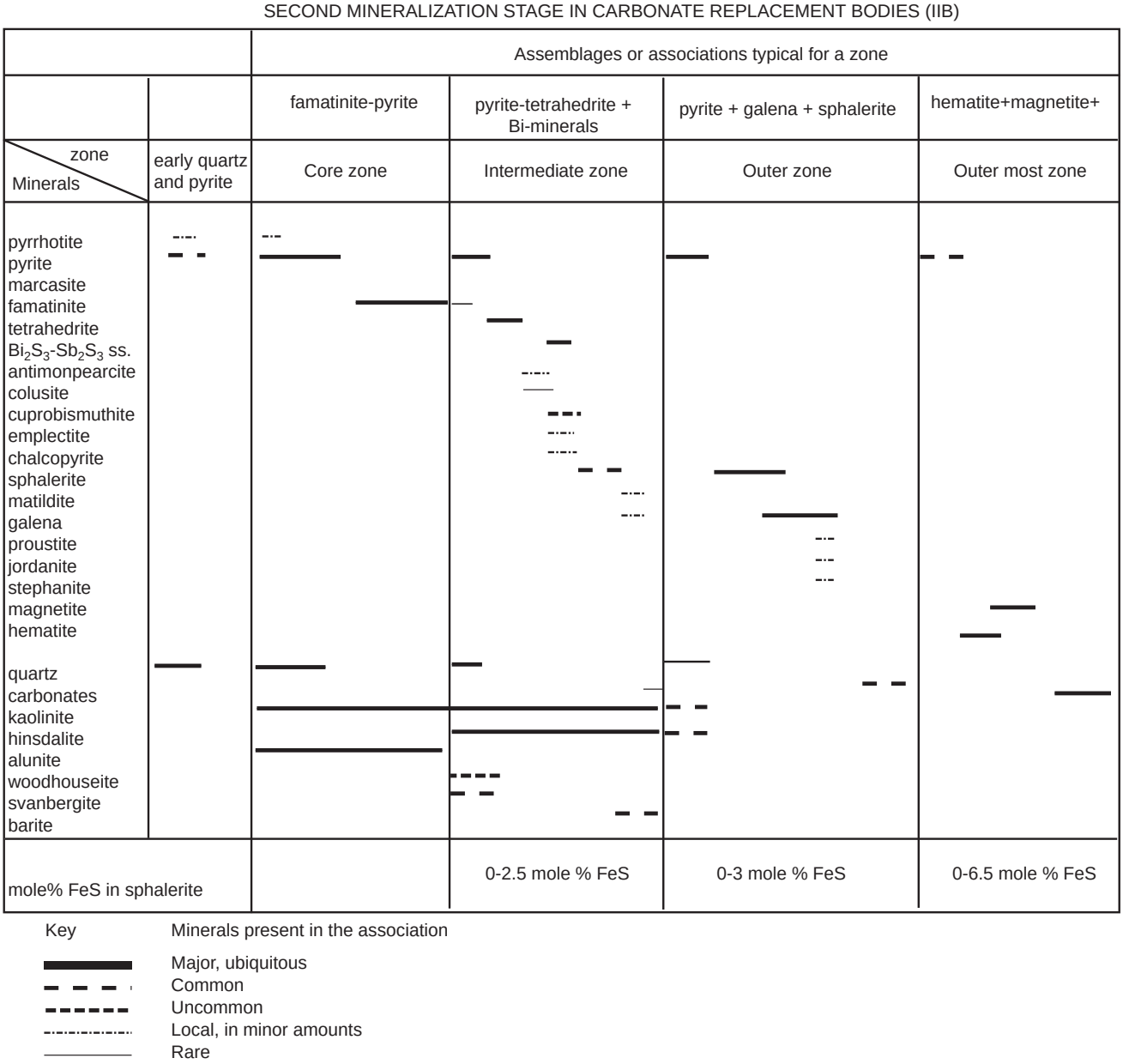

Fig. 14: *Paragenetic sequence of the carbonate replacement orebodies. This sequence must be viewed as the evolution of a fluid in time and space, therefore, minerals precipitating in the outer zones (right part of the diagram), may be contemporaneous with other minerals in the inner zones (left part of the diagram)*

(typically blades of 50-100 μm in length), and, adjacent to Pucará limestones, Fe-Mn-Zn carbonates. Sphalerite and galena are subordinate and constitutes 1-2 percent of the outer zone. These minerals occur intergrown with hematite and magnetite grains (up to 100 μm in size) and, rarely, with Fe-Mn-Zn carbonates. Sphalerite composition yields a slightly higher FeS content than in the outer zone (up to 4.7 mole %, Fig. 9J).

The FeS content of sphalerite is up to 4.5 mole percent. Mutual textural relationships between hematite and magnetite are complex. Locally, hematite is replaced by magnetite and subsequently replaced by pyrite (Fig. 18C and D). Late euhedral pyrite occurs with Fe-Mn-Zn carbonates.

The outer margins of these zones are in places constituted by massive Fe-Mn-Zn carbonates typically $(Fe_{0.4\text{-}0.9}, Mn_{0.1\text{-}0.4}, Zn_{0.1\text{-}0.25})CO_3$ (Table 5), that are easily recognized in the field because of their high specific gravity. These carbonate minerals contain euhedral pyrite grains that are up to 50 μm in size.

Summary

The main ore mineral assemblages in each zone can be summarized as following (Fig. 14): the core zone contains mainly Cu-rich sulfosalts (such as famatinite), the intermediate zone consists of Cu-Ag-Bi sulfides and sulfosalts (including tetrahedrite and Bi-mineral), the outer zone is mainly Zn-Pb-rich (with sphalerite and galena), while the outer zone is Fe-rich (with magnetite and hematite). The texture of the core and intermediate zones varies generally with the pyrite and clay content.

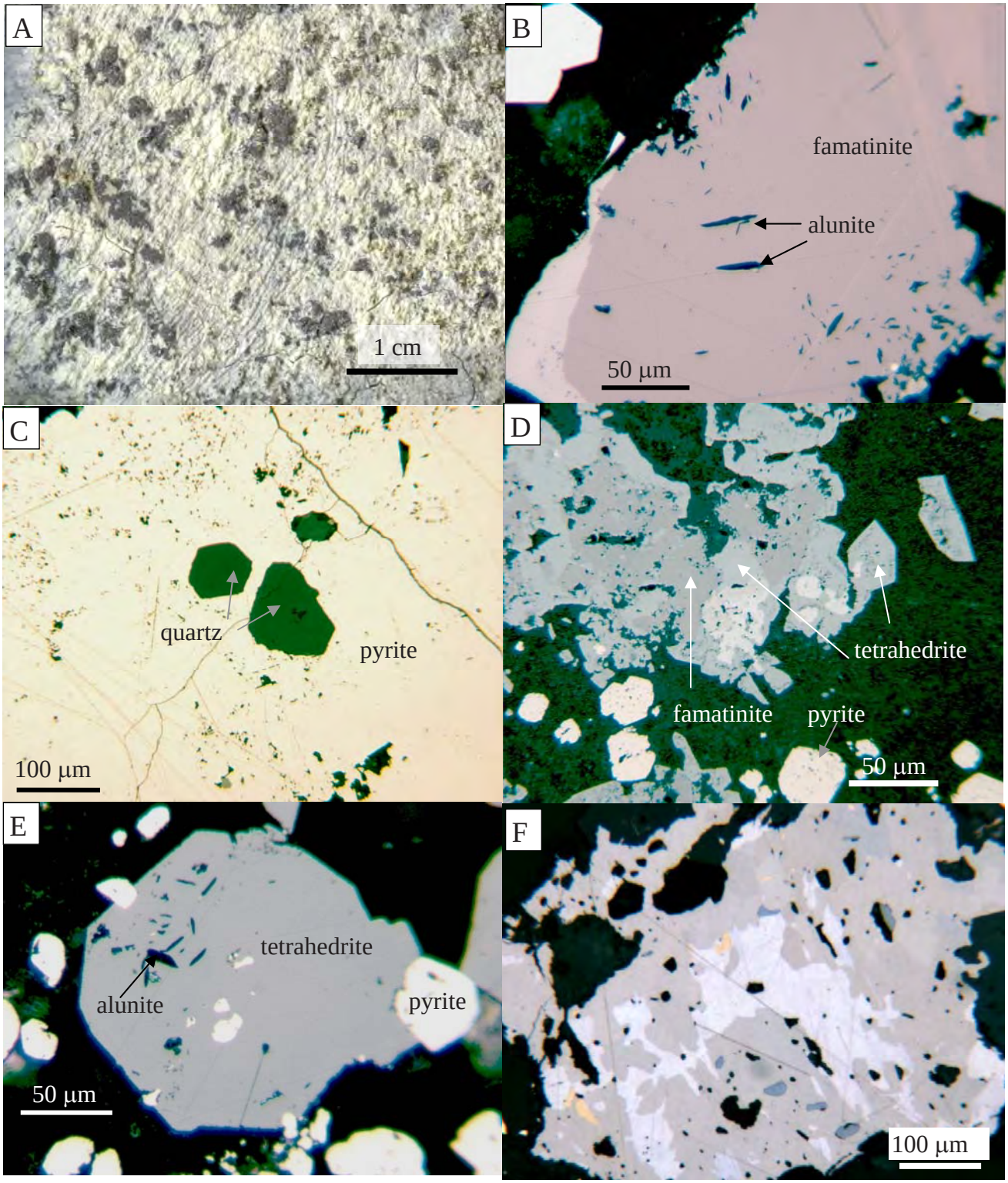

Fig. 15: *A) Hand specimen of the intermediate zone with abundant kaolinite and tetrahedrite (CPR 82). B-E) Typical views of the Cu-rich core and the Ag-B-rich intermediate zone in reflected light (plane polarized light if not indicated otherwise). B) Idiomorphic alunite within famatinite, Cuerpo Nuevo, oil immersion, CPR 149. C) Idiomorphic quartz within early pyrite, Diamante area, CPR 84. D) Tetrahedrite as subidiomorphic overgrowth on famatinite and partly as replacement, Cuerpo Nuevo, CPR 149. E) Idiomorphic alunite within pseudomorphic tetrahedrite after famatinite, oil immersion, CPR 149, Cuerpo Nuevo.*

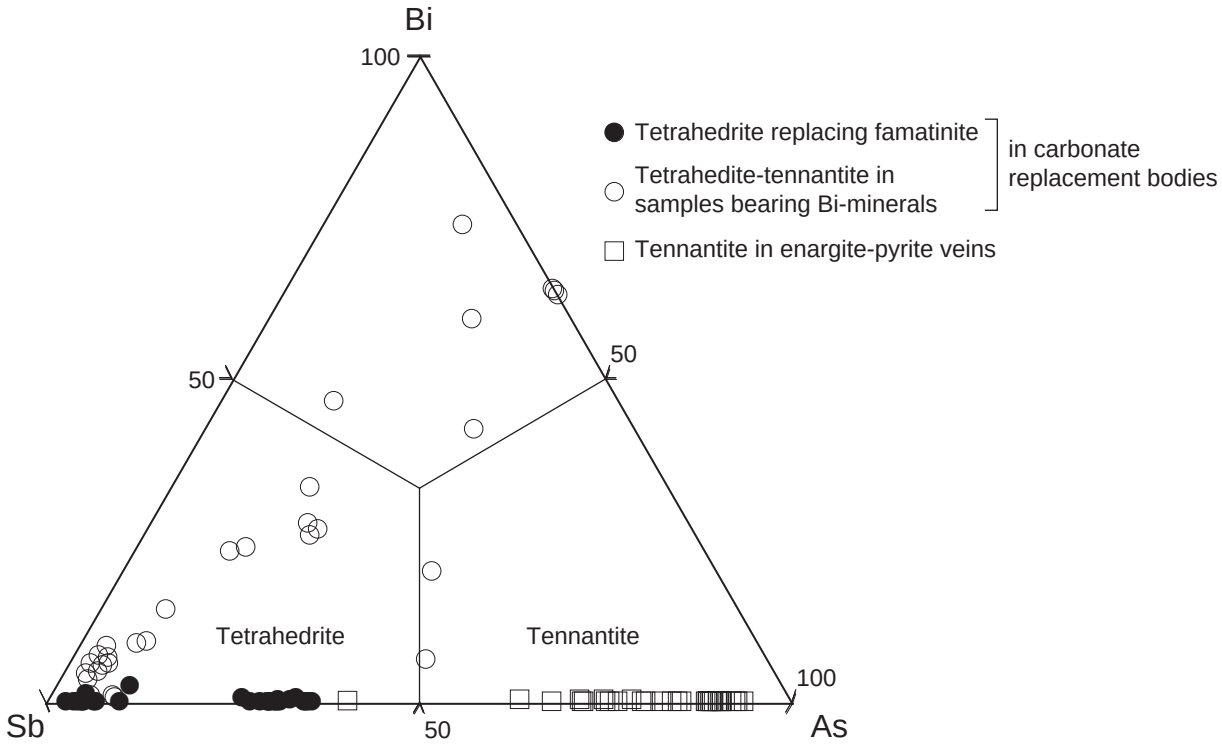

Fig. 16: *Tetrahedrite-tennantite composition in second stage veins and carbonate replacement bodies. Note the two tetrahedrite-tennantite populations in replacement bodies, one Bi-poor (solid circles) and another Bi-rich (note the positive Bi-As correlation). Bi-rich tetrahedrite-tennantite occurs only in samples carrying Bi minerals such as bismuthinite-stibnite solid solution, emplectite, or cuprobismuthite. Classification based on Nickel (1992).*

Table 3: Electron microprobe analyses on complex sulfosalts from the second stage replacement bodies and veins.

Mineral	Sample	S (wt %)	Fe (wt %)	Cu (wt %)	Zn (wt %)	As (wt %)	Ag (wt %)	Sn (wt %)	Sb (wt %)	Pb (wt %)	Bi (wt %)	Total
Core zone												
famatinite	cpr 149	30.12	0.04	43.50	0.02	4.00	0.02	0.17	22.46	0.00	0.00	100.33
famatinite	cpr 149	29.41	0.01	43.78	0.00	3.40	0.04	0.25	22.84	0.00	0.03	99.74
famatinite	cpr 149	29.98	0.02	43.88	0.00	3.59	0.01	0.13	22.70	0.00	0.03	100.33
enargite	cpr 109	32.79	0.06	48.04	0.02	17.76	0.03	b.d.l.	0.49	n.a.	1.57	100.87
luzonite	cpr 137	31.07	0.38	45.23	b.d.l.	11.76	0.03	n.a.	10.15	n.a.	0.03	98.74
Intermediate zone												
tetraedrite	cpr 149	24.98	0.15	37.07	7.73	0.79	0.39	0.20	28.45	0.00	0.00	99.77
Bi tetrahedrite	cpr 149	23.29	1.22	36.91	6.82	2.67	1.38	0.14	22.97	0.00	4.24	99.64
tennantite	cpr 109	28.15	1.64	43.82	6.12	18.00	0.00	n.a.	2.33	0.00	0.00	100.08
cuprobismutite	cpr 81	18.41	0.10	12.70	0.07	0.00	3.30	0.00	0.34	0.00	65.62	100.55
emplectite	cpr 81	18.36	0.08	19.81	0.06	0.00	0.12	0.00	0.14	0.00	62.07	100.68
matildite	cpr 82	16.55	0.09	1.25	0.15	0.00	27.90	0.00	0.00	0.00	54.65	100.59
antimonpearcite	cpr 82	15.07	0.05	7.77	0.14	0.65	65.70	0.00	7.54	0.00	3.38	100.31
bismutinite-stibnite ss. series	cpr 149	20.27	0.04	0.52	0.11	0.00	0.07	0.15	11.20	0.00	67.95	100.31
proustite	cpr 77	18.13	0.08	0.10	0.88	12.57	65.01	0.00	0.51	0.00	0.00	97.28
proustite	cpr 77	17.80	0.04	0.00	0.45	12.02	65.77	0.00	1.16	0.00	0.00	97.25
proustite	cpr 77	18.12	0.09	0.13	0.05	13.60	64.19	0.00	0.31	0.00	0.00	96.48

n.a. = not analyzed
b.d.l. = below detection limits
Cd was always below detection limits

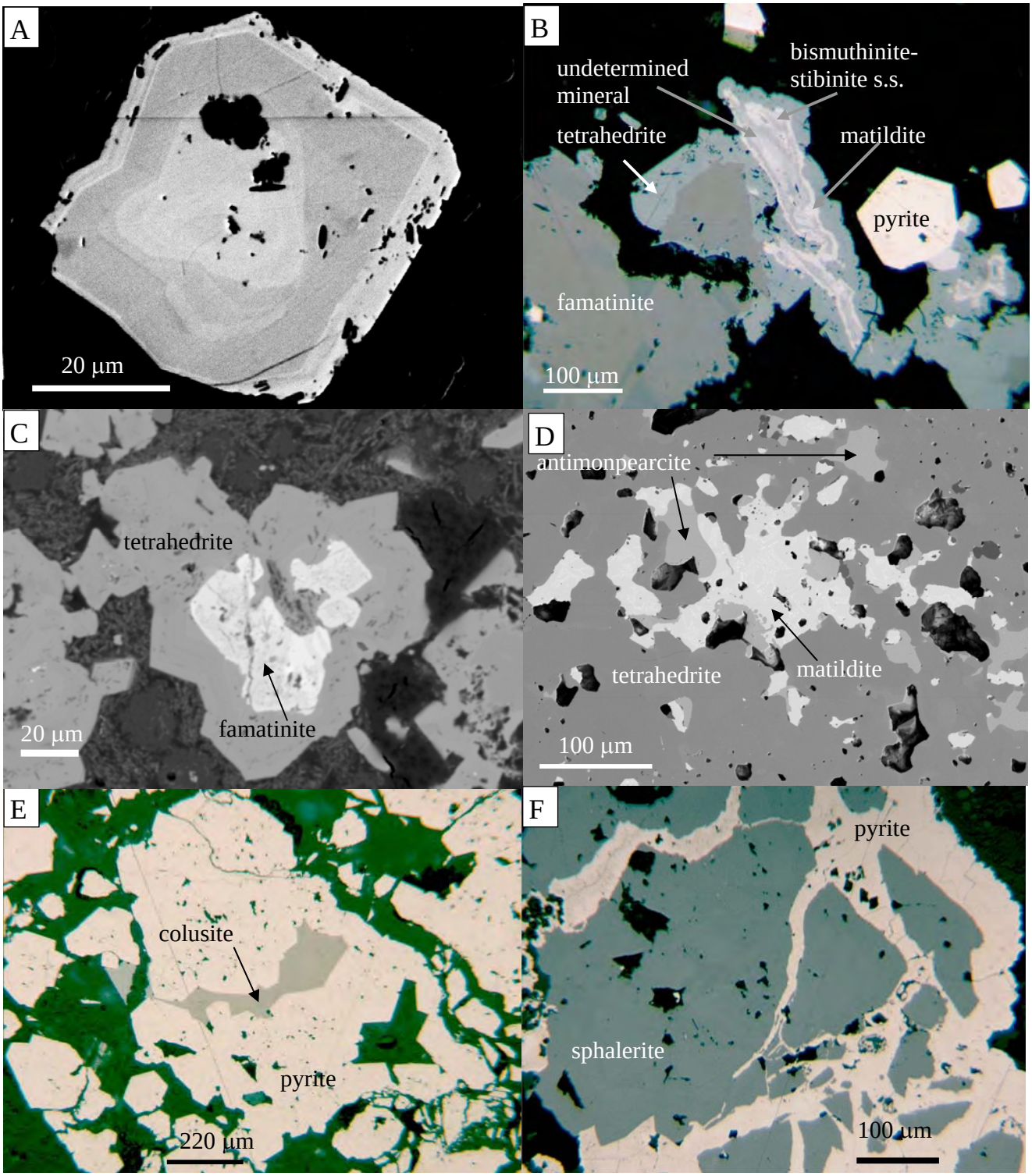

Fig. 17: *Microphotographs from the core and intermediate zones. A) Famatinite crystal showing As-Sb compositional variations (BSE image, CPR 149). B) Overgrowths of tetrahedrite and bismuthinite-stibnite solid solution series on famatinite. A rim of matildite is observed. Note reflection anisotropy of famatinite. The undetermined mineral (grey) is too small to be identify, Cuerpo Nuevo, reflected light, // nicols, CPR 149. C) Famatinite replaced and overgrown by idiomorphic tetrahedrite (BSE, CPR 149). D) BSE image showing blebs of antimonpearcite and matildite within tetrahedrite. Without BSE, antimonpearcite is difficult to distinguish from tetrahedrite. BSE image reveals the texture of antimonpearcite. Matildite may also be mistaken with galena without a careful BSE observation (BSE image, CPR 82). E) Local assemblage of pyrite-tetrahedrite-colusite (reflected light, // nicols, CPR 84). F) Brecciated sphalerite cemented by late pyrite, reflected light, // nicols, CPR 74.*

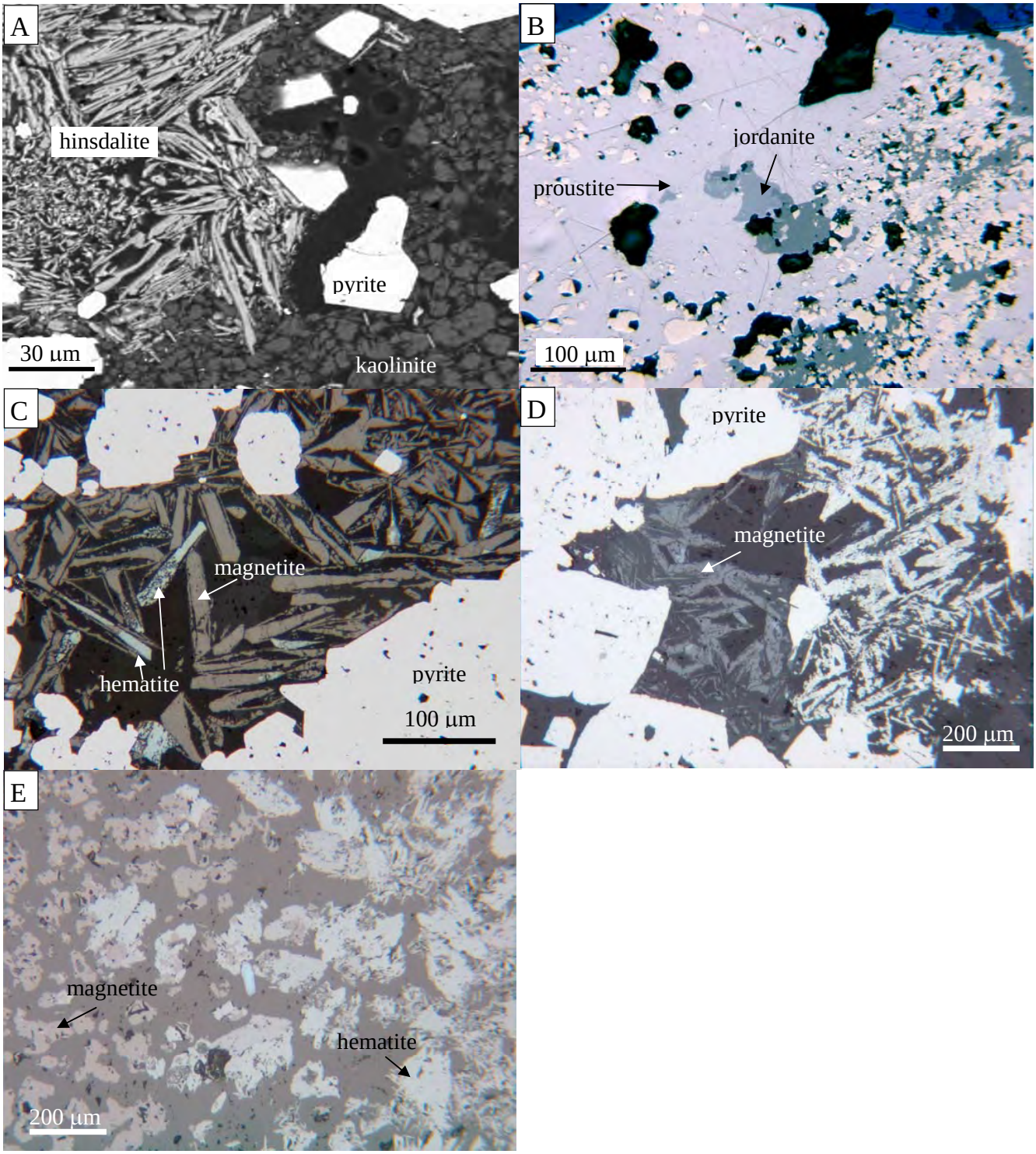

Fig. 18: *A) BSE image showing hinsdalite, kaolinite, and pyrite from the intermediate zone, CPR 81. B) Proustite and jordanite as inclusions in galena, Cayac Noruega, (reflected light, // nicols, CPR 77. C-E) Photomicrographs of the outermost zone. C) Hematite replaced by magnetite (reflected light, // nicols, CPR 433). D) Pyrite replacing magnetite, magnetite replacing hematite (reflected light, // nicols, CPR 433). E) Magnetite replaced by earthy hematite (reflected light, // nicols, CPR 439)*

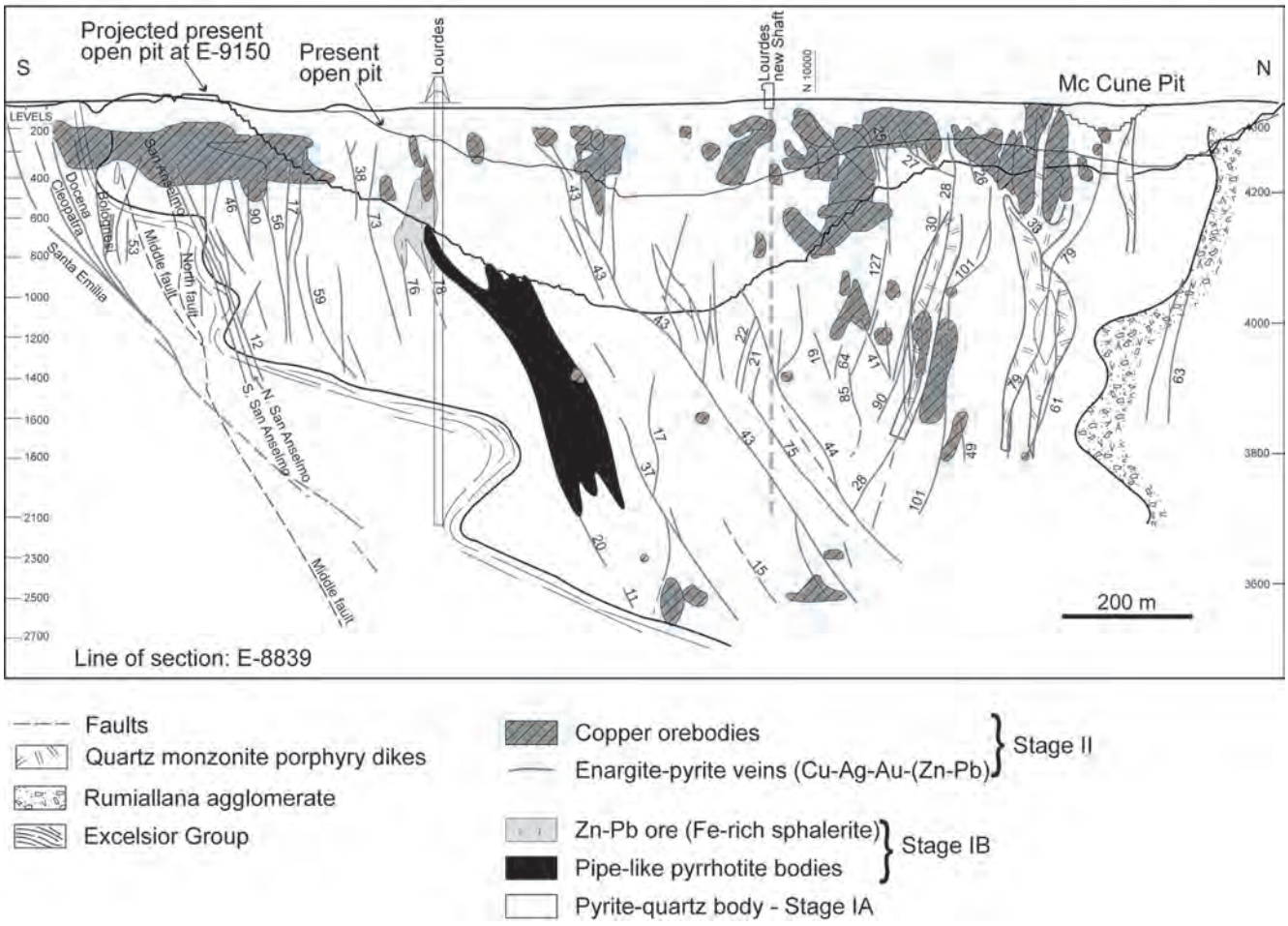

Fig. 19: *North-south cross section showing limits of the pyrite-quartz body and relative position (projection) of all estimated copper veins and orebodies. Modified after Rivera (1970).*

When pyrite is dominant over clays, the rock is massive, whereas when clays are dominant over pyrite, the rock is friable. For the latter texture Fontboté and Bendezú (2001) use the term "sulfide rock". In the core and intermediate zone, the clays consist of kaolinite and dickite and they are generally accompanied by APS minerals, typical of relatively acidic solutions, including alunite (restricted to the core zone) and hinsdalite, svanbergite, and woodhouseite in the intermediate zone. Rarely, hinsdalite occurs in the outer zone. Kaolinite and quartz are present in the outer zone. In the outermost zone, carbonates become the most abundant gangue.

Supergene oxidation of the carbonate-hosted ores

Supergene oxidation of the carbonate-hosted ores reach down to a depth of 250 m below surface. In the eastern part of the deposits, supergene mineralization produced Ag- and Pb-rich oxidized ores ("pacos") of economic importance in the past, mainly in the Matagente area. These ores consist of quartz, calcite, limonite, native silver, cerussite, jarosite, calamine, smithsonite, and anglesite (Bowditch, 1935; Amstutz and Ward, 1956).

Second mineralization stage: Western enargite-pyrite veins in the diatreme-dome complex

E-W trending fractures in the diatreme breccia, the pyrite-quartz body, and the Excelsior Group focused hydrothermal fluids which leached the rock and deposited enargite-pyrite veins forming relatively irregular and up to 2 m wide (Cu-Ag-Au-(Zn-Pb) veins (Fig. 2). The leaching of the diatreme breccia and pyroclastic rocks resulted in the formation of vuggy quartz. Leaching and fracture filling are important in the formation of the veins because leaching along veins increases the permeability of the diatreme breccia.

These veins superimpose and crosscut the pyrite-quartz body and the Zn-Pb ores of the first mineralization stage. The veins form horsetails within the pyrite-quartz body, which terminate to the east before entering in the carbonate rocks (Fig. 2). Veins strike generally N70-90°E; in the southern part of the pit the veins strike N120°E. The veins dip steeply, to the north in the southern part of the open pit, and to the south in the northern part (Fig. 19). They are anamostosing veins and reach a maximum length of 500 m, and extend to a depth of more than 760 m (Fig. 19). Width ranges from

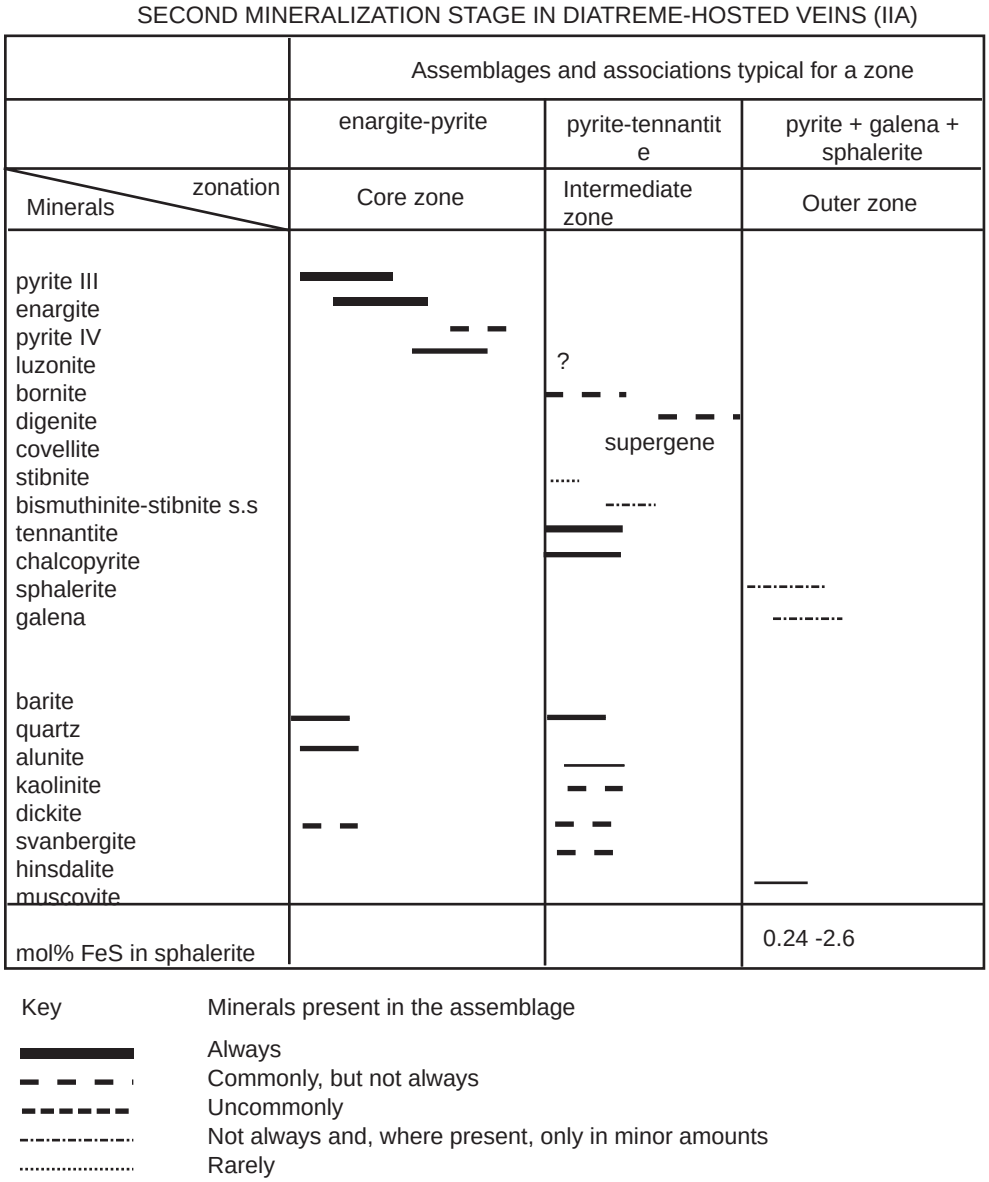

Fig. 20: *Paragenetic sequence of the second stage veins hosted in the diatreme breccia.*

a few cm to 2 m. Ward (1961) reported that some veins in the footwall of vein 43 were mined for enargite in their deeper levels and for galena and sphalerite in their upper portions, suggesting a vertical zonation. Locally, the mineralization is emplaced in a breccia composed of clasts of the pyrite-quartz body. Copper orebodies within the pyrite-quartz body were reported by Graton and Bowditch (1936) and Ward (1961) but not observed in our study. According to Ward (1961), the mineralogy of the E-W enargite-pyrite veins in the western side of the open pit and orebodies located on the eastern part of the pyrite-quartz body are similar, except that sphalerite and galena are more abundant in the orebodies. Tennantite is reported to be argentiferous and hypogene chalcocite replaces chalcopyrite and bornite (Ward, 1961). The following section synthesizes observations on veins number 25, 43, 44, and 79 (Fig. 2), in part integrating results of Jobin (2004).

Zoning and mineralogy

Zoning is present in the enargite-pyrite veins in the diatreme-dome complex but is less developed and the veins are thinner than in the replacement bodies in the carbonate rocks. A core zone (enargite-pyrite), an intermediate zone (tennantite-pyrite), as well as an outer zone (sphalerite + galena) are observed. From all zones, the best developed is the core, which was exploited until 1950 for copper. In contrast, the outer Zn-Pb zone is much less developed than in the carbonate replacement bodies. A paragenetic sequence for each zone is shown in Figure 20. Note that, again, this sequence must be viewed as the evolution of a fluid in time and space; therefore, minerals precipitating in the outer zones (right part of the diagram), may be contemporaneous with other minerals in the inner zones (left part of the diagram).

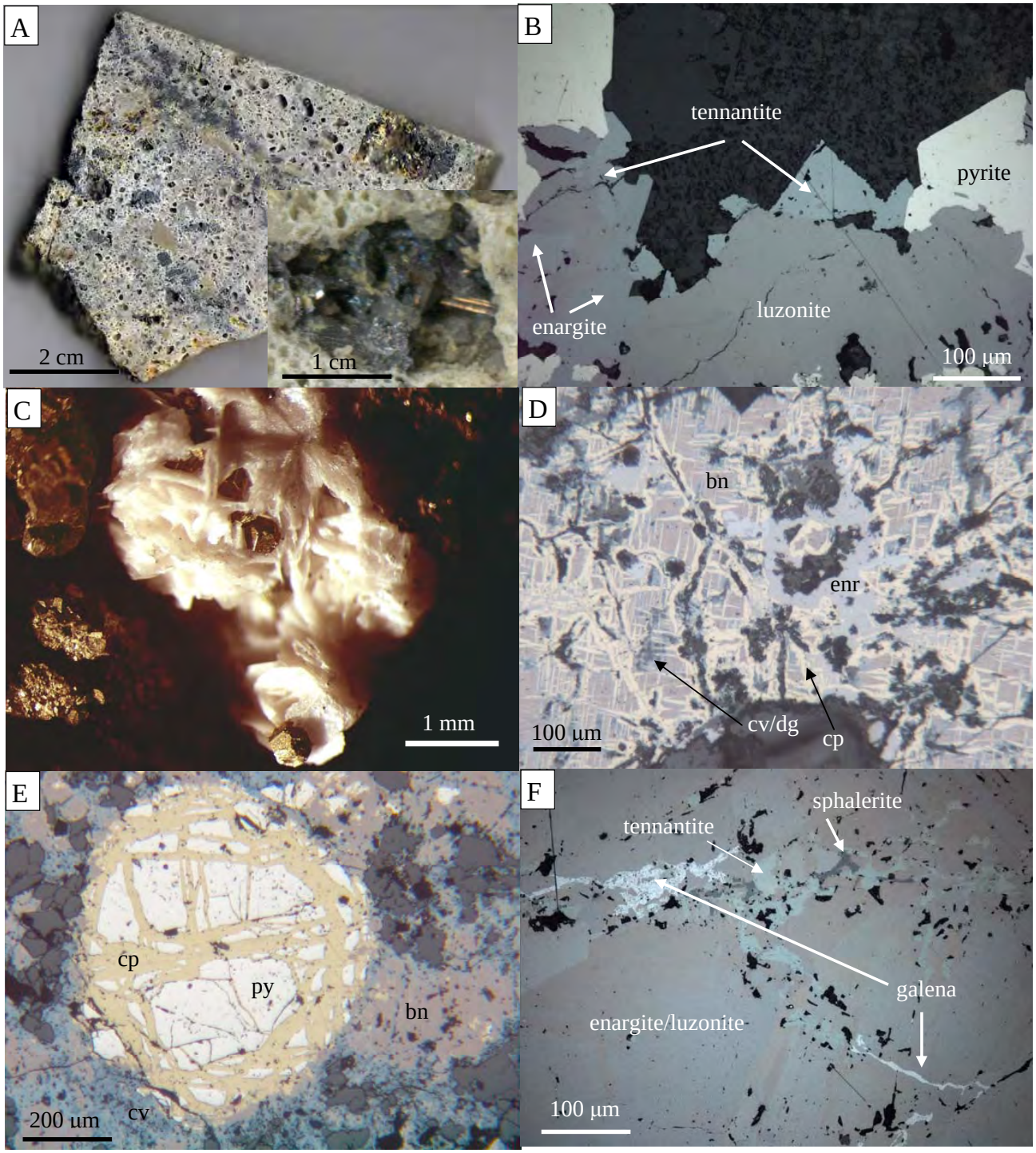

Fig. 21: *A) Vuggy quartz in the diatreme breccia with enargite filling the open spaces. B) Enargite-pyrite vein with luzonite replacing enargite and tennantite replacing luzonite (reflected light, // nicols, CPR 139). C) Alunite in pyrite-quartz body with pyrite coating alunite, indicating a hypogene origin of the latter (CPR 199). D) Chalcopyrite replacing bornite along crystallographic planes (reflected light, // nicols, CPR 607). E) Brecciated pyrite cemented by chalcopyrite. F) Tennantite, sphalerite, and galena replacing luzonite along grain boundaries in an enargite-pyrite veins (reflected light, // nicols, Fpe-131-4). Abbreviations: bn = bornite; cp = chalcopyrite; cv = covellite; py = pyrite.*

Table 4: Selected whole rock analyses of mineralized samples from the second stage replacement bodies hosted in Pucará carbonate rocks and from western veins hosted by the diatreme breccia.

Zone	Sample	Location	Analytical method[a]	Au (ppb)	Ag (ppm)	Bi (ppm)	Sb (ppm)	Cu (ppm)	As (ppm)	Sn (ppm)	Zn (%)	Pb (%)
Carbonate replacement bodies												
core	cpr 149	N-9964, E-9575, 4320m	ICP + INNA	<1	184	2385	31200	48018	4280	<1	0.8	1.3
intermediate	cpr 82	CP-00-108 (34.00m)	XRF	<1	29100	10100	56600	77200	3200	<1	1.16	0.38
outer (close to intermediate)	cpr 77	CP-00-108 (13.00m)	ICP + INNA	<1	348	<1	473	262	1250	<1	3.75	>10
outer	cpr 76	CP-00-108 (9.70m)	XRF	<1	150	<1	110	480	1090	<1	44.95	5.95
outermost	cpr 89	CP-00-108 (74.70m)	ICP + INNA	<1	5	<1	101	22	33	<1	2.6	0.25
Western enargite-pyrite veins												
core zone	cpr 109	W open pit	ICP + INNA	416	186	267	5860	>99999	43100	b.d.l.[b]	0.38	0.02
core zone	cpr 124	W open pit	ICP + INNA	b.d.l.[b]	103	14	7750	>99999	49700	b.d.l.[b]	0.08	0.1
core zone	cpr 135	W open pit	ICP + INNA	2960	81.2	49	795	8674	2670	b.d.l.[b]	0.004	0.03
intermediate	cpr 137	W open pit	ICP + INNA	11500	216	761	20300	>99999	10500	b.d.l.[b]	0.18	0.15
intermediate	cpr 139	W open pit	ICP + INNA	16200	216	268	11000	76404	27300	b.d.l.[b]	0.13	0.03

[a] Analytical methods: XRF = X-Ray Fluorescence Spectroscopy; INNA = instrumental neutron activation analysis; ICP = "near total" digestion ICP-MS.
[b] b.d.l. = below detection limit

Table 5: Representative electron microprobe analysis of carbonate minerals from the outermost zone from second stage replacement bodies.

Sample	$MgCO_3$ (wt%)	$CaCO_3$ (wt%)	$MnCO_3$ (wt%)	$FeCO_3$ (wt%)	$ZnCO_3$ (wt%)	$PbCO_3$ (wt%)	sum
CPR 12	3.40	1.12	33.05	60.83	0.73	0.02	99.15
CPR 12	4.56	0.89	40.36	52.88	0.35	0.00	99.04
CPR 16	2.06	0.50	47.21	50.49	0.08	0.03	100.36
CPR 16	3.57	0.90	40.26	54.65	0.11	0.08	99.56
CPR 89	0.42	0.64	6.61	87.75	4.64	0.17	100.22
CPR 89	1.82	1.08	14.86	78.64	2.81	0.11	99.32
CPR 406	8.92	7.66	26.58	52.37	5.40	0.17	101.11
CPR 406	2.53	1.36	24.90	69.03	2.07	0.01	99.89
CPR 429	2.11	0.10	14.37	84.07	0.08	0.04	100.76
CPR 429	1.45	0.03	11.50	87.51	0.00	0.11	100.60
FPE 136-6	1.43	4.75	34.38	47.86	10.26	0.26	98.93
FPE 136-6	0.91	3.38	31.21	42.88	20.59	0.05	99.03
FPE 136-6	2.44	0.57	37.09	58.35	1.81	0.05	100.32

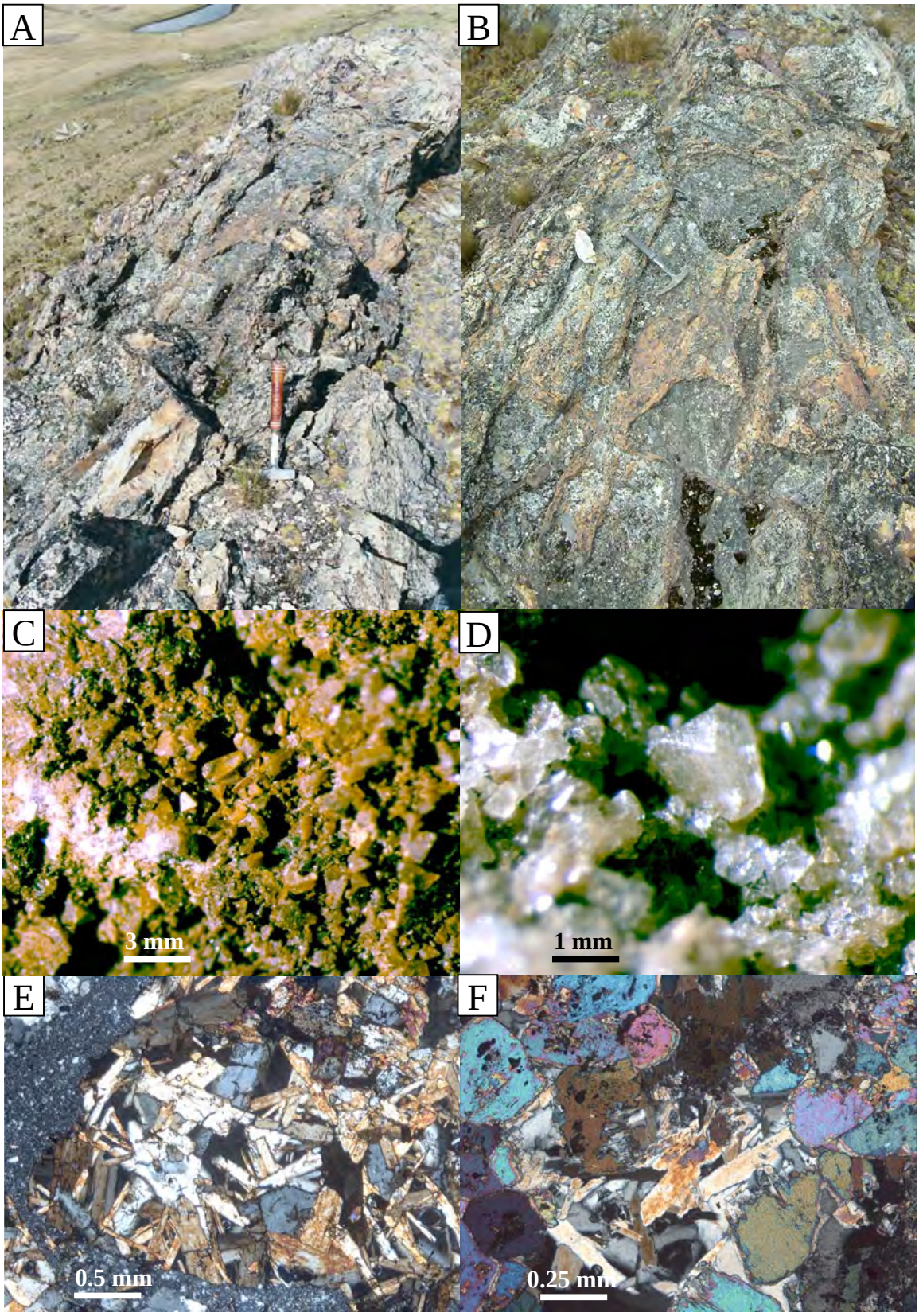

Fig. 22: *A) Network of oxidized veinlets containing goetite, jarosite, alunite, quartz, and zunyite. The outcrop is topographically prominent due to intense silicification, Venencocha area. B) Silicified body along a vein showing advanced argillic alteration with a central oxidized vein or a network of oxidized veinlets containing goethite, jarosite, alunite, quartz, and zunyite, Venencocha area. C) zunyite ($Al_{13}Si_5O_2$ (OH, F)$_{18}$Cl) occurring in oxidized veins with advanced argilllic alteration mineral assemblages. CPR 384, Venencocha area. D) Transparent zunyite crystal in an oxidized vein in the Venencocha area. CPR 384. E) Pervasive advanced argillic alteration next to a massive oxidized vein, with alunite and quartz replacing a tuff. CPR 361, Venencocha area. F) Enlargement of E) with diaspore coexisting with quartz and alunite. CPR 361.*

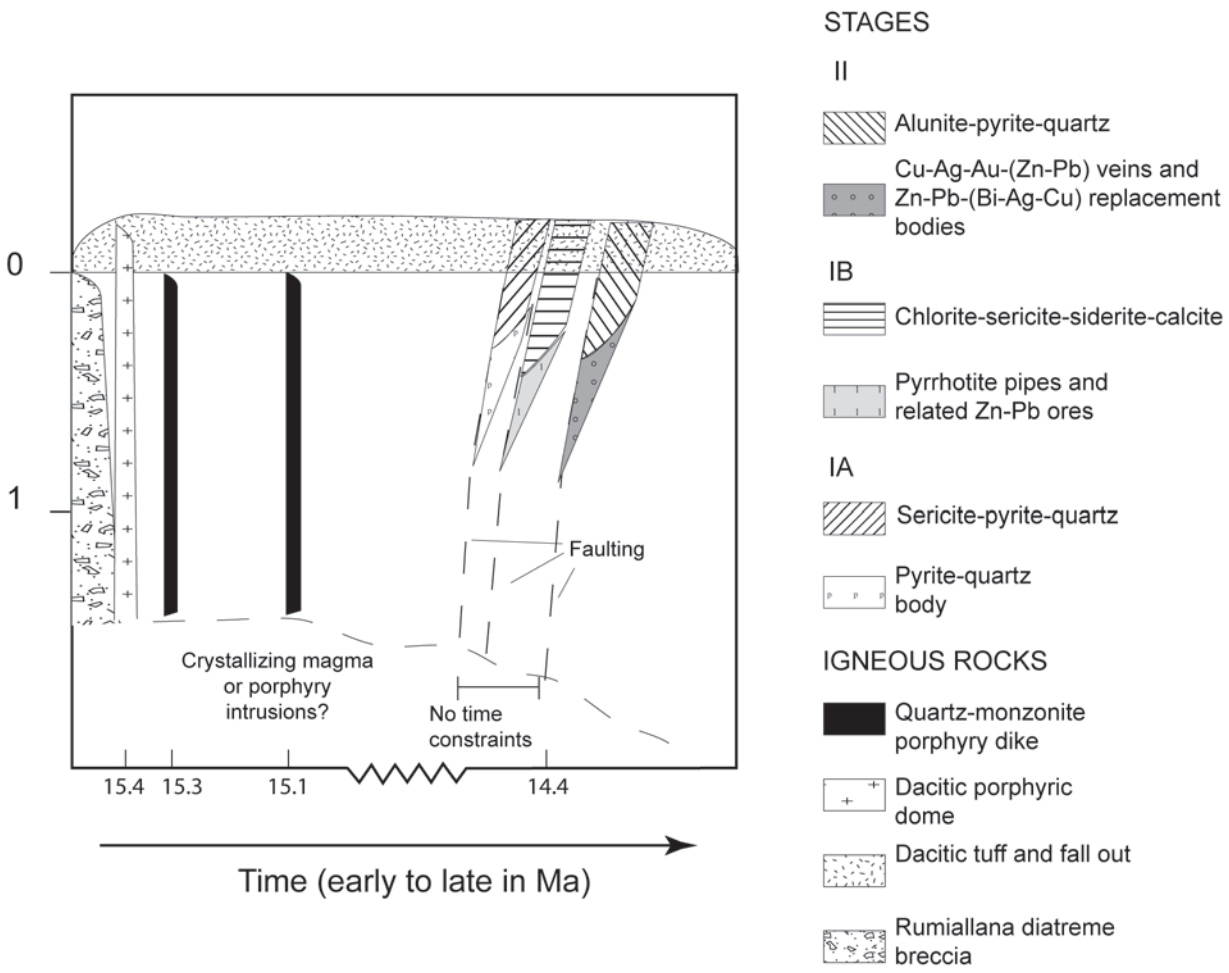

Fig. 23: *Time-space diagram for the magmatic-hydrothermal system of Cerro de Pasco. Geochronological data from Baumgartner et al. (Part II).*

Core zone (enargite+pyrite)

Prior to the deposition of enargite, early pyrite-quartz occurs, which is weakly developed. This pyrite is named pyrite III in our paragenetic sequence and corresponds to pyrite III of Lacy (1949). Enargite grains form massive aggregates and crystallize as well in the vugs of the vuggy quartz (Fig. 21A). Luzonite typically replaces enargite but in one sample, the contrary is observed. Pyrite (named here pyrite IV (same nomenclature as Lacy, 1949) replaces, coats, and is replaced by enargite and luzonite, indicating that pyrite precipitated during the entire enargite and luzonite deposition period. Repeated banding of pyrite and enargite occurs locally.

In the inner-most part of the veins, enargite occurs as xenomorphic grains (100 to 800 μm) which can reach up to 2 mm in size (Fig. 21B). Enargite As contents range from 15 to 18.3 wt percent, Sb contents are less than 4 wt percent (Table 3). Antimony contents in luzonite reach 10 wt percent and As ranges from 11.7 to 17.3 wt percent. Copper and arsenic grades in hand specimens are in the range of 8 percent and 2.6 percent, respectively (Table 4).

Alunite occurs in veins and is, in places, coated by pyrite (Fig. 21C). Alunite has not been observed in contact with enargite. Quartz and zunyite form an association with alunite. Barite plates, up to 1 cm, occur in the veins and overgrow enargite and pyrite, for example in veins 25.

Several samples show concentrations of Au ranging from 0.01 up to 16 g/t. These samples contain mainly enargite and tennantite.

Intermediate zone (tennantite-pyrite+chalcopyrite+bornite+chalcocite)

Tennantite, pyrite, chalcopyrite, bornite, chalcocite, minor stibnite, bismuthinite, as well as bismuthinite-stibnite s.s. are present in the intermediate zone. Tennantite replaces grain boundaries, as well as whole grains of enargite and luzonite. In turn, tennantite grain boundaries are replaced by sphalerite showing low FeS contents of < 2.6 mole percent. Chalcopyrite occurs as tiny grains (<150 μm) replacing enargite and luzonite, and overgrows tennantite. Furthermore, chalcopyrite replaces bornite along crystallographic planes (Fig. 21D). Ubiquitous chalcopyrite is less abundant than tennantite and locally infills brecciated pyrite (Fig. 21E). Stibnite, bismutinite, and bismutinite-stibnite s.s. generally consist of minute grains (< 20 μm) within enargite and

luzonite (Jobin, 2004). Arsenic and Sb contents in tennantite range from 13.3 to 18.8 wt percent As, 1.2 to 8 wt percent Sb (Table 3).

Svanbergite and hinsdalite, APS minerals, occur in the intermediate zone, and are accompanied by kaolinite and locally, sericite.

Outer zone (sphalerite + galena+ pyrite)

Sphalerite and galena occur in the outer zone which has a typical width of a few mm to cm and is weakly developed. They are present as small grains (50 to 200 μm), generally replacing tennantite. FeS content of sphalerite is low (< 2.6 mole %). Zinc and Pb were only economic in the upper portions of vein 43 (Ward, 1961).

Small amounts of kaolinite and sericite are the only observed alteration minerals. Sericite in the outer zone is difficult to distinguish from that of the sericite-pyrite-quartz alteration halo developed in the diatreme breccia at the contact with the pyrite-quartz body.

Enargite-pyrite veins in the southern part of the deposit

In the southern part of the diatreme, a series of large enargite-pyrite veins, presently inaccessible, occupy curved and branched fractures (San Anselmo vein system, Bowditch, 1935). These veins strike from N60°-70°E through E-W to S80°W (Ward, 1961). According to previous descriptions (Bowditch, 1935; Ward, 1961), the vein mineral assemblage is similar to the western E-W enargite-pyrite veins hosted by the diatreme-breccia and the pyrite-quartz body. However, in the enargite-pyrite veins in the southern part of the open pit, silver minerals such as Ag-rich tetrahedrite are more abundant and chalcopyrite is present. Gold contents are high (Ward, 1961), although no values are published. Native gold has been reported by Lacy (1949) but gold minerals were not reported by Bowditch (1935).

South of the main open pit, in the Santa Rosa pit (Fig. 2), high Au grades (up to 90 ppm, Henry, 2006) occur in strongly oxidized enargite-pyrite veins in the diatreme breccia and phyllite and shale of the Excelsior Group. These strongly oxidized veins contain goethite and earthy hematite accompanied by the alteration assemblage minerals alunite, zunyite, diaspore, and quartz. Pervasively advanced-argillic altered porphyritic rocks, probably quartz-monzonite dykes are present in the Santa Rosa open pit. Alunite crystals are often mantled with Fe-oxides and crystals do not exceed 300 μm in size. Petrographic observations on alunite reveal that inclusions of woodhouseite ($CaAl_3(PO_4)(SO_4)(OH)_6$), an aluminium-phosphate-sulfate (APS) mineral are abundant. The oxidized veins lie on the prolongation of the southern Excelsior phyllite-hosted enargite-pyrite veins (San Anselmo, Bolognesi, and Cleopatra veins).

Copper orebodies within the pyrite-quartz body

Ward (1961) reported more than 50 copper orebodies in the pyrite-quartz body (Fig. 19). The copper bodies in the eastern extremity of the pyrite-quartz body were described to be pipes, possibly indicating the replacement of limestones (Ward, 1961). The copper bodies contain enargite and tennantite, which is a similar assemblage to the enargite-pyrite veins in the diatreme-dome complex (Ward, 1961), rather than famatinite and tetrahedrite which is more typical of the sulfides in the carbonate-replacement orebodies.

Oxidized veins at Venencocha

In the Venencocha area, located 2.5 km northwest of the open pit, oxidized veins occur and are mainly controlled by ring structures around the north and northwestern margins of the diatreme, possibly subsidence faults. The veins are hosted in both sedimentary rocks (Excelsior Group) and in the diatreme breccia. They consist of massive goethite-jarosite and minor earthy hematite. These veins show an advanced argillic alteration halo (Fig. 22A and B) with, the mineral association alunite, quartz, diaspore with abundant zunyite (Fig. 22C-F). The same alteration pattern, with similar morphology and proportions, occurs in the enargite-pyrite veins in the western part of the open pit and could suggest that the oxidized veins at Venencocha represent an oxidized equivalent of the enargite-pyrite veins. Gold anomalies have been detected in the center of the oxidized veins and reach up to 1 g/t and decrease towards the borders of the veins.

At Venencocha, evidences of hydrothermal alteration in dacitic domes can be observed. This area was described by Noble et al. (1999) and interpreted as an epithermal disseminated high-sulfidation Au-Ag system. In this study, mapping was carried out in the Venencocha area and in the central-eastern part of the Cerro de Pasco diatreme. Alunite occurs only in small pervasively advanced argillic altered porphyritic intrusions and domes. The alteration is mainly composed of alunite and quartz with small amounts of zunyite. Pyrite is present almost exclusively as disseminations but only in small quantities and oxidized minerals are scarce. Locally, vuggy quartz is present. Gold anomalies in the altered domes attain 0.2 g/t, but they increase in the oxidized veins and veins bound to small domes and porphyritic intrusions. To date, no economic gold mineralization has been found at Venencocha. With the available data, it appears as the most likely hypothesis that the gold anomalies in the Venencocha area are all related to the oxidized enargite-pyrite veins and not to an epithermal disseminated high sulfidation Au-Ag system.

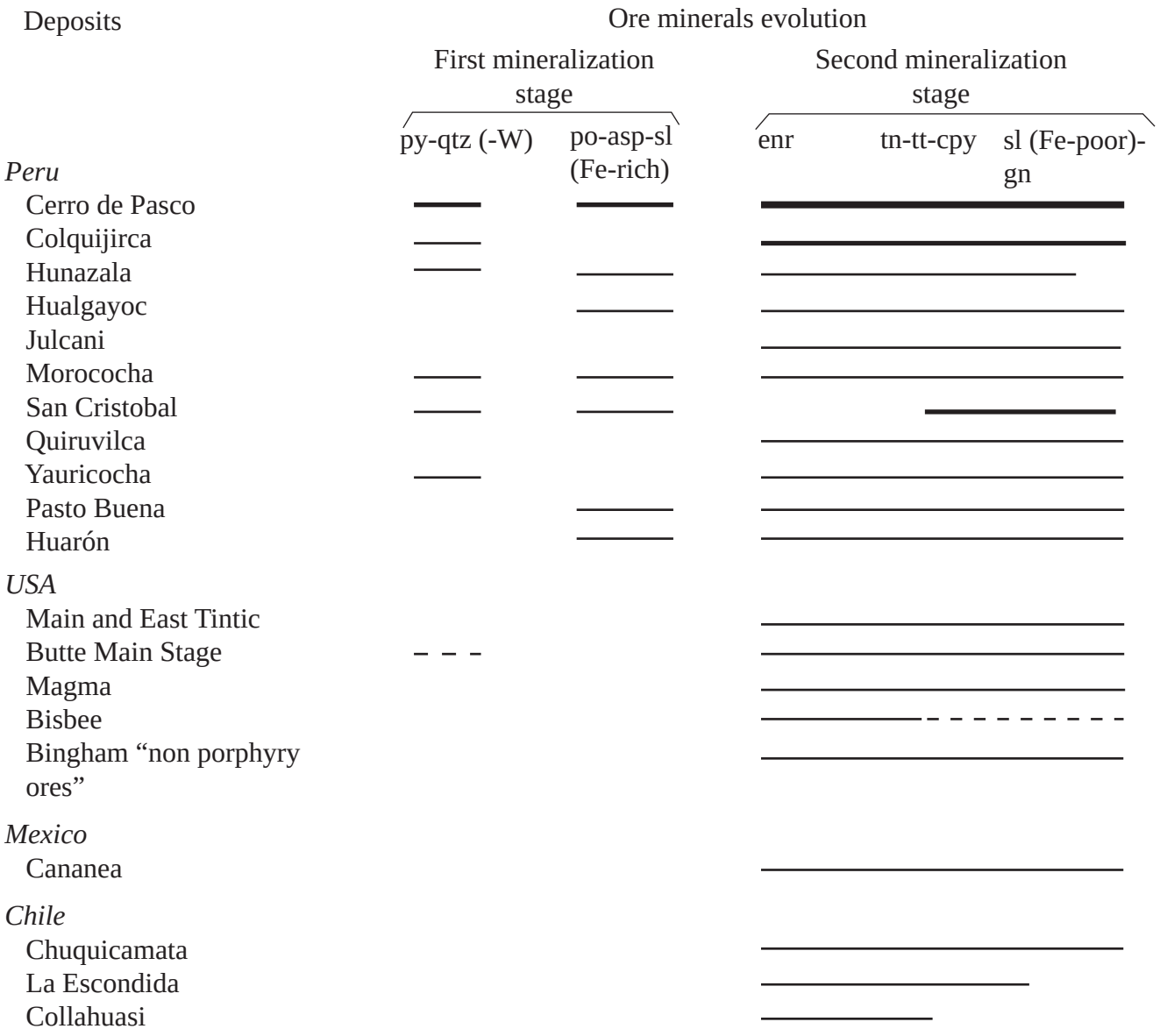

Fig. 24: *Diagrammatic summary of ore minerals evolution at various Cordilleran deposits.*

Discussion

Two mineralization stages

This present study confirms that two spatially related and partially superimposed mineralization stages can be distinguished at Cerro de Pasco, as already recognized by Einaudi (1977). Mineralization stage IA consists of a pyrite-quartz body which replaces the eastern part of a Mid-Miocene diatreme-dome complex and adjacent Mesozoic Pucará carbonate rocks. The pyrite-quartz body is, in turn, locally replaced during stage IB by pyrrhotite pipes which are zoned to arsenopyrite + pyrite and to Fe-rich sphalerite and galena, the latter mainly replacing carbonate rocks. The second mineralization stage is constituted by zoned enargite-pyrite veins hosted in the diatreme breccia and by carbonate replacement bodies in the Pucará rock located east of the diatreme.

A time-space diagram for the magmatic-hydrothermal system at Cerro de Pasco including the geochronological data of Baumgartner et al. (Part III) is shown in Figure 23. Stage II has been dated at 14.5 ± 0.08 - 14.4 ± 0.07 Ma and the diatreme-dome complex at 15.4 ± 0.07 Ma. The age of stage I is not further constrained than by crosscutting relationships which indicate that it took place between these two events; the possibility that stage I and II are close in time cannot be excluded.

Also in other Cordilleran base metal deposits (Table 1) including the Miocene Peruvian deposits of Huanzalá, San Cristobal, and Morococha in Peru, a first stage with pyrite-dominated mineral assemblages and Fe-rich sphalerite and a second stage with Fe-poor sphalerite has been recognized (Fig. 24). At San Cristobal, an early stage with pyrite-quartz-wolframite and

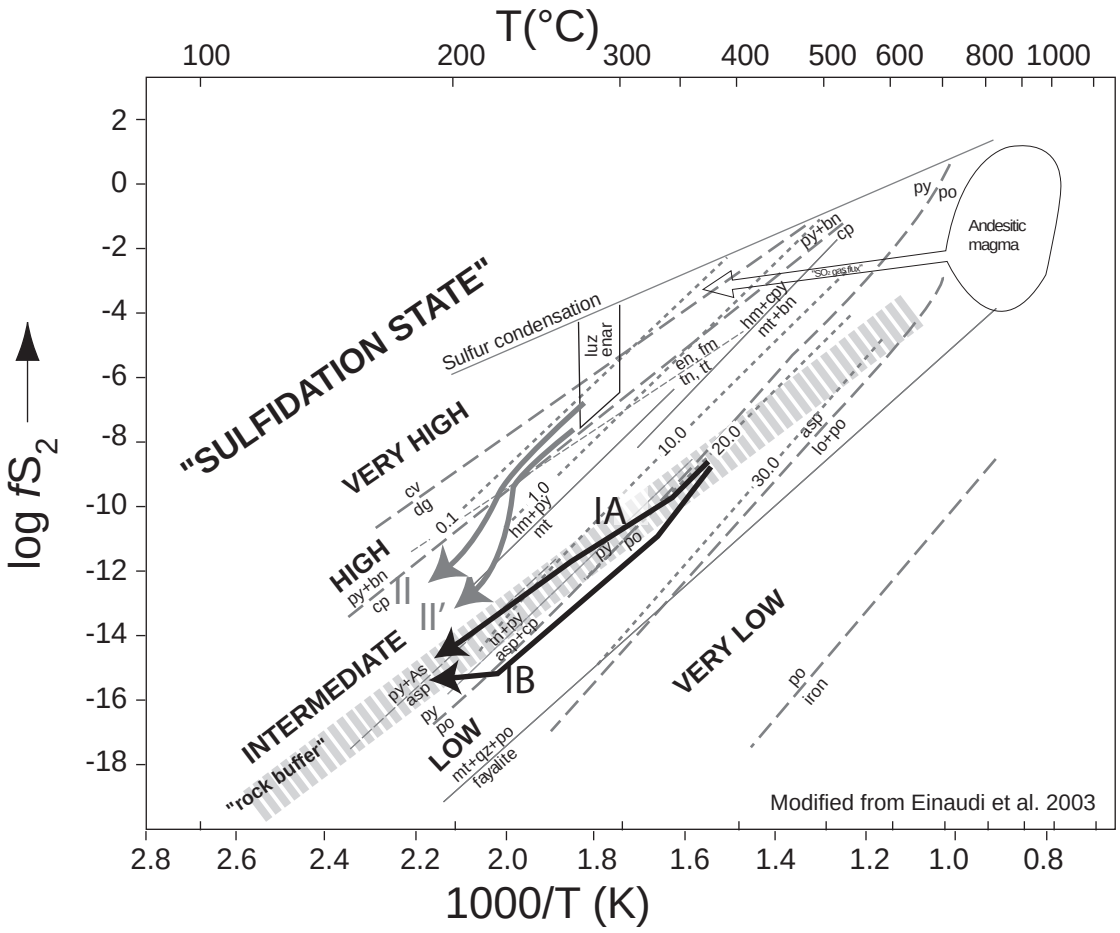

Fig. 25: *Log fS_2-1000/T diagram (modified from Einaudi et al., 2003) illustrating fluid environments for the first stage (stage IA) and second stage (stage II) including enargite-pyrite veins hosted by diatreme breccia (II) and for replacement bodies in carbonate rocks (II'). Fluid environment are based on sulfide assemblages described in the text, temperatures based on fluid inclusions from Baumgartner et al. (Part II), and sulfidation reactions from Barton and Skinner (1979). Dashed lines define the sulfidation state of hydrothermal fluids. Mineral abbreviations: asp = arsenopyrite, bn = bornite, cp = chalcopyrite, cv = covellite, dg = digenite, en = enargite, fm = famatinite, hm = hematite, lo = lollingite, mt = magnetite, po = pyrrhotite, py = pyrite, qtz = quartz. Contours of mole percent FeS in sphalerite coexisting with pyrite or pyrrhotite are from Scott and Barnes (1971) and Czamanske (1974). The fluids from the second mineralization stage follow, at high temperatures and water/rock ratios, the "SO_2 gas flux". At lower temperatures (around 300°C), the minerals from the core zone precipitate (famatinite/enargite with pyrite). Since the vein walls are sealed with an early deposition of pyrite and quartz, the log fS_2 decreases only slightly because sulfur is consumed. In the diatreme-hosted enargite-pyrite veins (arrow IIA), this slight log fS_2 decrease continues in the intermediate and outer zones because wall rock buffering is quasi inexistent, and thus, log fS_2 is dependent mainly on the sulfur content. In contrary, fluids from the replacement bodies (arrow IIB) show a drastic log fS_2 drop due to wall rock buffering and sulfur consumption. The black arrows shows the fluid environment of the first mineralization stage IA and IB), which is characteristic of low sulfidation states. Figure 25 illustrated in more detail these low sulfidation fluids. Enargite luzonite inversion between 275 and 300°C is after Maske and Skinner (1971). Brittle-ductile transition from Fournier (1999).*

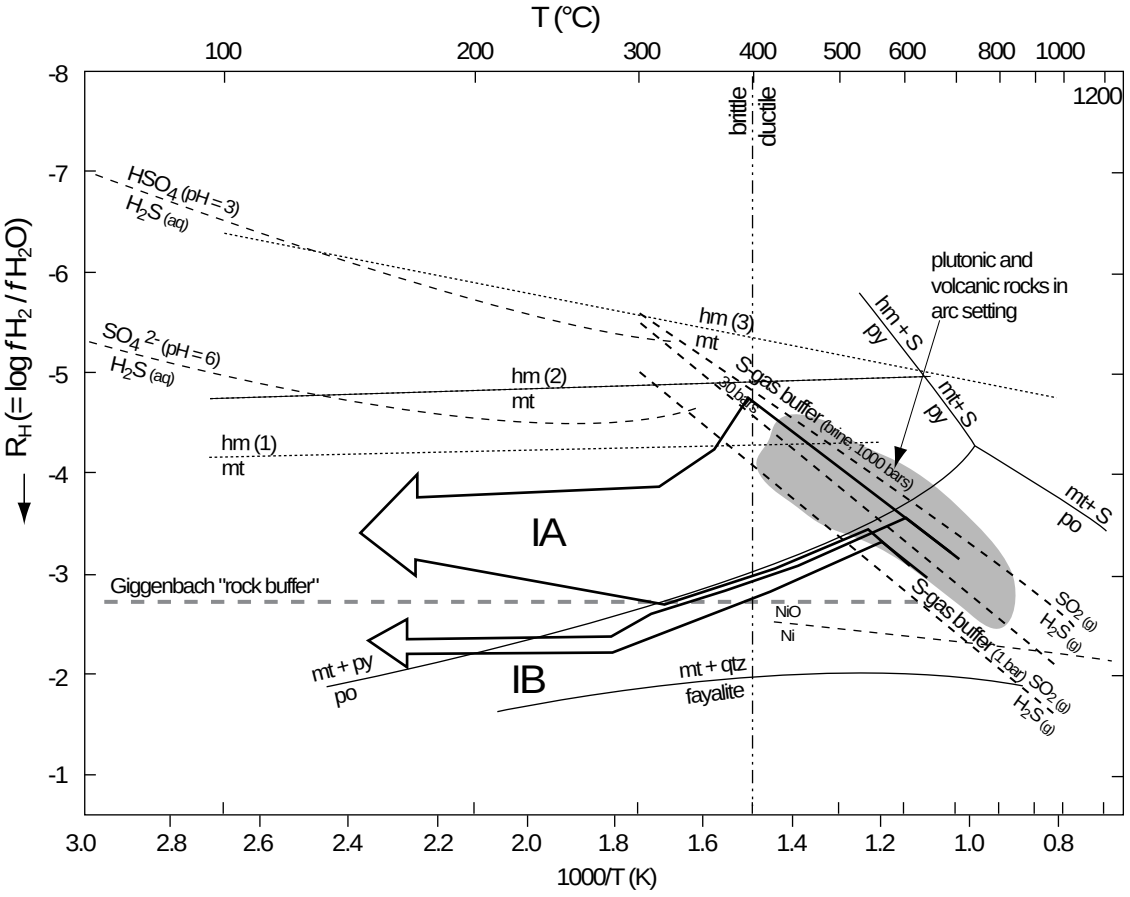

Fig. 26: R_H versus -1000/T diagram showing phase boundaries in the system Fe-S-H_2O and the position of the main redox buffers (after Einaudi et al. 2003). R_H = log (fH_2/fH_2O). Mineral abbreviations: hm = hematite, mt = magnetite, po = pyrrhotite, py = pyrite, qtz = quartz. The large unfilled arrow IA represents the general path followed by the fluids forming the first mineralization stage pyrite-quartz body and subsequently the pyrrhotite pipes zoned to Zn-Pb ores (IB). The first mineralization stage fluids follow probably the S-gas buffer at high temperature and water/rock ratios and at lower temperatures (approx. 300°C) precipitate the pyrite-quartz body. At lower water/rock ratios, the fluids react with the wall rocks so that the R_H drops until the "rock buffer" line is reached. At Cerro de Pasco, the rock buffer line was probably lower than the one of Giggenbach (1987). The rock buffer of Giggenbach is a fresh andesite while at Cerro de Pasco, the rock buffer are shale and phyllite (containing organic matter) from the Excelsior Group. The position of the hematite-magnetite phase boundary is after (1) De Haller et al. (2006), (2) Myers and Eugster (1983), and (3) Einaudi et al. (2003).

arsenopyrite and Fe-rich sphalerite is followed by a late Fe-poor sphalerite, sulfosalts, and galena (Campbell, 1983). At Huanzalá (Imai et al., 1985), pyrrhotite appears with pyrite as well as arsenopyrite and Fe-rich sphalerite, which is followed by a late stage with tennantite and enargite and Fe-poor sphalerite. At Morococha (Petersen, 1965; Kouzmanov et al., 2006), the mineralogy of the manto Italia consists of pyrrhotite, magnetite, sphalerite, and galena and a second stage with enargite and Fe-poor sphalerite is recognized. At Colquijjirca (Bendezú, 2007), a similar two stage evolution is recognized, whereby, the pyrite-quartz stage is not accompanied by pyrrhotite and Fe-rich sphalerite. In a diagrammatic summary of the ore evolution in several Cordilleran base metal deposits (Fig. 23), most of the Peruvian Cordilleran deposits show an early event with pyrrhotite, arsenopyrite, and Fe-rich sphalerite. Some deposits such as Huanzalá and Bisbee have no substantial (Fe-poor) sphalerite-galena present around the enargite and tennantite/tetrahedrite mineralization.

This twofold mineralizing evolution, therefore, appears to correspond to a systematic pattern which, for the case of Cerro de Pasco, will be deciphered in the next sections.

Environment of deposition

The environment of deposition for the first and second mineralization stages can be determined with reactions and mineral assemblages, temperature of fluids,

redox conditions, and FeS content of sphalerite. The sulfidation state is independent of metal content and texture (Einaudi, 1994).

The fluid inclusion study on quartz reported by Baumgartner et al. (Part III) suggests that the pyrite-quartz body formed at temperatures from 275 °C down to 200°C and fluid salinities ranging from 6.8 to 0.2 wt percent NaCl equiv., while the pipe-like pyrrhotite bodies zoned outward to Zn-Pb mineralization formed at temperatures between 250 and 185 °C with fluid salinities ranging from 4.3 to 1.1 wt percent NaCl equiv. The second stage of mineralization took place at temperatures between 293 and 170 °C and fluid salinities from 7.5 to 0.2 wt percent NaCl equiv. Minimum pressure estimates using liquid-vapor isochors (Brown and Lamb, 1989) for these salinities range between 50 to 70 bars which correspond to a minimum depth formation of both stages between approximately 400-700 m below the water table (Baumgartner et al., Part III).

The pyrrhotite + S_2 => pyrite mineral reaction (Table 6) and the presence of pyrrhotite is characteristic of low sulfidation states. The mineral reactions and assemblages (Table 6) of the core zones in the enargite-pyrite veins and carbonate replacement bodies, and in particular the presence of enargite and famatinite, indicate high sulfidation states. In the more external zones, the sulfidation states indicated by the mineral reactions (Table 6) suggest successively high and intermediate sulfidation states.

Iron content of sphalerite in equilibrium with pyrite or pyrrhotite is function of temperature and of the activity of S_2, i.e., of the sulfidation state (pressure may be neglected for shallow environments, Barton and Toulmin, 1964; Scott and Barnes, 1971; Hayba et al., 1985; Vaughan and Craig, 1997). Sphalerite in equilibrium with pyrite yielding very low Fe contents (< 0.1 mole % FeS) indicates high sulfidation states, whereas low (0.1–5 mole % FeS) contents indicate high to intermediate sulfidation states (Czamanske, 1974; Einaudi, 1977; Einaudi et al., 2003). The electron microprobe analyses from all sphalerite stages at Cerro de Pasco revealed two sphalerite populations (Fig. 9). The first population corresponds to sphalerite associated with first-stage pyrrhotite pipes (Fig. 9A), which yields with FeS contents from 10 to 23.9 mole percent (Table 6). These values are consistent with previous data of Einaudi (1977) in sphalerite from the first stage Zn-Pb ores. A second population is characterized by low FeS, ranging from 0.02 to 5 mole percent, with an average of 1 mole percent, and corresponds to second mineralization stage. It includes analyses of sphalerite from the intermediate, outer, and outer-most zones from carbonate replacement bodies and western enargite-pyrite veins (Fig. 9B-F). The fact that the second stage sphalerite from the outermost zone yields slightly higher FeS contents (up to 4.7 mol %) can be explained by a decrease of the sulfidation state due to interaction of the fluids with the carbonate host rock. The sulfidation state derived from the FeS content in sphalerite is thus concordant with that indicated by the mineral reactions shown in Table 6, i.e. the first mineralization stage was deposited under low sulfidation state conditions while the second mineralization stage took place under high to intermediate sulfidation states.

The fluid pH indicated by the mineral alteration assemblage is also consistent with these findings. The quartz-sericite alteration halo at the margin of the pyrite-quartz body suggests moderate acidic conditions for the first mineralization stage, typical of low sulfidation state fluids. The recognized alteration assemblages of the second mineralization stage with development of vuggy quartz in the diatreme and deposition of alunite both in the enargite-pyrite veins and carbonate replacement bodies, indicate very acidic fluids (below 2), a characteristic of high sulfidation state fluids (e.g., Einaudi et al., 2003).

In the pyrite-quartz body, red chalcedonic clasts suggest that locally oxidizing conditions were achieved in the first stage. However, the presence of pyrrhotite inclusions within pyrite and the development of stage IB with the pyrrhotite pipes indicate that the conditions were predominantly more reducing. The reaction hematite => magnetite + O_2 observed at the margin of carbonate replacement bodies indicates that second stage fluids were oxidizing, which is a characteristic of high sulfidation acidic fluids (Einaudi et al., 2003).

With this approach, it is possible to represent the evolutionary path of the depositional environment during the first and the second mineralization stages. The depositional environment for the first mineralization stage has been plotted on a R_H – 1000/T diagram (R_H = log (fH_2 / fH_2O) and on a log fS_2 – 1000/T (Fig. 25 and 26, respectively) while for the second mineralization stages, the deposition environment evolution is only shown on a log fS_2 – T diagram (Fig. 25).

The first mineralization stage evolutionary path is represented by a black arrow labeled “IA” for the pyrite-quartz body and “IB” for the pyrrhotite pipes and Zn-Pb ores (Fig. 25 and 26), whereas the second mineralization is symbolized by two grey arrows. Arrow II corresponds to the enargite-pyrite veins path, while the II’ arrow represents the carbonate replacement path.

First mineralization stage: Hydrothermal fluids were released from an underlying intrusion and channeled upward probably along open conduits. Most likely the fluid/rock ratio increased with time and only minor interaction with the host rocks took place, allowing the redox state of the fluid to be mainly controlled by the magmatic SO_2/H_2S gas buffer (arrow IA at T > 400°C in Fig. 25 and 26). Essentially pyrite precipitated at slightly acidic pH (constrained by the alteration assemblage sericite-pyrite-quartz in the alteration halo generated by the pyrite-quartz body) at 250-300°C and formed the pyrite-quartz body. Its size probably reflects a substantial hydrothermal system providing sulfur-rich fluids. The presence of hematite in red chalcedonic clasts within the pyrite-quartz body indicates that locally very oxidizing conditions were reached, possibly

Table 6: Reactions and assemblages used for determining the sulfidation state of the two mineralization stages at Cerro de Pasco

Mineralization	Zones	Reactions	Mineral assemblages	FeS content (% mol) in sphalerite	T (°C) estimate[1]	Sulfidation state[2]
First stage						
Pyrite quartz body with blebs of pyrrhotite (IA)		$2FeS + S_2 = 2FeS_2$ pyrrhotite pyrite	hematite-quartz		250-200	low
Pyrrhotite pipes (IB)		$2FeS + S_2 = 2FeS_2$ pyrrhotite pyrite			250-295	low
Zn-Pb ores (IB)			sphalerite-pyrite	6 - 23.9	212-183	low
Second stage						
Enargite-pyrite veins (II)	core	$0.67Cu_3AsS_4 + S_2 = 2.67Cu_{12}As_4S_{13}$ enargite tennantite	alunite-quartz		293-187	high
	intermediate	$Cu_5FeS_4 + 4FeS_2 = CuFeS_2$ bornite pyrite chalcopyrite	sphalerite-pyrite	no data	no data	high-intermediate
Carbonate replacement bodies (II)	core zone	$0.67Cu_3SbS_4 + S_2 = 2.67\ Cu_{12}Sb_4S_{13}$ famatinite tetrahedrite	alunite-quartz		265-178	high
	intermediate		kaolinite-quartz-APS[3]			intermediate
			sphalerite-pyrite	0.1 - 2.5		intermediate
	outer		sphalerite-pyrite	0.4 - 4.5	222-168	intermediate
	outer most	$Fe_2O_3 + FeS_2 = Fe_3O_4 + S_2$ hematite pyrite magnetite			no data	intermediate

[1] Temperature estimations in Baumgartner (2007) from fluid inclusions in quartz except for those in outer zone of carbonate replacement bodies which were measured in sphalerite
[2] Einaudi et al. (003)
[3] APS: aluminum phosphate sulfate minerals such as hinsdalite, svanbergite, and woodhouseite

due to low rock buffering. On the other side, the presence of pyrrhotite inclusions within pyrite suggests that at high temperature, the precipitation path crossed the pyrrhotite boundary. The pyrrhotite inclusions in pyrite might also represent an early history where the fluid was close to the pyrite-pyrrhotite boundary (Fig. 26) but then crossed the into the pyrite field around 250°C. In the late stages perhaps because decreasing fluid flux, the water/rock ratios decreased, favoring the precipitation of the pyrrhotite pipes at lower R_H values. At Cerro de Pasco, the position of the rock buffer, which is dependent of the mineral assemblage, is estimated to be lower than the Giggenbach "rock buffer" (an approximation for fresh andesite) plotted in Fig. 26. At depth, the rock buffer is the Excelsior shale and phyllite. These rocks, containing carbonaceous components, could lower the oxidation-sulfidation state of IB relative to IA.

Second mineralization stage: Subsequently, hydrothermal fluids which were probably (Baumgartner et al., part III) of the same source as those from the first mineralization stage were released. The fluid were channeled upward along numerous fractures and faults at high fluid/rock ratios, limiting the interaction with the Excelsior Group phyllite and shale, whose buffering capacity had been locally lowered by the first stage alteration. Thus, the sulfidation state of the fluid followed the magmatic SO_2/H_2S gas buffer (Fig. 25). Around 250-300°C, the core zone famatinite-pyrite in the carbonate rocks and enargite-pyrite in the diatreme breccia would have precipitated from acidic fluids, followed by the intermediate and outer zones (Fig. 25). The recognized ore mineral zonation suggests that in both carbonate and diatreme host rocks, vein walls were sealed due to early quartz and pyrite deposition, which minimized the wall rock buffering potential as reported by Bartos (1989) for Yauricocha and Quiruvilca (Peru), Butte, and Main Tintic (USA). On entering fresh carbonate rocks, a drastic drop of the sulfidation state of the fluid occurred as a response to pH increase (fS_2 is pH and sulfur content dependent) and resulted in the precipitation in the outer zone of sphalerite and galena accompanied by hinsdalite and kaolinite (arrow II', Fig. 25).

Carbonate precipitation is interpreted to result from the increasing pH of the fluid due to increased fluid-rock interaction while moving away from the vein, as proposed by Rimstidt (1997). Although the evolutionary path of the enargite-pyrite veins and carbonate replacement ores in fS_2-T space show similar paths in Figure 25, the path slopes are different, which reflect the contrasting effect of the different host rocks, buffering being a more important control in carbonate rocks.

We conclude that in the center of the depositional system, each successive increment of fluid, even at constant flux, would be further shielded from the rock buffer due to effects of wall-rock alteration. This has been proposed by Bartos (1989) for the progression with time in veins from relatively lower oxidation/sulfidation states to relatively higher oxidation/sulfidation states.

Despite the fact that large amounts of carbonate rocks are present in the Cerro de Pasco district, calc-silicate minerals are absent. This may be due to the fact that garnet and pyroxene require temperatures ≥ 350°C, temperatures, i.e., hotter than those that prevailed at Cerro de Pasco; although according to (Meinert, 1982), in H_2O-rich fluids nearly devoid of CO_2, which is expected in shallow environment such as Cerro de Pasco, garnet and pyroxene can form at temperatures lower than 350°C (Meinert, 1982). It cannot be excluded that in the places with the highest temperatures, in particular along the contact of the vent during its emplacement, calc-silicate minerals that might have formed were eradicated by later, lower temperature and acidic fluids.

Origin of zoning

The fluid evolution in time and space responsible for the zoning in the second stage base metal deposits can be explained in terms of fluid advances and retreats of the hydrothermal activity in the sense of Bartos (1989) and Hemley and Hunt (1992). In the core zone from the western veins, enargite replaces luzonite, suggesting a slight temperature increase with time at that point (Maske and Skinner, 1971). This is interpreted as fluid advances recorded by the mineral assemblages so that those from the inner zones prograde outwards and overprint minerals in the intermediate and/or the outer zones. According to Hemley and Hunt (1992), in the case of fluid progression, the preexisting minerals are destroyed and relics are scarce.

The fact that famatinite is replaced and overgrown by tetrahedrite indicates that the intermediate zone encroached on the core zone (e.g. Cuerpo Nuevo). These replacements of tennantite by Fe-poor sphalerite suggesting that outer zone encroached back on the intermediate one also indicates the effects of fluid retreat. This type of features have also been described by Meyer et al. (1968), Einaudi (1982), and Einaudi et al. (2003) as a late reversal of the overall temporal sequence, which occurs during the cooling of the hydrothermal system. When hydrothermal activity declines, the fluid flow retreats because of decreasing magmatic activity, and the amount of fluid circulating along structures through the rock diminishes.

The spatial and temporal extent of mineral zoning in the veins and replacement bodies is also a function of host rock. In the diatreme-hosted veins, sulfide deposition occurs within an irregular body of leached rocks (vuggy quartz), which may have been initially guided by a fault. The vuggy quartz, being a zone of weakness and readily fractured, is a site of high permeability, guiding later hydrothermal fluids. The host rock mineralogy and rate of precipitation govern the development of the size and mineralogy of the zone of deposition adjacent to the fault. In the veins hosted by the diatreme breccia and siliciclastic rocks, only the core zone is well developed, whereas the intermediate zone is less developed and the outer zone only weakly formed. This may be due to the non-reactive and relatively impermeable nature of the diatreme breccia and siliciclastic host rock, in places

where the vuggy quartz was not developed, or due to rapid deposition inhibiting infiltration or diffusion of the fluids in the wall rocks as suggested by Einaudi (1982). The more porous and soluble carbonate rocks permit percolation and formation of larger replacement orebodies with a well developed intermediate and outer zone due to buffering of the acidic fluids.

Fluids pathways

Einaudi (1977) reported that the Matagente vein system, eastern of the open pit, has the same strike and attitude as vein number 28 on the western side of the open pit (Fig. 2). He proposed that this spatial relationship corresponds to a single event, although he did not find evidence of through-going structures to link these two occurrences. An undated (pre-1970) structural map from the Cerro de Pasco geology staff shows through going structures, mainly faults. During this study, we were not able to observe if a lateral continuity between enargite-pyrite veins on the western part of the open pit and carbonate replacement bodies east of the open pit exists, because the central part of the deposit has been mined out. The replacement bodies in carbonate rocks contain Sb-bearing ores, which are virtually As- and Au-free and bear only minor amounts of copper, whereas enargite-pyrite veins contain Cu-As and Au bearing ores. Furthermore, most of the carbonate replacement bodies show an upward-flaring pipe-like morphology with inclined plunge (between 25 and 60°) in the direction of the diatreme-dome complex, suggesting that the hydrothermal fluids ascended from deeper levels and that no lateral feeding from the veins to the carbonate replacement bodies took place. Rather, both veins in the diatreme breccia and carbonate replacement bodies may be the result of parallel and divergent ascending fluid paths within the same hydrothermal system (Figure 10). The pyrite-quartz-body and the pyrrhotite pipes zoned to Zn-Pb ores were channeled mainly along a NS direction, probably along the Longitudinal Fault, while the enargite-pyrite veins were controlled by EW faults and the carbonate replacement bodies along N35°E, N°120E and N°170E.

Conclusions

In this study, it is confirmed that two stages of mineralization took place at Cerro de Pasco. The first mineralization stage consists of a pyrite-quartz body (stage IA) and vertical pyrrhotite pipes zoned outwards to Zn-Pb Fe-rich sphalerite-bearing ores (stage IB). The second mineralization stage comprises western enargite-pyrite veins hosted in diatreme breccia and in the pyrite-quartz body as well as carbonate replacement bodies, which are located on the eastern and central part of the present open pit. The second stage displays a marked mineral zonation, better developed in the carbonate replacement bodies and less marked in the enargite-pyrite veins. It consists of a core zone (famatinite/enargite-pyrite), an intermediate zone (tetrahedrite/tennantite, pyrite, and Bi-minerals), an outer zone (Fe-poor sphalerite-galena) which is poorly developed in the enargite-pyrite veins, and an outermost zone (magnetite-hematite-Fe-Mn-Zn carbonates).The outermost zone is absent in the enargite-pyrite veins.

The mineral assemblages of the first stage are characterized predominantly by low sulfidation states as indicated by pyrrhotite inclusions in pyrite and by the pyrrhotite pipes and related Zn-Pb ores bearing Fe-rich sphalerite. However, the presence of hematite within quartz from the pyrite-quartz body suggests that the fluids were locally oxidizing, which is typical for exsolving magmatic fluids. It is concluded that the magmatic fluids were reduced by interaction with Excelsior Group rocks. The second mineralization stage contains high to intermediate sulfidation state mineral assemblages bearing Fe-poor sphalerite. Alteration minerals from the first (quartz-sericite-pyrite) and second (alunite and other APS minerals, kaolinite) stage are consistent with the environment of deposition determined with reactions and mineral assemblages, temperature of fluids, redox conditions, and FeS content of sphalerite. High sulfidation states and very acidic and oxidizing conditions were achieved and maintained in the cores of the second stage orebodies, even in those replacing carbonate rocks. This suggests that each successive increment of fluid, even at constant flux, was shielded from the rock buffer due to the effects of the wall-rock alteration itself. The fluid progression with time in single veins and orebodies was from relatively low oxidation/sulfidation states to higher oxidation/sulfidation states and then returning to lower oxidation/sulfidation states. The second mineralization stage fluids had a limited interaction with the Excelsior Group phyllite and shale, whose buffering capacity had been locally lowered by the first stage alteration.

The first stage pyrite-quartz body and the pyrrhotite pipes zoned to Zn-Pb ores are emplaced N-S, following the Longitudinal Fault and the Cerro anticline whereas the second stage enargite-pyrite veins are controlled by EW faults and the carbonate replacement bodies along N35°E, N°120E and N°170E.

The morphology of the second mineralization stage Fe-poor sphalerite-bearing carbonate replacement bodies, located on the eastern side of the open pit, show an upward-flaring pipe-like form with inclined plunge (between 25° and 60°) in the direction of the diatreme-dome complex, suggesting that the hydrothermal fluids ascended from deeper levels and that no lateral feeding from the veins to the carbonate replacement bodies took place. It is concluded that both veins in the diatreme breccia and carbonate replacement bodies may be the result of parallel and divergent ascending fluid paths within the same hydrothermal system.

Acknowledgments

This work was conducted as part of the senior author's PhD. dissertation at the University of Geneva. The present investigation was carried out with the sup-

port of the Swiss National Science Foundation (FN 200020-108026). The authors would like to thank Jacob Timmers and Victor Gobitz from the Vólcan Compañía Minera S.A. for providing financial and logistical support. Special thanks to Hugo Alvarez, Romulo Sunny, Enrique Lopez, Luis Fuentes, and Carlos Vera from the Cerro de Pasco Geology staff. We gratefully acknowledge Ronner Bendezú for fruitful discussions as well as Kalin Kouzmanov. A revision by Steve Garwin of a preliminary version of the manuscript is acknowledged. A special thank to M. Einaudi for its careful reviewing which improved considerably the clearness of the manuscript.

References

Alvarez, A. A., and Noble, D. C., 1988, Sedimentary rock-hosted disseminated precious metal mineralization at Purisima Concepcion, Yauricocha District, central Peru: Economic Geology, v. 83, p. 1368-1378.

Amstutz, C., and Ward, H., J, 1956, Geología y mineralización del depósito de plomo de Matagente, Cerro de Pasco: Boletín de la Sociedad Geológica del Perú, v. 30, p. 13-31.

Angeles, C., 1999, Los sedimentos Cenozoicos de Cerro de Pasco; estratigrafia, sedimentacion y tectonica, *in* Machare, J., Benavides-Caceres, V., and Rosas, S., eds., Sociedad Geológica del Perú, Volúmen Jubilar, 5, p. 103-118.

Bartlett, M. W., 1984, Petrology and genesis of carbonate-hosted lead-zinc-silver ores, San Cristobal district, Department of Junin, Peru, Unpublished PhD Thesis, Oregon State University.

Barton, P. B., and Skinner, B. J., 1979, Sulfide mineral stabilities, *in* Barnes, H. L., ed., Geochemistry of Hydrothermal Ore Deposits, 2nd Edition, Wiley, New York, p. 278-403.

Barton, P. B., and Toulmin, P., 1964, The electrum-tarnish method for the determination of the fugacity of sulfur in laboratory sulfide systems: Geochimica et Cosmochimica Acta, v. 28, p. 619-640.

Barton, P. B. J., Bethke, P. M., and Toulmin, P. I., 1963, Equilibrium in ore deposits: Special Paper - Mineralogical Society of America, v. 1, p. 171-185.

Bartos, P. J., 1987, Quiruvilca, Peru; mineral zoning and timing of wall-rock alteration relative to Cu-Pb-Zn-Ag vein-fill deposition: Economic Geology, v. 82, p. 1431-1452.

Bartos, P. J., 1989, Prograde and retrograde base metal lode deposits and their relationship to underlying porphyry copper deposits: Economic Geology, v. 84, p. 1671-1683.

Baumgartner, R., Fontboté, L., and Bendezú, R., 2003, Low temperature, late Zn-Pb-(Bi-Ag-Cu) mineralization and related acid alteration replacing carbonate rocks at Cerro de Pasco, Central Peru: Mineral Exploration and Sustainable Development, Athen, 2003, p. 441-444.

Bendezú, R., 2006, Shallow polymetallic and precious metal mineralization associated to a Miocene diatreme-dome complex of the Peruvian Andes. The Colquijirca District., Unpublished PhD Thesis, University of Geneva, Switzerland.

Bendezú, R., and Fontboté, L., 2002, Late timing for high sulfidation Cordilleran base metal lode and replacement deposits in porphyry-related districts: the case of Colquijirca, central Peru: SGA News, v. 13, p. 9-13.

Bendezú, R., Fontboté, L., and Cosca, M., 2003, Relative age of Cordilleran base metal lode and replacement deposits, and high sulfidation Au-(Ag) epithermal mineralization in the Colquijirca mining district, central Peru: Mineralium Deposita, v. 38, p. 683-694.

Beuchat, S., 2003, Geochronological, structural, isotopes, and fluid inclusion constrains of the polymetallic Domo de Yauli district, Terre & Environnement, 130 p.

Bowditch, S. I., 1935, The geology and ore deposits of Cerro de Pasco, Peru, Unpublished PhD thesis, Harvard University, 160 p.

Brimhall, G. H., 1979, Lithologic determination of mass transfer mechanisms of multiple-stage porphyry copper mineralization at Butte, Montana; vein formation by hypogene leaching and enrichment of potassium-silicate protore: Economic Geology, v. 74, p. 556-589.

Brown, P. E., and Lamb, W. M., 1989, P-V-T properties of fluids in the system H2O±CO2±NaCl: New graphical presentations and implications for fluid inclusion studies: Geochimica et Cosmochimica Acta, v. 53 p. 1209-1221.

Bryant, D. G., 1964, Intrusive breccias and associated ore of the Warren (Bisbee) mining district, Cochise county, Arizona: Unpub. PhD thesis, Stanford University, 149 p.

Campbell, A. R., 1983, Genesis of the tungsten-base metal ores at San Cristobal, Peru, Unpublished PhD Thesis, University of Harvard, 176 p.

Clark, A. H., Archibald, D. A., Lee, A. W., Farrar, E., and Hodgson, C. J., 1998, Laser probe $^{40}Ar/^{39}Ar$ ages of early- and late-stage alteration assemblages, Rosario porphyry copper-molybdenum deposit, Collahuasi District, I Region, Chile: Economic Geology, v. 93, p. 326-337.

Czamanske, G. K., 1974, The FeS content of sphalerite along the chalcopyrite-pyrite-bornite sulfur fugacity buffer: Economic Geology, v. 69, p. 1328-1334.

De Haller, A., 2006, The Raúl-Condestable iron oxide copper-gold deposit, central coast of Peru, Terre and Environnement, 123 p.

Deen, J. A., Rye, R. O., Munoz, J. L., and Drexler, J. W., 1994, The magmatic hydrothermal system

at Julcani, Peru; evidence from fluid inclusions and hydrogen and oxygen isotopes: Economic Geology, v. 89, p. 1924-1938.

Dick, L. A., Chavez, W. X. J., Gonzalez, A., and Bisso, C., 1994, Geologic setting and mineralogy of the Cu-Ag-(As) Rosario vein system, Collahuasi district, Chile.: Society of Economic Geologists Newsletter, v. 19, p. 6-11.

Einaudi, M. T., 1968, Pyrrhotite-pyrite-sphalerite relations at Cerro de Pasco, Peru, Unpublished PhD Thesis, Harvard University, 381 p.

Einaudi, M. T., 1977, Environment of ore deposition at Cerro de Pasco, Peru: Economic Geology, v. 72, p. 893-924.

Einaudi, M. T., 1982, Description of skarns associated with porphyry copper plutons, *in* Titley, S., ed., Advances in geology of the porphyry copper deposits soutwestern north america, Univiversity of Arizona Press Tucson, AZ, United States., p. 139-183.

Einaudi, M. T., 1994, High Sulfidation and Low Sulfidation Porphyry Copper/Skarn Systems: Characteristics, Continua, and Causes, Society of Economic Geologists, international exchange lecture, http://pangea.stanford.edu/research/ODEX/marco-hilosulf.html.

Einaudi, M. T., Hedenquist, J. W., and Inan, E. E., 2003, Sulfidation state of hydrothermal fluids: The porphyry-epithermal transition and beyond: Society of Economic Geologists Special Publication, p. 285-313.

Emmons, S. F., 1910, Cananea mining district of Sonora, Mexico: Economic Geology, v. 5, p. 312-356.

Fischer, J., 1977, Silver mines and silver miners in colonial Peru 1776-1824. Centre for Latin-American studies: University of Liverpool, Monograph 7, p. 150p.

Fontboté, L., and Bendezú, R., 2001, The carbonate-hosted San Gregorio and Colquijirca (Zn-Pb-Ag) deposits (central Peru) as products of an epithermal high sulfidation system: Proexplo 2001 CD-ROM, Lima, Perú,, 2001, p. 19 p.

Fournier, R. O., 1999, Hydrothermal processes related to movement of fluid from plastic into brittle rock in the magmatic-epithermal environment: Economic Geology, v. 94, p. 1193-1211.

Friehauf, K., 1998, Geology and geochemistry of porphyryr-related, carbonate- hosted, massive replacement Cu-Au deposits – A case study of the superior district, Arizona, University of Stanford.

Geological staff of Cerro de Pasco Corporation, 1950, Lead and zinc deposits of the Cerro de Pasco Corporation in Central Peru: 18th International Geological Congress, Great Britain 1948, 1950, p. 154-186.

Giggenbach, W. F., 1987, Redox processes governing the chemistry of fumarolic gas discharges from White Island, New Zealand: Applied Geochemistry, v. 2, p. 143-161.

Gilbert, J. M., and Park, J., C. F., 1986, The Geology of Ore Deposits, Freeman and Co. New York, 750 p.

Graton, L. C., and Bowditch, S. I., 1936, Alkaline and acid solutions in hypogene zoning at Cerro de Pasco, Peru: Economic Geology, v. 31, p. 651-698.

Gustafson, L. B., 1961, Paragenesis and hypogene zoning at the Magma Mine, Arizona: Unpub. PhD thesis, Harvard University, 88 p.

Hammer, D. F., and Peterson, D. W., 1968, Geology of the Magma Mine area, Arizona, *in* Ridge, J. D., ed., Ore deposits of the United States, 1933-1967, 2, AIME, New York, p. 1282-1310.

Hayba, D. O., Bethke, P. M., Heald, P., and Foley, N. K., 1985, Geologic, mineralogic, and geochemical characteristics of volcanic-hosted epithermal precious-metal deposits, Reviews in Economic Geology 2, p. 129-167.

Hemley, J. J., and Hunt, J. P., 1992, Hydrothermal ore-forming processes in the light of studies in rock-buffered systems; II, Some general geologic applications: Economic Geology, v. 87, p. 23-43.

Henry, M., 2006, The Marcapunta Oeste prospect, Colquijirca district, and the Santa Rosa prospect, Cerro de Pasco district, Peru: Gold occurence types.: Unpublished MSc thesis, University of Geneva, Switzerland.

Hildreth, S. C., and Hannah, J. L., 1996, Fluid inclusion and sulfur isotope studies of the Tintic mining district, Utah; implications for targeting fluid sources: Economic Geology, v. 91, p. 1270-1281.

Hunt, J. P., 1985, Applied geology at Quebrada Blanca and Collahuasi, Chile, and in the future of U. S. metal mining: Economic Geology, v. 80, p. 794-800.

Imai, H., 1986, Mineralization and paragenesis on the Huanzala Mine, central Peru; reply: Economic Geology, v. 81, p. 196-199.

Imai, H., Kawasaki, M., Yamaguchi, M., and Takahashi, M., 1985, Mineralization and paragenesis of the Huanzala Mine, central Peru: Economic Geology, v. 80, p. 461-478.

Inan, E. E., and Einaudi, M. T., 2002, Nukundamite (Cu3.38Fe0.62S4)-Bearing Copper Ore in the Bingham Porphyry Deposit, Utah: Result of Upflow through Quartzite: Economic Geology, v. 97, p. 499-515.

Jankovic, S., Terzic, M., Aleksic, D., Karamata, S., Spasov, T., Jovanovic, M., Milicic, M., Miskovic, V., Grubic, A., and Antonijevic, I., 1980, Metallogenic features of copper deposits in the volcano- intrusive complexes of the Bor District, Yugoslavia, Special Publication of the Society for Geology Applied to Mineral Deposits, 1, p. 42-49.

Jenks, W. F., 1951, Triassic to Tertiary stratigraphy near Cerro de Pasco, Peru: The Geological Society

of America Bulletin, v. 62, p. 203-219.
Jiménez, C., 1924, Síntesis de la minería peruana en el centenario de Ayacucho, Ministerio de fomento, Minas y Petróleo, p. 3-71.
Jobin, Y., 2004, High sulfidation enargite-pyrite veins at Cerro de Pasco, Peru. A mineralogical study of ore and alteration minerals and an infra-red fluid inclusion study on enargite, Unpublished MSc thesis, University of Geneva, Switzerland, 139 p.
Kelley, V. C., 1935, Paragenesis of the Colorado copper sulphides, Cananea, Mexico: Economic Geology, v. 30, p. 663-688.
Kouzmanov, K., Ageneau, M., and Fontboté, L., 2006, Preliminary mineralogical study on polymetallic vein and manto samples from the northeastern part of the Morococha district (manto Italia and Huamachuco vein), Private report for Pan American Silver Corp., p. 1-11.
Lacy, W. C., 1949, Types of pyrite and their relations to mineralization at Cerro de Pasco, Peru, Unpublished PhD Thesis, Harvard University, 193 p.
Landis, G. P., and Rye, R. O., 1974, Geologic, fluid Inclusion, and stable Isotope studies of the Pasto Buena tungsten-base metal ore deposit, Northern Peru: Economic Geology, v. 69, p. 1025-1059.
Landtwing, M., 2004, Fluid evolution and ore mineral precipitation at the Bingham porphyry Cu-Au-Mo deposit, Utah., deduced from cathodoluminescence imaging and LA_ICPMS microanalysis of fluid inclusions, Unpublished PhD thesis, ETH Zürich, 260 p.
Macfarlane, A. W., and Petersen, U., 1990, Pb isotopes of the Hualgayoc area, northern Peru; implications for metal provenance and genesis of a Cordilleran polymetallic mining district: Economic Geology, v. 85, p. 1303-1327.
Maske, S., and Skinner, B. J., 1971, Studies of the sulfosalts of copper; I, Phases and phase relations in the system Cu-As-S: Economic Geology, v. 66, p. 901-918.
McLaughlin, D. H., 1924, Geology and physiography of the Peruvian Cordillera, Department of Junin and Lima: Geological Society of America Bulletin, v. 35, p. 591-632.
Mégard, F., 1978, Etude géologique des Andes du Pérou central-Contribution à l'étude écologique des Andes, Mémoire ORSTOM no. 86, Office de la Recherche Scientifique et Technique Outre-Mer, Paris,, 310 p.
Meinert, L. D., 1982, Skarn,Manto, and Breccia Pipe Formation in Sedimentary Rocks of the Cananea Mining District, Sonora, Mexico: Economic Geology, v. 77, p. 919-949.
Meyer, C., Shea, E. P., Goddard, C., and Staff, 1968, Ore deposits at Butte, Montana, *in* Ridge, J. D., ed., Ore deposits of the United States, 1933-1967, 2, AIME, New York, p. 1372-1416.
Morris, H. T., 1968, The Main Tinitc mining district, Utah, *in* Ridge, J. D., ed., Ore deposits of the United States, 1933-1967, 2, AIME, New York, p. 1043-1073.
Myers, J., and Eugster, H. P., 1983, The system Fe-Si-O: oxygen buffer calibrations to 1,500K: Contributions to Mineralogy and Petrology, v. 82, p. 75-90.
Nickel, E. H., 1992, Solid solutions in mineral nomenclature: Canadian Mineralogist, v. 30, p. 231-234.
Noble, D. C., and McKee, E. H., 1999, The Miocene metallogenic belt of central and northern Peru: Society of Economic Geologists Special Publication, v. 7, p. 155-193.
Noble, D. C., Tapia, P. O., Luna, R. B., and Alvarez, A. A., 1999, Venencocha Norte: A recently recognized Acid-Sulfate High-Sulfidation Gold System directly north of the Cerro de Pasco volcanic vent, Internal report for the Empresa Minera del Centro del Perú, p. 15.
Ossandón, C., Freraut, C. R., Gustafson, L. B., Lindsay, D. D., and Zentilli, M., 2001, Geology of the Chuquicamata Mine: A Progress Report: Economic Geology, v. 96, p. 249-270.
Padilla Garza, R. A., Titley, S. R., and Pimentel B., F., 2001, Geology of the Escondida Porphyry Copper Deposit, Antofagasta Region, Chile: Economic Geology, v. 96, p. 307-324.
Paul, A. H., and Knight, M. J., 1995, Replacement ores in the Magma Mine, Superior, Arizona, *in* Pierce, F. W., and Bolm, J. G., eds., Bootprints along the Cordillera; Porphyry copper deposits from Alaska to Chile, 20, Arizona Geological Society Digest, p. 366-372.
Perry, V. D., 1961, The significance of mineralized breccia pipes: Mining Engineering, v. 13, p. 367-376.
Petersen, U., 1965, Regional geology and major ore deposits of central Peru: Economic Geology, v. 60, p. 407-476.
Profett, J. M. J., 1979, Ore deposits of the western United States: A summary, Nevada Bureau of Mines and Geology, p. 13-32.
Ransome, F. L., 1912, Copper deposits near Superior, Arizona: USGS Bulletin, v. 540, p. 129-158.
Rimstidt, D., 1997, Gangue mineral transport and deposition, *in* Barnes, H. L., ed., Geochemistry of hydrothermal ore deposits., Wiley and Sons, inc, p. 487-515.
Rivera, N., 1970, Mina Cerro de Pasco, Geologia de los yacimientos minerales operandos por la Cerro de Pasco Corporation, La Oroya, Peru., Departamento de Geologia de la Cerro de Pasco Corporation, p. 12-40.
Rivera, N., 1997, The Pasco belt and the metallogenesis of the Cerro de Pasco mineral district: IX Congreso Geológico del Perú, 1997, p. 167-173.
Rogers, R., 1983, Structural and geochemical evolution

of a mineralized volcanic vent at Cerro de Pasco, Peru, Unpublished PhD Thesis, University of Arizona, 116 p.

Rubright, R. D., and Hart, O. J., 1968, Non-porphyry ores of the Bingham District, Utah, *in* Ridge, J. D., ed., Ore deposits of the Unites States 1933-1967, 1, AIME, New York, p. 886-908.

Sales, R. H., and Meyer, C., 1949, Results from preliminary studies of vein formation at Butte, Montana: Economic Geology, v. 44, p. 465-484.

Sawkins, F. J., 1972, Sulfide ore deposits in relation to plate tectonics: Journal of Geology, v. 80, p. 377-397.

Schwartz, G. M., and Park, C. F., 1932, A microscopic study of ores from the Campbell Mine, Bisbee, Arizona: Economic Geology, v. 27, p. 39-51.

Scott, S. D., and Barnes, H. L., 1971, Sphalerite geothermometry and geobarometry: Economic Geology, v. 66, p. 653-669.

Shepard, W. M., Morris, H. T., and Cook, D. R., 1968, Geology and ore deposits of the East Tintic mining district, Utah, *in* Ridge, J. D., ed., Ore deposits of the United States, 1933-1967, 1, AIME, New York, p. 941-965.

Short, M. N., and Ettlinger, I. A., 1926, Ore deposition and enrichment at the Magma mine, Superior, Arizona: American Institute of Mining, Metallurgical, and Petroleum Engineers Transactions, v. 74, p. 174-222.

Short, M. N., Galbraith, F. W., Harshman, E. N., Kuhn, T. H., and Wilson, E. D., 1943, Geology and Ore Deposits of the Superior Mining Area, Arizona: Arizona Bureau of Mines Bulletin, v. 151.

Silberman, M. L., and Noble, D. C., 1977, Age of igneous activity and mineralization, Cerro de Pasco, central Peru: Economic Geology, v. 72, p. 925-930.

Sillitoe, R. H., 1983, Enargite-bearing massive sulfide deposits high in porphyry copper systems: Economic Geology, v. 78, p. 348-352.

Sillitoe, R. H., 2000, Styles of high-sulfidation gold, silver and copper mineralization in porphyry and epithermal environments: PacRim '99, Bali, Indonesia, 2000, p. 29–44.

Soler, P., Carrascal, R., and Saez, J., 1986, Mineralization and paragenesis of the Huanzala Mine, central Peru; discussion: Economic Geology, v. 81, p. 195-196.

Thomson, D. R., 1960, The Yauricocha sulfide deposit, Central Peru: Unpub. PhD thesis, University of London, 170 p.

Thouvenin, J.-M., 1984, Le gisement polymétallique à Zn-Pb-Cu-Ag de Huaron (Pérou): description des corps minéralisés, étude paragénétique, datations K/Ar des altérations hydrothermales, répartition de l'argent: Chroniques de la recherche minière, v. 477, p. 35-54.

Vaughan, D. J., and Craig, J. R., 1997, Sulfide ore mineral stabilities, morphologies, and intergrowth textures, *in* H.L., B., ed., Geochemistry of hydrothermal ore deposits, Wiley and Sons, inc, p. 367-434.

Ward, H. J., 1961, The pyrite body and copper orebodies, Cerro de Pasco Mine, central Peru: Economic Geology, v. 56, p. 402-422.

Appendix 1: FeS content (% mol) in sphalerite from the Cerro de Pasco deposit

Sample	Fe wt%	Zn wt%	S wt%	sum	FeS mol%
Fe-rich sphalerite from mineralization stage IB					
3RD BENCH					
cpr 306	9.15	55.44	33.68	98.26	15.85
cpr 306	13.57	51.71	33.89	99.17	23.48
cpr 306	12.63	52.03	33.52	98.19	21.84
cpr 306	8.73	56.48	33.65	98.87	15.08
cpr 306	7.49	58.44	33.78	99.71	12.90
cpr 306	7.54	58.32	33.65	99.50	12.97
cpr 306	8.58	57.56	33.41	99.55	14.71
cpr 306	10.00	55.32	33.70	99.02	17.26
cpr 306	11.02	55.41	33.74	100.17	18.93
cpr 306	2.82	63.12	33.44	99.38	4.84
cpr 306	12.25	53.97	33.53	99.75	21.01
cpr 306	12.25	53.17	33.73	99.14	21.14
cpr 306	12.63	53.06	33.94	99.63	21.82
cpr 306	10.60	55.31	33.40	99.31	18.20
cpr 306	10.36	55.48	33.83	99.67	17.86
cpr 306	8.39	56.95	33.22	98.56	14.41
cpr 306	3.19	64.30	33.63	101.12	5.44
cpr 306	12.16	52.87	33.80	98.84	21.05
cpr 306	11.58	54.75	33.68	100.01	19.89
cpr 306	3.61	63.01	33.11	99.73	6.15
cpr 306	4.05	62.31	33.67	100.03	6.96
cpr 306	12.94	51.72	33.97	98.63	22.49
cpr 306	13.82	51.77	33.98	99.57	23.89
cpr 306	12.56	52.60	33.86	99.02	21.74
cpr 306	12.51	53.39	33.92	99.82	21.59
cpr 306	11.41	53.95	33.72	99.08	19.70
cpr 306	7.34	59.21	33.31	99.86	12.54
cpr 306	11.28	54.68	33.90	99.87	19.46
cpr 306	2.74	62.78	33.20	98.72	4.70
cpr 306	12.49	52.39	33.91	98.78	21.66
cpr 306	8.51	57.44	33.41	99.36	14.61
cpr 306	12.76	52.85	33.64	99.25	21.99
cpr 306	9.08	57.15	33.93	100.16	15.64
cpr 306	3.54	62.65	33.31	99.51	6.07
cpr 306	4.57	62.05	33.46	100.08	7.82
cpr 306	12.34	53.07	33.83	99.23	21.32
cpr 306	12.59	53.49	33.74	99.82	21.66
cpr 306	7.70	58.40	34.23	100.33	13.31
cpr 306	1.28	64.96	32.89	99.13	2.17
cpr 306	13.57	51.71	33.89	99.17	23.48
cpr 306	12.63	52.03	33.52	98.19	21.84
cpr 306	8.73	56.48	33.65	98.87	15.08
cpr 306	7.49	58.44	33.78	99.71	12.90
cpr 306	7.54	58.32	33.65	99.50	12.97
cpr 306	8.58	57.56	33.41	99.55	14.71
cpr 306	10.00	55.32	33.70	99.02	17.26
cpr 306	11.02	55.41	33.74	100.17	18.93
cpr 306	2.82	63.12	33.44	99.38	4.84

Appendix 1:(Cont.)

Sample	Fe wt%	Zn wt%	S wt%	sum	FeS mol%
cpr 306	12.25	53.97	33.53	99.75	21.01
cpr 306	12.25	53.17	33.73	99.14	21.14
cpr 306	12.63	53.06	33.94	99.63	21.82
cpr 306	10.60	55.31	33.40	99.31	18.20
cpr 306	10.36	55.48	33.83	99.67	17.86
cpr 306	8.39	56.95	33.22	98.56	14.41
cpr 306	3.19	64.30	33.63	101.12	5.44
cpr 306	12.16	52.87	33.80	98.84	21.05
cpr 306	11.58	54.75	33.68	100.01	19.89
cpr 306	3.61	63.01	33.11	99.73	6.15
cpr 306	4.05	62.31	33.67	100.03	6.96
cpr 306	12.94	51.72	33.97	98.63	22.49
cpr 306	13.82	51.77	33.98	99.57	23.89
cpr 306	12.56	52.60	33.86	99.02	21.74
cpr 306	12.51	53.39	33.92	99.82	21.59
cpr 306	11.41	53.95	33.72	99.08	19.70
cpr 306	7.34	59.21	33.31	99.86	12.54
cpr 306	11.28	54.68	33.90	99.87	19.46
cpr 306	2.74	62.78	33.20	98.72	4.70
cpr 306	12.49	52.39	33.91	98.78	21.66
cpr 306	8.51	57.44	33.41	99.36	14.61
cpr 306	12.76	52.85	33.64	99.25	21.99
cpr 306	9.08	57.15	33.93	100.16	15.64
cpr 306	3.54	62.65	33.31	99.51	6.07
cpr 306	4.57	62.05	33.46	100.08	7.82
cpr 306	12.34	53.07	33.83	99.23	21.32
cpr 306	12.59	53.49	33.74	99.82	21.66
cpr 306	5.40	60.75	32.85	98.99	9.21
cpr 306	7.70	58.40	34.23	100.33	13.31
cpr 306	1.28	64.96	32.89	99.13	2.17
cpr 306	9.15	55.44	33.68	98.26	15.85
undeground mine (Level 1200, 8920E-9860N, piso 19)					
cpr 315	0.06	67.53	33.33	100.92	0.10
cpr 315	0.53	66.79	33.26	100.58	0.90
cpr 315	0.73	64.47	33.67	98.88	1.27
cpr 315	0.75	65.53	33.89	100.17	1.29
cpr 315	0.39	66.26	33.38	100.03	0.67
cpr 315	0.77	66.53	33.46	100.77	1.31
cpr 315	0.07	67.03	33.17	100.28	0.12
cpr 315	0.05	66.91	33.18	100.14	0.08
cpr 315	0.37	65.93	33.48	99.79	0.64
cpr 315	0.75	64.34	33.46	98.56	1.30
cpr 315	0.10	67.27	33.42	100.79	0.16
cpr 315	0.97	66.01	33.32	100.31	1.66
cpr 315	0.17	67.18	33.13	100.47	0.29
cpr 315	0.44	66.88	33.53	100.84	0.75
cpr 315	0.05	67.73	33.23	101.00	0.08
cpr 315	0.22	67.36	34.07	101.64	0.37
cpr 315	0.58	66.01	33.13	99.72	0.99
cpr 315	1.11	66.11	32.91	100.13	1.88
cpr 315	1.49	64.15	33.39	99.03	2.56

Appendix 1:(Cont.)

Sample	Fe wt%	Zn wt%	S wt%	sum	FeS mol%
cpr 315	0.68	65.15	33.10	98.92	1.16
cpr 315	0.44	65.57	33.41	99.42	0.76
cpr 315	0.19	66.96	33.14	100.28	0.32
cpr 315	0.33	65.43	33.31	99.07	0.56
cpr 315	0.78	65.57	33.16	99.52	1.34
cpr 315	0.17	65.96	32.99	99.12	0.29
cpr 315	0.26	66.76	33.46	100.47	0.44
cpr 315	0.09	66.85	33.05	99.99	0.16
cpr 315	0.22	66.48	33.23	99.93	0.38
cpr 315	0.28	66.39	33.45	100.12	0.47
cpr 315	1.06	65.75	33.60	100.41	1.81
cpr 315	0.21	66.15	33.39	99.75	0.35
cpr 315	0.14	67.04	33.04	100.22	0.24
cpr 315	0.23	66.11	33.31	99.65	0.40
cpr 315	0.72	65.76	33.03	99.52	1.23
cpr 315	0.63	65.86	33.44	99.94	1.09
cpr 315	0.09	66.84	33.54	100.46	0.15
cpr 315	0.79	65.09	32.99	98.87	1.35
cpr 315	0.19	66.42	33.28	99.88	0.32
cpr 315	0.23	66.97	33.09	100.29	0.40
cpr 315	0.12	66.75	33.38	100.25	0.21
cpr 315	0.54	65.90	33.52	99.96	0.93
cpr 315	0.79	66.17	33.24	100.20	1.35
cpr 315	0.65	65.97	33.16	99.78	1.11
cpr 315	0.29	65.85	33.08	99.22	0.49
cpr 315	0.17	66.01	33.30	99.48	0.29
cpr 315	1.45	65.27	33.41	100.13	2.48
cpr 315	3.63	61.83	33.89	99.36	6.28
cpr 315	0.09	67.21	33.03	100.33	0.16
cpr 315	0.62	66.61	33.56	100.78	1.06
cpr 315	1.18	65.44	33.02	99.64	2.00
cpr 315	0.04	66.76	32.92	99.71	0.06
cpr 315	0.14	66.74	32.95	99.83	0.23
cpr 315	0.68	65.96	33.18	99.82	1.16
cpr 315	0.78	65.72	33.41	99.91	1.34
cpr 315	0.52	65.82	33.36	99.71	0.89
cpr 315	0.88	65.68	33.50	100.07	1.51
cpr 315	2.29	64.86	33.60	100.75	3.91
cpr 315	1.30	65.95	33.43	100.67	2.21
cpr 315	6.19	61.07	33.05	100.31	10.51
cpr 315	1.52	66.17	32.91	100.60	2.58
cpr 315	0.17	67.45	33.10	100.73	0.30
cpr 315	1.49	66.12	32.79	100.40	2.52
cpr 315	0.72	65.94	32.87	99.53	1.22
cpr 315	0.36	67.00	32.46	99.82	0.61
cpr 315	0.85	67.32	33.07	101.25	1.44
cpr 315	1.15	66.70	33.53	101.39	1.96
cpr 315	0.46	67.12	32.57	100.16	0.78
cpr 315	0.44	66.79	32.87	100.10	0.75
cpr 315	0.85	65.96	33.07	99.88	1.45
cpr 315	1.16	64.99	33.05	99.21	1.98

Appendix 1:(Cont.)

Sample	Fe wt%	Zn wt%	S wt%	sum	FeS mol%
cpr 315	5.44	61.17	33.47	100.08	9.31
cpr 315	0.22	66.72	33.40	100.34	0.37
cpr 315	0.71	67.02	33.30	101.03	1.21
cpr 315	0.13	67.09	32.97	100.19	0.22
cpr 315	11.88	55.50	33.93	101.30	20.34
cpr 315	2.29	65.57	33.22	101.08	3.88
cpr 315	1.13	66.36	33.19	100.69	1.93
cpr 315	0.41	66.42	33.42	100.25	0.71
cpr 315	1.13	66.36	33.19	100.69	1.93
cpr 315	0.34	67.84	32.94	101.13	0.57
cpr 315	1.13	66.36	33.19	100.69	1.93
Tajo W marmatite					
cpr 464	0.29	66.71	32.65	99.65	0.49
cpr 464	0.21	66.98	33.24	100.44	0.36
cpr 464	0.18	66.66	33.23	100.07	0.31
cpr 464	0.17	66.62	33.32	100.11	0.28
cpr 464	0.47	66.67	33.40	100.54	0.80
cpr 464	0.26	66.65	33.37	100.28	0.45
cpr 464	4.02	63.27	33.65	100.95	6.88
cpr 464	12.54	53.14	33.85	99.53	21.64
cpr 464	13.24	52.58	34.03	99.86	22.88
cpr 464	0.13	67.16	32.89	100.18	0.22
cpr 464	4.48	62.00	33.09	99.57	7.64
cpr 464	1.06	66.26	33.01	100.34	1.81
cpr 464	9.01	57.12	33.18	99.32	15.41
cpr 470	8.61	57.50	33.24	99.36	14.74
Fe-poor sphalerite from mineralization stage IIB					
Bench 4310 Matagente					
cpr 37	1.48	65.92	32.96	100.36	2.51
cpr 37	0.46	66.68	32.82	99.96	0.77
cpr 37	1.21	65.94	32.84	99.99	2.05
cpr 37	0.19	62.85	0.01	63.05	0.22
cpr 37	1.10	67.11	32.81	101.02	1.86
cpr 37	0.17	66.60	32.64	99.41	0.29
cpr 37	0.27	66.86	32.85	99.99	0.46
cpr 37	1.14	66.42	32.76	100.33	1.92
cpr 37	0.81	66.96	32.91	100.68	1.36
cpr 37	0.40	67.20	32.64	100.24	0.68
cpr 37	2.85	65.06	32.80	100.72	4.82
cpr 37	0.57	67.42	32.67	100.66	0.96
cpr 37	0.36	67.32	32.49	100.16	0.61
cpr 37	0.83	67.22	32.81	100.86	1.39
cpr 37	0.75	66.50	32.56	99.81	1.27
cpr 37	1.50	66.74	32.55	100.79	2.53
cpr 37	0.74	66.56	32.94	100.23	1.26
cpr 37	0.28	66.55	32.91	99.74	0.48
cpr 37	0.40	66.76	32.97	100.13	0.69
cpr 37	0.09	66.25	32.86	99.20	0.15
Matagente Cuerpo Nuevo					
cpr 51	0.85	66.43	33.09	100.38	1.45
cpr 51	0.33	65.54	33.40	99.27	0.56

Appendix 1:(Cont.)

Sample	Fe wt%	Zn wt%	S wt%	sum	FeS mol%
cpr 51	0.17	65.82	33.45	99.44	0.30
cpr 51	0.29	65.31	33.16	98.75	0.49
cpr 51	0.17	65.37	33.43	98.97	0.29
cpr 51	0.25	67.05	33.00	100.31	0.43
cpr 51	0.43	64.96	33.26	98.65	0.73
Bench 4310 Matagente area					
cpr 148	1.00	67.24	33.27	101.51	1.70
cpr 148	0.69	67.01	32.72	100.41	1.16
cpr 148	0.71	66.98	32.91	100.61	1.20
cpr 148	0.27	67.91	33.02	101.20	0.45
cpr 148	0.70	67.62	32.61	100.94	1.19
cpr 148	0.54	67.89	32.75	101.18	0.90
cpr 148	0.44	67.63	32.64	100.71	0.74
cpr 148	0.39	67.41	32.72	100.52	0.66
cpr 148	0.47	66.88	33.26	100.61	0.81
cpr 148	1.01	66.71	32.61	100.34	1.70
cpr 148	0.41	68.34	32.67	101.43	0.69
cpr 150	1.84	63.61	32.32	97.76	3.12
cpr 150	1.19	63.55	32.48	97.22	2.04
cpr 150	1.06	64.17	32.23	97.46	1.80
cpr 150	0.97	63.23	32.54	96.74	1.67
cpr 150	1.60	63.88	32.26	97.74	2.72
cpr 150	0.72	64.08	32.20	97.00	1.22
cpr 150	0.43	64.70	32.71	97.84	0.73
cpr 150	0.29	64.26	32.29	96.83	0.49
cpr 150	2.78	61.15	33.34	97.27	4.82
cpr 150	1.05	63.67	32.40	97.12	1.80
cpr 150	1.43	63.03	32.10	96.56	2.44
cpr 150	1.63	63.37	32.48	97.47	2.78
cpr 150	1.49	63.05	32.45	97.00	2.56
cpr 151	0.84	64.21	32.33	97.38	1.43
cpr 151	0.95	64.58	31.95	97.47	1.60
cpr 151	1.12	63.87	31.73	96.71	1.89
cpr 151	0.66	65.89	33.10	99.65	1.13
cpr 151	0.80	64.54	32.75	98.09	1.36
cpr 151	0.93	62.82	32.19	95.95	1.60
cpr 151	1.19	64.47	32.16	97.82	2.02
cpr 151	1.50	67.19	32.83	101.53	2.53
cpr 151	1.29	63.92	32.18	97.38	2.19
cpr 153	0.49	67.30	33.00	100.78	0.83
cpr 153	2.06	65.97	32.71	100.74	3.48
cpr 153	0.28	66.95	32.94	100.16	0.47
cpr 153	0.38	67.89	32.85	101.13	0.64
cpr 153	0.64	66.76	32.69	100.09	1.08
cpr 153	0.41	66.56	32.93	99.91	0.70
cpr 153	0.61	66.36	32.88	99.86	1.04
cpr 153	0.28	67.22	32.74	100.24	0.47
cpr 153	0.31	67.55	32.97	100.83	0.53
cpr 153	0.52	67.44	33.04	101.00	0.87

Appendix 1:(Cont.)

Sample	Fe wt%	Zn wt%	S wt%	sum	FeS mol%
San alberto					
cpr 483	0.43	66.58	33.64	100.65	0.73
cpr 483	0.71	65.20	33.65	99.55	1.22
cpr 483	0.70	66.90	33.73	101.33	1.19
cpr 483	0.31	66.57	33.42	100.30	0.53
cpr 483	1.23	67.04	33.36	101.63	2.08
cpr 483	1.24	66.00	33.35	100.59	2.12
cpr 483	0.78	66.57	33.45	100.79	1.32
cpr 483	1.31	65.63	33.66	100.59	2.25
cpr 483	1.15	64.66	33.03	98.84	1.97
cpr 483	0.49	66.70	33.47	100.66	0.83
cpr 483	1.22	65.57	33.59	100.37	2.08
cpr 483	0.55	66.11	33.32	99.97	0.93
cpr 483	0.55	66.14	33.34	100.03	0.93
cpr 483	1.40	65.50	33.65	100.55	2.39
cpr 483	0.96	66.85	33.57	101.38	1.64
cpr 483	2.00	65.17	33.69	100.86	3.42
cpr 483	0.67	67.21	33.84	101.72	1.14
cpr 483	1.13	66.83	33.80	101.76	1.93
cpr 483	0.90	66.47	33.13	100.50	1.53
cpr 483	1.70	65.70	33.07	100.48	2.89
cpr 483	0.78	67.24	33.46	101.48	1.33
cpr 483	1.11	66.61	33.55	101.27	1.89
cpr 483	0.86	66.80	33.59	101.25	1.47
cpr 483	0.90	66.46	33.54	100.91	1.54
cpr 483	0.48	67.40	33.63	101.51	0.81
Fe-rich mixed crosscut by Fe-poor sphalerite in the center of open pit and underground					
DDH CP-00-108					
cpr 75	10.96	55.79	33.75	100.50	18.80
cpr 75	6.80	61.04	34.17	102.01	11.65
cpr 75	11.32	55.90	33.77	100.99	19.38
cpr 75	1.30	64.91	33.03	99.25	2.22
cpr 75	0.70	66.04	32.97	99.71	1.19
cpr 75	1.21	63.78	33.07	98.06	2.09
cpr 75	0.79	64.83	32.58	98.20	1.35
cpr 75	11.32	55.90	33.77	100.99	19.38
cpr 75	1.30	64.91	33.03	99.25	2.22
cpr 75	0.70	66.04	32.97	99.71	1.19
cpr 75	1.21	63.78	33.07	98.06	2.09
cpr 75	0.79	64.83	32.58	98.20	1.35
cpr 75	10.96	55.79	33.75	100.50	18.80
cpr 75	6.80	61.04	34.17	102.01	11.65
cpr 76	5.89	61.85	33.79	101.54	10.06
cpr 76	0.53	66.58	33.72	100.82	0.90
cpr 76	1.34	65.62	33.26	100.22	2.29
cpr 76	0.50	65.44	33.53	99.46	0.86
cpr 76	0.23	67.80	33.28	101.31	0.39
cpr 76	0.71	66.64	33.18	100.53	1.21
cpr 76	0.50	67.60	33.35	101.44	0.84

Appendix 1:(Cont.)

Sample	Fe wt%	Zn wt%	S wt%	sum	FeS mol%
cpr 76	0.96	66.94	33.41	101.31	1.63
cpr 76	3.56	62.43	32.30	98.29	6.04
cpr 76	13.44	52.30	34.10	99.84	23.25
cpr 82	0.04	65.86	32.77	98.67	0.07
cpr 82	0.04	65.24	32.85	98.13	0.06
cpr 82	0.01	64.91	33.16	98.08	0.02
cpr 82	0.15	64.75	33.36	98.27	0.25
cpr 82	0.20	65.32	32.72	98.24	0.33
cpr 82	0.04	67.31	33.16	100.51	0.07
cpr 82	0.07	67.60	33.32	100.98	0.11
cpr 82	0.07	66.33	33.40	99.79	0.11
cpr 82	0.06	67.43	33.42	100.91	0.10
cpr 82	0.06	65.33	33.29	98.68	0.10
cpr 82	0.13	66.57	33.44	100.14	0.22
cpr 82	0.08	65.76	33.48	99.33	0.14
cpr 82	0.06	67.18	33.47	100.71	0.10
cpr 82	0.05	66.52	33.45	100.02	0.09
cpr 82	0.16	67.20	33.23	100.59	0.27
cpr 82	0.12	65.77	33.45	99.34	0.20
cpr 85	0.31	68.04	33.22	101.57	0.52
cpr 85	1.37	65.78	33.53	100.68	2.34
cpr 85	1.40	66.36	33.39	101.14	2.38
cpr 85	1.40	65.35	33.32	100.07	2.39
cpr 85	0.71	66.68	33.56	100.95	1.21
cpr 85	0.67	66.64	33.32	100.62	1.13
cpr 90	1.11	66.39	33.52	101.02	1.90
cpr 90	1.40	66.00	33.56	100.96	2.38
cpr 90	1.37	66.31	33.54	101.23	2.34
cpr 90	1.20	66.28	33.31	100.79	2.04
cpr 90	0.59	66.70	33.59	100.88	1.00
cpr 90	0.44	66.78	33.30	100.52	0.76
cpr 90	0.49	66.31	33.59	100.39	0.84
cpr 90	0.48	66.77	33.57	100.82	0.81
cpr 90	1.14	66.79	33.47	101.40	1.93
cpr 90	0.31	66.97	33.75	101.03	0.54
cpr 90	1.72	65.96	33.45	101.13	2.92
cpr 90	1.77	66.01	33.23	101.01	3.01
cpr 90	0.39	67.69	33.37	101.44	0.66
cpr 90	0.51	67.55	33.61	101.66	0.87
Diamante area 4200 bench					
cpr 417	12.64	51.66	33.43	97.72	21.87
cpr 417	10.38	55.26	33.21	98.86	17.81
cpr 417	7.13	57.64	32.81	97.57	12.23
cpr 417	5.00	61.53	32.94	99.47	8.51
cpr 417	5.39	59.12	32.93	97.45	9.28
cpr 417	0.44	65.54	32.49	98.47	0.75
cpr 417	0.31	64.75	32.59	97.65	0.53
cpr 417	0.25	65.41	32.61	98.27	0.43
cpr 417	0.19	66.82	32.92	99.93	0.32
cpr 417	0.14	67.12	33.19	100.45	0.24

Appendix 1:(Cont.)

Sample	Fe wt%	Zn wt%	S wt%	sum	FeS mol%
cpr 417	1.41	65.85	32.95	100.21	2.39
cpr 417	2.23	63.06	32.81	98.10	3.82
cpr 417	1.89	64.48	32.96	99.33	3.22
cpr 417	8.03	58.41	33.70	100.14	13.78
cpr 417	0.99	66.23	33.54	100.77	1.69
Diamante area 4200 bench					
cpr 418	2.40	65.02	32.29	99.72	4.05
cpr 418	1.14	66.91	33.30	101.35	1.93
cpr 418	1.05	66.58	33.08	100.71	1.77
cpr 418	1.10	66.52	33.24	100.86	1.87
cpr 418	1.25	65.85	32.54	99.64	2.12
cpr 418	1.50	65.47	32.57	99.54	2.53
cpr 418	0.72	67.24	32.77	100.74	1.22
cpr 428	1.38	67.36	32.72	101.45	2.32
cpr 428	0.65	67.74	32.53	100.92	1.09
cpr 428	0.69	67.03	32.76	100.49	1.16
cpr 428	0.72	66.82	32.70	100.24	1.22
cpr 428	1.00	67.84	32.42	101.26	1.68
cpr 428	0.71	66.81	32.91	100.42	1.20
cpr 428	0.67	67.67	32.91	101.26	1.14
cpr 428	0.72	67.36	32.96	101.04	1.22
cpr 428	0.98	66.84	32.36	100.17	1.64
cpr 428	1.01	67.17	33.37	101.55	1.71
cpr 428	0.92	67.24	33.12	101.29	1.56
cpr 428	0.93	67.28	33.25	101.46	1.58
cpr 428	1.45	66.73	33.11	101.30	2.46
cpr 428	1.67	66.83	32.70	101.20	2.81
cpr 428	1.34	66.40	32.66	100.40	2.26
cpr 428	2.02	65.85	32.58	100.45	3.40
cpr 428	1.62	66.36	32.82	100.80	2.74
cpr 428	1.29	65.98	33.03	100.30	2.19
cpr 428	1.62	66.57	32.99	101.18	2.73
cpr 428	1.76	65.80	32.89	100.45	2.99
cpr 428	2.65	65.06	33.31	101.02	4.50
cpr 428	1.73	66.25	32.65	100.62	2.91
cpr 428	12.51	53.59	33.64	99.74	21.50
cpr 428	9.02	58.22	32.20	99.44	15.19
cpr 428	8.99	58.41	33.28	100.67	15.29
cpr 428	2.81	64.58	32.64	100.02	4.75
cpr 428	3.52	64.45	32.19	100.15	5.90
cpr 428	2.06	65.98	32.30	100.34	3.45
cpr 428	1.40	67.36	32.84	101.59	2.35
cpr 428	1.44	66.65	32.91	101.00	2.43
cpr 428	1.20	66.73	32.77	100.69	2.02
cpr 428	0.92	66.43	32.61	99.96	1.55
cpr 428	1.28	66.25	32.95	100.47	2.17
cpr 428	0.99	67.40	32.74	101.14	1.67
cpr 431	7.70	58.43	33.80	99.93	13.26
cpr 431	6.13	61.26	33.64	101.03	10.47
cpr 431	6.35	60.49	33.45	100.29	10.85
cpr 431	0.29	67.21	33.14	100.63	0.49

Appendix 1:(Cont.)

Sample	Fe wt%	Zn wt%	S wt%	sum	FeS mol%
cpr 431	0.18	67.69	33.25	101.11	0.30
cpr 431	0.25	67.81	33.24	101.30	0.43
cpr 431	8.06	58.71	33.58	100.35	13.80
cpr 431	7.67	59.33	33.46	100.45	13.10
cpr 431	1.51	66.28	33.34	101.13	2.57
cpr 431	0.39	67.20	33.30	100.89	0.66
cpr 431	0.54	66.59	33.33	100.46	0.92
cpr 431	0.36	66.86	33.36	100.59	0.62
cpr 431	1.02	66.38	33.44	100.84	1.74
cpr 431	1.81	65.64	33.21	100.66	3.07
cpr 431	6.67	60.47	33.52	100.66	11.39
cpr 431	8.89	58.15	33.70	100.73	15.21
cpr 431	2.10	65.15	33.26	100.52	3.58
cpr 431	0.21	67.42	33.41	101.04	0.35
cpr 431	8.75	57.15	33.71	99.60	15.06
cpr 431	7.31	59.81	33.72	100.84	12.51
cpr 431	5.53	61.23	33.52	100.28	9.46
cpr 431	1.07	66.80	33.05	100.91	1.82
cpr 431	2.18	64.94	33.23	100.34	3.71
cpr 431	0.38	66.95	33.23	100.56	0.65
cpr 431	0.88	66.45	33.09	100.43	1.50
cpr 431	9.54	57.19	33.81	100.54	16.37
2nd ramp NE					
cpr 457	8.24	59.19	31.04	98.47	13.70
cpr 457	4.36	62.60	32.06	99.02	7.34
S open pit					
cpr 482	0.06	67.82	33.76	101.64	0.10
cpr 482	0.02	67.26	33.36	100.64	0.04
cpr 482	0.01	67.38	33.47	100.87	0.02
cpr 482	0.15	67.03	33.45	100.63	0.26
cpr 482	0.15	67.67	33.32	101.14	0.25
cpr 482	0.19	66.96	33.43	100.58	0.32
cpr 482	4.08	62.63	33.52	100.22	6.98
cpr 482	0.13	66.87	33.40	100.40	0.22
cpr 482	0.16	66.61	33.33	100.10	0.27
cpr 482	1.89	63.01	33.76	98.67	3.28
cpr 482	5.53	60.90	33.92	100.34	9.51
cpr 482	0.29	66.26	33.73	100.28	0.50
cpr 482	0.16	67.48	33.38	101.02	0.27
cpr 482	6.84	60.27	33.97	101.07	11.73
cpr 482	10.45	55.70	33.94	100.09	18.01
cpr 482	0.03	66.71	33.46	100.20	0.04
cpr 482	5.56	60.84	33.97	100.38	9.58
cpr 482	4.72	60.26	33.66	98.64	8.16
cpr 482	2.61	63.87	33.59	100.07	4.48
cpr 482	6.87	59.40	34.65	100.93	11.92
cpr 482	6.17	60.04	33.80	100.01	10.61
cpr 482	4.66	62.03	33.58	100.27	7.98
cpr 482	0.99	65.70	33.36	100.06	1.70
cpr 482	3.51	61.31	33.29	98.11	6.05

Part II

Timing and duration of the Mid-Miocene magmatic-hydrothermal system of the Cerro de Pasco polymetallic deposit, Central Peru: An integrative U-Pb, $^{40}Ar/^{39}Ar$, Rb-Sr, and Pb isotope study.

Regina Baumgartner, Lluís Fontboté Richard Spikings, Maria Ovtcharova, Jens Schneider

Department of Mineralogy, University of Geneva, 13 Rue des Maraichers, Switzerland

And Lawrence Page

Department of Geology, Lund University, Sölvegatan 12, 22362 Lund, Sweden

Abstract

The Cerro de Pasco epithermal Cordilleran base metal deposit, located in central Peru, is constituted by two mineralization stages which are spatially and genetically related to a Mid-Miocene diatreme-dome complex. In order to gain information on the absolute duration of the magmatic-hydrothermal system at Cerro de Pasco, U-Pb age determinations and Hf isotope determinations on single zircon grains as well as a step-wise IR-CO_2 laser $^{40}Ar/^{39}Ar$ age determinations on biotite from intrusive rocks, on sericite, and alunite related to the first and second mineralization stage, respectively, have been conducted. This study has been complemented by Rb-Sr and Pb isotope analyses of sericite and associated pyrite.

The single zircon U-Pb survey reveals that the ages of an accretionary lapilli tuff from a collapsed block within the diatreme (15.36 ± 0.03 Ma), a dacitic porphyry dome in the diatreme (15.40 ± 0.07 Ma) and two quartz-monzonite porphyritic dykes emplaced into the diatreme-dome complex (15.35 ± 0.35 Ma and 15.16 ± 0.03 Ma) are comprised within a time span of 350'000 yr . No field evidence has been found so far that magmatic activity at the surface could have started earlier than the formation of the diatreme-dome complex.

Step-wise IR-CO_2 laser $^{40}Ar/^{39}Ar$ ages have been obtained on the second mineralization stages alunite samples from advanced argillic altered domes and from halos of oxidized enargite-pyrite veins in the Venencocha and Santa Rosa, located on the northwestern margin of the diatreme-dome complex and on the southern part of the Cerro de Pasco open pit, respectively. $^{40}Ar/^{39}Ar$ alunite ages cluster between 14.54 ± 0.08 and 14.41 ± 0.07 Ma. This age consistency suggests that advanced argillic alteration related to the second mineralization stage at Cerro de Pasco has been produced during a short period of around 100'000 yr. Three alunite ages at 12.39 ± 0.06, 12.13 ± 0.07 Ma, and 10.94 ± 0.1 Ma, outliers of the main age cluster (14.5 - 14.4 Ma), are interpreted to have probably experienced resetting by late circulating fluids. Therefore, magmatic-hydrothermal activity at Cerro de Pasco appears to have lasted for around 1 My, from 15.4 to 14.5 Ma, a relatively short time span for such a large mineralized system but in the same range as at the nearby Mid Miocene Colquijirca District.

An attempt to date more precisely the first mineralization stage, bracketed in time between the quartz-monzonite dykes and the second mineralization stage, i.e. between 15.1 and 14.5 Ma, has failed because $^{40}Ar/^{39}Ar$ ages obtained on sericite occurring in the alteration halo of the pyrite-quartz body are not reliable probably due to inherited argon derived from micas contained in Paleozoic clasts within the diatreme breccia.

Rb-Sr data for sericite and Pb isotopes measured on pyrite and sericite indicates binary geochemical mixing between Miocene magmatic and Paleozoic basement sources. Lead isotopic compositions of pyrite and sericite ($^{206}Pb/^{204}Pb$ = 18.743 - 18.922, $^{207}Pb/^{204}Pb$ = 15.629 - 15.660, $^{208}Pb/^{204}Pb$ = 38.789 - 38.958) are comparable to those published previously of galena at Cerro de Pasco, Colquijirca, San Cristobal, and Morococha, and are explained by magmatic mixing of enriched upper mantle-derived lead and radiogenic upper crustal rocks lead.

Introduction

The timing and duration of ore-forming magmatic-hydrothermal systems is a fundamental question for the genesis of mineral deposits related to magmatic intrusions, such as porphyry copper deposits, epithermal precious metal high-sulfidation and epithermal Cordilleran-type base metal deposits. These are known worldwide in settings of various geological ages but are most common in Tertiary host rocks. During the last 20 years, geochronological research on intrusion-related deposits has been conducted in order to constrain the lifespan of hydrothermal activity (e.g. Warnaars et al., 1978; Snee et al., 1988; Marsh et al., 1997; Masterman et al., 2005). It appears that protracted magmatic-hydrothermal systems persisting several million years and comprising multiple magmatic events and two or more main hydrothermal pulses are common characteristics of porphyry copper systems (e.g., Chuquicamata and La Escondida, Ossandón et al., 2001; Padilla Garza et al., 2001). Single hydrothermal pulses would last generally in the order of 50'000 to 100'000 y (Henry et al., 1997; Muntean and Einaudi, 2001; Seedorff et al., 2005).

The Cerro de Pasco polymetallic deposit is located in central Peru and is spatially related to a Mid-Miocene diatreme-dome complex. The deposit is mainly hosted by Mesozoic carbonate rocks (Pucará Group) and the diatreme-dome complex itself. The timing of the ore-forming, magmatic-hydrothermal events at Cerro de Pasco was only poorly known. Silberman and Noble (1977) reported a K/Ar study on the magmatic rocks but no ages were available for minerals related to the mineralization. This paper presents a geochronological study of volcanic rocks, intrusive dykes, and selected hydrothermal mineral phases from the Cerro de Pasco district. High-precision single zircon U-Pb and stepwise IR-CO_2-laser $^{40}Ar/^{39}Ar$ geochronology on biotite, sericite and alunite has been combined with field observations to resolve the chronology and duration of magmatic and of ore-forming hydrothermal events. This study has been complemented by Rb-Sr and Pb isotope analyses of sericite and associated pyrite in order to trace the source of these elements and by a petrographic and geochemical study of the analyzed volcanic rocks.

This paper is a companion paper of Baumgartner and Fontboté (Part I) where a detailed mineralogical study on the first and second mineralization stages with an emphasis on the environment of deposition is reported. In addition, a detailed fluid inclusion and stable isotope study is reported by Baumgartner et al. (Part III) indicating that the ore-forming fluids were principally issued from mixing between magmatic fluids and isotopically exchanged meteoric waters for both mineralization stages. In the second stage, sporadic incursions of SO_2 vapor plumes acidified the diluted brines.

Regional Geology

The Cerro de Pasco district (10°41S, 76°16W) lies on the Andean plateau, at an elevation of 4300 m.a.s.l.. It is located in the flat slab segment of the Peruvian Andes, corresponding to the Nazca ridge subduction since the Mid-Miocene (Rosenbaum et al., 2005 and references therein) and causing the gap of the present-day volcanism (Barazangi and Isacks, 1976; Hasegawa, 1981; Pilger, 1981; Gutscher et al., 2000; Rosenbaum et al., 2005). Recent studies (Rosenbaum et al. 2005; Hampel 2002, Gutscher et al. 1999) have attempted a kinematic reconstruction for the Nazca ridge and Inca plateau (Gutscher et al., 1999) for the Miocene (15-5 Ma) and concluded that the arrival of the Nazca ridge at the subduction zone occurred in the mid-Miocene (15 Ma, Rosenbaum et al., 2005). This timing may correspond approximately to the magmatic and related hydrothermal activity at Cerro de Pasco.

A regional N-S "Longitudinal Fault" juxtaposes Paleozoic metamorphic rocks with Mesozoic sedimentary rocks in the area (Fig. 1). In the Cerro de Pasco open pit, the Longitudinal Fault is believed to be represented by high-angle N15°W striking reverse faults (Fig. 2). The main part of the Longitudinal Fault is probably not observable because it most likely coincides with the emplacement of the diatreme but it is more obvious N and S of the diatreme. The oldest rocks exposed in the Cerro de Pasco district are Devonian metamorphosed shale, phyllite, and quartzite, which belong to the Excelsior Group (Jenks, 1951). This Group is unconformably overlain by Permo-Triassic Mitu Group redbeds consisting of sandstone and conglomerate derived from continental erosion of mainly volcanic sequences. They contain milky quartz pebbles and Excelsior Group-derived argillaceous material. In the eastern part of the district, the Mitu Group is covered by a thick (up to 3000 m) Upper Triassic-Lower Jurassic carbonate sequence belonging to the Pucará Group (McLaughlin, 1924; Jenks, 1951; Angeles, 1999). This sequence is mainly composed of dolomite, doloarenite, cherty dolomite, bituminous dolomite, and fossiliferous massive dolomite. To the west of the longitudinal fault, the Pucará Group is only 300 m thick and consists of thin-bedded, light colored limestone (Jenks, 1951; Angeles, 1999). Following multiple Early Miocene deformation episodes, the region was affected by intense magmatic activity during the Mid-Miocene, forming large diatreme-dome complexes in the Cerro de Pasco and Colquijirca districts, the latter located 10 km to the south of Cerro de Pasco (Fig. 1). At Yanamate, located 4 km to the southeast of Cerro de Pasco, a smaller diatreme-dome complex occurs (Fig. 1).

Mineralization at Cerro de Pasco is mainly concentrated along the eastern margin of a diatreme-dome complex (Fig. 1 and 2) which is 2.5 km in diameter and emplaced along the Longitudinal Fault separating the Pucará Group limestone and Excelsior Group phyllite (Fig. 1). The diatreme-dome complex is composed mainly of a diatreme breccia, dacitic porphyritic domes and quartz-monzonite porphyritic dykes, described below. The diatreme breccia (historically named Rumiallana agglomerate) mostly occupies at present the larger, inner portion of the diatreme (Fig. 2). In the Santa Rosa

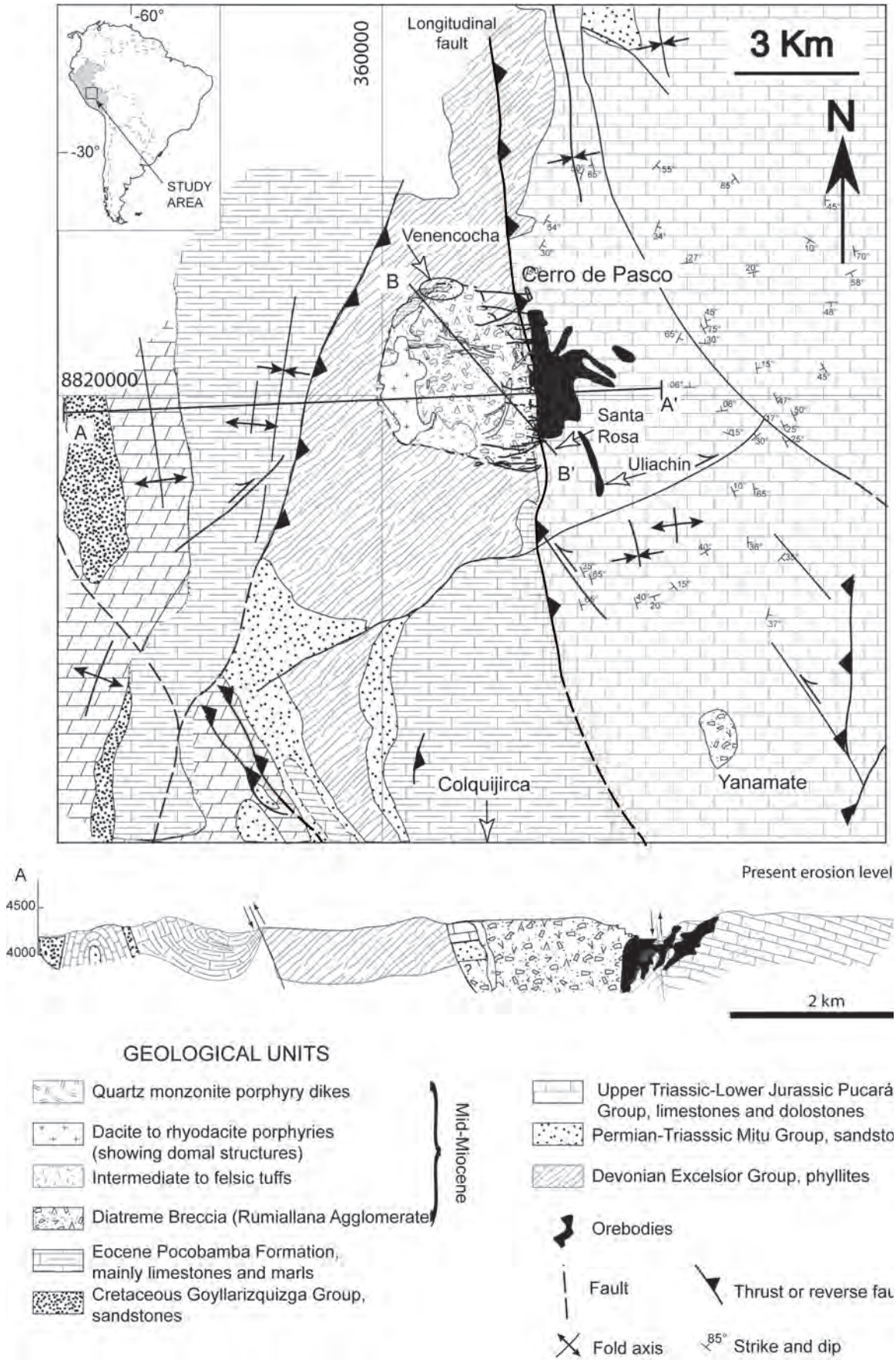

Fig. 1: *Geology (modified from Bendezú et al. 2003) and schematic west-east (A-A') cross section of the Cerro de Pasco district. The lower cross-section illustrates the Mid-Miocene topography at Cerro de Pasco.*

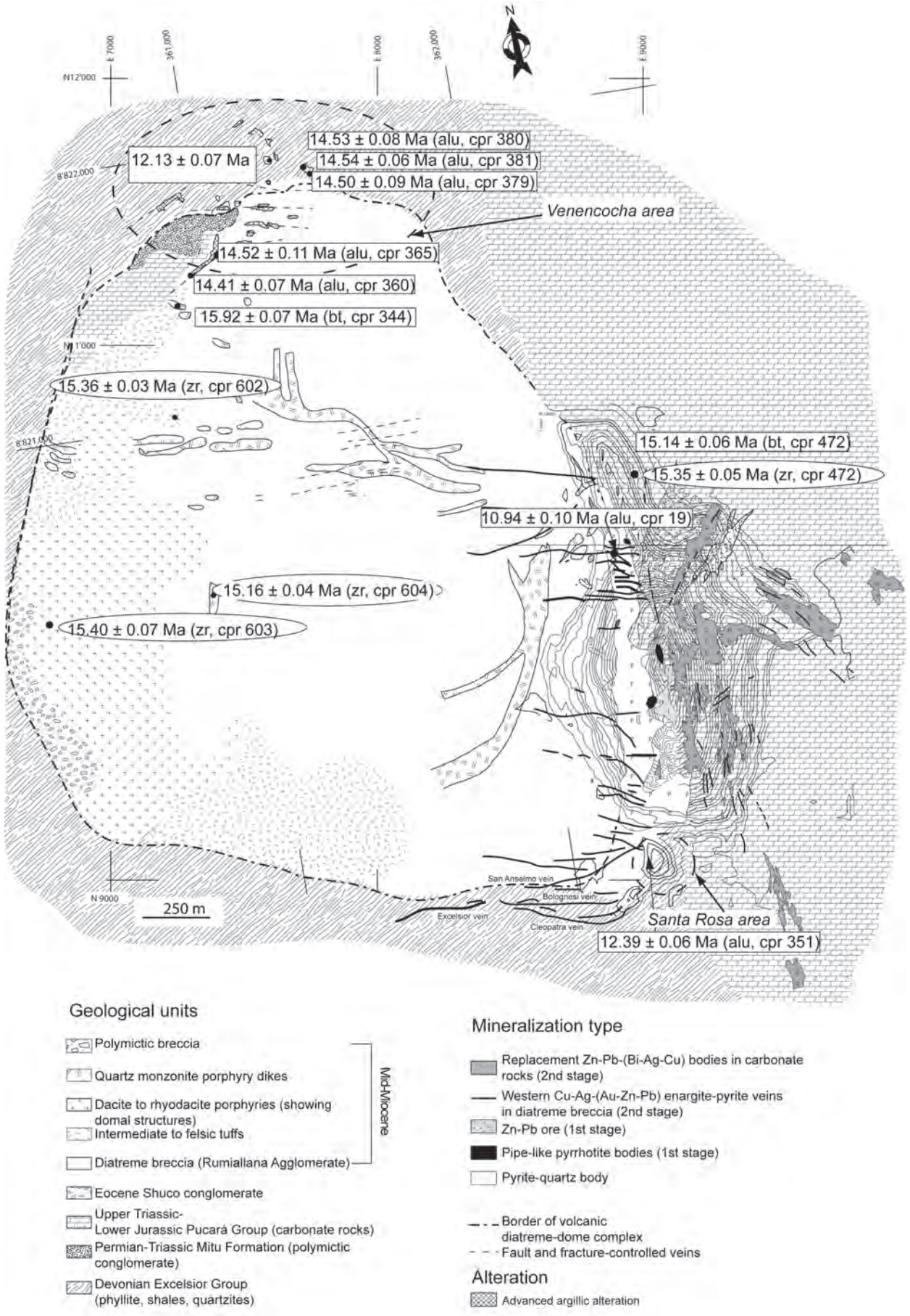

Fig. 2: *Geological map of the diatreme-dome complex, compiled from Rogers, (1983) and Huanqui (1994) and of the Cerro de Pasco open pit. U-Pb ages on zircon and $^{40}Ar/^{39}Ar$ ages on biotite and alunite are shown. Abbreviations are: alu = alunite, bt = biotite, and zr = zircon.*

area, in the southern part of the open pit, diatreme breccia occurs outside the diatreme probably as a pyroclastic flow. It consists of angular to sub-rounded clasts of variable size (1-100 mm) and of different origin (Fig. 3A) including clasts of Excelsior phyllite, Mitu sandstone, Pucará limestone, tuff clasts, and a small portion of altered porphyritic igneous rocks occur within the breccia. Lacy (1949) reported the presence of volcanic glass which was either altered to sericite or recrystallized to form a fine mat of intercalating feldspar laths.

Base surge deposits such as accretionary lapilli showing cross-bedding have been observed in the northwestern part of the diatreme (Fig. 3B and C). The base surge deposits present in the diatreme do not show lateral continuity and are thus believed to be blocks of subaerial ring tuff collapsed into the diatreme. Large blocks of Mitu and Pucará Group wall-rock collapsed into the diatreme occur mainly on the northwestern side of the diatreme.

Dacitic to rhyodacitic porphyritic domes are emplaced at the southwestern (Rogers, 1983) and northern margins of the diatreme (Fig. 2 and 3E). Flow banding defining domal structures can be observed and Silberman and Noble (1977) report local subhorizontal flow foliation.

The diatreme-dome complex is cut by E-W-trending dykes and irregular bodies of quartz-monzonite porphyries (Fig. 2). These magmatic bodies pass into the Pucará carbonate rocks (Fig. 3G). In the vicinity of the pyrite-quartz body, the dykes are altered to sericite-pyrite. Lacy (1949) and Silberman and Noble (1977) report the presence in the underground mine of albitized quartz-monzonite porphyry dykes which cut the E-W enargite-pyrite veins. They cut a vein at the 1400 and 1600 levels (3915 and 3855 m) of the underground mine and similar dykes are observed at the 2500 level (3565 m) along the northeastern side of the diatreme.

Structural aspects characteristic of the diatreme, such as ring faults can be observed mainly along its northern and eastern margins. Furthermore, a structural control of the diatreme emplacement is obvious since it lies on a major regional fault, the Longitudinal Fault. A complex fault set is present in the open pit and follows N35°E, N90°E, N120°E, and N170°E orientations and dip vertically (Fig. 4). The N35°E, N120°E, and N170°E faults are interpreted by Ward (1961) sinistral and/or dextral strike slip faults which formed by compression in the later stages of folding.

Hydrothermal alteration and mineralization

Mineralization at Cerro de Pasco is mainly concentrated along the eastern margin of a diatreme-dome complex (Fig. 1 and 2) in carbonate rocks as well as in the diatreme breccia rocks and consists of two mineralization stages. A detailed mineralogical study on the two mineralization stages has been presented by Einaudi (1977) and Baumgartner and Fontboté (Part I) and the following section is a summary of their descriptions.

The first mineralization stage includes a large pyrite-quartz body and pyrrhotite bodies zoned to Zn-Pb ores bearing Fe-rich sphalerite emplaced in Pucará carbonate rocks. An alteration halo composed of sericite, pyrite, and quartz is present in the quartz-monzonite porphyritic dykes and the diatreme breccia rocks in contact with the pyrite-quartz body (Fig. 5A and C). The pipe-like pyrrhotite bodies zoned to Zn-Pb ores bearing Fe-rich sphalerite (Fig. 6) are characterized by low sulfidation state assemblages (pyrrhotite, Fe-rich sphalerite, arsenopyrite as well as pyrite, Fe-rich sphalerite). The first mineralization stage is possibly formed by diluted brines (0-11 wt % NaCl equiv at 190 to 275 °C, Baumgartner et al., Part III)

The second mineralization stage consists of Cu-Ag-(Au-Zn-Pb) enargite-pyrite veins hosted in the diatreme breccia on the western part of the open pit and Zn-Pb-(Bi-Ag-Cu) Pucará carbonate-hosted replacement bodies in the eastern and central open pit. The core zone of both veins and replacement bodies are characterized by high sulfidation assemblages (enargite/famatinite-pyrite) and advanced argillic alteration including alunite ($KAl_3(SO_4)_2(OH)_6$) and quartz while the intermediate and outer zones are characterized by intermediate sulfidation state assemblages (tennantite/tetrahedrite- and Fe-poor sphalerite-pyrite) and advanced argillic to argillic alteration (hinsdalite, dickite, kaolinite). On the northwestern margin of the diatreme-dome complex, in the Venencocha area, located 2.5 km away from the open pit (Fig. 2), pervasively altered domes and altered halos of oxidized veins, trending N50°E to N90°E and hosted in sedimentary rocks and diatreme breccia, contain alunite, zunyite ($Al_{13}Si_5O_{20}(OH,F)_{18}Cl$), and quartz, typical of advanced argillic alteration (Fig. 7 and 8). The same alteration pattern occurs also in the Santa Rosa area. The oxidized veins at Venencocha and Santa Rosa are interpreted to be the equivalent of the second mineralization stage enargite-bearing veins in the western part of the Cerro de Pasco open pit (Baumgartner et al. Part III) because they show the same orientation and contain the same alteration minerals. The oxidized and acidic ore-forming fluids of the second mineralization stage were possibly diluted brines (0.5 to 11 wt % NaCl equiv at 180 to 260°C).

Relative chronology of magmatic-hydrothermal events and previous geochronological work

At Cerro de Pasco, the following observations concerning the crosscutting relationships of magmatic rocks and mineralization stages can be made: (i) the quartz-monzonite porphyry dykes cut the diatreme and pass into the carbonate rocks, (ii) the quartz-monzonite porphyry dykes are cut by the two mineralization stages; Lacy (1949) reports the presence of late albitized dykes which would cut the enargite-pyrite veins of the second mineralization stage. During this work, this observation could not be reproduced. Concerning the mineralization

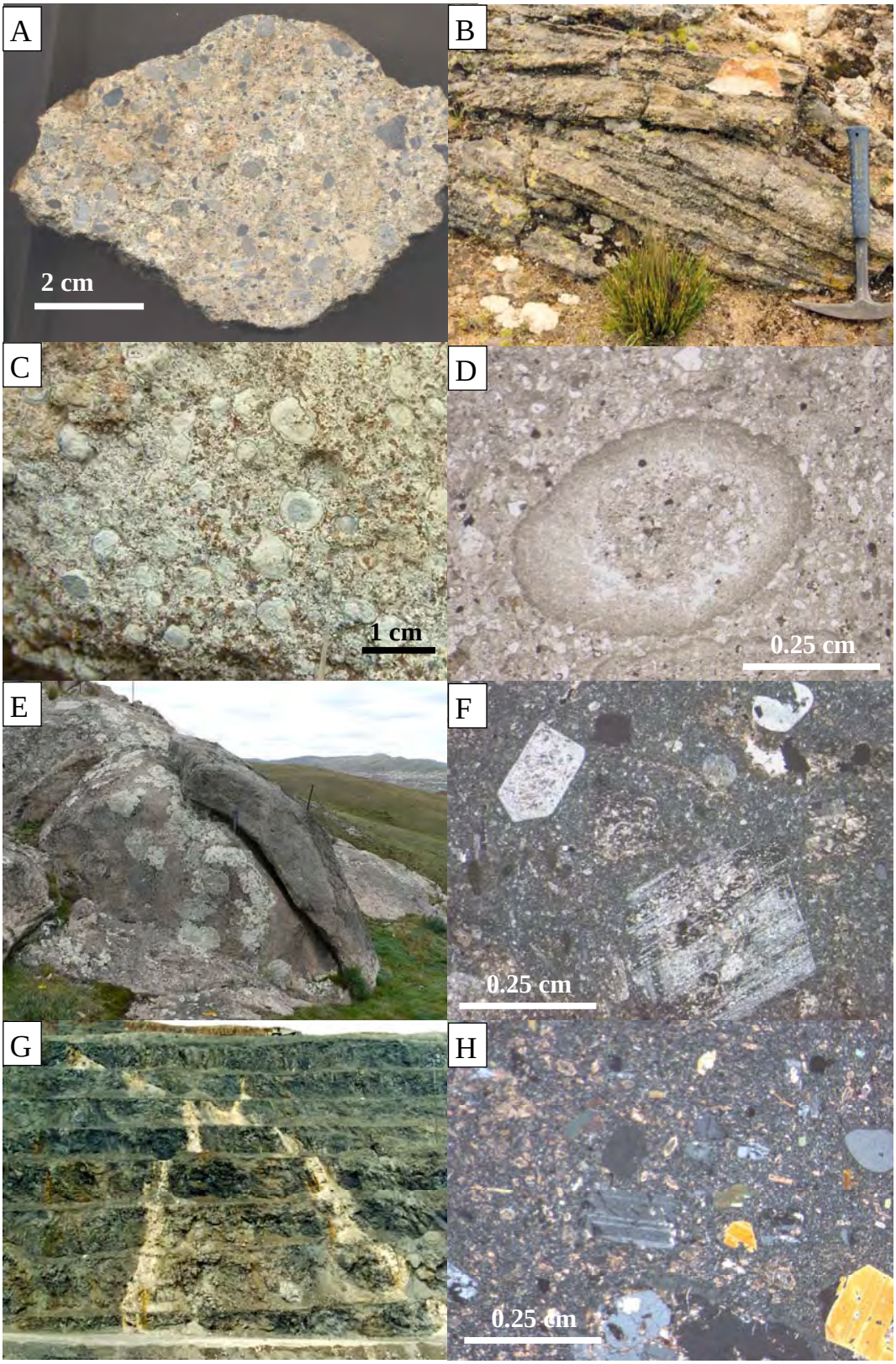

Fig. 3: *Photo and microphotographs of rocks and textures from the diatreme-dome complex. A) Diatreme breccia showing clasts of the Excelsior, the Mitu and the Pucará Group. Note that the sample is slightly propyllitic altered. B) Outcrop of accretionary lapilli inside the diatreme showing cross bedding. C) Macroscopic sample showing the accretionary lapilli in a matrix of ash. D) Microscopic view of an accretionary lapilli with a rim-type texture (double crossed nicols, CPR 602). E) Dacitic dome cropping out in the southwestern margin of the diatreme-dome complex. Sample location of CPR 603. F) Microscopic view and texture of a dacitic dome (CPR 603) showing a slight propyllitic alteration. G) Open pit view (looking to the east)with quartz-monzonite porphyry dykes passing into carbonate rocks. Sample location for CPR 472. H) Microphotograph of a quartz-monzonite porphyry dyke (CPR 472, double crossed nicols).*

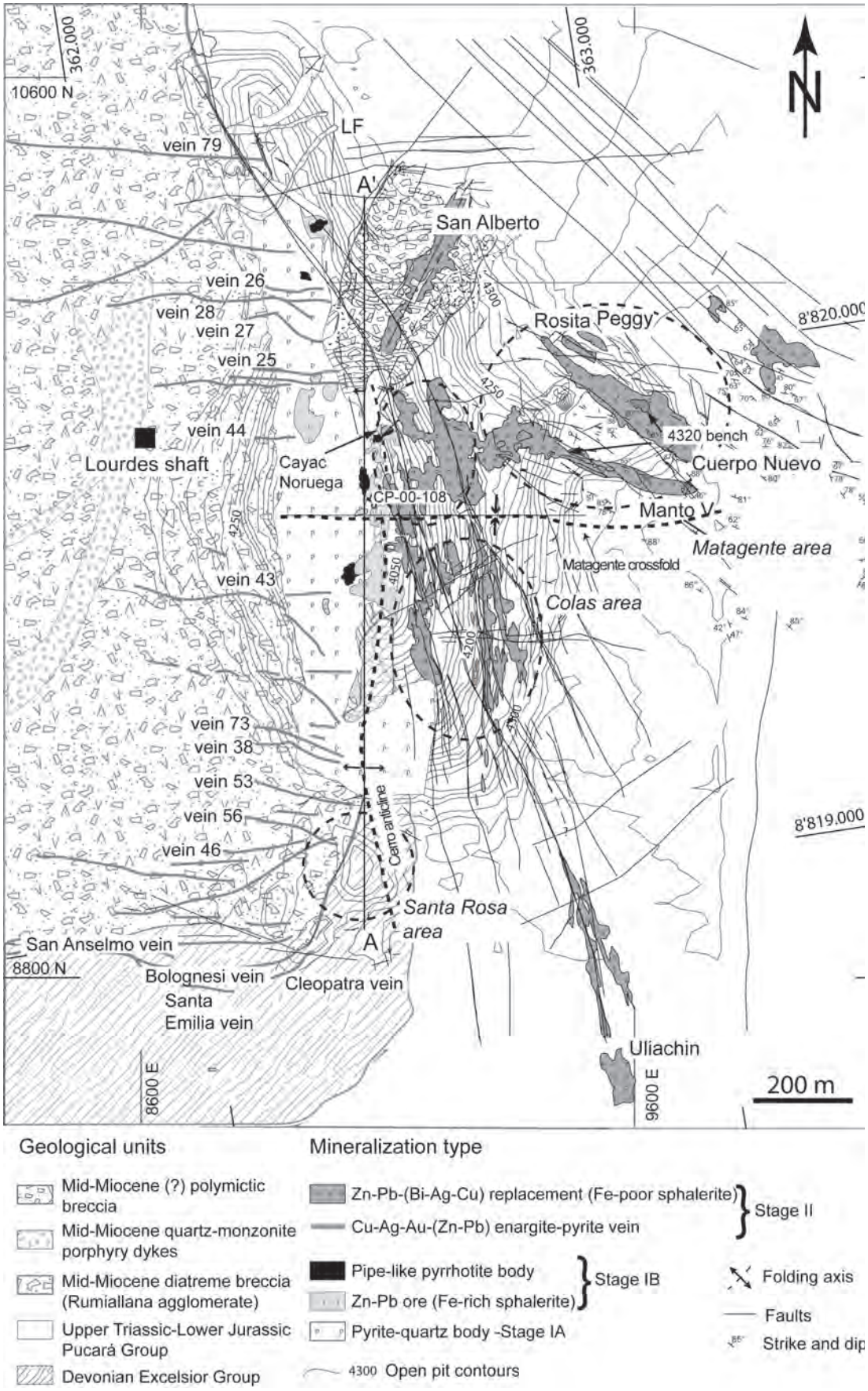

Fig. 4: *Geological map of the Cerro de Pasco open pit showing the rock units, the structure, and the different mineralization stages, based on maps of the Cerro de Pasco Geology staff. Lines labeled A-A' indicate location of cross sections in Fig. 6*

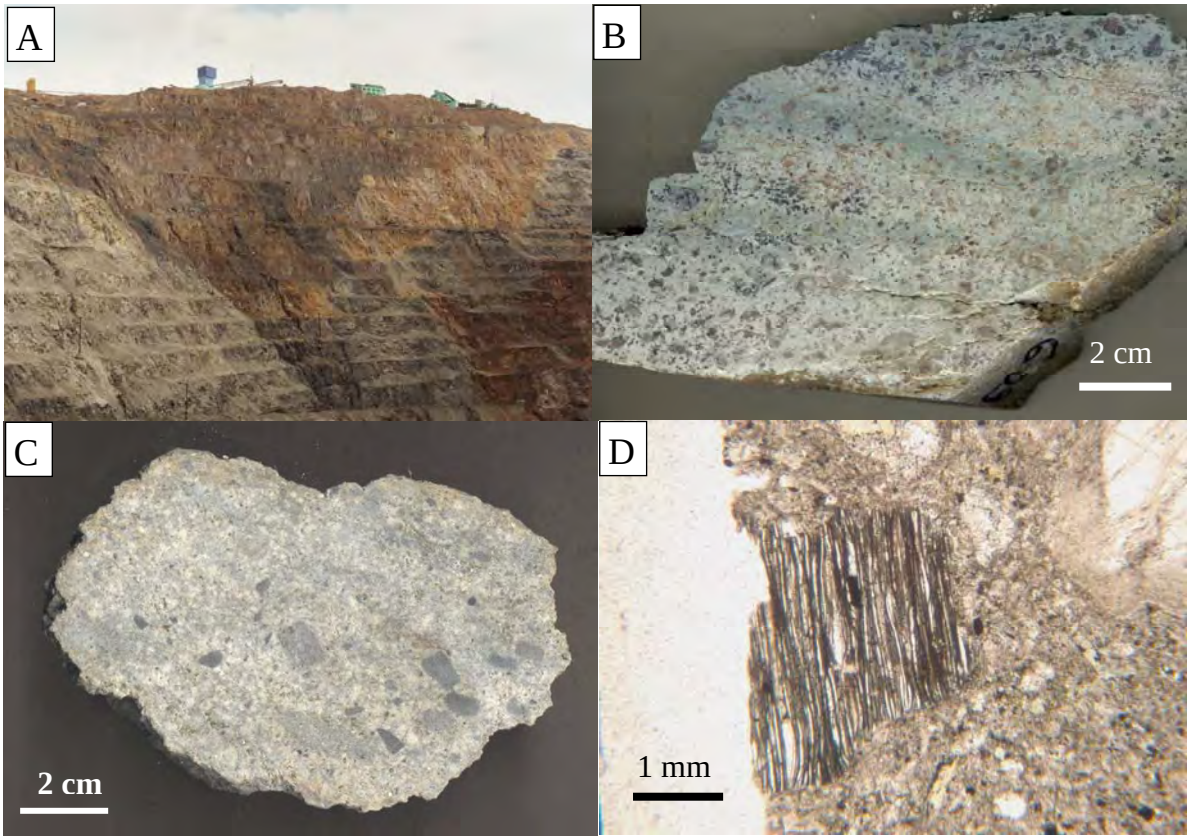

Fig. 5: *A) Open-pit view of the pyrite-quartz body with its sericite-pyrite alteration halo in the diatreme breccia. B) Albitized dyke occurring in the underground mine. C) Diatreme breccia altered to sericite-pyrite. D) Book biotite in transversal section showing expanded accordion-like textures with interbanded calcite and muscovite, occurring in the albitized quartz-monzonite dykes.*

stages, crosscutting relationships indicate that (i) the pyrite-quartz body is replaced by the pyrrhotite pipes; (ii) the first stage Zn-Pb ores bearing Fe-rich sphalerite constitute the external part of a zoned sequence around the pyrrhotite pipes; and (iii) the first mineralization stage pyrite-quartz body and the Zn-Pb ores bearing Fe-poor sphalerite are cut by the second stage enargite-pyrite veins and carbonate replacement bodies (Fig. 9).

In a previous geochronological study (K-Ar) of the diatreme-dome complex rocks, Silberman and Noble (1977) reported five K-Ar ages from biotite, plagioclase and sanidine samples. According to Silberman and Noble (1977) biotite, plagioclase and sanidine were collected from "units intruded after the emplacement of the Rumillanana Agglomerate" i.e. the diatreme breccia, and "before the formation of the pyrite-quartz body and various economically important orebodies". The quartz-monzonite porphyry dykes were dated at 15.0 ± 0.5 Ma, 14.6 ± 0.4 Ma, and 14.2 ± 0.4 Ma and the dacitic domes at 14.8 ± 0.4 Ma and 14.0 ± 0.4 Ma (Fig. 2). A sanidine from an albitized quartz-monzonite porphyry dyke, interpreted as cutting the enargite-pyrite veins, yielded an age of 15.2 ± 0.2 Ma. Silberman and Noble (1977) concluded that the latter age suffered from extraneous argon and should be around 1 Ma younger. In addition they concluded that the 14 Ma ages were possibly reset by hydrothermal alteration because most of the sanidine samples were sericitized.

In the Colquijirca district, 10 km to the south of Cerro de Pasco, a porphyritic dacitic dome occurring at Huacchuacaja at the western part of the diatreme dome complex of Marcapunta, (Fig. 1) has been dated with $^{40}Ar/^{39}Ar$ on three biotite concentrates by Bendezú et al. (2003), yielding ages at 12.43 ± 0.06 Ma, 12.7 ± 0.1 Ma, and 12.9 ± 0.1 Ma. This dome is slightly altered, with biotite being locally replaced by chlorite, which might affect the $^{40}Ar/^{39}Ar$ age. At the Colquijirca deposit, Bendezú et al. (2003) and Bendezú (2007) report absolute ages of Cordilleran base metal and high sulfidation Au-(Ag) mineralization using $^{40}Ar/^{39}Ar$ on alunite. Alunite samples related to the Au-(Ag) epithermal ores have been dated between 11.90 ± 0.07 and 11.10 ± 0.06 Ma and those from the Cordilleran base metal ores yield ages ranging from 10.83 ± 0.06 to 10.56 ± 0.08 Ma. These authors conclude that the duration of the magmatic-hydrothermal cycle was at least of 1.5 My.

At Yanamate, the diatreme-dome complex located between Cerro de Pasco and Colquijirca (Fig. 1), two slightly discordant plagioclase and whole rock K/Ar ages on a granodioritic porphyry stock are reported by Soler and Bonhomme (1988). The dated plagioclase phenocrysts and the whole rock are partly sericitized and give two ages of 13.1 ± 1.1 and 15.2 ± 0.4 Ma, respectively, both of which are considered by the authors

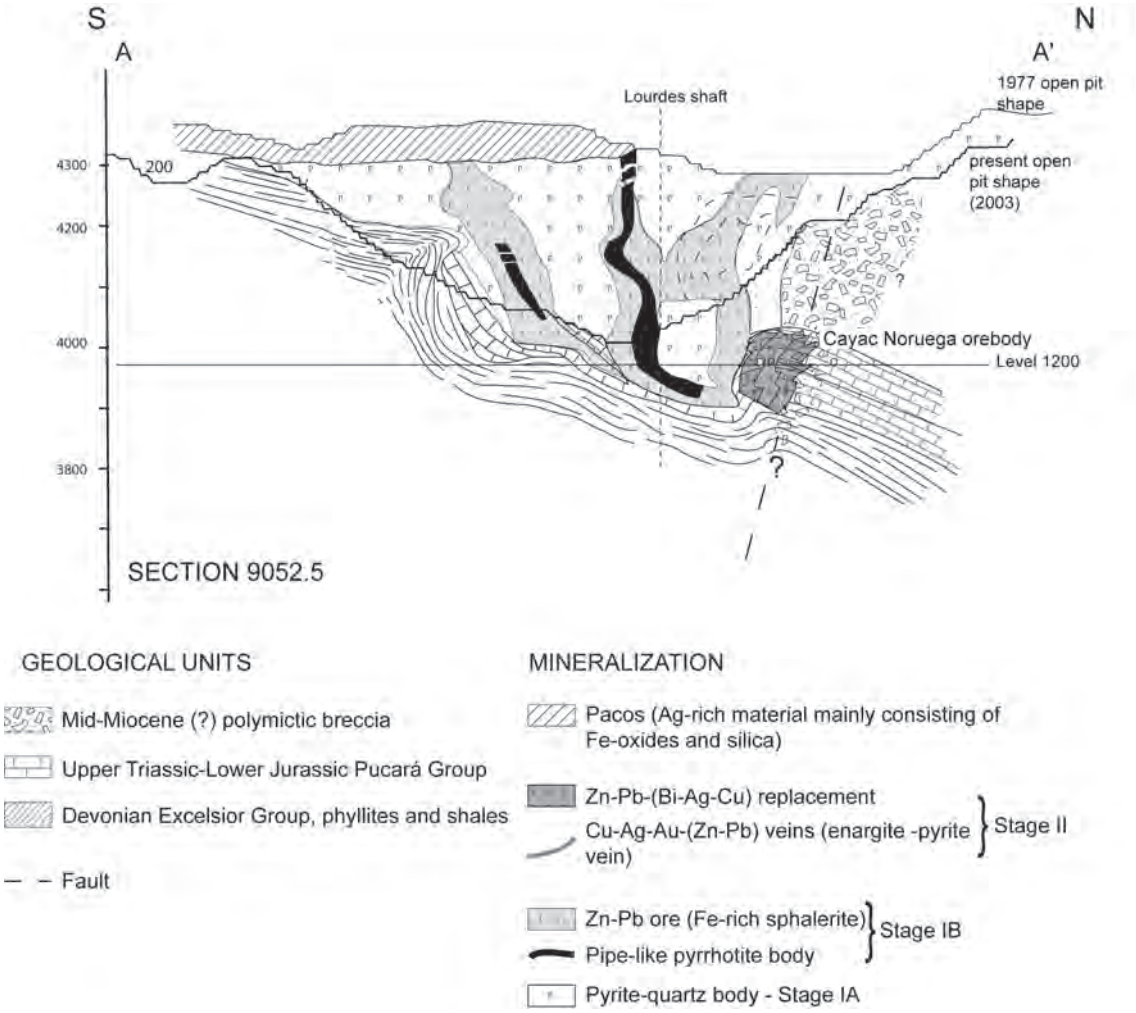

Fig. 6: *N-S cross section (A-A' in Fig. 4) showing pipe-like pyrrhotite bodies and related Zn-Pb mineralization emplaced in the pyrite-quartz body and in the Pucará carbonate rocks. Modified from Einaudi (1977).*

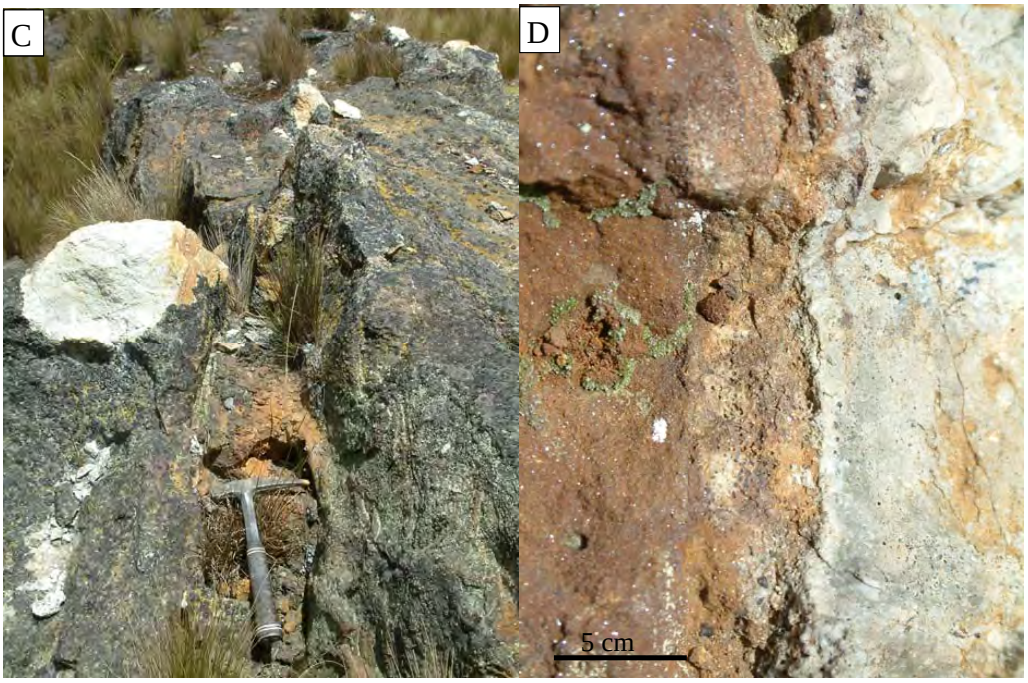

Fig. 7: *A) Oxidized vein with goetite, jarosite, alunite, quartz, and zunyite ($Al_{13}Si_5O_2$ (OH, F)$_{18}$Cl). The advanced argillic alteration halo in the host rock (here the diatreme breccia) is composed of quartz, alunite, zunyite, and diaspore, Venencocha area. B) Enlargement of an oxidized vein with its advanced argillic halo. Outcrop of sample CPR 360, Venencocha area.*

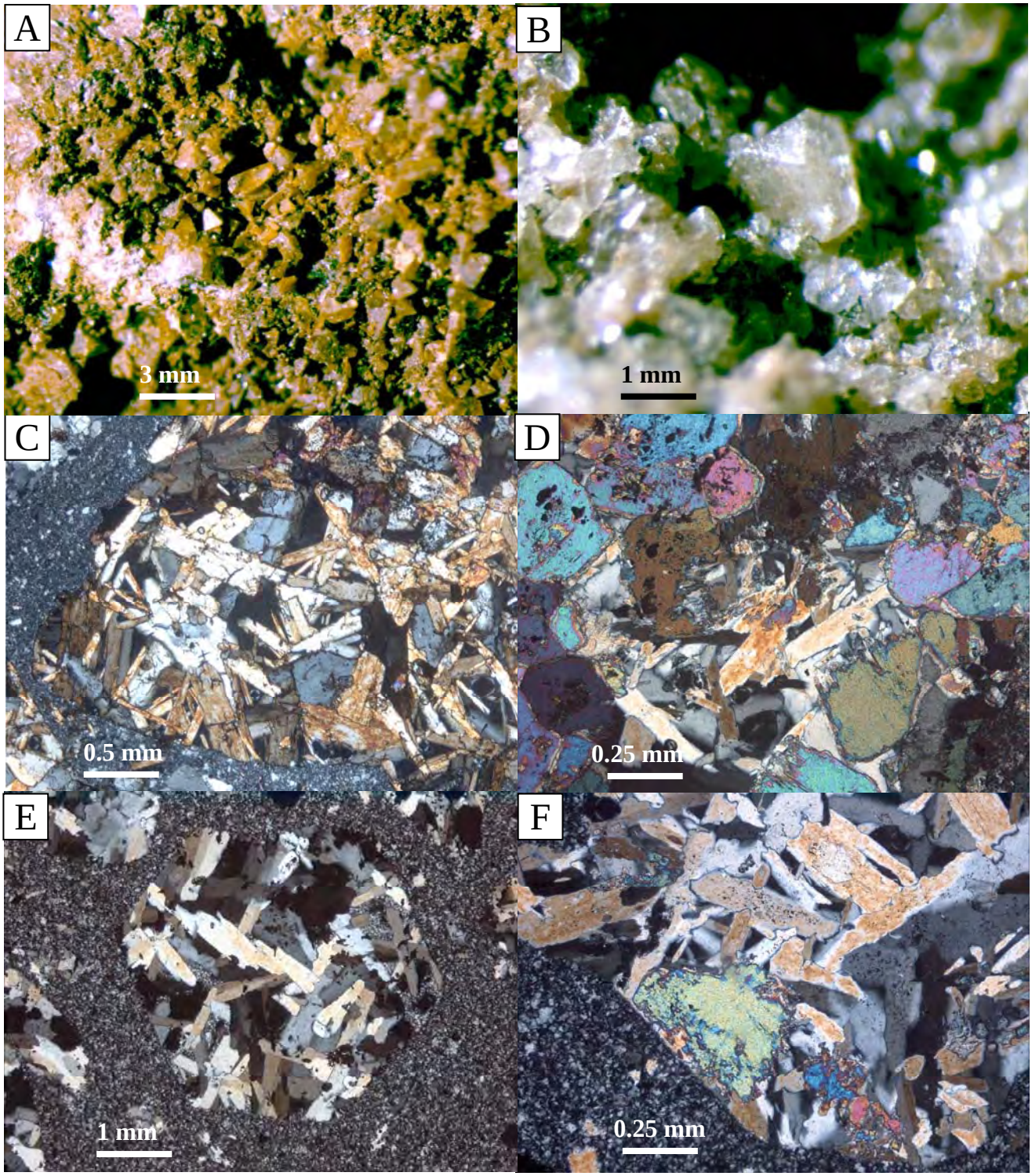

Fig. 8: *A) zunyite ($Al_{13}Si_5O_2$ (OH, F)$_{18}$Cl) occurring in oxidized veins with advanced argilllic alteration mineral assemblage. CPR 384, Venencocha area. B) Transparent zunyite crystal in an oxidized vein in the Venencocha area. CPR 384. C) Pervasive advanced argillic alteration next to a massive oxidized vein, with alunite and quartz replacing a tuff. CPR 361, Venencocha area. D) Enlargement of C) with diaspore coexisting with quartz and alunite. CPR 361. E) Advanced argillic altered dome with phenocryst of biotite leached and filled with quartz and alunite. Matrix of porphyric rock is mainly composed of quartz. CPR 347, Venencocha area. F) Enlargement of E) showing that diaspore is also present in the advanced argillic alteration (CPR 347).*

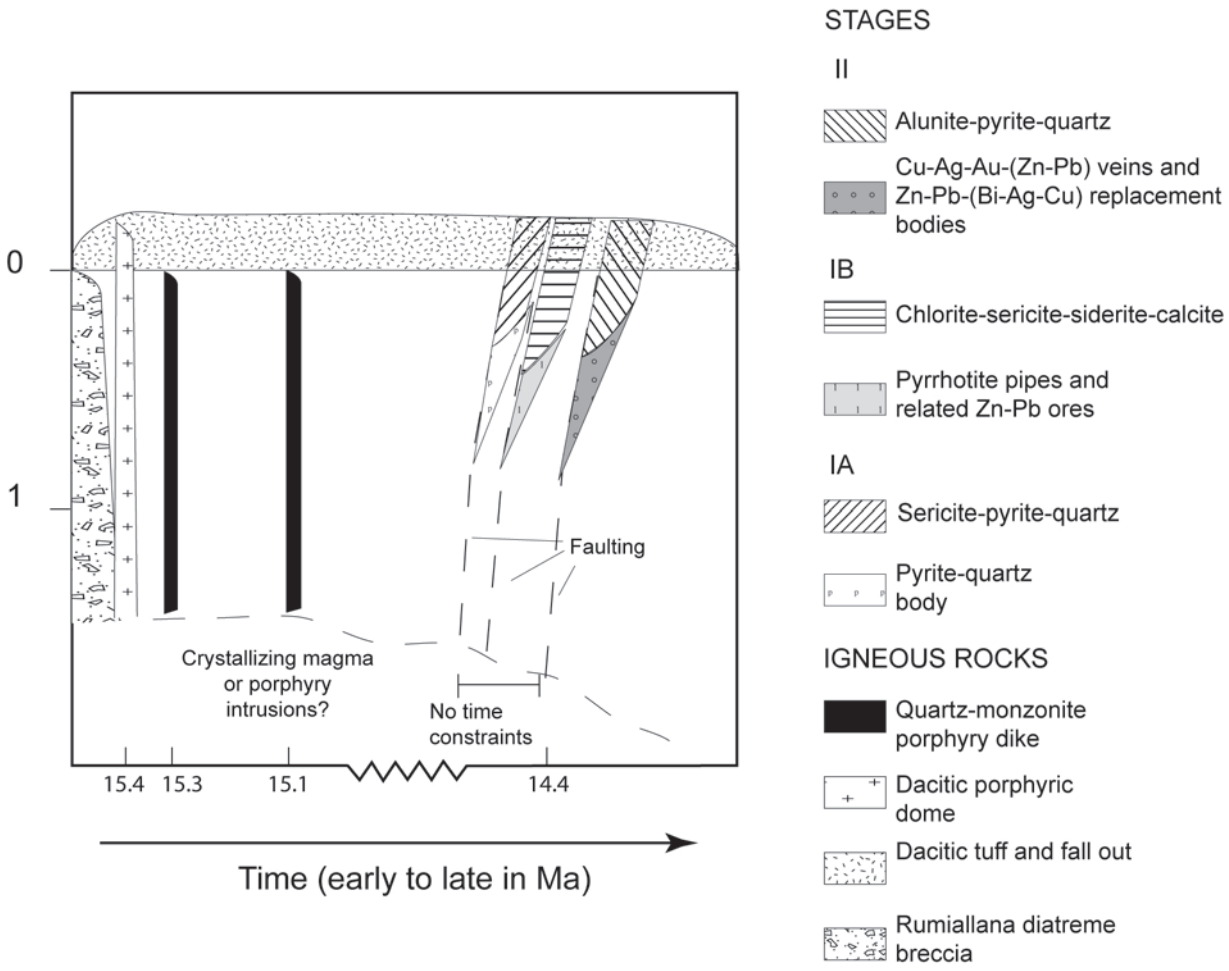

Fig. 9: *Time-space diagram for the magmatic-hydrothermal system of Cerro de Pasco.*

as a minimum age for the emplacement of the stock.

Analytical techniques

Major and trace elements of selected volcanic and intrusive rocks from Cerro de Pasco were determined by XRF at the University of Lausanne, Switzerland. Rare-earth elements were analyzed at the Ecole Polytechnique Fédérale, Lausanne, Switzerland, using a Perkin-Elmer Plasma 2000 ICP-AES

Zircons were prepared by standard mineral separation and purification methods (crushing and milling; concentration via Wilfley Table or hand washing; magnetic separation; heavy liquids). A selection of least-magnetic zircon crystals from each sample was mounted in epoxy resin and imaged by cathodoluminescence to control whether the population contains inherited cores.

In order to minimize the effects of secondary lead loss, the "CA (chemical abrasion) - TIMS" technique was employed involving high-temperature annealing followed by a HF leaching step (Mattinson, 2005). Annealing was performed by loading 20-40 zircon grains of each sample in quartz crucibles and placing them into a furnace at 880°C for approximately 60 hours. Subsequently, zircon from each sample was transferred in 3ml screw-top Savillex vials together with ca. 120 µl concentrated HF for the leaching (chemical abrasion) step. Savillex vials were arranged into a Teflon par vessel with 2 ml concentrated HF, and placed in an oven at 180°C for 12-15 hours. After the partial dissolution step the leachate was completely pipetted out and the remaining zircon were fluxed for several hours in 6N HCl on a hotplate at ~80°C, rinsed in ultrapure H_2O and then placed back onto the hot plate for an additional 30 minutes 4N HNO_3 "clean-up" step. The acid solution was removed and the fractions were again rinsed several times in ultra-pure water and acetone in an ultrasonic bath. Single zircon (or rarely 2 zircons) were selected, weighed and loaded for dissolution into precleaned miniaturized Teflon vessels. After adding a mixed ^{205}Pb-^{235}U spike, the zircon samples were dissolved in 63 µl concentrated HF with a trace of 7N HNO_3 at 180°C for 6 days, evaporated and redissolved overnight in 36 µl 3N HCl at 180°C. Pb and U were separated by anion exchange chromatography (Krogh, 1973) in 40 µl micro-columns, using minimal amounts of ultra-pure HCl, and finally dried down with 3 µl 0.2N or 0.06N H_3PO_4.

The majority of U-Pb isotopic analyses were performed at ETH Zurich using a Finnigan MAT 262 mass

spectrometer equipped with an ETP electron multiplier backed by a digital ion counting system. The multiplier was calibrated by repeated analyses of the NBS 982 standard using the $^{208}Pb/^{206}Pb$ ratio of 1.00016 for mass bias correction (Todt et al., 1996), and the U500 standard, in order to correct for the 0.3% multiplier inherent logarithmic rate effect (Richter et al., 2001). Some of the isotopic analyses were performed at the University of Geneva (Switzerland) on a THERMO ELECTRON TRITON mass spectrometer equipped with a linear MasCom electron multiplier, showing no second-order non-linearity. Mass fractionation effects were corrected for 0.09±0.05 per a.m.u. for the MAT 262 and 0.12±0.05 per a.m.u. for the TRITON. Both lead and uranium were loaded with 1 μl of silica gel-phosphoric acid mixture (Gerstenberger and Haase, 1997) on outgassed single Re-filaments, and isotope ratios determined by sequential measurement of all ion beams on the electron multiplier. Total procedural common Pb concentrations were measured at values between 0.4 and 7 pg (two extreme values of 11 and 43 pg, respectively) and were attributed solely to laboratory contamination. Based on the average values for 13 blank determinations in the Geneva laboratory 2004–2005, the common lead contribution was corrected for using the following Pb isotopic composition: $^{206}Pb/^{204}Pb$: 18.5±0.6% (1σ), $^{207}Pb/^{204}Pb$: 15.5±0.5% (1σ), $^{208}Pb/^{204}Pb$: 37.9±0.5% (1σ), The uncertainties of the spike and blank lead isotopic composition, mass fractionation correction, and tracer calibration were taken into account and propagated to the final uncertainties of isotopic ratios and ages. The ROMAGE program was used for age calculation and error propagation (Davis, unpublished). The international R33 standard zircon (Black et al., 2004) has been dated at an age of 419.3 ± 0.3 Ma (2 σ) for 18 repeated determinations on both MAT 262 (ETHZ) and Triton (Univ. of Geneva) mass spectrometers. Calculation of concordant ages and averages was done with the Isoplot/Ex v.3 program of Ludwig (1999). Ellipses depicted in concordia diagrams represent 2 sigma uncertainties. Averages at 95% confidence level.

The Hf fraction was isolated using Eichrom Ln-spec resin, and measured in static mode on a NuPlasma multicollector ICP-MS using an Aridus nebulizer for sample introduction at ETH Zürich. Zircons are commonly characterized by extremely low $^{176}Lu/^{177}Hf$ of less than 0.005. Hf isotopic values were corrected for *in-situ* radiogenic ingrowth from ^{176}Lu, but remained within the analytical uncertainty of the measured $^{176}Hf/^{177}Hf$ ratios. The Hf isotopic ratios were corrected for mass fractionation using a $^{179}Hf/^{177}Hf$ value of 0.7325 and normalized to $^{176}Hf/^{177}Hf = 0.28216$ of the JMC-475 standard; isotopic ratios for CHUR are according to Blichert-Toft and Albarède (1997).

A total of 17 samples were prepared for $^{40}Ar/^{39}Ar$ analysis. Samples containing sericite and biotite were crushed and sieved, followed by careful handpicking under a binocular microscope to obtain high-quality separates. Alunite samples were directly extracted from cavities and handpicked under the binocular. All samples were ultrasonically cleaned for 5 - 15 min. in demineralized water. Final samples amounts attained ca. 0.1 to 18.9 mg of alunite (100 μm and 2 mm in size), 6.5 to 7.5 mg of biotite (400 μm and 1.2 mm in size), and 6 to 15.9 mg of sericite (100-400 μm in size).

The irradiation of mineral separates for $^{40}Ar/^{39}Ar$ analysis was carried out in two batches in the Triga reactor at Oregon State University (OSU), USA. All minerals were irradiated for 15 hours in the 1 MW, Cd-lined CLICIT facility at OSU and J values were calculated via the irradiation of fish canyon tuff sanidines (28.02 ± 0.16 Ma, Renne et al., 1998), which were separated by distances of <1 cm, throughout the columnar irradiation package.

The majority of step-wise IR-CO_2 laser $^{40}Ar/^{39}Ar$ analyses were performed at the Lund University, Sweden, using a Micromass 5400 mass spectrometer, equipped with a faraday and an electron multiplier. The stainless steel extraction line includes two SAES C50-ST101 Zr-Al getters.

Some of the isotopic analyses were carried out at the University of Geneva, Switzerland, using an Argus (GV Instruments), multi-collector mass spectrometer, equipped with four high-gain (10E12 ohms) faraday collectors for the analysis of ^{39}Ar, ^{38}Ar, ^{37}Ar and ^{36}Ar, as well as a single faraday collector (10E11 ohms) for the analysis of ^{40}Ar. At Geneva, the automated, UHV stainless steel gas extraction line incorporates one SAES AP10 getter, and one SAES GP50-ST707 getter. In both Lund and Geneva labs, the extracted gas from alunite grains was cooled to ~-150°C by a Polycold P100 cryogenic refrigeration unit mounted over a cold finger. Single grains of alunite, biotite, and sericite were step-heated using a defocused 50W CO_2 laser (30W, MIR10 IR (CO_2) at the Geneva University laboratory) rastered over the samples to provide even-heating of the grains. Samples were measured on the electron multiplier and time-zero regressions were fitted to data collected from ten cycles (twelve in the Geneva laboratory) over the m/e range 40-36. Peak heights and backgrounds were corrected for mass discrimination, isotopic decay of ^{39}Ar and ^{37}Ar and interfering nucleogenic Ca-, K- and Cl-derived isotopes. The high stability of the faraday baseline measurements renders it unnecessary to record baselines during each analysis. Error calculations include the errors on mass discrimination measurement, and the J value. ^{40}Ar, ^{39}Ar, ^{38}Ar, ^{37}Ar and ^{36}Ar blanks were calculated before every new sample and after every three heating steps.

For samples measured in the Lund Laboratory (Sweden), ^{40}Ar blanks were between 4.0 and 2.0E-16 moles. Blank values for m/e 39 to 36 were all less than 7E-18 moles. Age plateaus were determined using the criteria of Dalrymple and Lamphere (1971), which specify the presence of at least three contiguous incremental heating steps with concordant ages, that constitute >50% of the total ^{39}Ar released during the step-heating experiment. The entire analytical process is automated and utilizes the

Mass Spec software modified specifically for this laboratory and originally developed at the Berkeley Geochronology Center by Al Deino.

For samples measured in the Geneva laboratory, ^{40}Ar blanks were between 6.5E-16 and 1.0E-15 moles. Blank values for m/e 39 to 36 were all less than 6.5E-17 moles. Age plateaus were determined using the criteria of Dalrymple and Lamphere (1971). The automated analytical process uses the software ArArCalc (Koppers, 2002).

Rb-Sr and Pb isotope analysis of sericite samples CPR 3, CPR 21, CPR 498, and CPR 499 involved a leaching step using weak HCl to remove possible contaminants from the surface and easily exchangable sites of the sheet silicates that may disturb their Rb-Sr system (e.g. Schneider et al., 2003). Separate isotope analyses were performed on both leached residues (R) and corresponding leachates (L) of the sericite samples. For the leaching experiments, purified 1 N HCl (1 ml) was used. Each sample was weighed and leached on a hot plate (80°C) for 15 min. Residues and leachates were separated by repeated centrifugation and rinsing with ultrapure water until neutral reaction of the supernate. Only the first 1 N HCl leachate was used for Rb-Sr analysis, all water washes were discarded. The sample splits were dried and the dry residues weighed again and completely dissolved in a 3:1 mixture of 22 N HF and 14 N HNO_3. Two pyrite separates carefully handpicked from samples CPR 3 and CPR 499 were repeatedly washed with clean ethanol and ultrapure water and subsequently weighed and dissolved in 14 N HNO_3 without further chemical pretreatment. All solutions were totally spiked with a highly enriched, mixed ^{87}Rb-^{84}Sr tracer that allows for determination of Sr concentrations by isotopic dilution and $^{87}Sr/^{86}Sr$ ratios from one mass-spectrometric run. They were then dried at 110°C and subsequently rewetted with 3 N HNO_3. Rubidium, strontium and lead were chemically separated with 3 N HNO_3 using EICHROM Sr resin on 50 µl Teflon columns, following the methods of Horwitz et al. (1991a; 1991b). The first 600 µl of HNO_3 wash were collected and used for measurement of Rb. Sr was stripped from the columns with 1 ml of H_2O. Subsequently, Pb was eluted from the same column with 1 ml of HCl 6 N. The Pb cut was further processed through a 50 µl column containing precleaned EICHROM Pre Filter Resin.

For mass spectrometry, Sr was loaded with $TaCl_5$-HF-H_3PO_4 solution (Birck, 1986) onto W single filaments. Rb was loaded with DDW onto the evaporation ribbon of a Ta double-filament assemblage and Pb loaded onto single Re filaments using silica gel-H_3PO_4 bedding. All isotopic measurements were performed on a FINNIGAN MAT 262 solid-source mass spectrometer running in static multicollection mode at ETHZ. Sr isotopic ratios were normalized to $^{88}Sr/^{86}Sr$ = 0.1194. Repeated static measurements of the NBS 987 standard over the duration of this study yielded an average $^{87}Sr/^{86}Sr$ ratio of 0.71025 ± 4 (2σ mean, n = 22). Pb isotopic ratios were corrected for mass fractionation using a mean discrimination factor of 0.085 ± 0.006 (2σ) %/[amu], based on replicate measurements of the NBS SRM 981 common lead (n=31) standard. Errors and error correlations were calculated after Ludwig (1980). Individual uncertainties (2σ) are given for Pb isotope ratios and Rb-Sr elemental concentrations and isotope ratios (Table 1). Samples containing less than 10 ppm Sr were corrected for maximum total procedure blanks (n=6) of 30 pg Sr, for all other samples the blank values were found to be negligible (< 0.5 wt-% of the analyzed sample Pb, Rb and Sr amounts).

Model isochron regressions of Rb-Sr data were calculated after Ludwig (2001) using the ISOPLOT/Ex version 2.49 program, palaeomixing line regressions were performed after Schneider et al. (2003). All regressions are based on individual analytical errors. The goodness of fit has been tested by means of the MSWD parameter, according to Wendt and Carl (1991). The decay constant used for the age calculations was $\lambda^{87}Rb = 1.42 \times 10^{-11}\ a^{-1}$ (Steiger and Jäger, 1977) and errors on the model ages are quoted at the 2σ level.

Petrology and geochemistry of the magmatic rocks

The accretionary lapilli tuffs occurring in the northwestern part of the diatreme-dome complex show lapilli particles size varying from ca. 0.2 to 0.5 cm in diameter and are composed of a core of coarse-grained ash surrounded by a fine-grained rim; the change of grain size between the core and the rim is abrupt (Fig. 3D). They are classified as *rim-type* accretionary lapilli after the nomenclature of Schumacher and Schmincke (1995).

Dacitic porphyritic domes show medium grain-sized phenocryst of plagioclase (0.2 - 0.5 cm), biotite, resorbed quartz, and amphibole (Fig. 10B). Biotite is much more abundant than amphibole, which can be locally absent. The fine-grained groundmass is composed of the same minerals as the phenocrysts, with zircon and apatite as common accessories. Within altered domes, plagioclase is replaced by calcite and sericite, while amphibole and biotite are replaced by rutile and chlorite (Fig. 3F).

Porphyritic dykes intruding the diatreme and the Pucará carbonate rocks are light grey, medium to fine grained and carry phenocrysts of sanidine up to 6 cm long, resorbed quartz (up to 5 mm in size), plagioclase (1 to 2 mm), biotite (2 mm) and scarce amphibole (Fig. 3H, 10A and C). Biotite is the major ferromagnesian mineral and is characterized by abundant inclusions of rutile and apatite. Remnants of amphibole are occasionally found within irregular patches of biotite. Sphene occurs in wedge-shaped crystals and apatite is common as euhedral grains up to 1 mm long. Zircon grains are small (up to 400 µm) and elongated. There is little variation in texture or grain size within the intrusive dykes. In the central portions they carry abundant xenoliths (Lacy, 1949).

Porphyritic albitized dykes vary in color from beige to green and the texture is porphyritic with phe-

Table 1. Rb-Sr and Pb isotope analyses of sericite and pyrite samples from Cerro de Pasco (R: HCl-treated sericite, L: corresponding HCl leachates, P: pyrite)

Sample		Sample wt. [mg]*	Rb [ppm] ± 2s	Sr [ppm] ± 2s	$^{87}Rb/^{86}Sr$ ± 2s	$^{87}Sr/^{86}Sr$ ± 2s	$^{206}Pb/^{204}Pb$ ± 2s	$^{207}Pb/^{204}Pb$ ± 2s	$^{208}Pb/^{204}Pb$ ± 2s
Cerro de Pasco district									
CPR 3	R	3.6	685.1 ± 8.2	6.846 ± 0.066	290.90 ± 2.7	0.75561 ± 0.00003	18.922 ± 0.004	15.660 ± 0.004	38.958 ± 0.012
	L	3.1	-	-	12.16 ± 0.08	0.70828 ± 0.00002	18.765 ± 0.003	15.655 ± 0.004	38.868 ± 0.011
	P	6.9	0.230 ± 0.003	0.280 ± 0.003	2.38 ± 0.02	0.70712 ± 0.00004	18.781 ± 0.002	15.658 ± 0.003	38.888 ± 0.010
CPR 21	R	3.8	559.4 ± 6.2	781.8 ± 6.6	2.07 ± 0.03	0.70781 ± 0.00001	18.813 ± 0.009	15.633 ± 0.009	38.813 ± 0.013
	L	3.6	-	-	19.05 ± 0.21	0.71088 ± 0.00002	18.746 ± 0.007	15.642 ± 0.007	38.800 ± 0.018
CPR 498	R	2.9	820.2 ± 7.5	14.25 ± 0.14	166.8 ± 1.5	0.72547 ± 0.00001	18.854 ± 0.004	15.630 ± 0.004	38.862 ± 0.011
	L	2.4	-	-	2.30 ± 0.01	0.70682 ± 0.00001	18.849 ± 0.006	15.646 ± 0.007	38.854 ± 0.017
CPR 499	R	1.4	448.4 ± 4.6	8.27 ± 0.07	157.38 ± 0.99	0.73770 ± 0.00004	18.850 ± 0.003	15.646 ± 0.004	38.854 ± 0.011
	L	1.3	-	-	3.61 ± 0.02	0.70701 ± 0.00002	18.767 ± 0.003	15.639 ± 0.003	38.813 ± 0.010
	P	10.8	0.289 ± 0.003	0.296 ± 0.003	2.83 ± 0.02	0.70711 ± 0.00001	18.761 ± 0.002	15.629 ± 0.003	38.789 ± 0.010
Colquijirca District									
PBR 179	G						18.728	15.638	38.761
PBR 162	G						18.731	15.644	38.776
PBR 126	G						18.715	15.640	38.759
PBR 116	G						18.719	15.643	38.748
PBR 108	G						18.697	15.621	38.672
Excelsior phyllite									
PBR 206L	L						18.775	15.655	39.158
PBR 206R	R						20.276	15.760	39.753
Mitu Group sandstone and siltstone									
PBR 155R	R						19.965	15.711	39.315
PBR 180L	L						18.575	15.673	38.736
PBR 180R	R						20.077	15.769	39.424
Dacite W Marcapunta and Huacchuacaja									
PBR 215L	L						18.685	15.644	38.741
PBR 215R	R						18.702	15.613	38.649
PBR 216R	R						18.703	15.612	38.639

* weights given for L and R correspond to dry sample weights prior to and after leaching, respectively
Abbreviations are: G: galena; L: leach P: pyrite; R: residue;
Pb isotopic compositions of PBR samples are from Fontboté and Bendezú (2001)

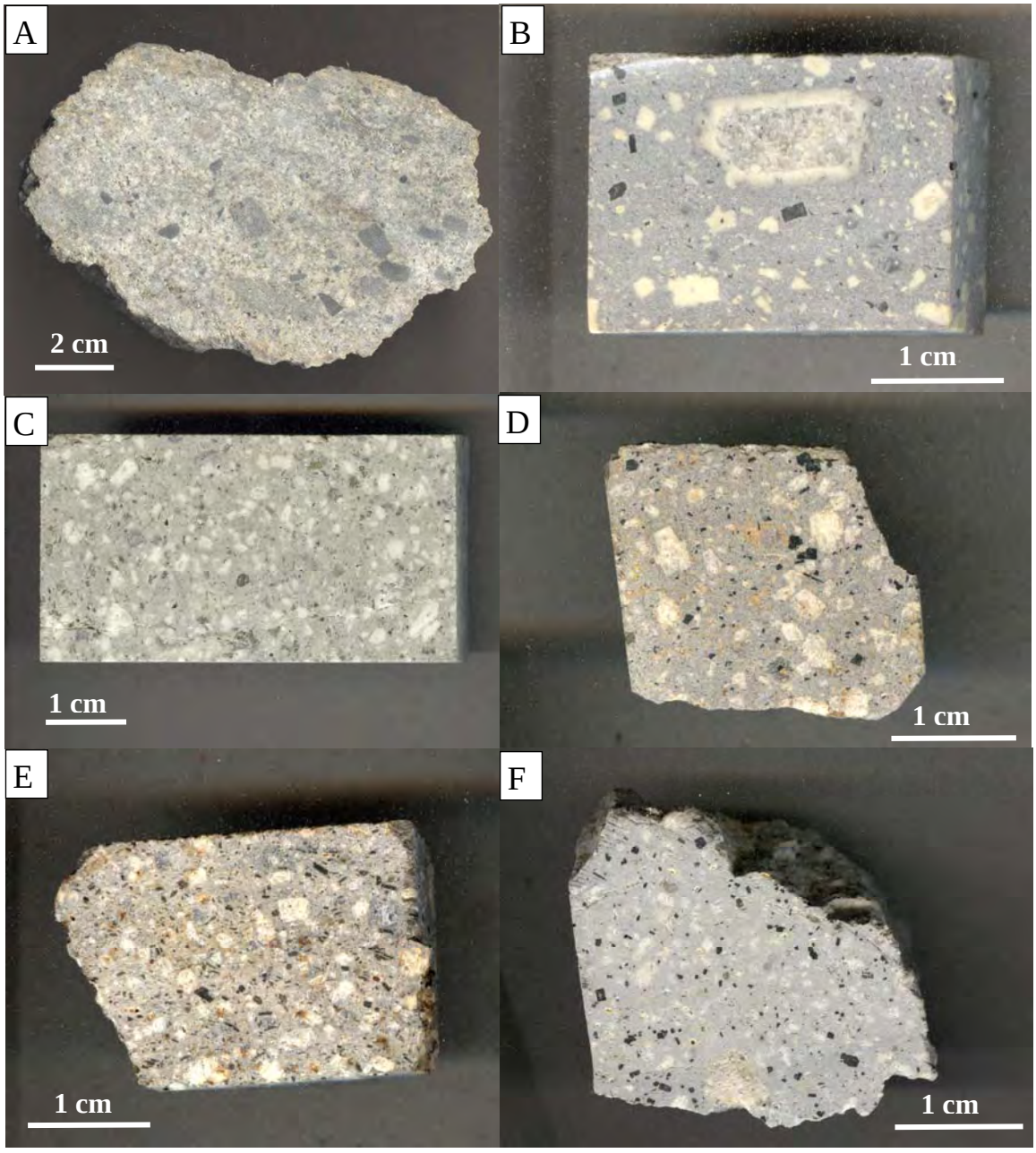

Fig. 10: *Photographs of igneous rocks. A) Quartz-monzonite porphyry showing phenocrysts of plagioclase altered to calcite (CPR 472). B) Dacite from a dome in the southwestern part of Venencocha showing propyllitic alteration (CPR 603). C) Quartz-monzonite porphyry dyke within the diatreme-dome complex with phenocrysts of biotite and plagioclase (CPR 604). D) Porphyritic granodiorite from Yanamate (CPR 605). E) Sample for the dacitic dome at Huacchuacaja in the Colquijirca district (CPR 606).*

nocrysts of orthoclase and blocky plagioclase (Fig. 5B). Quartz and biotite are less abundant than in the quartz-monzonite porphyry. The groundmass is composed of quartz, orthoclase, albite and chlorite and generally shows flow textures. Book biotite is frequently chloritized or altered to muscovite. In transversal section, the book biotite often shows expanded accordion-like textures with interbanded calcite (Fig. 5C).

Major and trace element results for selected representative samples of magmatic rocks (accretionary lapilli, dacitic porphyritic domes, quartz-monzonite porphyry dykes) from Cerro de Pasco are presented in Table 2. Due to important hydrothermal circulation in the diatreme-dome complex and in the mine area, most of the rocks are altered. Only rocks showing weak alteration (generally propyllitic) were selected. Furthermore, only samples with LOI lower than 5 percent have been taken into account. Figure 11A shows the total alkali versus silica (TAS) diagram after Le Bas et al. (1986) and Figure 11B shows the Zr/TiO2 versus Nb/Y and SiO2 versus Zr/TiO2 ratios diagrams (cf. Winchester and Floyd, 1977). In the total alkali versus silica TAS diagram after Le Bas et al. (1986) the volcanic rocks plot in the dacite field whereas one intrusive rock plots

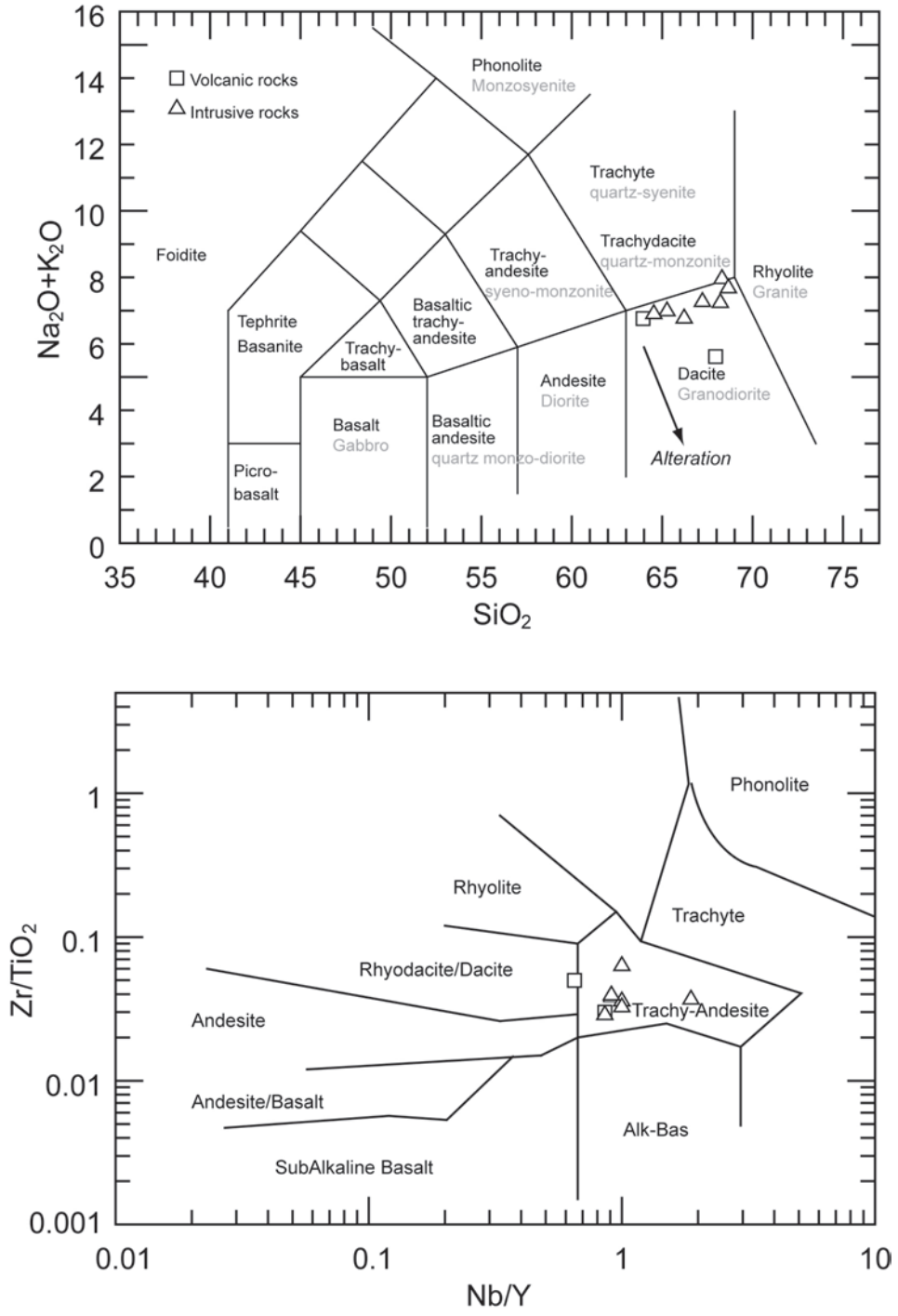

Fig. 11: *A) Total alkali versus silica (TAS) diagram after Le Bas et al. (1986) and B) shows the Zr/TiO_2 versus Nb/Y and SiO_2 versus Zr/TiO2 ratios diagrams (cf. Winchester and Floyd, 1977).*

at the limit of the quartz-monzonite and granodiorite field and the a second intrusive rock is depleted in total alkali due to hydrothemal alteration. In the Zr/TiO2 versus Nb/Y diagram (cf. Winchester and Floyd, 1977), Figure 11B, most of the samples lie in the trachy-andesite field, which could suggest that the analyzed samples are enriched in incompatible elements, probably due to alteration.

Trace element abundances show high Sr contents (350 - 1260 ppm) and Sr/Y ratios (20 to 100). Cr (9 - 44 ppm), Ni (3 - 22 ppm), and Nb (8 - 15 ppm) contents are relatively low. REE patterns normalized to chondrite (Nakamura, Potts et al., 1981) are characterized by a strong fractionation, with LREE enrichment and HREE depletion (Fig. 12), low Yb (0.5 - 1.17 ppm), and high La_N/Yb_N (20 - 60). Kay (1978) introduced the term *adakite* for magmatic and volcanic rocks characterized by $SiO_2 \geq 56$ wt-%, $Al_2O_3 \geq 15$ wt-% (rarely lower), MgO < 3 wt-%, strongly fractionated REE with the HREE depleted (Yb < 1.8 ppm, Y < 18 ppm) and LREE enriched

Table 2: Representative major and trace element abundances in the Cerro de Pasco rocks. QM, quartz-monzonite; QMP, quartz-monzonite porphyry; D, dacite; DP, dacite porphyry

Sample	CPR 472 QMP	CPR 602 D	CPR 603 DP	CPR 604 QMP	CPR 372 QMP	CPR 392 QMP	CPR 344 QM	CPR 388 QMP	CPR 389 QMP
SiO_2	65.30	64.43	64.89	64.06	60.63	62.27	67.24	62.49	65.51
TiO_2	0.64	0.72	0.76	0.79	0.98	0.85	0.70	0.92	0.72
Al_2O_3	14.87	15.75	15.25	15.47	15.46	15.64	16.16	15.68	15.30
Fe_2O_3	2.80	5.24	3.35	3.87	4.37	4.15	3.62	4.35	3.14
MnO	0.13	0.10	0.07	0.06	0.07	0.13	0.03	0.07	0.06
MgO	1.07	1.21	1.67	1.81	1.87	1.81	0.66	1.78	1.08
CaO	2.87	1.72	3.16	3.79	4.56	3.41	1.64	4.38	2.92
Na_2O	0.71	2.21	4.00	3.44	4.05	3.29	3.58	3.83	3.41
K_2O	6.93	3.16	3.05	3.15	2.39	3.41	3.98	2.89	3.57
P_2O_5	0.27	0.27	0.34	0.31	0.45	0.42	0.32	0.44	0.32
LOI[a]	4.21	4.88	3.70	3.77	5.05	4.06	1.76	2.35	3.43
Total	99.69	99.69	100.23	100.51	99.87	99.46	99.69	99.18	99.46
Mg#[b]	27.65	18.73	33.21	31.86	29.98	30.39	15.37	28.98	25.63
Ba	934	603	990	741	909	2283	576	3362	883
Rb	466	150	96	110	67	92	129	77	109
Sr	89	342	944	650	1260	1175	569	1491	1088
Y	8	20	11	12	14	13	8	14	11
Cr	14	23	17	17	13	9	9	14	13
Ni	6	12	7	9	6	5	3	7	3
Nb	8	13	10	12	12	13	15	12	10
Zr	241	215	173	169	176	165	154	158	169
Hf	7	8	7	5	7	8	7	8	8
La	41.80	47.87	50.69	60.78	51.30	43.80	30.80	41.80	49.40
Ce	93.00	95.09	101.97	101.37	115.00	98.80	67.50	102.50	102.50
Pr	10.30	11.01	11.66	10.81	13.20	11.80	7.70	11.80	11.30
Nd	43.20	42.26	45.07	40.64	55.60	47.30	29.90	51.30	46.00
Sm	7.50	6.69	5.56	6.88	9.80	8.50	5.40	9.50	8.00
Eu	1.57	1.64	1.33	1.31	2.02	1.88	1.25	1.95	1.72
Gd	2.80	3.72	4.92	3.40	3.80	3.60	2.20	4.00	3.20
Tb	n.d	0.62	0.41	0.40	n.d	n.d	n.d	n.d	n.d
Dy	1.70	3.33	2.53	2.36	2.10	2.10	1.50	2.30	2.00
Ho	0.34	0.64	0.20	0.42	0.43	0.36	0.35	0.44	0.37
Er	0.80	2.27	0.89	1.07	1.00	0.80	0.80	0.90	0.90
Tm	0.10	0.31	0.22	0.23	0.15	0.10	0.12	0.13	0.12
Yb	0.50	1.97	0.90	1.65	0.60	0.50	0.50	0.60	0.60
Lu	0.07	0.26	0.18	0.15	0.08	0.06	0.06	0.08	0.09
Th	12	4	9	9	6	6	11	8	11
Pb	17	19	17	20	12	15	179	49	27
Ga	23	23	21	22	22	22	24	21	23
Zn	64	66	159	78	84	80	67	78	105
Cu	8	55	17	79	14	20	12	15	12
Co	21	11	8	10	31	55	6	11	8
V	51	101	76	91	108	82	71	89	70
S	165	2788	2508	163	1900	2051	87	635	743
Sc	3	9	9	9	10	7	5	10	7
As	10	29	10	<3<	4	7	7	5	28

[a]Loss On Ignition at 950°C
[b]$100*MgO/(MgO+Fe_2O_3)$
Abbreviations are: QMP = Quartz-monzonite porphyry, QM = Quartz-monzonite, DP = dacite porphyry, D = dacite

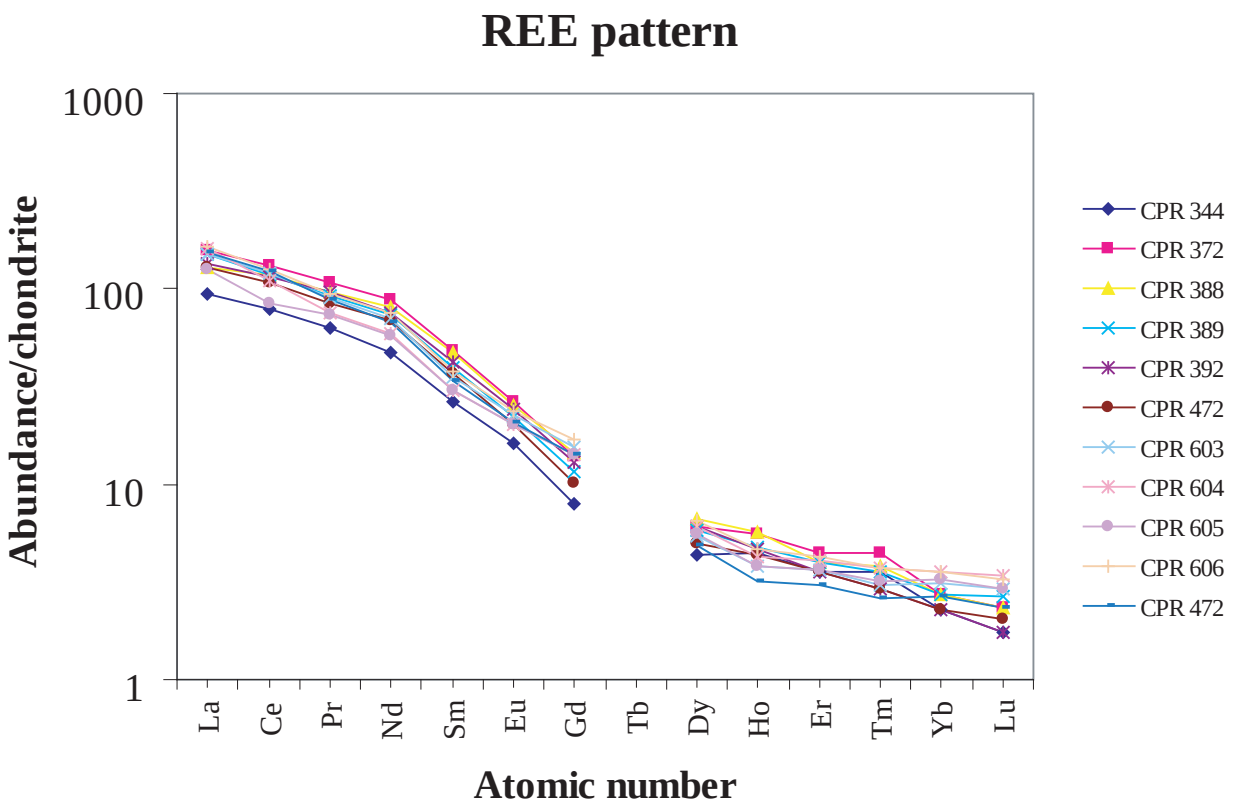

Fig. 12: *Chondrite-normalized REE diagram from domes and dykes at Cerro de Pasco. Normalizing factors after Nakamura (Potts et al., 1981).*

(Martin, 1999), and high Sr concentrations (rarely < 400 ppm, Defant and Drummond, 1990). In a Sr/Y vs. Y and a (La_N/Yb_N) vs. Yb_N discrimination diagram, both which are the most relevant for characterizing adakitic rocks (Reich et al., 2003), extrusive and intrusive rocks at Cerro de Pasco plot well in the adakite field of Martin (1999; Fig. 13). The possibility that the elevated Nb/Y ratio and the position of these rocks in the adakite field may be due to removal of Y and HREE during alteration cannot be discarded.

U-Pb geochronology results

Zircon U-Pb dating was carried out on magmatic rocks from the diatreme-dome complex at Cerro de Pasco, including the accretionary lapilli tuff, the dacitic dome, quartz-monzonite porphyritic dykes, and an albitized quartz-monzonite dyke. Additionally, zircon U-Pb dating in a dacitic dome at the Yanamate diatreme-dome complex (CPR 605, Fig. 10D) and in a dacitic dome in the Colquijirca district, at Huacchuacaja (CPR 606, Fig. 1 and 10E) has also been achieved. This latter dome has been previously dated by Bendezú et al. (2003) on biotite using $^{40}Ar/^{39}Ar$. Sample locations are given in Figure 2, except for the albitized quartz-monzonite sample which has been collected in the underground mine (level 1400, gallery 1484-E). Analyzed zircons are euhedral, up to 300 μm in size, slightly pink, and short and long prismatic. When observed under cathodoluminescence (Fig. 14), all zircons display oscillatory and sector zoning that is typically igneous (Hoskin and Schaltegger, 2003). All zircons except those from sample CPR 472 from a quartz-monzonite dyke contain magmatic sector zoning which often shows replacement by structureless high-luminescent zones. In a quartz-monzonite sample (CPR 604), replacement or recrystallization processes occur in the magmatic zones. Old inherited zircon cores have not been observed. Some grains are cracked or contain inclusions of apatite.

Table 3 gives all U-Pb results, Table 4 gives Hf isotopes results, and Concordia plots are reported in Figure 15. In Figure 16, εHf data are plotted versus the $^{206}Pb/^{238}U$ ages. Hafnium isotopes were analyzed from zircon of each sample except for CPR 606 and CPR 609).

Accretionary lapilli tuff (CPR 602)

One accretionary lapilli tuff sample has been collected on the northwestern part of the diatreme-dome complex (Fig. 2). Two U-Pb analyses of zircons (CPR-602/2 and CPR-602/10) yield older ages and are assumed to represent xenocrysts or contain inherited components (see Fig. 14B). The remaining six zircons analyses are concordant and yield a weighted mean $^{206}Pb/^{238}U$ age of 15.36 ± 0.03 Ma (MSWD = 0.76; Fig. 15B) is considered to be the crystallization age. Hf isotopic ratios were determined from two of the zircons and yielded initial eHf values between -1.1 and -1.5 (Table 4, Fig. 16).

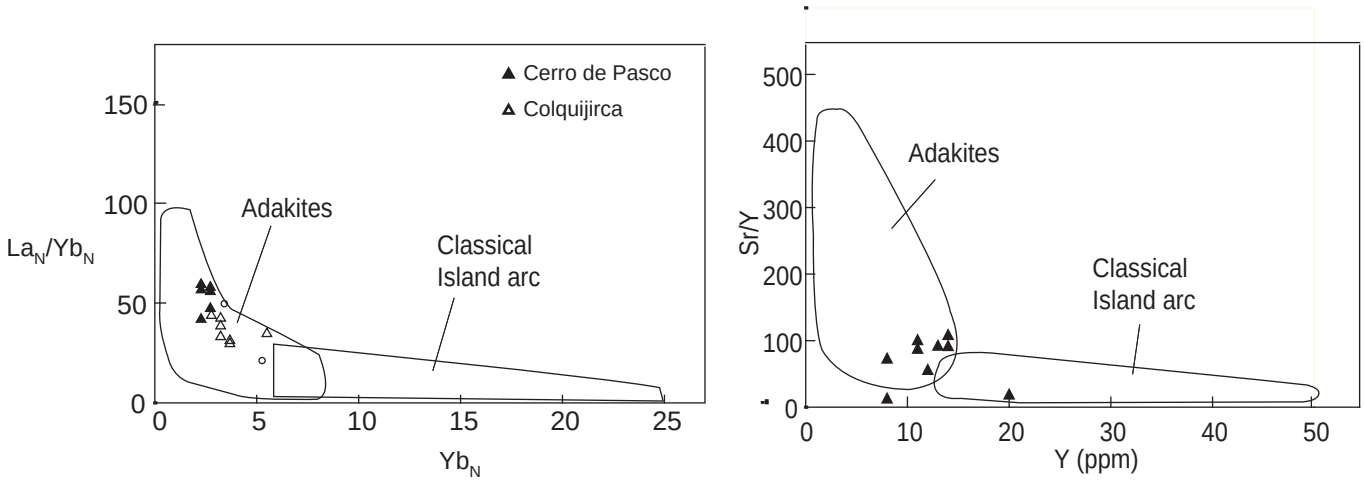

Fig. 13: *Sr/Y versus Y, and La_N/Yb_N versus Yb_N discrimination diagrams for domes and intrusions ar Cerro de Pasco. The adakitic and ADR (Andesite-Dacite-Rhyolite) fields were taken from Martin (1999)*

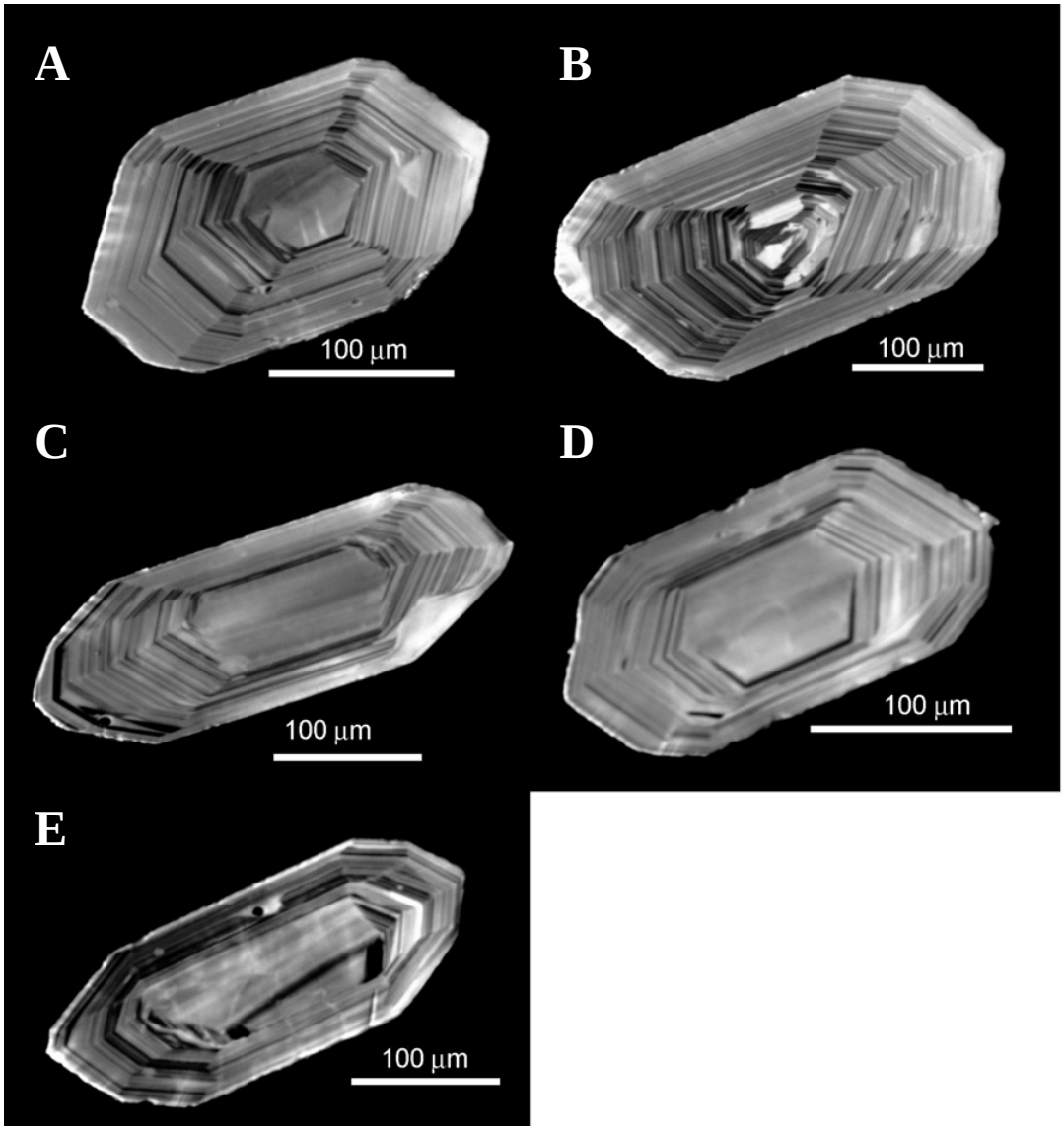

Fig. 14: *Cathodoluminescence photomicrographs of analyzed zircon A) from a quartz-monzonite porphyry dyke outside the diatreme (CPR 472), B) From an accretionary lapilli tuff (CPR 602) C) From a dacitic dome on the south western margin of the diatreme-dome complex (CPR 603), D) From a quartz-monzonite porphyry dyke in the diatreme (CPR 604),E) from a porphyritic dacite at Yanamate (CPR 605).*

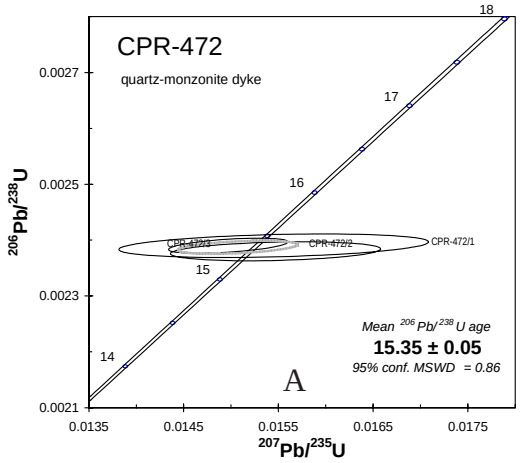
CPR-472
quartz-monzonite dyke
Mean 206Pb/238U age
15.35 ± 0.05
95% conf. MSWD = 0.86
A
CPR-472/1
CPR-472/2
CPR-472/3
206Pb/238U
207Pb/235U

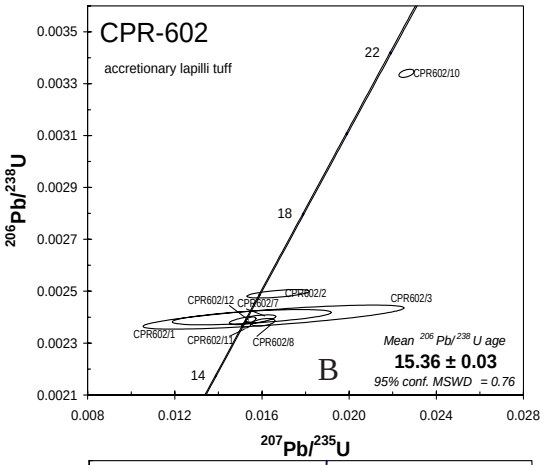
CPR-602
accretionary lapilli tuff
Mean 206Pb/238U age
15.36 ± 0.03
95% conf. MSWD = 0.76
B
CPR602/10
CPR602/1
CPR602/2
CPR602/3
CPR602/8
206Pb/238U
207Pb/235U

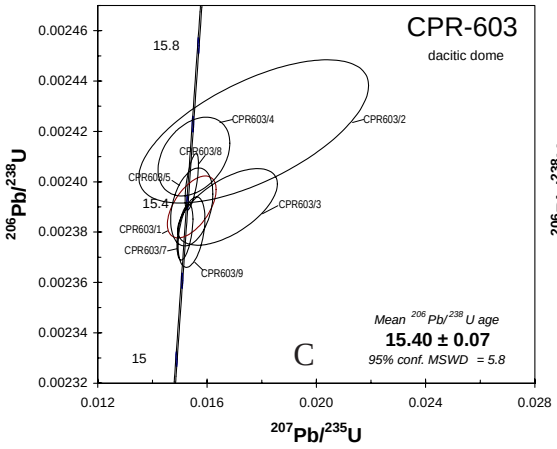
CPR-603
dacitic dome
Mean 206Pb/238U age
15.40 ± 0.07
95% conf. MSWD = 5.8
C
CPR603/1
CPR603/2
CPR603/3
CPR603/4
CPR603/5
CPR603/7
CPR603/8
CPR603/9
206Pb/238U
207Pb/235U

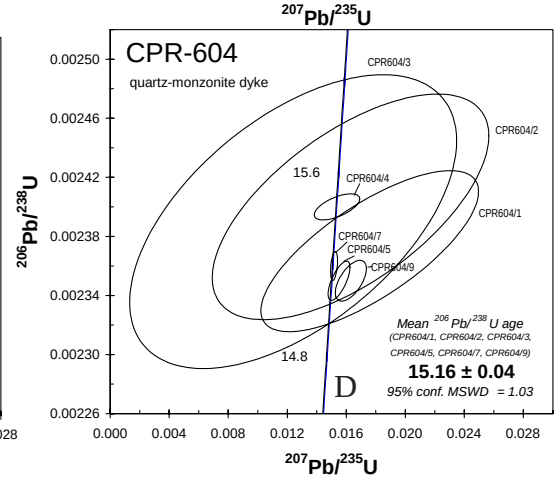
CPR-604
quartz-monzonite dyke
Mean 206Pb/238U age
(CPR604/1, CPR604/2, CPR604/3, CPR604/5, CPR604/7, CPR604/9)
15.16 ± 0.04
95% conf. MSWD = 1.03
D
CPR604/1
CPR604/2
CPR604/3
CPR604/4
CPR604/5
CPR604/7
CPR604/9
206Pb/238U
207Pb/235U

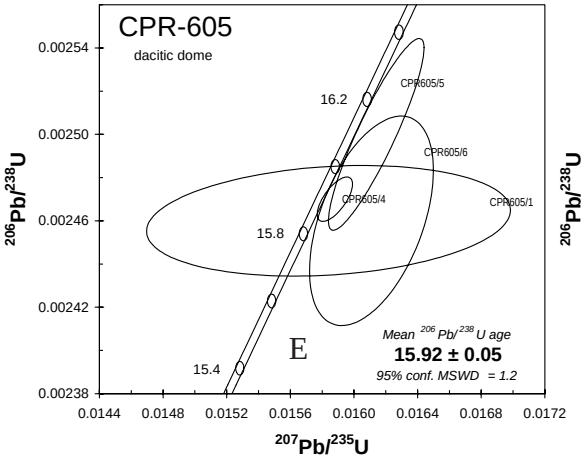
CPR-605
dacitic dome
Mean 206Pb/238U age
15.92 ± 0.05
95% conf. MSWD = 1.2
E
CPR605/1
CPR605/4
CPR605/5
CPR605/6
206Pb/238U
207Pb/235U

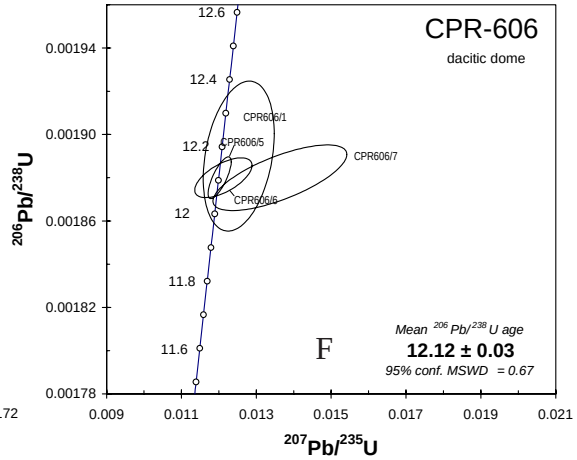
CPR-606
dacitic dome
Mean 206Pb/238U age
12.12 ± 0.03
95% conf. MSWD = 0.67
F
CPR606/1
CPR606/5
CPR606/6
CPR606/7
206Pb/238U
207Pb/235U

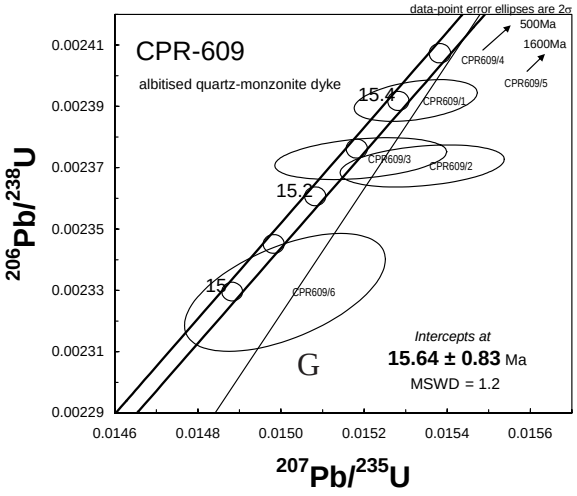
data-point error ellipses are 2σ
CPR-609
albitised quartz-monzonite dyke
500Ma
1600Ma
Intercepts at
15.64 ± 0.83 Ma
MSWD = 1.2
G
CPR609/1
CPR609/2
CPR609/3
CPR609/4
CPR609/5
CPR609/6
206Pb/238U
207Pb/235U

Dacitic dome (CPR 603)

A porphyritic dactic dome located at the western margin of the diatreme (Fig. 2) has been sampled. Eight analyzed zircons (sample CPR 603) show a large variation in $^{206}Pb/^{238}U$ age in excess of analytical variations. All analyses are concordant within the analytical errors and a weighted mean $^{206}Pb/^{238}U$ age of 15.40 ± 0.07 Ma (MSWD = 5.8; Fig. 15C) is regarded to be the best estimate for the crystallization age. Hf isotopic ratios were determined from two of the zircons and yielded initial εHf values between -2.8 and -3.9 (Table 4, Fig. 16).

Quartz-monzonite porphyritic dykes (CPR 472 and 604)

Two quartz-monzonite porphyritic dykes have been analyzed. The first sample (CPR 604) has been collected in the central part of the diatreme-dome complex (Table 5, Fig. 2) and shows propyllitic alteration (Table 2) while the second one (CPR 472) is hosted in carbonate rocks in the northern part of the open pit (Fig. 2) and is nearly unaltered. Three zircon grains from sample CPR 472 are concordant within analytical errors and give a weighted mean $^{206}Pb/^{238}U$ age of 15.35 ± 0.05 Ma (MSWD = 0.86, Fig. 15A. Hf isotopic ratios yield initial εHf values scattering between -1 and -3.4 (Table 4 and fig. 16).

Seven zircons from sample CPR 604 (Table 3) were analyzed and the data define two partly overlapping clusters in the concordia diagram (Fig. 15D). Three of the seven analyzed zircons (CPR-604/1; CPR-604/2; CPR-604/3) have a high analytical error due to the excess common lead in analysis. They are overlapping the remaining four analyses and thus are part of the upper and lower cluster. The upper cluster of four ellipses (CPR-604/1; CPR-604/2; CPR-604/3 and CPR-604/4) is concordant and gives a weighted mean $^{206}Pb/^{238}U$ age of 15.47 ± 0.04 Ma (MSWD = 0.66). The younger cluster is also concordant and six points (CPR-604/1; CPR-604/2; CPR-604/3; CPR-604/5; CPR-604/7 and CPR-604/9) define a weighted mean $^{206}Pb/^{238}U$ age of 15.16 ± 0.04 Ma (MSWD = 1.03; Fig. 15D). All seven analyses give a weighted mean $^{206}Pb/^{238}U$ age of 15.27 ± 0.15 Ma (MSWD = 20). Only one grain (CPR-604/7) with a small analytical error contributes to the upper cluster. This does not allow to conclude whether this is a result of inheritance of a slightly older lead component, or of protracted growth. Since the majority of data with small analytical errors belongs to the cluster giving younger ages, it is proposed that the weighted mean $^{206}Pb/^{238}U$ age of 15.16 ± 0.04 Ma may be considered as the minimum age of this quartz-monzonite porphyry dyke. Hf isotopic ratios were determined from three of the zircons and yielded initial εHf values between -0.3 and -2.4 (Table 4, Fig. 16).

Albitized quartz-monzonite dykes (CPR 609)

Four long prismatic and two short prismatic fractions were analyzed from this sample. The short-prismatic ones show inheritance of old lead component (CPR-609/4 and CPR-609/5). The remaining four long prismatic zircons have variable degree of lead loss, which is not eliminated by the applied technique. A single analysis (CPR-609/1) is close to the concordia curve at 15.40 Ma. Therefore, based on analyses CPR-609/1, CPR-609/2, CPR-609/3 and CPR-609/6 we calculate an upper intercept at 15.63 ± 0.83 Ma (MSWD = 1.2, Fig. 15G), and consider this result is regarded to be the best estimate for the age of these zircons.

Yanamate granodiorite porphyry stock (CPR 605)

At Yanamate, the granodioritic stock has been sampled (Fig. 1) and the four analyzed zircon (CPR 605) are concordant within analytical errors or subconcordant and yield a weighted mean $^{206}Pb/^{238}U$ age of 15.92 ± 0.05 Ma (MSWD = 1.2, Fig. 15E). The slight shift towards higher $^{207}Pb/^{235}U$ values is considered to be an analytical artifact due to unresolved molecular interferences on masses 204 and 207. This does not influence the $^{206}Pb/^{238}U$.

Huacchuacaja dacitic dome (CPR 605)

A dacitic dome, the same as the one dated by Bendezú et al. (2003), has been sampled and four zircons from sample CPR 606 yield data which are concordant within analytical error, defining a weighted mean $^{206}Pb/^{238}U$ age of 12.12 ± 0.03 Ma (MSWD = 0.67, Fig. 15F)

$^{40}Ar/^{39}Ar$ geochronology

Due to its high K contents (7-8%), biotite is generally suitable for $^{40}Ar/^{39}Ar$ geochronology. Nevertheless, biotite is highly susceptible to alteration to chlorite and even minor amounts of chlorite seems to have serious effects on biotite's argon systematics, generally due to ^{39}Ar recoil in low-retentivity chlorite (Lo and Onstott, 1989). Moreover, they demonstrated that this kind of

Fig. 15: *U-Pb Concordia diagrams: A) Zircon from an E-W quartz-monzonite porphyry dyke, B) zircon from an accretionary lapilli tuff inside the diatreme-dome complex, C) Zircon from a dacitic dome, D) Zircon from a quartz-monzonite porphyry dyke in the southwestern part of the diatreme-dome complex, E) Zircon from a porphyric dacite from the Yanamate, F) Dacitic dome from Huacchuacaja, Colquijirca district. G) Zircon from albitized quartz-monzonite dyke, the lower intercept is undistinguished from 0. Intercepts and 2σ uncertainties were calculated using a program by Ludwig (1999)*

Table 3: Results of U–Pb dating of zircon

No	description	weight	Concentration			Th/U[a]	Atomic ratios							Corelation	Ages		
		(mg)	U (ppm)	Pb (ppm)	Pb com. pg		206/204[b]	207/206[cd]	error 2σ (%)	207/235[c]	error 2σ (%)	206/238[cd]	error 2σ (%)	coeficient	206/238	207/235	207/206
CPR472																	
CPR-472/1	1 lpr	0.002	279	0.80	1.40	0.05	84	0.050	6.40	0.016	6.80	0.002	0.58	0.71	15.37	16.45	178.22
CPR-472/2	1 lpr	0.002	43	0.11	1.61	0.05	106	0.049	5.40	0.016	5.70	0.002	0.50	0.63	15.31	16.24	156.19
CPR-472/3	1 lpr	0.005	266	0.68	1.10	0.23	192	0.046	3.00	0.015	3.20	0.002	0.42	0.53	15.38	15.43	22.61
CPR602																	
CPR602/1	1 lpr	0.002	341	1.06	4.40	0.16	42	0.047	18.60	0.016	19.20	0.002	1.00	0.62	15.48	15.65	42.39
CPR602/2	1 lpr	0.002	667	1.81	2.71	0.05	84	0.049	6.70	0.017	7.00	0.002	0.53	0.59	16.11	16.85	124.10
CPR602/3	1 lpr	0.003	190	0.54	4.70	0.04	34	0.050	28.40	0.017	29.60	0.002	1.58	0.77	15.45	16.65	194.16
CPR602/7	1 spr	0.002	479	2.00	1.12	0.19	121	0.047	5.20	0.016	5.60	0.002	0.64	0.66	15.37	15.68	64.18
CPR602/8	1 spr	0.004	291	0.76	0.89	0.06	213	0.049	2.54	0.016	2.70	0.002	0.50	0.40	15.33	16.18	143.56
CPR602/10	2 lpr	0.003	437	1.66	0.61	0.11	516	0.049	1.14	0.023	1.26	0.003	0.38	0.45	21.50	22.72	153.45
CPR602/11	2 spr	0.007	360	0.92	0.51	0.23	745	0.046	1.08	0.015	1.12	0.002	0.41	0.28	15.35	15.39	22.97
CPR602/12	1 lpr	0.003	402	1.09	0.41	0.13	445	0.047	1.15	0.015	1.272	0.002	0.37	0.45	15.37	15.60	22.97
CPR603																	
CPR603/1	1 lpr	0.004	486	2.96	6.22	0.11	55	0.047	4.50	0.015	4.72	0.002	0.42	0.56	15.41	15.56	54.94
CPR603/2	1 lpr	0.004	118	0.44	3.35	0.05	38	0.053	18.80	0.018	19.40	0.002	0.96	0.64	15.57	17.83	334.05
CPR603/3	1 lpr	0.009	334	0.85	7.10	0.03	67	0.051	8.60	0.017	8.90	0.002	0.52	0.60	15.38	16.86	233.56
CPR603/4	1 lpr	0.002	322	0.89	0.70	0.20	126	0.047	6.76	0.016	6.92	0.002	0.53	0.34	15.54	15.63	30.47
CPR603/5	1 lpr	0.003	263	0.91	0.88	0.18	133	0.047	3.95	0.015	4.09	0.002	0.53	0.33	15.37	15.56	44.47
CPR603/7	2 lpr	0.004	317	0.87	0.52	0.29	375	0.046	1.42	0.015	1.56	0.002	0.38	0.47	15.29	15.31	18.15
CPR603/8	2 spr	0.003	432	1.16	0.35	0.21	564	0.047	1.10	0.015	1.30	0.002	0.38	0.63	15.47	15.56	29.57
CPR603/9	3 spr	0.003	381	1.21	1.05	0.13	184	0.047	2.46	0.015	2.60	0.002	0.48	0.38	15.34	15.55	48.46
CPR604																	
CPR604/1	1 lpr	0.011	324	0.86	43.08	0.03	31	0.054	32.90	0.018	34.26	0.002	1.88	0.74	15.28	17.71	361.21
CPR604/2	1 spr	0.002	301	0.79	11.00	0.06	28	0.049	45.40	0.016	47.00	0.002	2.60	0.63	15.45	16.41	159.69
CPR604/3	1 lpr	0.008	60	0.20	4.80	0.54	33	0.038	69.00	0.012	73.00	0.002	3.40	0.55	15.41	12.51	0.00
CPR604/4	1 lpr	0.001	517	1.52	0.88	0.30	101	0.046	8.02	0.015	8.20	0.002	0.30	0.61	15.48	15.49	16.92
CPR604/5	1 lpr	0.003	320	0.97	0.95	0.18	157	0.048	3.60	0.016	3.90	0.002	0.46	0.69	15.15	15.63	90.76
CPR604/7	3 spr	0.007	396	1.03	0.65	0.21	623	0.047	1.18	0.015	1.26	0.002	0.34	0.36	15.17	15.29	34.71
CPR604/9	3 spr	0.002	304	0.82	1.00	0.05	106	0.050	5.00	0.016	5.27	0.002	0.48	0.59	15.12	16.42	211.27

Table 3: (Cont.)

No	description	weight	Concentration			Th/U[a]	Atomic ratios							Corelation	Ages		
		(mg)	U	Pb	Pb com.		206/204[b]	207/206[cd]	error	207/235[c]	error	206/238[cd]	error	coeficient	206/238	207/235	207/206
			(ppm)	(ppm)	pg				2σ (%)		2σ (%)		2σ (%)				
CPR605																	
CPR605/1	1 lpr	0.001	1141	2.78	0.79	0.10	231	0.047	5.80	0.016	5.90	0.002	0.85	0.19	15.86	15.96	30.84
CPR605/4	2 lpr	0.004	999	2.48	0.45	0.12	1315	0.047	0.42	0.016	0.57	0.002	0.34	0.68	15.92	16.00	28.29
CPR605/5	3 lpr	0.008	442	1.12	0.49	0.12	1144	0.047	0.66	0.016	1.52	0.003	1.45	0.90	16.10	16.26	39.20
CPR605/6	2 lpr	0.007	868	2.32	0.67	0.12	1498	0.047	1.86	0.016	1.97	0.002	1.61	0.48	15.85	16.23	72.50
CPR606																	
CPR606/1	1 lpr	0.002	494	1.15	0.71	0.03	143	0.048	5.90	0.013	6.18	0.002	1.50	0.30	12.20	12.65	98.34
CPR606/5	2 lpr	0.003	455	0.93	0.53	0.25	335	0.046	1.80	0.012	2.1	0.002	0.42	0.76	12.13	12.13	11.75
CPR606/6	2 lpr	0.001	705	1.46	0.67	0.15	170	0.047	4.92	0.012	5.16	0.002	0.4	0.62	12.13	12.23	32.24
CPR606/7	2 lpr	0.003	489	1.10	4.34	0.03	63	0.053	10.26	0.014	10.72	0.002	0.66	0.71	12.08	13.75	315.18
CPR609																	
CPR609/1	1 lpr	0.008	412	1.19	0.95	0.24	533	0.046	0.73	0.015	0.79	0.002	0.23	0.38	15.40	15.44	23.67
CPR609/2	3 lpr	0.004	396	1.01	0.47	0.16	556	0.047	1.00	0.015	1.05	0.002	0.24	0.32	15.26	15.46	44.13
CPR609/3	1 lpr	0.006	336	0.90	0.74	0.14	425	0.047	0.94	0.015	1.11	0.002	0.24	0.33	15.28	15.42	18.49
CPR609/4	1 spr	0.004	1086	5.62	0.44	0.21	3428	0.057	0.15	0.042	0.33	0.005	0.29	0.88	34.00	41.38	493.44
CPR609/5	1 spr	0.004	315	2.48	0.41	0.24	1415	0.100	0.21	0.100	0.49	0.007	0.44	0.90	46.58	96.74	1623.39
CPR609/6	3 lpr	0.004	488	1.24	0.47	0.16	589	0.047	0.93	0.015	1.32	0.002	0.67	0.56	15.00	15.21	33.86

[a] calculated on the basis of radiogenic Pb^{208}/Pb^{206} ratios, assuming concordancy

[b] corrected for fractionation and spike

[c] corrected for fractionation, spike, blank and common lead (Stacey & Kramers, 1975)

[d] corrected for initial Th disequilibrium, using an estimated Th/U ratio of 4 for the melt

lpr - long-prismapic; spr - short-prismatic

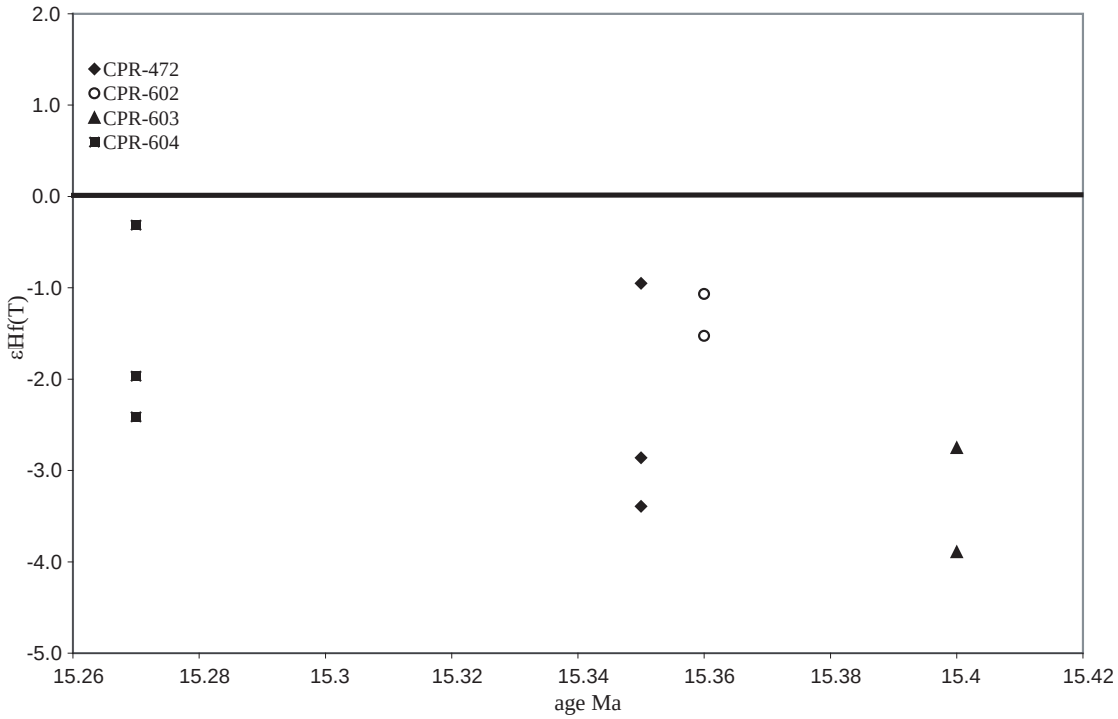

Fig. 16: *U-Pb age versus epsilon Hf for zircon from volcanic and plutonic rocks at Cerro de Pasco. All zircon plot in negative values, see text for explanations*

Table 4. Hf results on zircon

sample	Age (Ma)	176Hf/177Hf	± 2s	176Hf/177Hf standard value	176Hf/ 177Hf normalised	176Hf/ 177Hf (T)	eps Hf (0)	eps Hf (T)	±2s	T2 (DM) (Ga) model age
CPR 472										
CPR 472/1	15.35	0.283	0.000	0.282	0.283	0.283	-3.7	-3.4	0.5	1.21
CPR 472/2	15.35	0.283	0.000	0.282	0.283	0.283	-1.3	-1.0	0.5	1.07
CPR 472/3	15.35	0.283	0.000	0.282	0.283	0.283	-3.2	-2.9	0.5	1.18
CPR 602										
CPR 602/1	15.36	0.283	0.000	0.282	0.283	0.283	-1.9	-1.5	0.5	1.10
CPR 602/2	15.36	0.283	0.000	0.282	0.283	0.283	-1.4	-1.1	0.5	1.08
CPR 603										
CPR 603/1	15.4	0.283	0.000	0.282	0.283	0.283	-4.2	-3.9	0.5	1.24
CPR 603/3	15.4	0.283	0.000	0.282	0.283	0.283	-3.1	-2.8	0.5	1.18
CPR 604										
CPR 604/1	15.27	0.283	0.000	0.282	0.283	0.283	-2.8	-2.4	0.5	1.16
CPR 604/2	15.27	0.283	0.000	0.282	0.283	0.283	-0.7	-0.3	0.5	1.03
CPR 604/3	15.27	0.283	0.000	0.282	0.283	0.283	-2.3	-2.0	0.5	1.13

disturbances in a biotite spectrum will result if as little as 1% chlorite is present. The closing temperature for biotite ranges from 345 to 280°C (Snee, 2002).

The amenability to date hydrothermal sericite by the $^{40}Ar/^{39}Ar$ method has been shown by Perkins et al. (1990) and Snee et al. (1988). White mica separated from sericitized diatreme breccia and quartz-monzonite porphyry was in general coarse-grained (100-400 μm). Pervasive ground mass sericite was not selected for dating. Impurities, most commonly rutile, generally constituted between less than 1 to 3 % of each sample. The susceptibility to the effects of reactor-induced loss of ^{39}Ar (recoil) in sericite has been documented by Turner and Cadogan (1974) as well as to incorporation of extraneous argon (Dalrymple and Lanphere, 1969). The closing temperature for muscovite (2M1 structural state, Snee et al., 1988) ranges from 325 to 270°C.

Alunite is amenable for the $^{40}Ar/^{39}Ar$ method because potassium is an important cation in the structure of this mineral (McDougall and Harrison, 1999). Furthermore, Vasconcelos et al. (1994) suggested that ^{39}Ar loss during neutron irradiation is not creating a problem despite the fine-grained crystal size of alunite, in contrast to muscovite. The closing temperature for alunite has been evaluated between 200 and 210°C by Juliani et al. (2005) and Landis et al. (2005).

All step-wise IR-CO_2 laser $^{40}Ar/^{39}Ar$ experiments results are displayed as age spectra (Fig. 17 and 18). Plateaus were defined using the criteria of Dalrymple and Lamphere (1971) and Fleck et al. (1977) specifying the presence of at least three contiguous gas fractions that together represent more than 50% of the total ^{39}Ar released from the sample and for which no age difference can be detected between any two fractions at the 95% confidence level. Furthermore, ages have also been calculated with the inverse isochron method (Fig. 19 and Table 6, McDougall and Harrison, 1999). Inverse isochron diagrams allow to test the assumption made in the plateau ages where any trapped non-radiogenic Ar has an atmospheric composition ($^{40}Ar/^{36}Ar$ = 295.5). Most alunite isochron ages calculated using plateau steps are indistinguishable from the plateau ages and give atmospheric trapped Ar compositions. On the contrary, all sericite and one biotite calculated isochrons give trapped $^{40}Ar/^{36}Ar$ ratios equivalent to 295.5 within

Table 5: Location of dated samples in the Cerro de Pasco and Colquijirca districts

Sample	Location	UTM coordinates	Description
CPR 602	Venencocha	360806 E, 8821005N,	acretionnary lappili tuff
CPR 603	Diatreme SW	360255E, 8820377N	dactitic to rhyodacitic porphyry
CPR 604	Diatreme S	360838E, 8820315 N	quartz-monzonite porphyric dyke with magmatic pyrite (separate for S isotopes
CPR 605	Yanamate	18361524E, 8810913N	porphyric rock from Yanamate
CPR 606	Huacchuacaja		Porphyric dome from Huacchuacaja near Colqui
CPR 96[1]	W part of main open pit		sericite
CPR 115[1]	W part of main open pit		sericite
CPR 3[1]	W part of main open pit		sericite
CPR 21[1]	W part of main open pit		sericite
CPR 498[2]	W part of main open pit		sericite
CPR 499[2]	W part of main open pit		sericite
CPR 344[1]	Venencocha		biotite
CPR 472[1]	dyke in main open pit		biotite
CPR 19[1]	W part of main open pit		alunite
CPR347[1]	Venencocha		alunite
CPR 379[1]	Venencocha		alunite
CPR 380[1]	Venencocha		alunite
CPR 351[1]	Santa Rosa pit		alunite
CPR 360[1]	Venencocha		alunite
CPR 365[1]	Venencocha		alunite
CPR 381[1]	Venencocha		alunite
CPR 508[2]	Santa Rosa pit		alunite

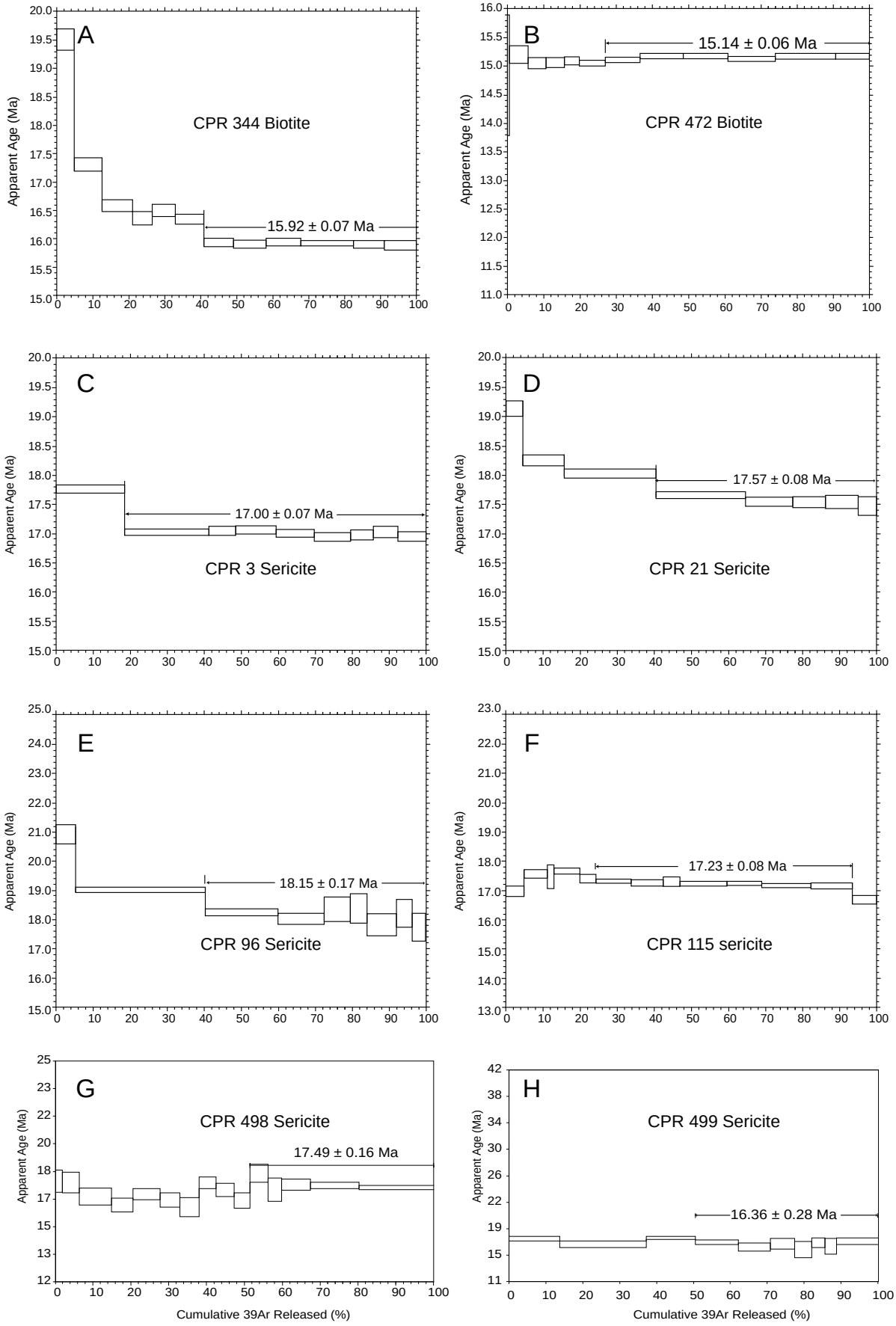

Fig. 17: *$^{40}Ar/^{39}Ar$ age spectra for biotite and sericite samples analyzed by step-wise IR-CO2 laser*

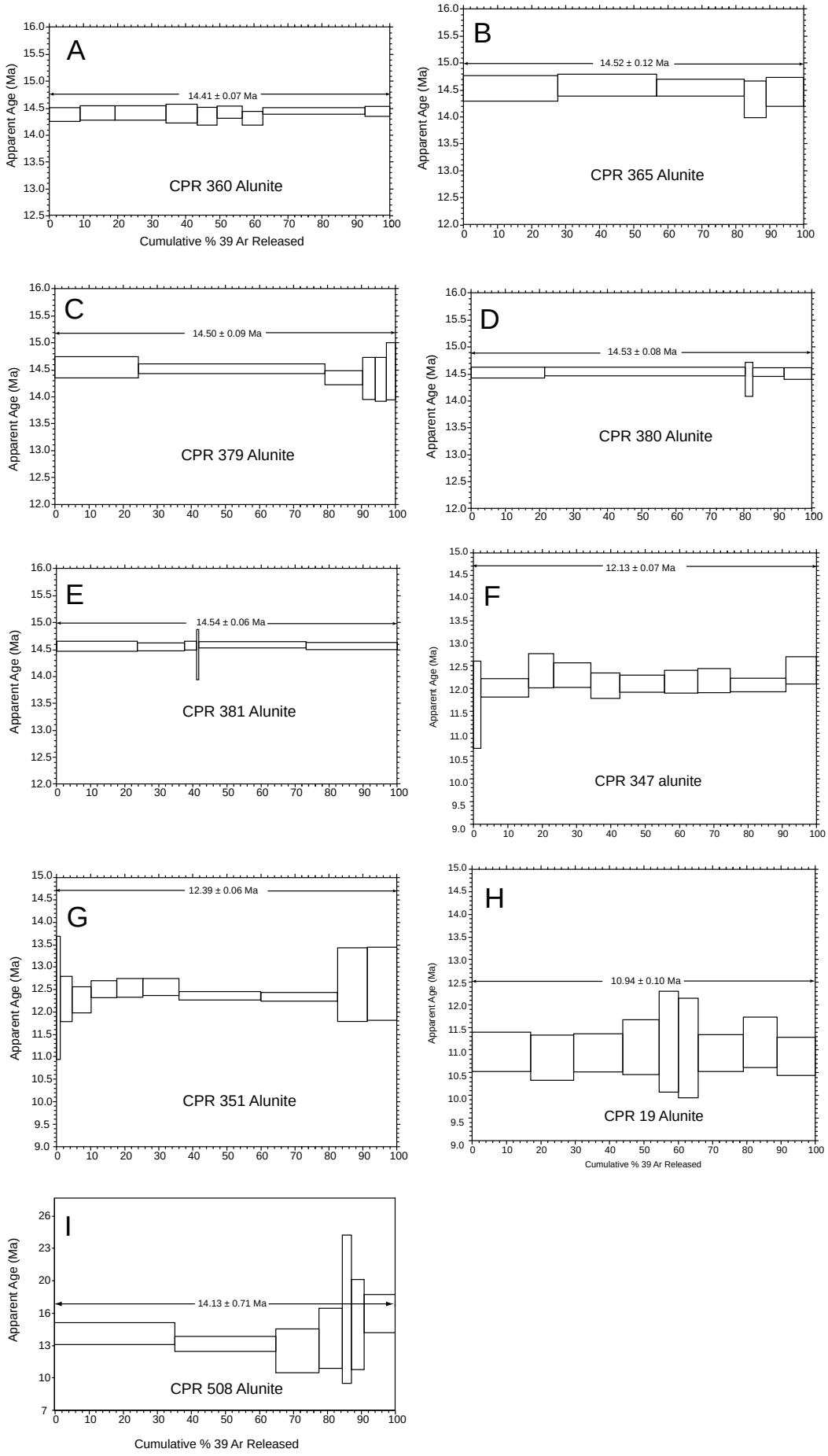

Fig. 18: *$^{40}Ar/^{39}Ar$ age spectra for alunite samples analyzed by step-wise IR-CO2 laser*

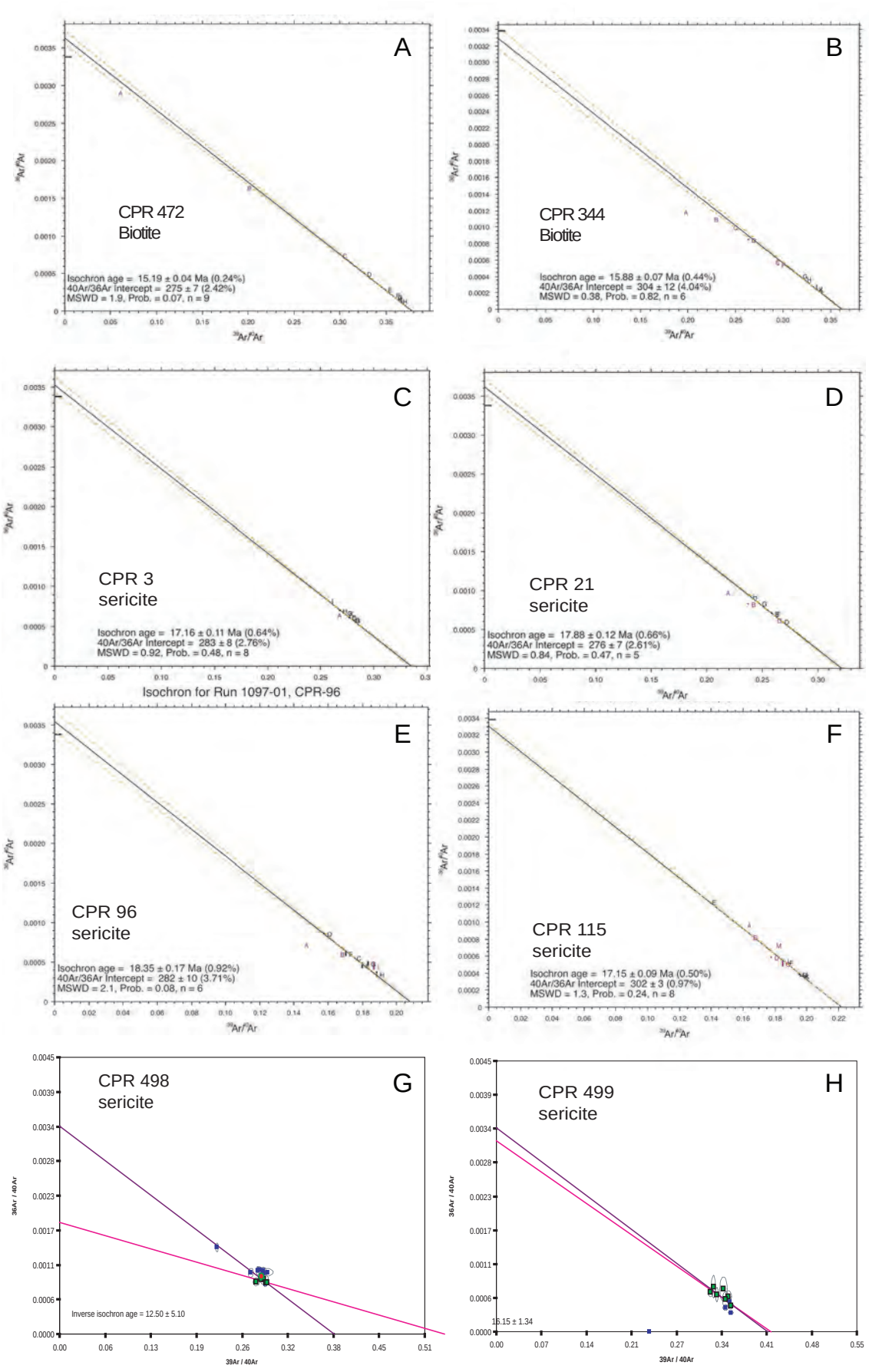

Fig. 19: *Inverse isochron correlation diagram for biotite, sericite, and alunite.*

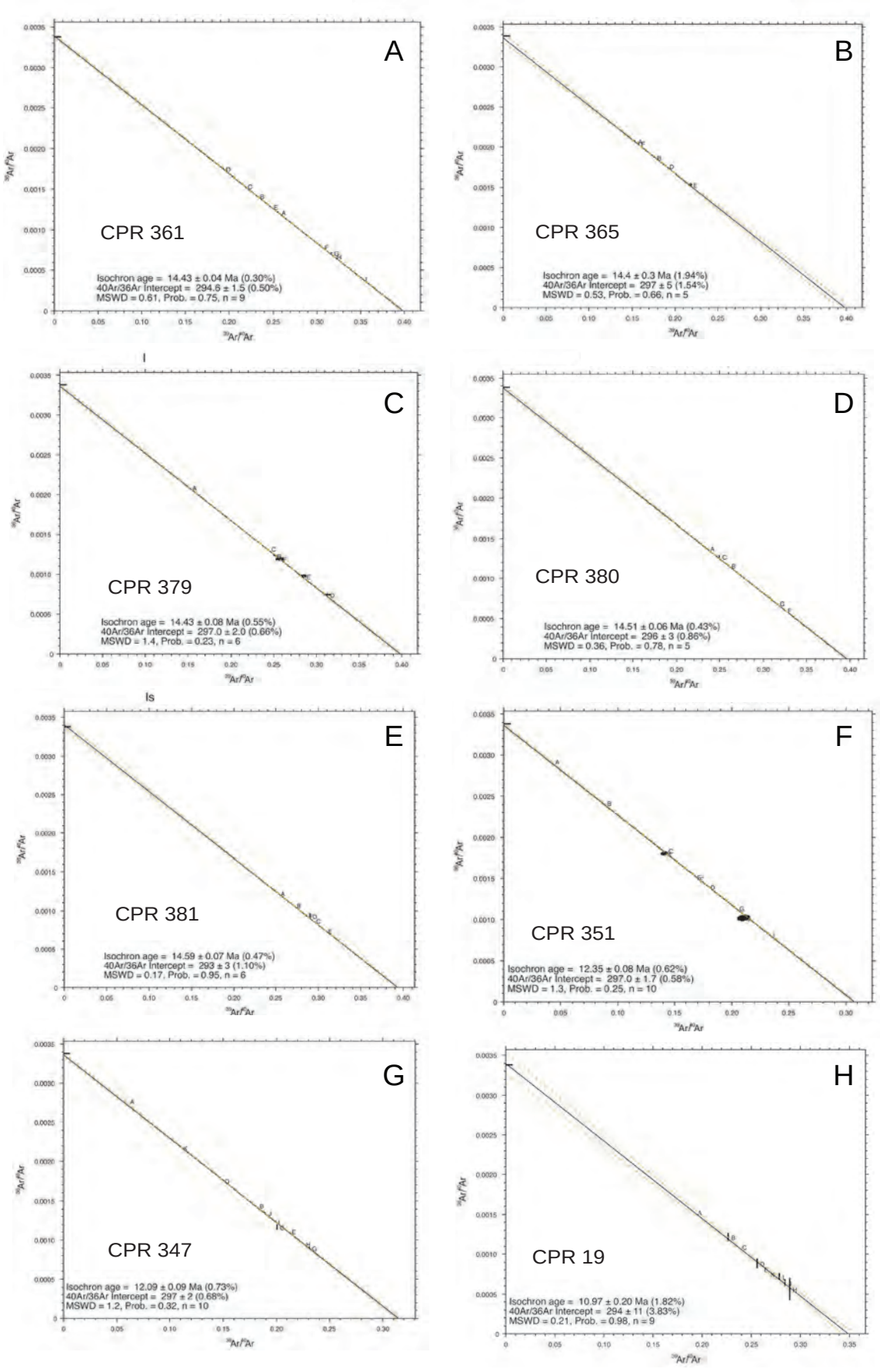
A
CPR 361
Isochron age = 14.43 ± 0.04 Ma (0.30%)
40Ar/36Ar Intercept = 294.6 ± 1.5 (0.50%)
MSWD = 0.61, Prob. = 0.75, n = 9
B
CPR 365
Isochron age = 14.4 ± 0.3 Ma (1.94%)
40Ar/36Ar Intercept = 297 ± 5 (1.54%)
MSWD = 0.53, Prob. = 0.66, n = 5
C
CPR 379
Isochron age = 14.43 ± 0.08 Ma (0.55%)
40Ar/36Ar Intercept = 297.0 ± 2.0 (0.66%)
MSWD = 1.4, Prob. = 0.23, n = 6
D
CPR 380
Isochron age = 14.51 ± 0.06 Ma (0.43%)
40Ar/36Ar Intercept = 296 ± 3 (0.86%)
MSWD = 0.36, Prob. = 0.78, n = 5
E
CPR 381
Isochron age = 14.59 ± 0.07 Ma (0.47%)
40Ar/36Ar Intercept = 293 ± 3 (1.10%)
MSWD = 0.17, Prob. = 0.95, n = 6
F
CPR 351
Isochron age = 12.35 ± 0.08 Ma (0.62%)
40Ar/36Ar Intercept = 297.0 ± 1.7 (0.58%)
MSWD = 1.3, Prob. = 0.25, n = 10
G
CPR 347
Isochron age = 12.09 ± 0.09 Ma (0.73%)
40Ar/36Ar Intercept = 297 ± 2 (0.68%)
MSWD = 1.2, Prob. = 0.32, n = 10
H
CPR 19
Isochron age = 10.97 ± 0.20 Ma (1.82%)
40Ar/36Ar Intercept = 294 ± 11 (3.83%)
MSWD = 0.21, Prob. = 0.98, n = 9

Fig. 19: *(Cont.)*

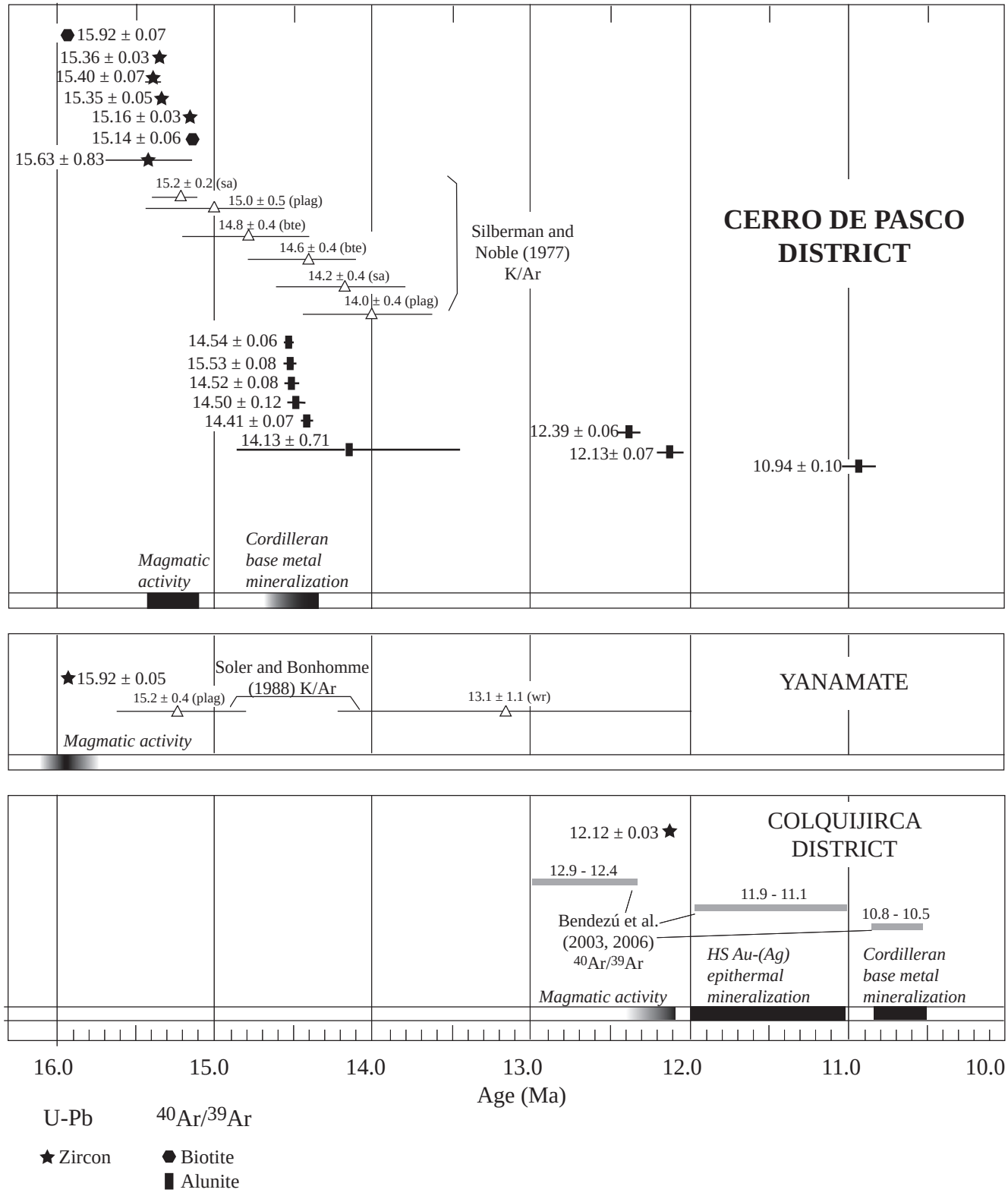

Fig. 20: *Summary geochronology diagram of U-Pb and $^{40}Ar/^{39}Ar$ results from this study and including previous studies. Error bars shown are ± 2σ. Abbreviations are sa = sanidine, plag = plagioclase, wr = whole rock.*

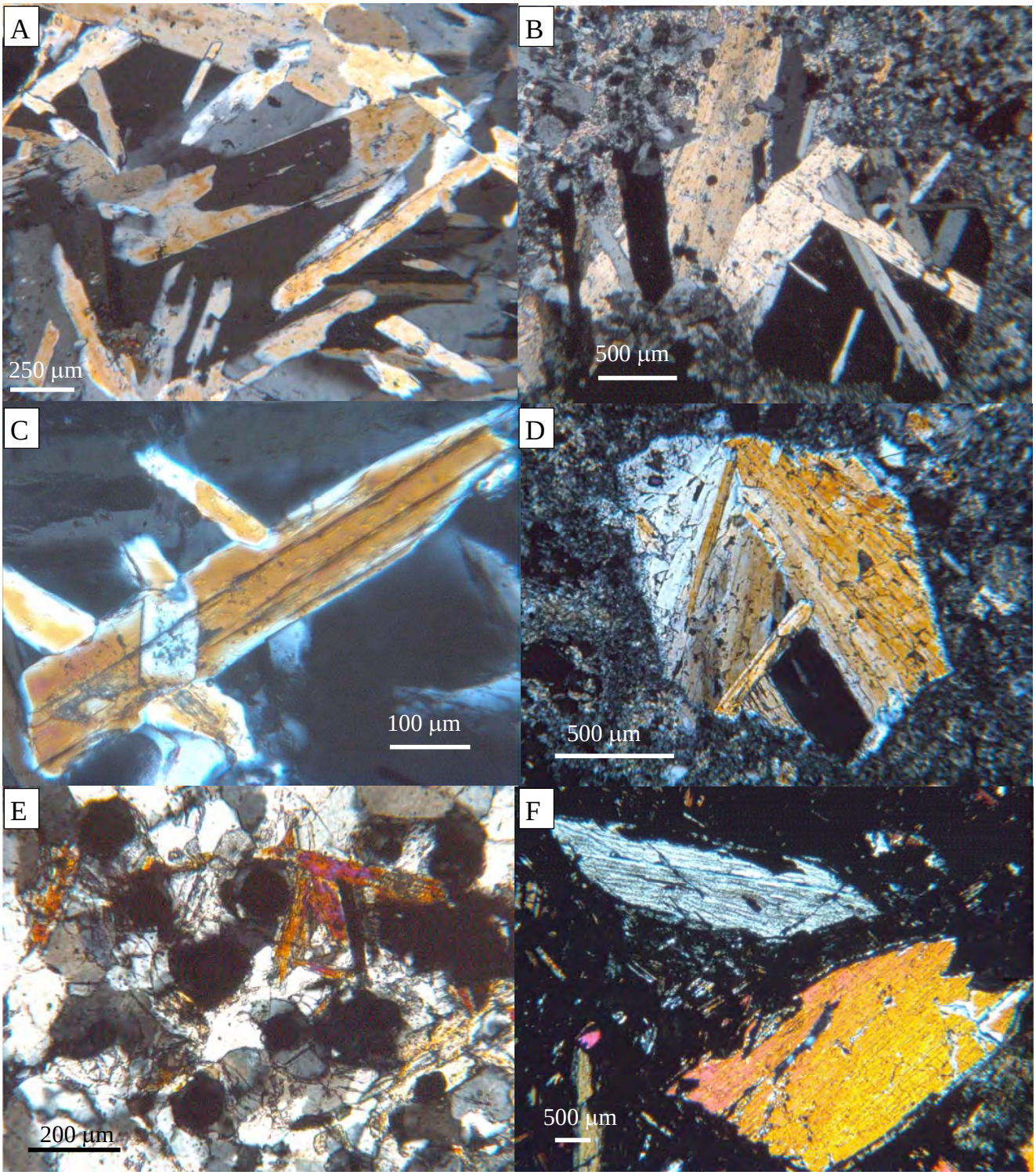

Fig. 21: *Photomicrographs of dated alunite. A) Woodhouseite inclusion in alunite present in the advanced argillic alteration of a dome. CPR 347, Venencocha area. B) Alunite present in the advanced argillic alteration assemblage in a dome, CPR 380, Venencocha area. C) Idiomorphic grain of woodhouseite in alunite, CPR 351, Venencocha area. D) Alunite filling a leached vug in the advanced argillic altered halo from an oxidized vein in the diatreme breccia. CPR 365, Venencocha area. E) Alunite present with quartz in the advanced argillic alteration assemblage in a dome. CPR 379, Venencocha area. F) Coarse-grained alunite from a vein, CPR 381, Venencocha area. For sample locations, see Fig. 2.*

Table 6: Summary of $^{40}Ar/^{39}Ar$ age data from Cerro de Pasco

Sample	Location	Mineral	Plateau age (Ma ± 2 σ)[a]	Inverse isochron age (Ma ± 2 σ)[b]	Isochron-derived MSWD[c]	40/36 ratio of intercept (± 2 σ)
Alteration halo produced by pyrite-quartz						
CPR 96[1]	W open pit (in diatreme breccia)	sericite	18.15 ± 0.17	18.35 ± 0.17	2.1	282 ± 10
CPR 115[1]	W open pit (in diatreme breccia)	sericite	17.23 ± 0.08	17.15 ± 0.09	1.3	302 ± 3
CPR 3[1]	W open pit (in diatreme breccia)	sericite	17.00 ± 0.07	17.16 ± 0.11	0.92	283 ± 8
CPR 21[1]	W open pit (in quartz-monoznie dyke)	sericite	17.57 ± 0.08	17.88 ± 0.12	0.84	276 ± 7
CPR 498[2]	W open pit (in diatreme breccia)	sericite	17.49 ± 0.16	12.50 ± 5.10	1.46	524 ± 310
CPR 499[2]	W open pit (in diatreme breccia)	sericite	16.36 ± 0.28	16.15 ± 1.34	1.71	315 ± 138
Diatreme tuff and crosscutting dyke, respectively						
CPR 344[1]	Venencocha	biotite	15.92 ± 0.07	15.88 ± 0.07	0.38	304 ± 12
CPR 472[1]	dyke in main open pit	biotite	15.14 ± 0.06	15.19 ± 0.04	1.9	275 ± 7
Cordillleran veins in volcaniclastic rocks						
CPR 19[1]	W part of main open pit	alunite	10.94 ± 0.10	10.97 ± 0.20	0.21	294 ± 11
Advanced argillic altered domes and dyke						
CPR 347[1]	Venencocha	alunite	12.13 ± 0.07	12.09 ± 0.09	1.2	297 ± 2
CPR 379[1]	Venencocha	alunite	14.50 ± 0.09	14.43 ± 0.08	1.4	297.0 ± 2.0
CPR 380[1]	Venencocha	alunite	14.53 ± 0.08	14.51 ± 0.06	0.36	296 ± 3
CPR 351[1]	Santa Rosa pit	alunite	12.39 ± 0.06	12.35 ± 0.08	1.3	297.0 ± 1.7
Advanced argillic altered halos of oxidized veins						
CPR 360[1]	Venencocha	alunite	14.41 ± 0.07	14.43 ± 0.04	0.61	294.6 ± 1.5
CPR 365[1]	Venencocha	alunite	14.52 ± 0.12	14.4 ± 0.3	0.53	297 ± 5
CPR 381[1]	Venencocha	alunite	14.54 ± 0.06	14.59 ± 0.07	0.17	293 ± 3
CPR 508[2]	Santa Rosa pit	alunite	14.13 ± 0.71	13.78 ± 1.08	1.96	310 ± 11

[1]Samples analyzed in the $^{40}Ar/^{39}Ar$ lab at Lund University, Sweden
[2]Samples analyzed in the $^{40}Ar/^{39}Ar$ lab at the University of Geneva, Switzerland

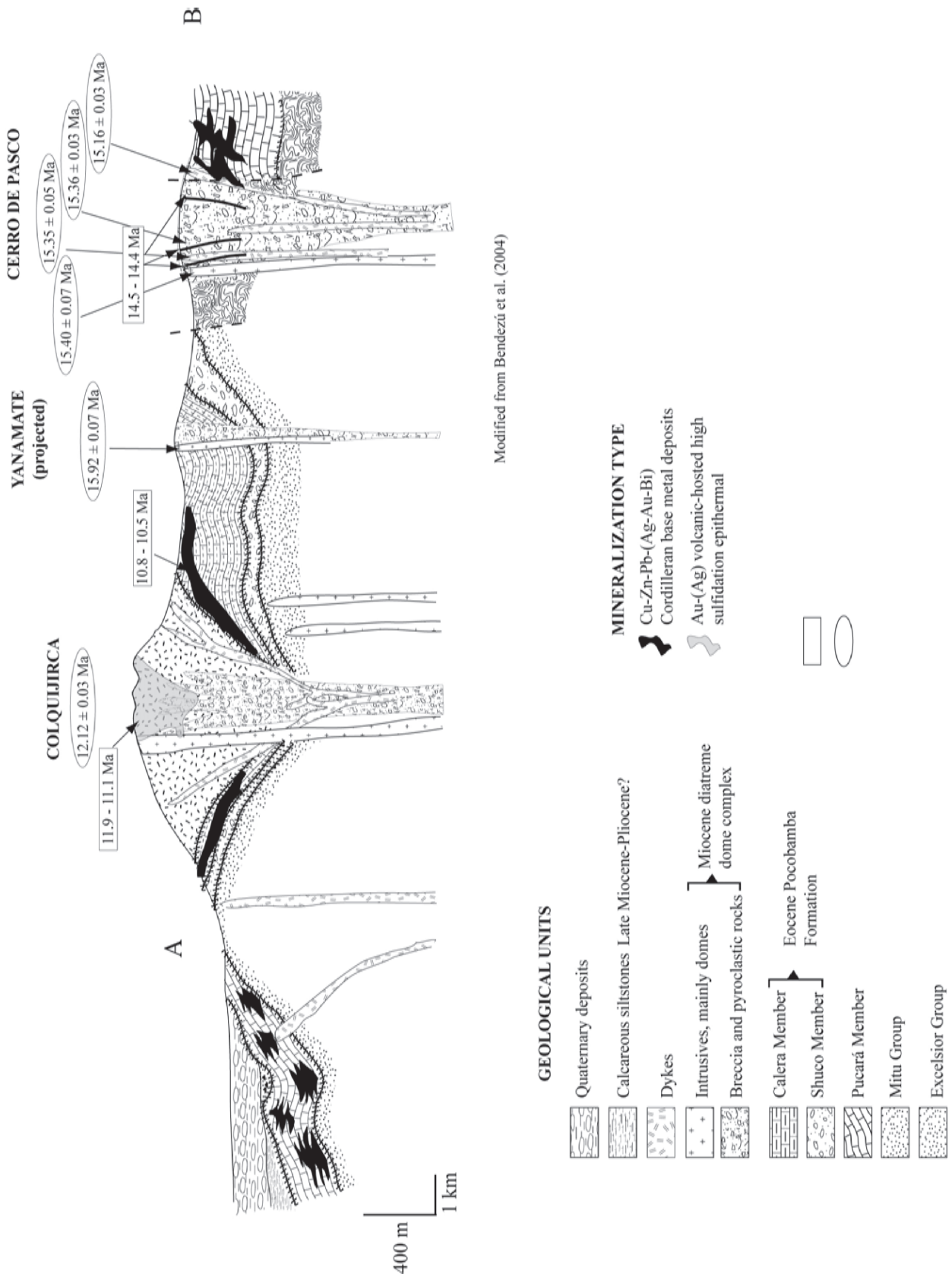

Fig. 22: *Schematic north-south longitudinal section of the Cerro de Pasco-Colquijirca districts following the main ore bodies (AB section in Fig. 1). Selected alunite $^{40}Ar/^{39}Ar$ and U-Pb ages are shown (modified from Bendezú et al., 2004).*

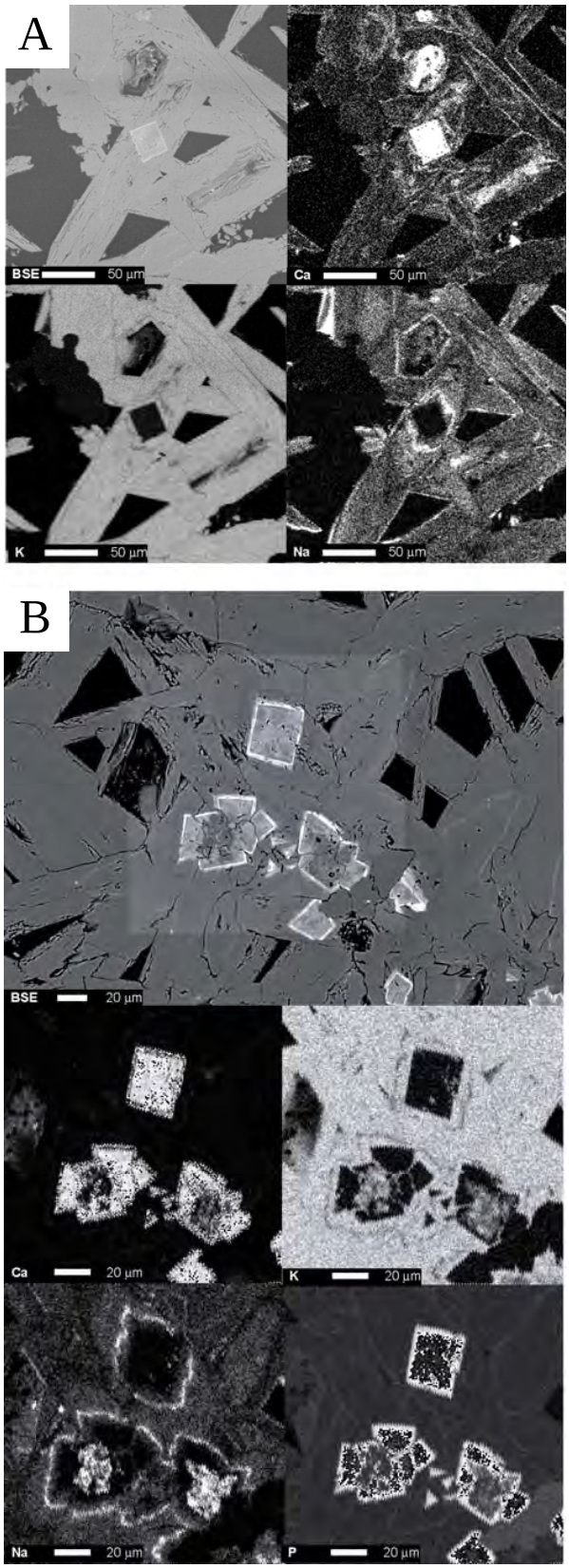

Fig. 23: *Backscattered and element distribution mapping images in alunite on sample CPR 351, Venencocha area. A) BSE image of alunite with an inclusion of woodhouseite and Ca, K, and Na distribution maps. B) BSE image of woodhouseite inclusions in alunite (CPR 351, Venencocha area) with Ca, K, Na, and P distribution maps.*

For the $^{40}Ar/^{39}Ar$ ages, errors are at 2σ level of precision for the plateau. Integrated results of $^{40}Ar/^{39}Ar$ and U-Pb analysis are summarized in Fig. 20 and a numerical summary is shown in Table 6. In order to give some informations on the analyzed samples, microphotographs are shown in Figure 21. A Colquijirca-Cerro de Pasco district cross section in Fig. 22 illustrates the obtained geochronologic ages (AB in Fig. 1).

Quartz-monzonite dyke

Two age spectra on biotite from two quartz-monzonite porphyry dykes were obtained. The sample CPR 472 shows an undisturbed age spectrum and yields a plateau at 15.14 ± 0.06 Ma (Fig. 17B). The inverse isochron age is 15.19 ± 0.04 Ma and the $^{40}Ar/^{36}Ar$ ratio is 275 ± 7 (Fig. 19A). The $^{206}Pb/^{238}U$ age for zircons from the same sample yields an age of 15.35 ± 0.05 Ma (Fig. 15A). This latter age is slightly older than the $^{40}Ar/^{36}Ar$ one but can be considered concordant within the ^{40}K and ^{238}U decay constant uncertainties (ca. 1% younger K-Ar, Min et al., 2000).

The age spectrum of sample CPR 344 is highly disturbed and L-shaped. The plateau gives an age of 15.92 ± 0.07 Ma and the inverse isochron gives 15.88 ± 0.07 Ma (Fig. 17A and 19B). This sample is fairly altered and the presence of chlorite in biotite could account for the disturbed spectra. The presence of chlorite affects the argon systematic due to ^{39}Ar recoil, and disturbs the age spectra. During the step-heating, early gas releases may consist of weakly-held argon formed during ^{39}Ar recoil and consequently, the obtained plateau gives probably an anomalously high apparent age (also higher than the zircon U-Pb age of CPR 472).

Hydrothermal event

First mineralization stage (sericite)

Five age spectra obtained on sericite (CPR 3, CPR 98, CPR 115, CPR 498, and CPR 499) from the altered diatreme breccia adjacent to the pyrite-quartz body are all disturbed (Fig. 17C-H) and the plateaus range between 16.36 and 18.15 Ma.

The age spectrum for sample CPR 3 shows excess argon ($^{40}Ar_E$) in the first degassing step while the next steps form a plateau (Fig. 17C). The plateau gives an age at 17.00 ± 0.07 Ma and an inverse isochron age of 17.16 ± 0.11 Ma (Fig. 19C, Table 6). This suggests that extraneous argon was trapped in the sericite and could have affected the plateau age.

The CPR 96 age spectrum also shows excess argon and the plateau gives an age of 18.15 ± 0.17 Ma (Fig. 17E) and an inverse isochron age of 18.35 ± 0.17 Ma (Fig. 19E, Table 6).

The age spectrum of sample CPR 115 reveals a disturbed spectrum in the first degassing steps and yields a plateau at 17.23 ± 0.08 Ma (Fig. 17F) and an inverse isochron age of 17.15 ± 0.09 Ma (Fig. 19F, Table 6).

The sample CPR 498 age spectrum is disturbed

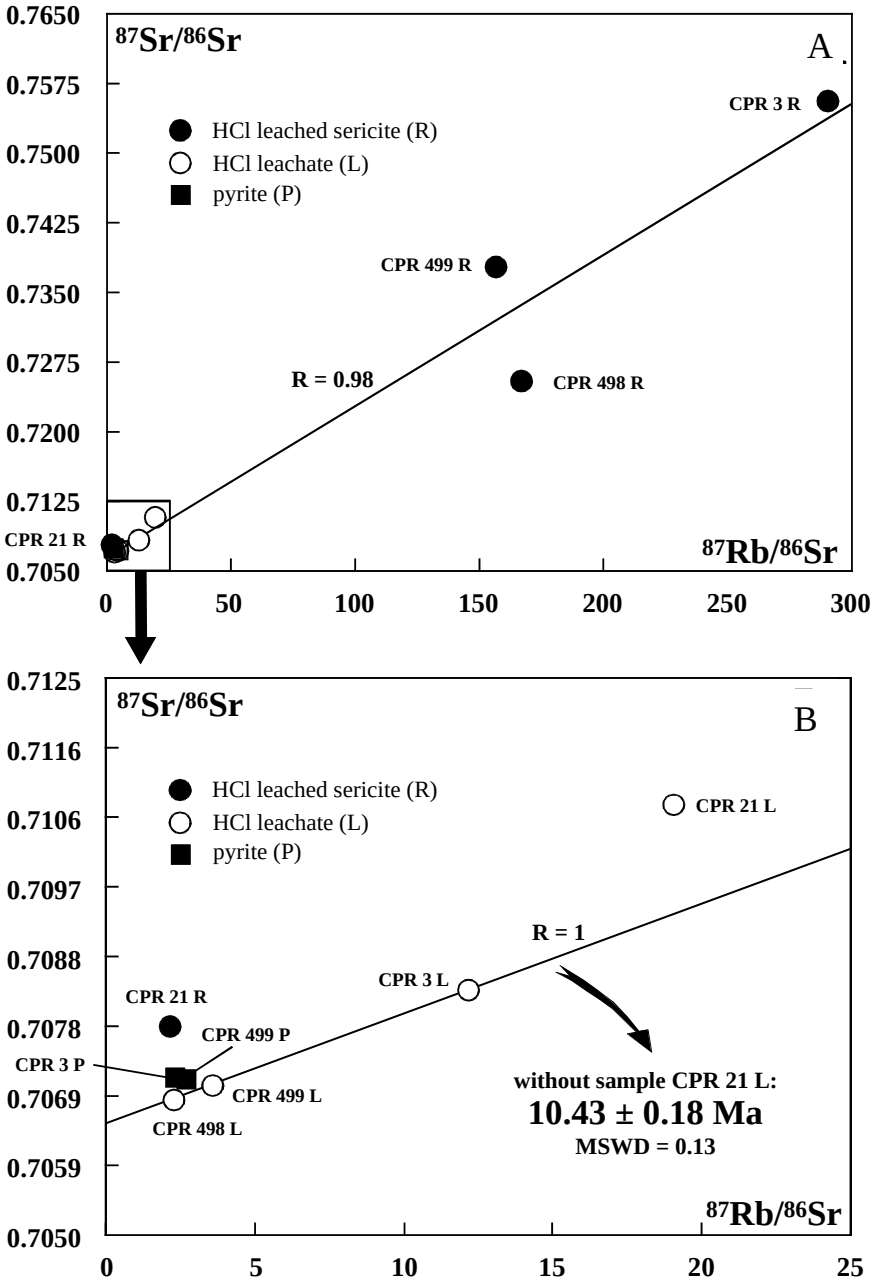

Fig. 24: *A) and B) $^{87}Sr/^{86}Sr$ vs. $^{87}Rb/^{86}Sr$ diagram where all samples display a linear correlation with R = 0.98 but reflect a high data scatter around the best-fit line which is obvious especially for the sericite residues. Abbreviations are: R = residue, L = leachate, P = pyrite.*

but a plateau age can be calculated at 17.49 ± 0.16 Ma (Fig. 17G), with an inverse isochron age of 12.50 ± 5.10 Ma. The inverse isochron age shows a large error that deviates significantly from the plateau age (Fig 19G, Table 6).

Sample CPR 499 yields an age spectrum which is slightly disturbed and gives a plateau age at 16.36 ± 0.28 Ma (Fig. 17H) and an inverse isochron age of 16.15 ± 1.34 Ma (Fig. 19H, Table 6).

A sericite sample (CPR 21) from a dyke adjacent to the pyrite-quartz body and altered to sericite, pyrite, and quartz, reveals an age spectra at 17.57 ± 0.08 Ma errors and in some cases, different ages.

Most of the analyzed alunite and biotite samples yield apparently undisturbed age spectra displaying a plateau and all of them (except biotite sample CPR 344) appear to represent simple argon closure with no subsequent thermal disturbances (McDougall and Harrison, 1999), although thermal disturbances are not always reflected in the spectra (Hanson et al., 1975; Lee et al., 1991). The analyzed sericite samples show disturbed age spectra and discordant isochron ages with trapped $^{40}Ar/^{36}Ar$ ratios differing from the standard value of 295.5.

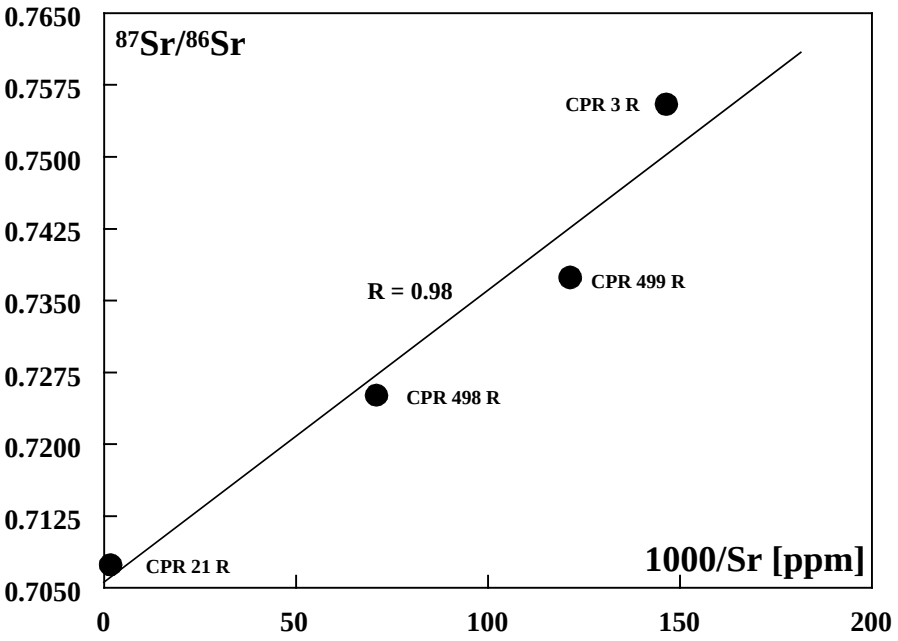

Fig. 25: *$^{87}Sr/^{86}Sr$ vs. 1000/Sr mixing diagram where the sericite residues (R) form a linear array (R = 0.98) that may reflect a disturbed binary mixing line. Abbreviations are R = residue.*

and shows excess argon ($^{40}Ar_E$) at least in the 3 first steps and probably also in the following steps (Fig. 17D and 19D).

Second mineralization stage

The alunite sample CPR 19 from an enargite-pyrite vein (fine-grained ~50 μm) located on the western side of the open pit, yields an undisturbed age spectrum with a plateau at 10.94 ± 0.1 Ma (Fig. 18H) and a concordant 10.97 ± 0.2 Ma inverse isochron age (Fig. 19H, Table 6).

All alunite samples from the Venencocha area related to advanced argillic altered veins (CPR 360, CPR 365, and CPR 381) and domes (CPR 379, and CPR 380). Alunite crystals from veins are generally between 300 and 800 μm in size and in one sample (CPR 381), coarse-grained crystals occur 1-4 mm in size). Petrographic examination of alunite crystals reveals that it contains inclusions. These include woodhouseite ($CaAl_3(PO_4)(SO_4)(OH)_6$), quartz, and rutile. Generally, the latter two inclusions contribute to no more than 1 volume percent of the sample. SEM images and element mapping show that Ca, K, Na and P concentrations vary widely within a single grain of alunite and woodhouseite (Fig. 23). K_2O contents are 8.88 and 9.08 wt percent (Table 7). Alunite crystals from domes are generally euhedral, pinkish and up to 500 μm in size. Electron microprobe analyses on alunite from domes reveal K_20 contents between 7.51 and 8.11 wt percent (Table 7).

Most of the alunite samples gave well-defined plateaus at around 14.5 Ma (Fig. 18, Table 6) except for sample CPR 347 which yields a younger age (12.13 Ma). Within errors, all these ages are nearly indistinguishable.

The vein alunite from sample CPR 360 yields an undisturbed age spectra at 14.41 ± 0.07 Ma, sample CPR 365 gives an age at 14.52 ± 0.12 Ma, and sample CPR 381 gives an age of 14.54 ± 0.06 Ma (Fig. 18A, B, E, Table 6). Corresponding inverse isochron ages for CPR 360, CPR 365, and CPR 381 are all concordant and $^{40}Ar/^{36}Ar$ ratios are close to the atmospheric value within errors (Fig. 19B and E, Table 6).

Three alunite samples (CPR 347, CPR 379 and CPR 380) from altered dome at Venencocha have been dated. Sample CPR 347 yields a distinctly younger plateau age of 12.13 ± 0.07 Ma (Fig. 18F). The age spectrum looks undisturbedand the inverse isochron is concordant (12.09 ± 0.09 Ma, Fig. 19G, Table 6). The spectrum of sample CPR 379 from an altered dome at Venencocha shows a plateau at 14.50 ± 0.09 Ma (Fig. 18C) and appears to be undisturbed. The inverse isochron (14.43 ± 0.08 Ma) is concordant with the plateau age (Fig. 19C, Table 6). The other altered dome sample from Venencocha (CPR 380) gives an undisturbed age spectrum at 14.53 ± 0.09 Ma and the plateau age is concordant with the isochron age (14.51 ± 0.06 Ma, Fig. 18D and 19D).

The two alunite samples from the Santa Rosa area from an advanced argillic altered dome and from oxidized veins surrounded by an advanced argillic halo have been analyzed. The first alunite sample (CPR 508) yields a slightly disturbed age spectrum with a plateau age at 14.13 ± 0.71 Ma (Fig. 18I). This age is comparable to the other ages of about 14.5 Ma within errors. The inverse isochron age is less precise, giving 13.78 ± 1.08 Ma (Table 6). The second alunite sample (CPR

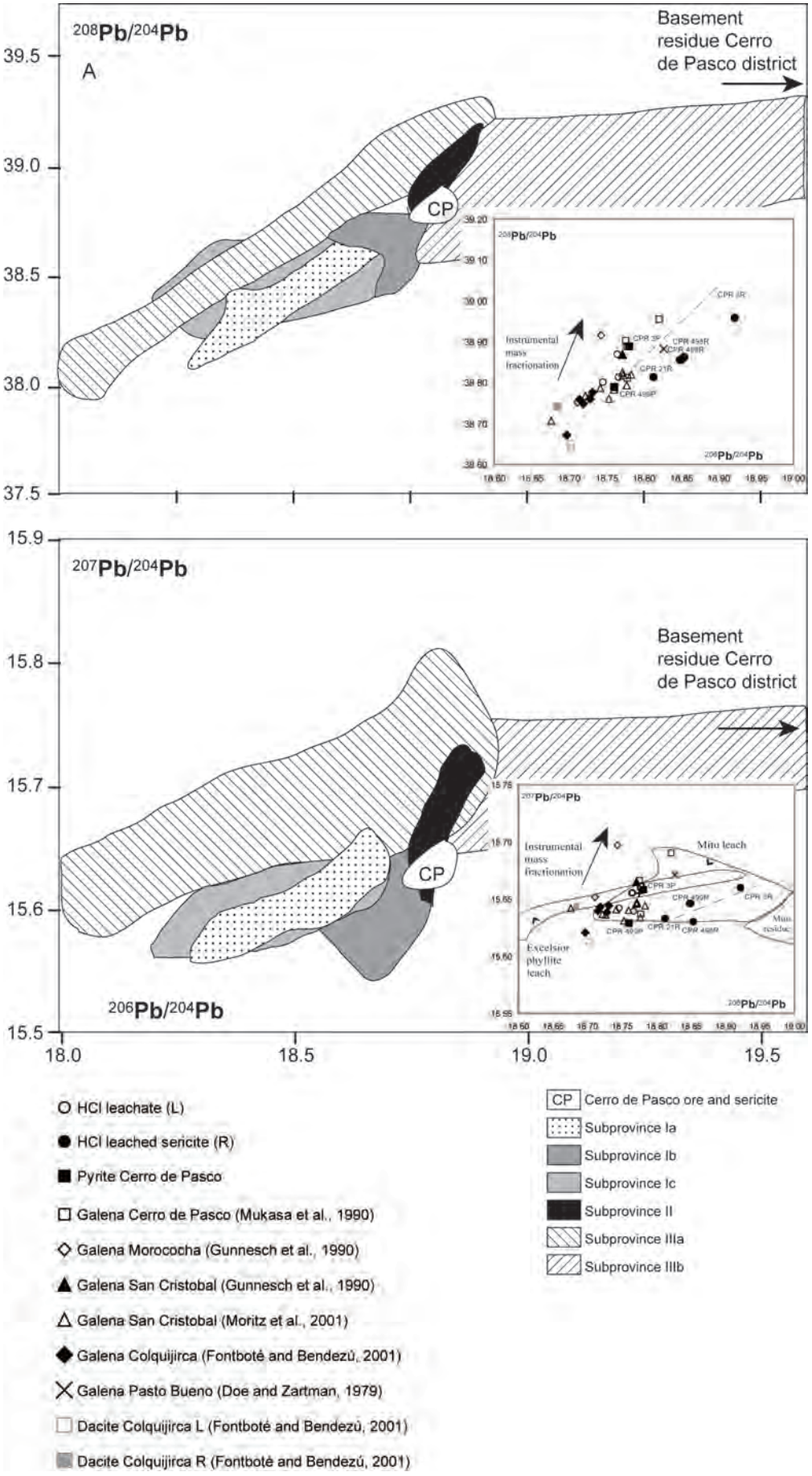

Fig. 26: *Conventional Pb-Pb diagrams showing subprovinces Pb isotope composition after Macfarlane et al. (1990). Inserts show Pb isotope composition sericite and pyrite analyzed in this study and galena from Cerro de Pasco (Mukasa et al., 1990) and other localities (see legend).*

351) yields an undisturbed age spectrum at 12.39 ± 0.06 Ma (Fig. 18G) with a concordant inverse isochron age of 12.35 ± 0.08 Ma (Fig. 19F, Table 6). The age of 12.39 ± 0.06 Ma is slightly older but approaches the 12.13 Ma of an oxidized vein at Venencocha.

Rb-Sr analyses

The results of Rb-Sr isotopic analyses on sericite residues (R), corresponding HCl leachates (L) and pyrites (P) are presented in Table 1. Rb and Sr concentrations of residues are based on their dry sample weights after leaching. Since the mass of components removed by HCl leaching cannot be exactly determined with confidence and may be biased due to material loss during centrifugation, we give no Rb and Sr concentrations for the HCl leachates. Sericite residues CPR 3, CPR 489 and CPR 499 from altered diatreme breccias have low Sr concentrations between ca. 7 and 15 ppm, whereas sericite CPR 21 from an altered quartz-monzonite porphyry has about 782 ppm Sr. This may result from the different nature of the altered host rocks (89 ppm for CPR 472). The sericite Rb contents are all high (448 - 820 ppm) which results in generally high $^{87}Rb/^{86}Sr$ ratios between 157 and 291, except for sample CPR 21 which has an exceptionally low $^{87}Rb/^{86}Sr$ ratio of 2.07. The $^{87}Sr/^{86}Sr$ ratios of the high-Rb/Sr samples CPR 3, CPR 498 and CPR 499 (0.72547 - 0.75561) reflect significant accumulation of radiogenic Sr, whereas $^{87}Sr/^{86}Sr$ of CPR 21 remains at a low value of 0.70781. The corresponding HCl leachates vary in $^{87}Rb/^{86}Sr$ between 2.3 and 19.05, with $^{87}Sr/^{86}Sr$ = 0.70682 - 0.71088. As can be expected for sulfides, both the Rb and Sr elemental concentrations of pyrites CPR 3 and CPR 499 do not exceed the ppb range (230 - 290 ppb). Their $^{87}Sr/^{86}Sr$ ratios are identical within errors at ca. 0.7071 and $^{87}Rb/^{86}Sr$ shows different but comparable values of 2.38 and 2.83, respectively.

In the $^{87}Sr/^{86}Sr$ vs. $^{87}Rb/^{86}Sr$ space (Fig. 24A), all samples display a linear correlation with R = 0.98 but reflect a high data scatter around the best-fit line which is obvious especially for the sericite residues (R). This *a priori* excludes any geochronologically meaningful isochron regression for both the entire sample set and the sericite residues alone. In a $^{87}Sr/^{86}Sr$ vs. 1000/Sr mixing diagram (Fig. 25), the sericite residues (R) form a linear array (R = 0.98) that may reflect a disturbed binary mixing line. However, time-integrated palaeomixing line calculations following Schneider et al. (2003) yielded no geochronologically interpretable results. This may indicate either unsystematic, heterogeneous isotopic and compositional mixing, or post-formational disturbance of the Rb-Sr system in the sericite, or both.

HCl leachates (L) CPR 3, CPR 498 and CPR 499 are well correlated (R = 1) in the $^{87}Sr/^{86}Sr$ vs. $^{87}Rb/^{86}Sr$ diagram whereas leachate CPR 21 deviates significantly towards higher $^{87}Rb/^{86}Sr$ and $^{87}Sr/^{86}Sr$ values (Fig. 24B). Isochron regression of these leachates excluding sample CPR 21 results in a statistically robust Rb-Sr age of 10.43 ± 0.18 Ma (MSWD = 0.13), comparable to the $^{40}Ar/^{39}Ar$ age of 10.94 Ma obtained for alunite sample CPR 19 from an enargite-pyrite vein (Fig. 18). The initial $^{87}Sr/^{86}Sr$ of the isochron is 0.70648 ± 0.00001.

Assuming that the sericite samples (R) and the components removed by HCl leaching (L) were precipitated coevally from the same alteration fluids, two-point isochron model ages can be calculated from corresponding R-L samples pairs (Table 8). All ages obtained are discordant between 7.98 and 14.05 Ma, corresponding inititial $^{87}Sr/^{86}Sr$ ratios $Sr_{i(t)}$ are similar only in the case of sample pairs CPR 3 and CPR 499. R-L pairs CPR 3, CPR 21 and CPR 499 give Rb-Sr ages comparable to some of the $^{40}Ar/^{39}Ar$ ages obtained for alunite. In this context, the 7.98 Ma Rb-Sr age defined by sample pair CPR 498 appears to be unusually young.

The pyrite (P) from samples CPR 3 and CPR 499 plot next to the correlation line defined by HCl leachates CPR 3, CPR 498 and CPR 499 but do not display a clear overall relationship to the Rb-Sr systematics of the leached sericite samples (R) and corresponding HCl leachates (L) (Fig.24b). Three-point isochron regressions of R-L-P triplets for samples CPR 3 and CPR 499 give very high MSWD values (197 and 1564, respectively) and are therefore insignificant. Two-point isochrons calculated for corresponding pyrite (P) and leached sericite (R) yield 11.83 ± 11 Ma ($Sr_{i(t)}$ = 0.70672 ± 0.00004) for sample CPR 3 and 13.94 ± 0.09 Ma ($Sr_{i(t)}$ = 0.70655 ± 0.00003) for CPR 499, respectively. These ages are again discordant but comparable to the corresponding R-L ages calculated for samples CPR 3 and CPR 499 (Table 8).

Pb isotopes

Pb isotope data for the sericite residues (R), corresponding HCl leachates (L) and associated pyrite (P) are listed in Table 1 and depicted in conventional Pb-Pb diagrams (Fig. 26). These also include four data points for Cerro de Pasco galena samples from Mukasa et al. (1990), as well as galena samples from Morococha (Gunnesch et al., 1990), San Cristobal (Gunnesch et al., 1990; Moritz et al., 2001), Colquijirca (Fontboté and Bendezú, 2001), and Pasto Bueno (Doe and Zartman, 1979) for comparison. All Cerro de Pasco samples ($^{206}Pb/^{204}Pb$ = 18.743 - 18.922, $^{207}Pb/^{204}Pb$ = 15.629 - 15.660, $^{208}Pb/^{204}Pb$ = 38.789 - 38.958) plot along the extension of the Stacey and Kramers (1975) average crustal Pb growth curve which indicates lead sources located in crustal reservoirs. Overall, they form relatively homogeneous populations in both Pb-Pb diagrams (Fig. 26). Variations may partly result from instrumental mass fractionation effects. The pyrite samples CPR 3 (P) and CPR 499 (P), the HCl leachates of sericite (L) and most of the Cerro de Pasco galena lead isotope compositions from Mukasa et al. (1990) plot all within a narrow range of $^{206}Pb/^{204}Pb$ values (18.746 - 18.781), indicating similar lead sources. The leached sericite samples (R) are shifted systematically towards higher Pb isotope ratios).

Table 7: Representative electron microprobe composition of alunite[a] from Cerro de Pasco

Sample	CPR 347	CPR 360	CPR 361	CPR 367	CPR 380	CPR 381	CPR 383	CPR 394	CPR 37	CPR 15
Na_2O	0.82	1.29	1	0.86	0.71	0.64	0.94	1.85	2.79	2.31
K_2O	8.11	9.08	6.9	7.41	7.51	8.88	8.86	7.69	6.34	5.85
BaO	0	0.05	0.19	0.22	0.07	1.11	0.13	0.21	0.25	0.07
SrO	0.03	0.06	0.1	0.1	0.14	0.36	0.2	0.1	0.13	0.1
Al_2O_3	33.9	30.83	33.85	33.57	33.92	30.23	33.33	34.2	33.97	33.57
SO_3	40.76	41.12	40.66	40.62	40.99	40.88	40.61	39.49	39.87	42.14
P_2O_5	0	0	0.17	0.1	0.27	0.04	0.15	0.05	0.03	0.05
H_2O[b]	16.68	18.38	16.54	16.92	16.27	18.26	16.72	15.12	15.7	18.19
F-	0.12	0.07	0.39	0.05	0.91	0.53	0.06	0.18	0.06	0.05
Total	100.42	100.87	99.8	99.85	100.78	100.91	101	98.89	99.15	102.32
Na	0.11	0.17	0.13	0.11	0.09	0.09	0.12	0.24	0.36	0.3
K	0.74	0.84	0.64	0.68	0.69	0.84	0.8	0.69	0.57	0.53
Ba	0	0	0.01	0.01	0	0.03	0	0.01	0.01	0
Sr	0	0	0	0	0.01	0.02	0.01	0	0.01	0
∑A site	0.85	1.01	0.78	0.81	0.79	0.97	0.93	0.94	0.94	0.83
Al	2.98	2.75	3.01	2.99	2.99	2.75	2.9	2.97	2.95	2.93
∑R site	2.98	2.75	3.01	2.99	2.99	2.75	2.9	2.97	2.95	2.93
S	2.18	2.24	2.2	2.2	2.2	2.27	2.15	2.09	2.11	2.24

[a]Alunite samples were analysed using a Cameca SX50 electron microprobe at the University of Lausanne, Switzerland. Instrumental conditions were: accelerating voltage 15 kV, beam current of 10 nA, and a sport size of 15 mm.
[b]Weight% H2O calculations were based on observed values for sulfur, phosphorus, potassium, sodium, barium, strontium, and fluorine, and alunite stochimonetry using formula $AR_3(SO_4)_2(F,OH)_6$, in which A refers to the large cations K^+, Na^+, Ba^+, and Sr^+, and R is Al^{3+}

Table 8. Two-point isochron model ages for R-L pairs of sericite, samples CPR 3, CPR 21, CPR 498, and CPR 499

R-L-Pair	Two-point isochron model age ± 2 σ [Ma]	$Sr_{i(t)}$ ± 2 σ
CPR 3	11.96 ± 0.11	0.70622 ± 0.00003
CPR 21	12.42 ± 0.18	0.70745 ± 0.00001
CPR 498	7.98 ± 0.07	0.70656 ± 0.00001
CPR 499	14.05 ± 0.09	0.70629 ± 0.00002

Discussion

Geochronologic and Hf isotopic constraints of the magmatic rocks

Figures 20 and 22 summarize the U-Pb and $^{40}Ar/^{39}Ar$ ages presented in this study, the diatreme-dome complexes at Cerro de Pasco, Colquijirca, and Yanamate, together with regional geochronologic data from the literature (Silberman and Noble, 1977; Soler, 1991; Bendezú et al., 2003). The oldest zircon age is that of Yanamate (15.92 ± 0.05 Ma), which is the only diatreme-dome complex for which related mineralization is not known. The obtained age is older than the possibliy reset K/Ar (whole rock and sanidine) ages of 15.2 ± 0.4 Ma and 13.1 ± 1.1 Ma, respectively, reported by Soler and Bonhomme (1988). The zircon age for the Colquijirca diatreme-dome complex is the youngest (12.12 ± 0.03 Ma) of the three dated diatreme-dome complexes. This age is younger than the biotite $^{40}Ar/^{39}Ar$ ages reported by Bendezú et al. (2003) ranging from 12.4 ± 0.06 and 12.9 ± 0.1 Ma. Two of the biotite ages are inverse isochron ages because no plateau ages could be obtained, which reflect that the system has been disturbed. The third biotite age (12.43 ± 0.06 Ma) yields a good plateau and is older than the U-Pb age on zircon obtained in this study (12.12 ± 0.03 Ma). At Colquijirca, precious-metal high sulfidation mineralization dated on alunite between 11.9 and 11.1 Ma and Cordilleran base metal mineralization dated on alunite between 10.5 and 10.8 Ma are closely related in time and space with the diatreme-dome complex (Bendezú et al., 2003; Bendezú, 2007).

At Cerro de Pasco, the U-Pb zircon ages on the magmatic rocks at Cerro de Pasco range from 15.40 ± 0.07 to 15.16 ± 0.04 Ma and are in agreement with the relative chronology deduced from field observations (Fig. 22). The accretionary lapilli tuff within the diatreme is the first recorded magmatic event at 15.36 ± 0.03 Ma. The dated dacitic dome yields an age at 15.40 ± 0.07 Ma. This age is within errors identical to that of the accretionary lapilli tuff. The U-Pb ages on quartz-monzonite porphyry dykes suggest that their emplacement lasted for at least 20'000 yrs from 15.35 ± 0.05 Ma to 15.16 ± 0.04 Ma. In one sample (CPR 603), the seven analyzed zircon grains define two clusters at 15.47 ± 0.04 Ma and 15.16 ± 0.04 Ma. These ages may reflect protracted zircon growth, which could suggest that magmatism might have started before the first recorded magmatic ages (15.40 ± 0.07 Ma). The biotite $^{40}Ar/^{39}Ar$ of one of the quartz-monzonite dykes yields an age at 15.14 ± 0.06, Ma which is considered to be concordant to the zircon U-Pb on the same dyke (15.35 ± 0.05 Ma). The other dated biotite of two quartz-monzonite dyke shows an age at 15.92 ± 0.07 Ma is older than the obtained U-Pb ages on magmatic rocks. This biotite has certainly been affected by alteration which transformed it partly to chlorite, disturbing the Ar system.

The age obtained on the albitized quartz-monzonite dyke (15.63 ± 0.83 Ma) has an error larger than the other analyzed zircons. This is due to the presence of inherited old lead components. Even considering the large errors, this age is older than the hydrothermal event (14.5-14.4 Ma) and it has to be concluded that the dated quartz-monzonite dyke was emplaced before the enargite-pyrite veins and not after as assumed for a similar dyke by Silbermann and Noble (1977) based on field descriptions of Lacy (1949). It should be noted that Silbermann and Noble (1977) obtained a 15.2 ± 0.02 K/Ar age which they considered to be incorrect, but in the light of the new zircon U-Pb age at 15.65±0.83 Ma could be geologically meaningful.

εHf values for all zircon samples from magmatic rocks are negative and range between -1 and -4 (Fig. 16, Table 4), indicating crustal sources of magmatic liquids. Model ages range between 1.2 and 1.0 Ga which are ages typical for the Grenville-Sunsas orogeny (Dalziel et al., 1994; Santos et al., 2002; Chew and Schaltegger, 2007). This implies that the Mid-Miocene magmas at Cerro de Pasco (and probably at Colquijirca and Yanamate) were derived or strongly contaminated by old continental crust mainly formed during the Grenville-Sunsas orogeny. There is no significant difference in εHf between the accretionary lapilli tuff, the dykes and the dome.

Failed attempt to date the first mineralization stage

The sericite samples from the alteration halo adjacent to the pyrite-quartz body present in the diatreme breccia rocks and from the quartz-monzonite dyke yield ages between 18.15 ± 0.17 and 16.36 ± 0.28 Ma. These ages are considered to be geologically not significant because they are older than the zircon U-Pb ages obtained for the host rocks (15.4 to 15.1 Ma, the diatreme breccia is assumed to have an age close that of the accretionary lapilli tuff, 15.36 ± 0.03 Ma, and to that of the dated dome, 15.40 ± 0.07 Ma). Various factors can lead to older apparent ages. In the case of sericite, nuclear recoil occurs generally during the irradiation if the material is fine-grained. In the nuclear reaction $^{39}K(n,p)^{39}Ar$, the resulting $^{39}Ar_K$ can be potentially lost, which increases the $^{40}Ar/^{39}Ar$ ratio of the material and yields anomalously old ages (Turner and Cadogan, 1974). During the separation, therefore only coarse-grained sericite was selected (100-400 μm). Since the recoil distance, which will vary with the energy of the incoming neutrons, has been calculated to extend up to 0.5 μm (Turner and Cadogan, 1974), $^{39}Ar_K$ recoil on coarse-grained (>100 μm) mineral separates appears to be unimportant (Huneke and Smith, 1976). Nevertheless, the existence of subgrain diffusional domains could permit $^{39}Ar_K$ recoil even in coarse-grained sericite.

Alternatively, the presence of extraneous radiogenic argon can lead to older apparent ages (Dalrymple and Lanphere, 1969), and may consist of two types – excess ^{40}Ar and inherited ^{40}Ar. Excess ^{40}Ar results from other than in-place radioactive decay while inherited

^{40}Ar is incorporated in a system from mineral grains that retain an older reservoir of argon (Snee, 2002). As previously noted, some age spectra show argon excess. Small quantities of excess ^{40}Ar are involved in sample CPR 3, CPR 21, and CPR 96, because only the lower temperature extraction steps are affected, which results in a L-shaped spectrum. The age spectrum of the sericite sample CPR 21 (hosted in a quartz-monzonite dyke) reveals until the last steps, a decrease in the apparent age, suggesting that excess argon affected the whole sample. Since the other anomalously old sericite age spectra (CPR 115, CPR 498, and CPR 499) do not show argon excess, another process must be suggested. The elevated $^{40}Ar/^{36}Ar$ ratios of samples CPR 115, CPR 498, and CPR 499 can be explained as a result of incorporating radiogenic ^{40}Ar from degassing potassium-rich or old rocks (Heizler and Harrison, 1988). That the analyzed sericite contains inherited ^{40}Ar from an older reservoir is likely and this is supported by the Rb-Sr results on sericite and pyrite (see below). In a Sr mixing diagram (Fig. 25), a good linearity between $^{87}Sr/^{86}Sr$ vs. 1000/Sr is observed, suggesting that the different sericite samples reflect mixtures between detrital and newly-formed mica. The detrital mica could derive from the Excelsior Group phyllite present as clasts in the diatreme breccia. Thus, a significantly older reservoir of argon could have been incorporated in sericite grains and would therefore lead to older $^{40}Ar/^{39}Ar$ ages. We conclude that the obtained sericite ages do not have any geological significance.

Age constrains for the second mineralization stage

The first and possibly more significant age cluster for the second mineralization stage ranges from 14.5 to 14.4 Ma and is defined by alunite samples from the Venencocha area. Taking into account its large error, the alunite age at 14.1 ± 0.71 Ma from Santa Rosa (Table 6) is also compatible with the 14.5 - 14.4 Ma range. This age range is overlapped by K/Ar ages obtained by Silberman and Noble (1977) on altered plagioclase, sanidine and biotite from a dacitic dome and a quartz-monzonite dyke from the diatreme-dome complex at Cerro de Pasco. Therefore, it can be suggested that around 14.5 Ma, a hydrothermal event took place producing the advanced argillic alteration in domes, quartz-monzonite dykes and formed the enargite-pyrite veins at Venencocha and Santa Rosa. $^{40}Ar/^{39}Ar$ of alunite from altered domes and from halos around oxidized veins at Venencocha are in the same range (Fig. 20, Table 4).

The 12.39 ± 0.06 Ma, 12.13 ± 0.07 Ma, and 10.94 ± 0.10 Ma ages of the second cluster have the problem that each sample gives different ages over a time span which, in addition, is unrealistically long. The age scatter could point to a disturbance of the Ar system. Perhaps, late fluid circulation could have reset the alunite ages. That the fluid circulation can not be excluded is supported by the fact that the nearby Colquijirca district experienced the main phases of fluid circulation between 12.43 and 10.5 Ma (Bendezú, 2007). The hypothesis that the alunite ages have been in part reset by late fluid circulation is also supported by the stable isotope study which showed that oxygen and hydrogen isotope composition of fluids in equilibrium with the two alunite samples giving ages at 12.13 ± 0.07 and 12.39 ± 0.06 Ma (CPR 347 and CPR 351) deviate from the assumed mixing line meteoric-magmatic water (Baumgartner et al, Part III). Furthermore, these alunite samples have inclusions of woodhouseite (Ca-bearing aluminium-phosphate-sulfate mineral), which are absent in the first cluster alunite age. These inclusions could act as pathways for Ar loss during late fluid circulation, disturbing the alunite crystals. When these disturbed grains are step-heated, they should show evidence of argon loss in the age spectrum. The fact that this cannot be observed in the spectra shown in Fig. 18 could be due to dehydroxilation of the alunite during heating which would mask the disturbance, and result in an apparent undisturbed age.

From the geological and metallogenic point of view, there are also reasons to question the younger alunite ages at 12.39 ± 0.06, 12.13 ± 0.07 Ma, and 10.94 ± 0.1 Ma. If these ages were correct, they would imply the existence of three hydrothermal pulses (~14.5 Ma, ~12.2 Ma, and ~10.9 Ma) during the formation of essentially the same type of high sulfidation ores during the second mineralization stage and that the time gap separating each of the three pulses would be in the order of 1-2 Ma. Although this scenario is not impossible, it cannot be sustained by only three alunite scattered $^{40}Ar/^{39}Ar$ ages which, in addition, present indications of disturbance in the argon system.

Pb isotopes and Rb-Sr analyses

The obtained Pb isotope composition of pyrite coincides with that of galena of Cerro de Pasco (Mukasa et al. 1990) and falls in a cluster defined by galena samples from Morococha (Gunnesch et al., 1990), San Cristobal (Gunnesch et al., 1990; Moritz et al., 2001), Pasto Bueno (Doe and Zartman, 1979), and Colquijirca (Fontboté and Bendezú, 2001). These compositions were interpreted by Macfarlane et al. (1990) to correspond to magmatic mixing of enriched upper mantle-derived lead and radiogenic upper crustal rocks lead, i.e., a typical feature of the Miocene Metallogenic Belt in central Peru (Noble and McKee, 1999) and other deposits of the Subprovince II of Macfarlane et al. (1990) (Fig. 26).

The leachates of three sericite samples (L) from the phyllic alteration halo (first mineralization stage) fall also in the same cluster and are less radiogenic than the residal fractions. This observation is consistent with the hypothesis that the alteration halo was formed by the magmatic ore forming fluids. The fact that the residual fractions (R) and one leachate are slightly shifted towards more radiogenic ratios could reflect minor binary geochemical mixing between the magmatic lead component defined by the cluster mentioned above and a radiogenic end-member (Excelsior Group phyllite) or

could correspond to the fact reported by Chiaradia and Fontboté (2003) that in general, phyllosilicate residues are more radiogenic than the leached fractions because common lead is preferentially leached from labile sites. In-situ growth of radiogenic Pb by U-Th decay cannot explain the shift because with an alteration/mineralization age of 14 Ma, too high μ values, between 33.5 and 104, would be required.

In conclusion, at Cerro de Pasco the Pb isotope composition of ore minerals and sericite leachates reflect a predominant magmatic Pb input from the Miocene intrusions and the basement rocks contribution was minor. Similar interpretations have been proposed for other deposits in porphyry environment in central Peru (e.g., San Cristobal, Moritz et al., 2001 and Colquijirca, Fontboté and Bendezú, 1999).

Rb-Sr data of HCl leached sericite from argillic alteration halos at Cerro de Pasco display excess scatter in a $^{87}Sr/^{86}Sr$ vs. $^{87}Rb/^{86}Sr$ correlation diagram and therefore do not allow a geochronologically straightforward interpretation in terms of a Rb-Sr isochron (Fig. 24A), despite high Rb/Sr and variable $^{87}Sr/^{86}Sr$ ratios. This may indicate that the analyzed sericite samples are not cogenetic or were formed in the presence of geochemically heterogeneous, small-scale alteration fluid systems that had interacted with the wall rocks. These fluids were not capable of homogenizing the Rb-Sr system in the alteration products. The $^{87}Sr/^{86}Sr$ vs. $1000/^{86}Sr$ mixing diagram (Fig. 25) indicates that the analyzed sericite samples reflect geochemical mixtures of an unradiogenic Sr component and Sr derived from more radiogenic sources. Therefore, it can be suspected that the analyzed sericite samples contain inherited Rb-Sr components of preexisting mica. This is supported by the fact that their initial $^{87}Sr/^{86}Sr$ values corrected for in-situ ^{87}Rb decay partly unrealistically low values below 0.702 for ages of 10 Ma to 14 Ma. The unradiogenic Sr component may be represented by the overprinted, Sr-rich wall rocks with a $^{87}Sr/^{86}Sr$ ratio of ca. 0.7056 given by the y-intercept of the mixing line (R = 0.98) in Figure 25. This value is in good agreement with $^{87}Sr/^{86}Sr$ values of 0.7058 and 0.7057 for a dacitic dome and a quartz-monzonite dike within the Cerro de Pasco diatreme-dome complex reported by Noble and McKee (1999).

Given the obvious presence of inherited components in the sericite from the phyllic alteration, which would also fully explain the unrealistically old $^{40}Ar/^{39}Ar$ ages obtained for these samples, the geochronological significance of two-point Rb-Sr isochron ages calculated from R-L pairs (Table 8) as well as from leached sericite/corresponding pyrite data are highly doubtful. These ages are highly discordant internally and the isochron calculations reflect variable initial $Sr_{i(t)}$ ratios, which is again suggestive of non-cogenetic mixed components (cf. Schneider et al., 2003).

The Rb-Sr isochron age of 10.43 ± 0.18 Ma obtained for three of the HCl leachates (CPR 3, CPR 498, CPR 499; Fig. 24B), could to be significant from the analytical point of view. These leachates were produced from sericite derived from the same type of altered diatreme breccia, whereas the aberrant HCl leachate CPR 21 L in Figure 24b represents material sampled from a quartz-monzonite porphyritic dyke. In the Pb-Pb diagrams, the HCl leachates are more homogeneous compared to the leached residual sericite samples and also show more affinity to the pyrite and galena data (Fig. 26). From this, it may be suspected that the initial Rb-Sr system in the material removed by HCl leaching was also homogeneous, i.e. the preconditions of the isochron model are fulfilled.

However, if the age is correct, it would imply that HCl leaching of the sericite selectively removed components that were formed at a later time than the rest of the sericite. The obtained age of 10.43 ± 0.18 Ma could have been reset by the same event which, perhaps, was responsible of the presumed resetting of the "young" alunite ages (12-4- 10.9 Ma) discussed above.

Duration of magmatic-hydrothermal activity

Estimates of the longevity of igneous-related hydrothermal ore deposits vary significantly among deposits. Short-lived hydrothermal systems ranging from 100'000 to 300'000 yr include Koloula (Solomon Islands), Divide (Nevada), FSE-Lepanto, (Philippines) Round Mountain (Montana), Potrerillos, (Chile, Marsh et al., 1997 and references therein). Long-lived hydrothermal systems can last for several million years such as Butte, Montana (Meyer et al., 1968), La Escondida, Chile (Padilla Garza et al., 2001), Chuquicamata, Chile (Ossandón et al., 2001), Collahuasi, Chile (Masterman et al., 2005), Panasqueira, Portugal (Snee et al., 1988), and Colquijirca, Peru (Bendezú et al., 2003; Bendezú, 2007), among others. These long-lived hydrothermal systems consist of several short-lived hydrothermal pulses.

The zircon U-Pb ages attest magmatic activity at Cerro de Pasco between 15.4 and 15.1 Ma. One $^{40}Ar/^{39}Ar$ biotite age (15.1 Ma) falls in the same age range. These data indicate that for at least 350'000 yr, the magmatic system produced, successively, the diatreme, dacitic domes around the diatreme, and quartz-monzonite dykes within the diatreme-dome complex. No field evidences have been found so far that magmatic activity could have initated before the formation of the diatreme-dome complex. The K-Ar ages obtained by Silberman and Noble (1977) at ~14.5 Ma are younger than the U-Pb ages of this study and probably represent partial loss of radiogenic Ar, perhaps during the extensive hydrothermal activity at ~14.5 Ma at Cerro de Pasco.

Most alunite $^{40}Ar/^{39}Ar$ ages from alteration related to the second mineralization stage enargite-pyrite veins in Santa Rosa and Venencocha fall in a narrow range between 14.5 and 14.4 Ma. This age consistency suggests that the advanced argillic alteration in the domes and in the oxidized polymetallic veins east and west of the diatreme was produced during a short period of around 100'000 yr. $^{40}Ar/^{39}Ar$ age determinations on the carbonate replacement bodies were not possible because of the scarcity and small size of alunite; the geological evi-

dence point to a similar mineralization age. Therefore, and under the assumption that the younger alunite ages are reset, mineralization at Cerro de Pasco would end at around 14.4 Ma, i.e. around 500'000 yr after the main magmatic activity (15.4 – 15.1 Ma).

Since no reliable ages are available for the first mineralization stage, it can only stated that it is bracketed between the quartz-monzonite porphyry dykes and the second mineralization stage, i.e. between 15.1 and 14.5 Ma. Taking into account the similarity of the fluids forming both mineralization stages (Baumgartner et al, Part III), it is likely that the mineralization age for the first stage is close to that of the second one.

Conclusions

The conducted U-Pb and $^{40}Ar/^{39}Ar$ geochronological survey and additional published data reveal at least three Mid-Miocene magmatic events in the region between Cerro de Pasco and Colquijirca. They produced each a diatreme-dome complex at Yanamate (15.92 Ma), Cerro de Pasco (15.4 – 15.1 Ma), and Colquijirca (12.4 –12.12 Ma). Large mineralized systems are related to the last two complexes.

At Cerro de Pasco, the geochronology records magmatic activity between 15.4 and 15.16 Ma. During at least 350'000 yr, several magmatic pulses produced, successively, the diatreme, dacitic domes around the diatreme, and quartz-monzonite dykes which were mainly emplaced within the diatreme-dome complex and to a lesser extent, in the Pucará carbonate rocks. No field evidences have been found so far that magmatic activity could have begun before the formation of the diatreme-dome complex.

The timing of the hydrothermal system has been partly constrained by $^{40}Ar/^{39}Ar$ dating on alunite from altered domes and enargite-pyrite veins in the Venencocha and Santa Rosa areas, which are considered to be the equivalent of the second stage mineralization enargite-pyrite veins occurring on the western part of the open pit. Most of the $^{40}Ar/^{39}Ar$ ages on alunite related to the second mineralization stage fall within a narrow time span between 14.5 – 14.4 Ma. This age consistency suggests that the advanced argillic alteration in the domes and the enargite-pyrite veins in Venencocha and Santa Rosa have been produced during a short period of around 100'000 yr. $^{40}Ar/^{39}Ar$ age determinations on the second stage Fe-poor sphalerite bearing carbonate replacement bodies were not possible because of the scarcity and small size of alunite; the geological evidence point to a similar mineralization age. Three younger ages scattered at 12.39 ± 0.06, 12.13 ± 0.07 Ma, and 10.94 ± 0.1 Ma are believed to have been reset, perhaps by late circulating fluids. Therefore, magmatic-hydrothermal activity at Cerro de Pasco appears to have lasted for less than 1 My from 15.4 to 14.5 Ma, a relatively short time span for such a large mineralized system but a similar duration than that recognized at the nearby Colquijirca magmatic-hydrothermal system (in the order of 1.5 Ma, Bendezú et al., 2003, Bendezú, 2007).

Rb-Sr data for sericite indicate binary geochemical mixing between Miocene magmatic and Paleozoic basement sources. Pb isotopic compositions of pyrite and sericite, similar to those previously published of galena at Cerro de Pasco, Colquijirca, San Cristobal, and Morococha, are explained by magmatic mixing of enriched upper mantle-derived lead and radiogenic upper crustal rocks lead.

$^{40}Ar/^{39}Ar$ ages on sericite obtained for the first mineralization stage (pyrite-quartz body, pyrrhotite pipes and related Zn-Pb ore bearing Fe-rich sphalerite) are not reliable, probably due to inherited argon derived from micas contained in Paleozoic clasts within the diatreme breccia. This hypothesis is also supported by Rb-Sr data for sericite and Pb isotopes on pyrite and sericite. Thus, it can only stated that the first mineralization stage is bracketed in time between the quartz-monzonite dykes and the second mineralization stage, i.e. between 15.1 and 14.5 Ma.

This study points out the difficulties encountered during the $^{40}Ar/^{39}Ar$ analyses of sericite and to a lesser extent alunite. Sericite dating should be done with caution and a more robust geochronologic tool (e.g. U-Pb on zircon) must be combined to $^{40}Ar/^{39}Ar$ dating in altered terrains. Concerning alunite, a careful petrographic examination of alunite combined with electron microprobe analyses is necessary.

Acknowledgments

The present investigation is being carried out with the support of the Swiss National Science Foundation (FN 200020-108026) and of Volcan Compañía Minera, S.A. Ronner Bendezú and Urs Schaltegger, Geneva, are thanked for fruitful discussions. Catherine Ginibre is thanked for the SEM images and element distribution mapping and Pia Voldet for the REE analysis.

References

Angeles, C., 1999, Los sedimentos Cenozoicos de Cerro de Pasco; estratigrafia, sedimentacion y tectonica, *in* Machare, J., Benavides-Caceres, V., and Rosas, S., eds., Sociedad Geológica del Perú, Volúmen Jubilar, 5, p. 103-118.

Barazangi, M., and Isacks, B. L., 1976, Spatial distribution of earthquakes and subduction of the Nazca plate beneath South America: Geology, v. 4, p. 686-692.

Bendezú, R., 2007, Shallow polymetallic and precious metal mineralization associated to a Miocene diatreme-dome complex of the Peruvian Andes. The Colquijirca District., Terre & Environnement, p. 221.

Bendezú, R., Baumgartner, R., Fontboté, L., Page, L., Pecskay, Z., and Spikings, R., 2004, ~2 My of pulsed high sulfidation hydrothermal activity in the Cerro de Pasco-Colquijirca "super district", Peru. Com-bining furnace and infra-red laser $^{40}Ar/^{39}Ar$, and K/Ar analysis on alunite.: SEG Conference, Predicitve Mineral Discorvery under Cover, Perth,

p. 340-342.

Bendezú, R., Fontboté, L., and Cosca, M., 2003, Relative age of Cordilleran base metal lode and replacement deposits, and high sulfidation Au-(Ag) epithermal mineralization in the Colquijirca mining district, central Peru: Mineralium Deposita, v. 38, p. 683-694.

Birck, J. L., 1986, Precision K-Rb-Sr isotopic analysis: Application to Rb-Sr chronology: Chemical Geology, v. 56, p. 73-83.

Blichert-Toft, J., and Albarède, F., 1997, The Lu-Hf isotope geochemistry of chondrites and the evolution of the mantle-crust system: Earth and Planetary Science Letters, v. 148, p. 243-258.

Chew, D., and Schaltegger, U., U, Košler, J., Whitehouse, MJ, Gutjahr, M., Spikings, R.A., Mišković, A., 2007 U-Pb geochronologic evidence for the evolution of the Gondwanan margin of the north-central Andes. Geological Society of America Bulletin: Vol. preprint, No. 2006 pp. 0000

Chiaradia, M., and Fontboté, L., 2003, Separate lead isotope analyses of leachate and residue rock fractions: implications for metal source tracing in ore deposit studies: Mineralium Deposita, v. 38, p. 185-195.

Dalrymple, G. B., and Lanphere, M. A., 1969, Potassium-argon dating - Principles, techniques, and applications to conventional technique: Earth and Planetary Science Letters, v. 12, p. 300-308.

Dalrymple, G. B., and Lanphere, M. A., 1971, $^{40}Ar/^{39}Ar$ technique of K-Ar dating: a comparison with the conventional technique: Earth and Planetary Science Letters, v. 12, p. 300–308.

Dalziel, I. W. D., Dalla Salda, L. H., and Gahaghan, L. M., 1994, Paleozoic Laurentia-Gondwana interaction and the origin of the Appalachian-Andean mountain system: Geological Society of America Bulletin, v. 106, p. 243-252.

Defant, M. J., and Drummond, M. S., 1990, Derivation of some modern arc magmas by melting of young subducted lithosphere, v. 347, p. 662-665.

Doe, B. R., and Zartman, R. E., 1979, Plumbotectonics I, The Phanerozoic *in* Barnes, H. L., ed., Geochemistry of Hydrothermal Ore Deposits, 2ª ed., Wiley p. 22-70.

Einaudi, M. T., 1977, Environment of ore deposition at Cerro de Pasco, Peru: Economic Geology, v. 72, p. 893-924.

Fleck, R. J., Sutter, J. F., and Elliot, D. H., 1977, Interpretation of discordant $^{40}Ar/^{39}Ar$ age spectra of Mesozoic tholeiites from Antarctica.: Geochimica and Cosmochimica Acta, v. 41, p. 15-32.

Fontboté, L., and Bendezú, R., 1999, The carbonate hosted Zn-Pb San Gregorio deposit, Colquijirca District, central Peru, as a high sulfidation epithermal system, in (eds.), v. 1, Fifth Biennial SGA Meeting, Mineral Deposits: Processes to Processing, 1999, p. 495-498.

Fontboté, L., and Bendezú, R., 2001, The carbonate-hosted San Gregorio and Colquijirca (Zn-Pb-Ag) deposits (central Peru) as products of an epithermal high sulfidation system: Proexplo 2001 CD-ROM, Lima, Perú,, 2001, p. 19 p.

Gerstenberger, H., and Haase, G., 1997, A highly effective emitter substance for mass spectrometric Pb isotope ratio determinations: Chemical Geology, v. 136, p. 309-312.

Gunnesch, K. A., Baumann, A., and Gunnesch, M., 1990, Lead isotope variations across the central Peruvian Andes: Economic Geology, v. 85, p. 1384-1401.

Gutscher, M.-A., Maury, R., Eissen, J.-P., and Bourdon, E., 2000, Can slab melting be caused by flat subduction?: Geology, v. 28, p. 535-538.

Gutscher, M.-A., Olivet, J.-L., Aslanian, D., Eissen, J.-P., and Maury, R., 1999, The "lost Inca Plateau'': cause of flat subduction beneath Peru?: Earth and Planetary Science Letters, v. 171, p. 335-341.

Hanson, G. N., Simmons, K. R., and Bence, A. E., 1975, $^{40}Ar/^{39}Ar$ spectrum ages for biotite, hornblende, and muscovite in a contact metamorphic zone: Geochimica et Cosmochimica Acta, v. 39, p. 1269-1277.

Hasegawa, A. S., I, Selwyn, 1981, Subduction of the Nazca Plate beneath Peru as determined from seismic observations: Journal of Geophysical Research, v. 86, p. 4971-4980.

Heizler, M. T., and Harrison, T. M., 1988, Multiple trapped argon isotope components revealed by $^{40}Ar/^{39}Ar$ isochron analysis: Geochimica et Cosmochimica Acta, v. 52, p. 1295-1303.

Henry, C., Elson, H., McIntosh, W., Heizler, M., and Castor, S., 1997, Brief duration of hydrothermal activity at Round Mountain, Nevada determined from 40Ar/39Ar geochronology: Economic Geology v. 92, p. 807-826.

Horwitz, E. P., Dietz, M. L., and Fischer, D. E., 1991a, SREX: a new process for the extraction and recovery of strontium from acidic nuclear waste streams: Solvent Extraction Ion Exchange, v. 9, p. 1-25.

Horwitz, E. P., Dietz, M. L., and Fischer, D. E., 1991b, Separation and preconcentration of Sr from biological, environmental and nuclear waste samples by extraction chromatography using a crown ether: Analytical Chemistry, v. 63, p. 522-525.

Hoskin, P., and Schaltegger, U., 2003, The composition of zircon and igneous and metamorphic petrogenesis.: Reviews in Mineralogy and Geochemistry, v. 53, p. 27-62.

Huanqui, F., 1994, Ocurrencias de mineralización en la chimenea volcanica de Cerro de Pasco, Unpublished internal memorandum to A. Alvarez, Empresa Minera del Centro del Perú, p. 15.

Huneke, J. C., and Smith, S. P., 1976, The realities of recoil: ^{39}Ar recoil out of small grains and anomalous patterns in ^{40}Ar-^{39}Ar dating: Geochimica and Cosmochimica Acta, v. Suppl. 7 (Proceedings of the Seveth Lunar Science Conference), p. 1987-2008.

Jenks, W. F., 1951, Triassic to Tertiary stratigraphy near Cerro de Pasco, Peru: The Geological Society of America Bulletin, v. 62, p. 203-219.

Juliani, C., Rye, R. O. N., C.M.D., Snee, L. W., Correa-Silva, R. H., Monteiro, L. V. S., Bettencourt, J.

S., Neumann, R., and Alcover-Neto, A., 2005, Paleoproterozoic high-sulfidation mineralization in the Tapajos gold province, Amazonian Craton, Brazil; geology, mineralogy, alunite argon age, and stable-isotope constraints: Chemical Geology, v. 215, p. 95-125.

Koppers, A., 2002, ArArCALC: Software for $^{40}Ar/^{39}Ar$ age calculations: Computer Geosciences, v. 28, p. 605-619.

Krogh, T. E., 1973, A low-contamination method for hydrothermal decomposition of zircon and extraction of U and Pb for isotopic age determinations: Geochimica et Cosmochimica Acta, v. 37, p. 485-494.

Lacy, W. C., 1949, Types of pyrite and their relations to mineralization at Cerro de Pasco, Peru, Unpublished PhD Thesis, Harvard University, 193 p.

Landis, G. P., Snee, L. W., and Juliani, C., 2005, Evaluation of argon ages and integrity of fluid-inclusion compositions; stepwise noble gas heating experiments on 1.87 Ga alunite from Tapajos Province, Brazil: Chemical Geology, v. 215, p. 127-153.

Le Bas, M. J., Le Maitre , R. W., Streckeisen, A., and Zanettin, B., 1986, A Chemical Classification of Volcanic Rocks based on the Total-Alkali-Silica Diagram: Journal of Petrology, v. 27, p. 745-750.

Lee, J. K. W., Onstott, T. C., Cashman, K. V., Curebest, R. J., and Johnson, D., 1991, Incremental heating of hornblende in vacuo: Implications for $^{40}Ar/^{39}Ar$ geochronology and the interpretation of thermal histories: Geology, v. 19, p. 872-876.

Lo, C. H., and Onstott, T. S., 1989, ^{39}Ar recoil artifacts in chloritized biotite: Geochimica and Cosmochimica Acta, v. 53, p. 2697-2711.

Ludwig, K. R., 1980, Calculation of uncertainties of U-Pb isotope data: Earth and Planetary Science Letters, v. 46, p. 212-220.

Ludwig, K. R., 1999, Isoplot/Ex version 2.03. A geochronological tool kit for Microsoft Excel.: Berkeley Geochronological Center, Special Publication, p. 1-43.

Ludwig, K. Y., 2001, Isoplot/Ex, rev. 2.49. A Geochronological Toolkit for Microsoft Excel.: Berkeley Geochronology Center, Special Publication, v. 1a.

Macfarlane, A. W., Marcet, P., LeHuray, A. P., and Petersen, U., 1990, Lead isotope provinces of the Central Andes inferred from ores and crustal rocks: Economic Geology, v. 85, p. 1857-1880.

Marsh, T. M., Einaudi, M. T., and McWilliams, M., 1997, 40 Ar/ 39 Ar geochronology of Cu-Au and Au-Ag mineralization in the Potrerillos District, Chile: Economic Geology, v. 92, p. 784-806.

Martin, H., 1999, Adakitic magmas: modern analogues of Archaean granitoids: Lithos, v. 46, p. 411-429.

Masterman, G. J., Cooke, D. R., Berry, R. F., Walshe, J. L., Lee, A. W., and Clark, A. H., 2005, Fluid Chemistry, Structural Setting, and Emplacement History of the Rosario Cu-Mo Porphyry and Cu-Ag-Au Epithermal Veins, Collahuasi District, Northern Chile: Economic Geology, v. 100, p. 835-862.

Mattinson, J. M., 2005, Zircon U-Pb chemical abrasion ("CA-TIMS") method: Combined annealing and multi-step partial dissolution analysis for improved precision and accuracy of zircon ages: Chemical Geology, v. 220, p. 47-66.

McDougall, I., and Harrison, T. M., 1999, Geochronology and Thermochronology by the $^{40}Ar/^{39}Ar$ Method. 2nd ed., Oxford Univ. Press, Oxford, UK.

McLaughlin, D. H., 1924, Geology and physiography of the Peruvian Cordillera, Department of Junin and Lima: Geological Society of America Bulletin, v. 35, p. 591-632.

Meyer, C., Shea, E. P., Goddard, C., and Staff, 1968, Ore deposits at Butte, Montana, *in* Ridge, J. D., ed., Ore deposits of the United States, 1933-1967, 2, AIME, New York, p. 1372-1416.

Min, K., Mundil, R., Renne12, P. R., and Ludwig, K. R., 2000, A test for systematic errors in 40Ar/39Ar geochronology through comparison with U/Pb analysis of a 1.1-Ga rhyolite: Geochimica et Cosmochimica Acta, v. 64, p. 73-98.

Moritz, R., Beuchat, S., Chiaradia, M., Sallier, B., and Lisboa, H., 2001, Zn-Pb mantos and veins at Domo de Yauli, Central Peru: two products of one hydrothermal system with common Pb and S sources, but contrasting fluid inclusion characteristics: Mineral Deposits at the beginning of the 21st Century, Crakow, 2001, p. 173-176.

Mukasa, S. B., Vidal C., C. E., and Injoque-Espinoza, J., 1990, Pb isotope bearing on the metallogenesis of sulfide ore deposits in central and southern Peru: Economic Geology, v. 85, p. 1438-1446.

Muntean, J., and Einaudi, M., 2001, Porphyry-epithermal transition: Maricunga belt, Northern Chile: Economic Geology, v. 96, p. 743-772.

Noble, D. C., and McKee, E. H., 1999, The Miocene metallogenic belt of central and northern Peru: Society of Economic Geologists Special Publication, v. 7, p. 155-193.

Ossandón, C., Freraut, C. R., Gustafson, L. B., Lindsay, D. D., and Zentilli, M., 2001, Geology of the Chuquicamata Mine: A Progress Report: Economic Geology, v. 96, p. 249-270.

Padilla Garza, R. A., Titley, S. R., and Pimentel B., F., 2001, Geology of the Escondida Porphyry Copper Deposit, Antofagasta Region, Chile: Economic Geology, v. 96, p. 307-324.

Perkins, C., McDougall, I., Claoue-Long, J., and Heithersay, P. S., 1990, $^{40}Ar/^{39}Ar$ and U-Pb geochronology of the Goonumbla porphyry Cu-Au deposits, New South Wales, Australia: Economic Geology, v. 85, p. 1808-1824.

Pilger, R. H. J., 1981, Plate reconstructions, aseismic ridges, and low-angle subduction beneath the Andes: Geological Society of America Bulletin, v. 92, p. 448-456.

Potts, P. J., Thorpe, O. W., and Watson, J. S., 1981, Determination of the rare-earth element abundances in 29 international rock standards by instrumental neutron activation analysis: A critical appraisal of

calibration errors: Chemical Geology, v. 34, p. 331-352.

Reich, M., Parada, M. A., Palacios, C., Dietrich, A., Schultz, F., and Lehmann, B., 2003, Adakite-like signature of Late Miocene intrusions at the Los Pelambres giant porphyry copper deposit in the Andes of central Chile: metallogenic implications: Mineralium Deposita, v. 38, p. 876-885.

Renne, P. R., Swisher, C. C., Deino, A. L., Karner, D. B., Owens, T. L., and DePaolo, D. J., 1998, Intercalibration of standards, absolute ages and uncertainties in $^{40}Ar/^{39}Ar$ dating: Chemical Geology, v. 145, p. 117-152.

Richter, S., Goldberg, S. A., Mason, P. B., Traina, A. J., and Schwieters, J. B., 2001, Linearity tests for secondary electron multipliers used in isotope ratio mass spectrometry: International Journal of Mass Spectrometry, v. 206, p. 105-127.

Rogers, R., 1983, Structural and geochemical evolution of a mineralized volcanic vent at Cerro de Pasco, Peru, Unpublished PhD Thesis, University of Arizona, 116 p.

Rosenbaum, G., Giles, D., Saxon, M., Betts, P. G., Weinberg, R. F., and Duboz, C., 2005, Subduction of the Nazca Ridge and the Inca Plateau: Insights into the formation of ore deposits in Peru: Earth and Planetary Science Letters, v. 239, p. 18-32.

Santos, J. O., Easton, R. M., Potter, P. E., Rizzotto, G. A., Hartmann, L. A., and McNaughton, N. J., 2002, The Sunsas Orogen in western Amazon Craton, South America and correlation with the Grenville Orogen of Laurentia, based on U-Pb isotopic study of detrital and igneous zircons: Geological Society of America Abstracts with Programs, 2002, p. 272.

Schneider, J., Haack, U., and Stedingk, K., 2003, Rb-Sr dating of epithermal vein mineralization stages in the eastern Harz Mts. (Germany) by paleomixing lines: Geochimica and Cosmochimica Acta, v. 67, p. 1803-1819.

Schumacher, R., and Schmincke, H.-U., 1995, Models for the origin of accretionary lapilli: Bulletin of Volcanology, v. 56, p. 626-639.

Seedorff, E., Dilles, J., Proffett, J., Einaudi, M., Zurcher, L., Stavast, W., Johnson, D., and Barton, M., 2005, Porphyry deposits: characteristics and origin of hypogene features: Economic Geology One Hundred Anniversary Volume p. 251-298.

Silberman, M. L., and Noble, D. C., 1977, Age of igneous activity and mineralization, Cerro de Pasco, central Peru: Economic Geology, v. 72, p. 925-930.

Snee, L. W., 2002, Argon thermochronology of mineral deposits - A review of analytical methods, formulations, and selected applications, U.S. Geological Survey Bulletin, 2194, p. 1-39.

Snee, L. W., Sutter, J. F., and Kelly, W. C., 1988, Thermochronology of economic mineral deposits; dating the stages of mineralization at Panasqueira, Portugal, by high-precision $^{40}Ar/^{39}Ar$ age spectrum techniques on muscovite: Economic Geology, v. 83, p. 335-354.

Soler, P., 1991, Contribution à l'étude du magmatisme associé aux marges actives. Pétrographie, géochimie et géochimie isotopique du magmatisme Crétacé à Pliocene le long d'une transversale des Andes du Pérou central. Implications géodynamques et métallogéniques., Unpublished PhD thesis, Université Pierre et Marie Curie, Paris VI, 777 p.

Soler, P., and Bonhomme, M., 1988, Oligocene magmatic activity and associated mineralization in the polymetallic belt of central Peru: Economic Geology, v. 83, p. 657-663.

Stacey, J. S., and Kramers, J. D., 1975, Approximation of terrestrial lead isotope evolution by a two-stage model.: Earth and Planetary Science Letters, v. 26, p. 207-221.

Steiger, R. H., and Jäger, E., . 1977, Subcommission on geochronology: Convention on the use of decay constants in geo- and cosmochronology: Earth and Planetary Science Letters, v. 36, p. 359-362.

Todt, R. A., Cliff, A., Hanser, A. W., and Hofmann, 1996, Evaluation of a 202Pb-205Pb double spike for high-precision lead isotope analysis, *in* Basu, A., and Hart, S., eds., Earth Processes: Reading the Isotopic Code, Geophys. Monograph 95, Am. Geophys. Union, p. 429-437.

Turner, G., and Cadogan, P. H., 1974, Possible effects of ^{39}Ar recoil in ^{40}Ar-^{39}Ar dating: Geochimica and Cosmochimica Acta, v. Suppl. 5 (Proceedings of the Fifth Lunar Science Conference), p. 1601-1615.

Vasconcelos, P. M., Brimhall, G. H., Becker, T. A., and Renne, P. R., 1994, $^{40}Ar/^{39}Ar$ analysis of supergene jarosite and alunite: implications to the paleoweathering history of the western USA and West Africa: Geochimica and Cosmochimica Acta, v. 58, p. 401-420.

Ward, H. J., 1961, The pyrite body and copper orebodies, Cerro de Pasco Mine, central Peru: Economic Geology, v. 56, p. 402-422.

Warnaars, F. W., Smith, W. H., Bray, R. E., Lanier, G., and Shafiqullah, M., 1978, Geochronology of igneous intrusions and porphyry copper mineralization at Bingham, Utah: Economic Geology, v. 73, p. 1242-1249.

Wendt, I., and Carl, C., 1991, The statistical distribution of the mean squared weighted deviation: Chemical Geology, v. 86, p. 275–285.

Winchester, J. A., and Floyd, P. A., 1977, Geochemical discrimination of different magma series and their differentiation products using immobile elements: Chemical Geology, v. 20, p. 325-343.

Part III

A fluid inclusion and stable isotope study of the Cerro de Pasco district: Implications for the depositional environment of polymetallic mineralization.

Regina Baumgartner, Lluís Fontboté

Department of Mineralogy, University of Geneva, 13 Rue des Maraichers, Switzerland

And Torsten Vennemann

Institute of Mineralogy and Geochemistry, University of Lausanne Anthropole, Switzerland

Abstract

The large Cerro de Pasco epithermal Cordilleran base-metal deposit in central Peru is located on the eastern margin of a Mid-Miocene diatreme-dome complex and comprises two mineralization stages. The first mineralization stage (I) consists of a large pyrite-quartz body (IA) emplaced mainly in carbonate rocks from the Pucará Group, and to a lesser extent, the diatreme breccia. This pyrite-quartz body was, in part, replaced by pipe-like pyrrhotite bodies zoned outwards to carbonate replacement Zn-Pb ores (IB). The second mineralization stage is composed of zoned Cu-Ag-(Au-Zn-Pb) enargite-pyrite veins with advanced argillic alteration hosted in the diatreme breccia and zoned Zn-Pb-(Bi-Ag-Cu) carbonate replacement bodies. In the Venencocha and Santa Rosa areas, located 2.5 km northwest of Cerro de Pasco, advanced argillic altered dacitic domes and oxidized veins with advanced argillic altered halos occur. The latter veins are possibly the oxidized equivalent of the enargite-pyrite veins.

Microthermometric data on fluid inclusions in quartz indicate that the different ores of the first mineralization stage formed at similar temperatures and moderate salinities (pyrite-quartz body: 200 – 275°C and 0.2 – 6.8 wt % NaCl equiv, pyrrhotite bodies: 192 – 250°C and 1.1 – 4.3 wt % NaCl equiv, and Zn-Pb ores: 183 – 212°C and 3.2 – 4.0 wt % NaCl equiv). These values are in the same range as those obtained for fluid inclusions of quartz and sphalerite from the second stage ores (enargite-pyrite veins: 187–293°C and 0.2–5.2 wt % NaCl equiv, carbonate replacement bodies quartz: 178–265°C and 0.2–7.5 wt % NaCl equiv, carbonate replacement bodies sphalerite: 168–222°C, and Venencocha: 245–261 and 3.2–7.7 wt % NaCl equiv). Oxygen and hydrogen isotope compositions have been measured for kaolinite from carbonate replacement bodies ($\delta^{18}O$ = 5.3 to 11.5 ‰, δD = –82 to –114 ‰) and in alunite from the Venencocha and Santa Rosa areas ($\delta^{18}O$ = 1.9 to 6.9 ‰, δD = –56 to –73 ‰). Oxygen isotope compositions of quartz from the first and second mineralization stages have $\delta^{18}O$ values from 9.1 to 17.8 permil. Calculated fluids in equilibrium with kaolinite and alunite have $\delta^{18}O$ values of 2.0 to 8.2 permil and δD values of –69.4 to –96.8 permil, l and –1.4 to –6.4 ‰ and –62 to –79 ‰, respectively. Sulfur isotope compositions of sulfides from both stages have a narrow range of $\delta^{34}S$ values between –3.7 and 4.2 permil and sulfates from the second stage between 4.2 to 31.2 permil. The microthermometric data and the stable isotope studies show that the ore-forming fluids define two mixing trends. The first trend reflects mixing between a saline magmatic end-member and an isotopically exchanged hydrothermal end-member of meteoric origin. According to the available data, for all ore types, except for the enargite-pyrite veins from the western part of the open pit, the saline end-member could correspond to a hypersaline magmatic fluid. For the enargite-pyrite veins, the saline magmatic end-member could also correspond to a contracted vapor separated at great depth or a single phase fluid. The second trend is revealed by the stable isotope results of alunite and points toward mixing of volcanic SO_2 vapor plumes and unexchanged meteoric water.

The hydrothermal system at Cerro de Pasco was emplaced at shallow levels (on the order of 500 m) in the epithermal part of a porphyry environment. The similar temperatures and salinities obtained for the first (pyrite-quartz body, pyrrhotite pipes and related Zn-Pb ores) and second mineralization stages (enargite-pyrite veins and carbonate replacement bodies) jointly with the stable isotope study has permitted to conclude that they are linked and represent successive mineralizing stages of Cordilleran base metal deposits.

Introduction

Recent studies have mainly concentrated on fluid evolution in magmatic-hydrothermal systems by focusing on porphyry copper and epithermal disseminated high sulfidation Au-(Ag) deposits (Einaudi et al., 2003; Bethke et al., 2005; Fifarek and Rye, 2005; Heinrich, 2005). However, less focus has been placed on epithermal Cordilleran base-metal deposits. A number of Cordilleran base metal deposits are known to occur superimposed on porphyry-copper deposits (e.g. Butte, Morococha) while others have no identified link to mineralized porphyries (Einaudi et al., 2003). Furthermore, in a porphyry environment, epithermal high sulfidation Au-(Ag) deposits may be superimposed by Cordilleran deposits (e.g. Bendezú et al., 2003).

Cerro de Pasco, an epithermal Cordilleran base-metal deposit located in central Peru and spatially related to a Mid-Miocene diatreme-dome complex , is a Zn-Pb-Ag-Cu-Bi deposit, with post 1950 production plus known resources amounting to more than ~175 Mt @ 7 percent Zn and 2 percent Pb as well 3 oz/t Ag (compiled according to and Cerro de Pasco geological staff, 1950 and Einaudi, 1977). In addition, prior to 1950, 1200 Moz Ag, 2 Moz of Au, and around 50 Mt @ 2 percent Cu were mined (our estimation according to data of Jiménez, 1924; Geological staff of Cerro de Pasco Corporation, 1950; Einaudi, 1977; Fischer, 1977; Baumgartner et al., 2006). Contributions on the geology and mineralization of Cerro de Pasco include McLaughlin (1924); Bowditch (1935), Graton and Bowditch, (1936), Lacy (1949), Geological staff of Cerro de Pasco Corporation (1950), Jenks (1951), Ward (1961), Petersen (1965), Einaudi (1968, 1977), Silberman and Noble (1977), Mégard (1978), Rivera (1997), Angeles (1999), Baumgartner et al. (2003). Several unpublished reports of Cerro de Pasco Corporation, CENTROMIN, and Volcán Compañía Minera S.A contain additional information on Cerro de Pasco.

The Cerro de Pasco deposit comprises two mineralization stages with contrasting mineralogy and depositional environments (Baumgartner and Fontboté, Part I). The first mineralization stage occurs on the eastern margin of a Mid-Miocene diatreme-dome complex and consists of a large pyrite-quartz body replacing Upper Triassic-Lower Jurassic Pucará carbonate rocks and, to a lesser extent, the diatreme breccia. Pipe-like pyrrhotite bodies, which are zoned outwards to Zn-Pb mineralization, were subsequently emplaced within the pyrite-quartz body and mainly replaced the Pucará Group rocks. The second mineralization stage superimposes partially the first stage and includes Cu-Ag-(Au-Zn-Pb) enargite-pyrite zoned veins hosted by the diatreme breccia, located in the western part of the deposit, and Zn-Pb-(Bi-Ag-Cu) replacement bodies hosted by the Pucará Group rocks, situated in the eastern and central part of the deposit.

The present contribution presents a fluid inclusion and stable isotope study of ore and gangue minerals. Samples have been collected from the first and second mineralization stages within the open pit as well as in the Venencocha area, located on the northwestern margin of the diatreme, 2.5 km NW of the open pit. The Venencocha area contains advanced argillic alteration zones in domes and as halos around oxidized veins. Fluid inclusions have been measured in quartz (from the first and second mineralization stages) and sphalerite (second mineralization stage). Cathodoluminescence imaging has been used in the fluid inclusion survey in order to highlight different quartz generations. The microthermometric and stable isotope measurements of sulfide, sulfate, carbonate, and silicate minerals from the first and second mineralization stages constrain the temperature, salinity and origin of the ore-forming fluids and provide information on the spatial and temporal evolution of these hydrothermal fluids at Cerro de Pasco.

District and Deposit Geology at Cerro de Pasco

Cerro de Pasco is located on the high Andean plateau of central Peru, at an elevation of 4300 m. A regional NS "Longitudinal Fault" juxtaposes Paleozoic metamorphic rocks with Mesozoic sedimentary rocks (. 1). In the mine area, the Longitudinal Fault is believed to be represented by high-angle N15°W striking reverse faults (Fig. 2). The oldest exposed rocks at Cerro de Pasco are slightly metamorphosed shale, phyllite and quartzite of the Devonian Excelsior Group. On the eastern side of the diatreme dome complex, the Excelsior Group phyllite forms an anticline, named the Cerro anticline (Fig. 2). This Group is overlain in an angular unconformity by sandstone and conglomerate with pebbles of quartz and Excelsior-type argillaceous clasts belonging to the Permo-Triassic Mitu Group (McLaughlin, 1924; Jenks, 1951). Outcrops of the Mitu Group are rare in the vicinity of the Cerro de Pasco district and become more widespread to the south (Fig. 1). Above the half eastern part of the district, the Mitu Group is covered by a thick (up to 3000m) Upper Triassic-Lower Jurassic carbonate sequence belonging to the Pucará Group (Angeles, 1999). This carbonate sequence is principally composed of thick-bedded, dark-colored limestone and dolomite with occasional shale interbeds and zones of siliceous concretions (Jenks, 1951). In the Cerro de Pasco open pit area, the Pucará Group is thinner (probably less than 500 m) because of the presence of the Cerro anticline. On the western part of the district, the Pucará Group is only 300m thick and consists of thin-bedded, light-colored limestone (Jenks, 1951). From the Eocene to Lower Miocene, multiple folding episodes with a NE-SW axial direction occurred and brought the Excelsior and the Mitu Group rocks to shallower levels. In the Mid-Miocene, magmatic activity affected the region (Silberman and Noble, 1977; Bendezú et al, 2003; Baumgartner et al., Part II; Bendezú, 2007). At Cerro de Pasco, similarly as in the nearby Colquijirca district, magmatism consisted of the formation of a dacitic diatreme fol-

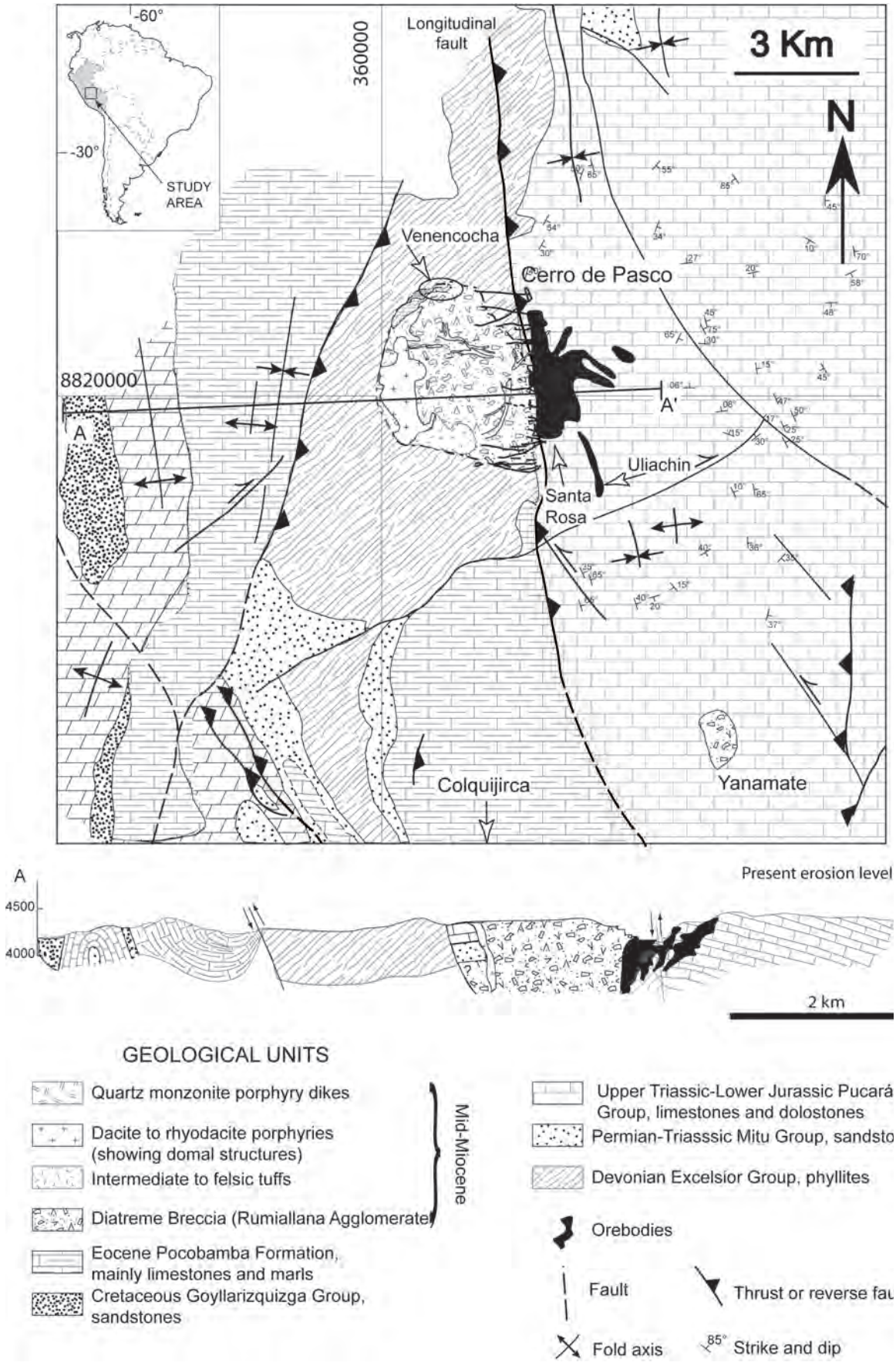

Fig. 1: *Geology (modified from Bendezú et al. 2003) and schematic west-east (A-A') cross section of the Cerro de Pasco district. The lower cross-section illustrates the Mid-Miocene topography at Cerro de Pasco.*

lowed by multiple dacitic porphyritic domes (15.4 Ma) and quartz-monzonite porphyritic dykes (15.4 – 15.1 Ma, Baumgartner et al. Part II).

Erosion removed part of the diatreme-dome complex as well as surrounding rocks, as suggested by the presence of collapsed blocks of Mitu and Pucará Group rocks inside the diatreme and the absence of them in the vicinity of the diatreme (Fig. 1 and 2). Most probably, the total erosion from the Mid-Miocene to present is in the order of 500 m.

At Cerro de Pasco, two mineralization stages have been recognized (Einaudi, 1977, Baumgartner and Fontboté, Part I). The first stage include a large pyrite-quartz body and pyrrhotite pipes zoned to Zn-Pb ores in carbonate rocks while the second stage comprises EW trending Cu-Ag-Au-(Zn-Pb) enargite-pyrite veins hosted in the diatreme breccia and Zn-Pb-(Bi-Ag-Cu) carbonate replacement bodies.

First mineralization stage

The large pyrite-quartz body replaced mainly the Pucará Group carbonate rocks and to a lesser extent the rocks from the diatreme-dome complex (Fig. 2 and 3). Sedimentary textures as well as breccia textures are locally recognizable. Pyrite constitutes more than 90 percent of the body and black and red chalcedonic silica and quartz account for the remaining 10 percent. Following the contour of the pyrite-quartz body and up to a distance of 50 m, an alteration halo occurs and is characterized by the assemblage sericite-pyrite-quartz, typical of phyllic alteration.

Vertical steep pipe-like pyrrhotite bodies partly replaced the pyrite-quartz body along its whole vertical extension (Figs. 4 and 5). These pyrrhotite pipes show an upward and outward zonation with the metal suite W-Sn-Cu-Zn-Pb. The core zone, only observed in deep levels, is composed of the assemblage pyrrhotite-quartz-wolframite. The intermediate level assemblage consists of pyrrhotite-sphalerite-chalcopyrite-stannite (Einaudi, 1977). The outer zone, which is present in the whole vertical extension of the pyrrhotite bodies and which includes the Zn-Pb ore, consists of the association pyrrhotite, sphalerite Fe-rich sphalerite (up to 25 mol % FeS, Baumgartner and Fontboté, Part I) and arsenopyrite with minor marcasite, tennantite, chalcopyrite, chlorite, sericite, siderite, and calcite. The Zn-Pb ores, characterized by Fe-rich sphalerite, form extensive carbonate replacements in the Pucará Group rocks (Fig. 3). The pipe-like pyrrhotite bodies The transition zone between the pyrrhotite pipes and the Zn-Pb ores contains a fine-grained mixture of pyrite and marcasite, attesting to the alteration of pyrrhotite. The mineral assemblages of the first mineralization stage are typical of low sulfidation states (Baumgartner and Fontboté, Part I). The pyrite-quartz body and the Fe-rich sphalerite-bearing Zn-Pb ores are crosscut on the western part of the deposit by enargite-pyrite veins belonging to the second mineralization stage.

Second mineralization stage

The second mineralization stage is composed of east-west Cu-Ag-Au-(Zn-Pb) enargite-pyrite veins hosted by the diatreme breccia on the western side of the open pit and of Zn-Pb-(Bi-Ag-Cu) carbonate replacement bodies located mainly on the eastern but also central part of the open pit (Fig. 3, 4, and 6). This second stage is structurally controlled, the western veins following steep dipping E-W faults and the carbonate replacement bodies along sub-vertical faults with N35°E, N120°E, and N170°E orientations (Fig. 3 and 6); subordinately, the carbonate replacement bodies are controlled by favorable Pucará Group carbonate horizons. The second mineralization stage is characterized by a well-developed zonation. In the orebodies hosted by Pucará carbonate rocks, the main orebodies studied in this work, i.e. Cuerpo Nuevo, Cayac Noruega, several orebodies in the Colas area, and San Alberto (Fig. 3), the core contains pyrite-famatinite and shows advanced argillic alteration assemblages, including alunite-quartz. This core grades out to an intermediate zone containing tetrahedrite, Bi- and Ag-rich phases, and pyrite; aluminum phosphate-sulfate minerals (APS) such as hinsdalite ($(Pb,Sr)Al_3(PO_4)(SO_4)(OH)_6$) and woodhouseite ($CaAl_3(PO_4)(SO_4)(OH)_6$). Kaolinite-(dickite) are common alteration minerals of this zone. The outer zone is the best developed and consists of sphalerite and galena plus kaolinite, barite, and alunite group minerals such as hinsdalite. Locally barite appears late in the paragenetic sequence and does not precipitate with sulfides. The outermost zone is composed of magnetite, hematite and Fe-Mn-Zn carbonates. Small late calcite veins are present in this zone. The carbonate-hosted Ag- and Bi-rich intermediate and Zn-Pb-Ag outer zones constitute most of the present economic resource of Cerro de Pasco. In addition to the main carbonate replacement orebodies, small uneconomic centimeter-scale sphalerite-galena-Fe-Mn-Zn carbonate veins occur in the northeastern part of the open pit (NE small vein in Fig. 2 and 3) and are also part of the carbonate replacement bodies.

The veins hosted by the diatreme breccia, on the western part of the deposit, show a less developed zonation consisting of an enargite-pyrite core with advanced argillic alteration including alunite, quartz, zunyite, diaspore and APS-minerals such as svanbergite ($SrAl_3(PO_4)(SO_4)(OH)_6$) and woodhouseite. The intermediate zone is composed of tennantite, stibnite, and Bi-minerals, accompanied by APS-minerals and an outer zone that is poorly developed with small amounts of Fe-poor sphalerite and galena. The presence of porous volcanic rocks, interpreted as vuggy quartz, in the vein walls suggests that the enargite-pyrite veins were emplaced in a zone of enhanced permeability. Enargite and quartz fill vugs present in the vuggy quartz.

In this study, samples from an area located on the northwestern margin of the diatreme-dome complex, the Venencocha area, which is 2.5 km NW of the Cerro de Pasco open pit, have also been analyzed. Venencocha presents two occurrences with advanced argillic

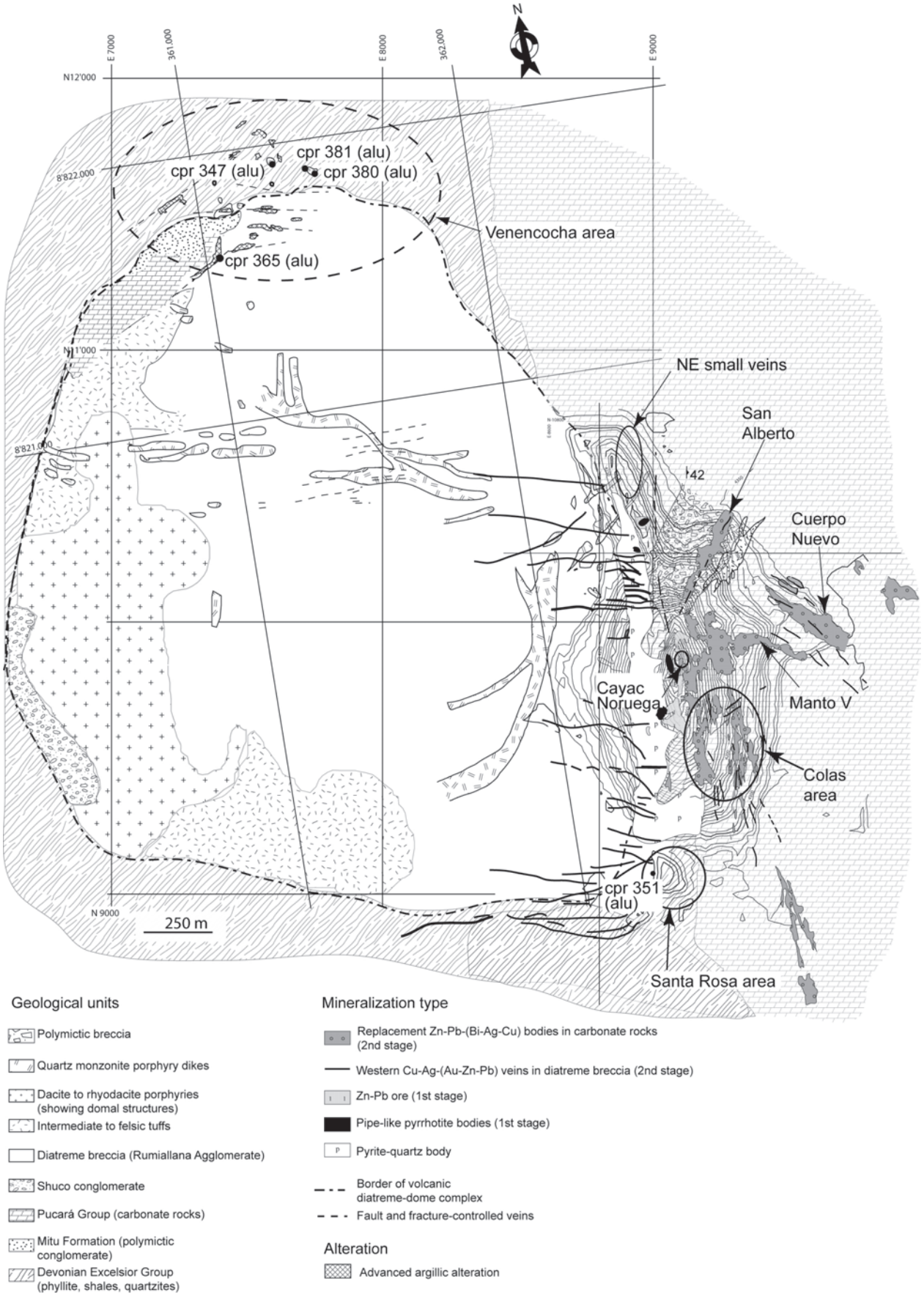

Fig. 2: *Geological map of the diatreme-dome complex at Cerro de Pasco, compiled from Rogers (1983) and Huanqui (1994). The mineralization types occurring in the open pit (plain topographic black lines) are shown, as well as the names of the principal orebodies studied in this contribution.*

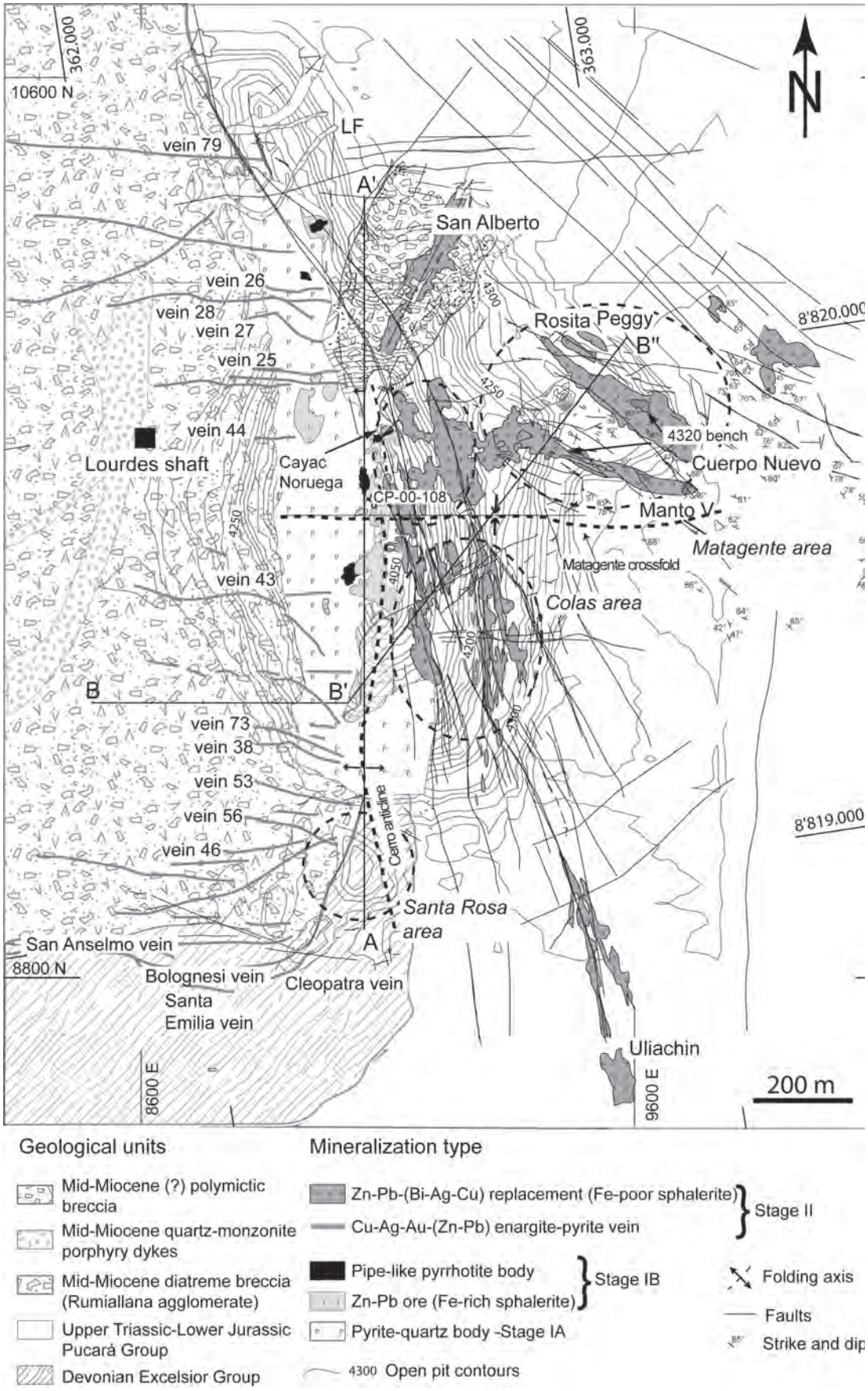

Fig. 3: *Geological map of the Cerro de Pasco open pit showing the rock units, the structure, and the different mineralization stages, based on maps of the Cerro de Pasco Geology staff. Lines labeled A-A' and B-B' indicate locations of cross sections in Figure 4 and 5.*

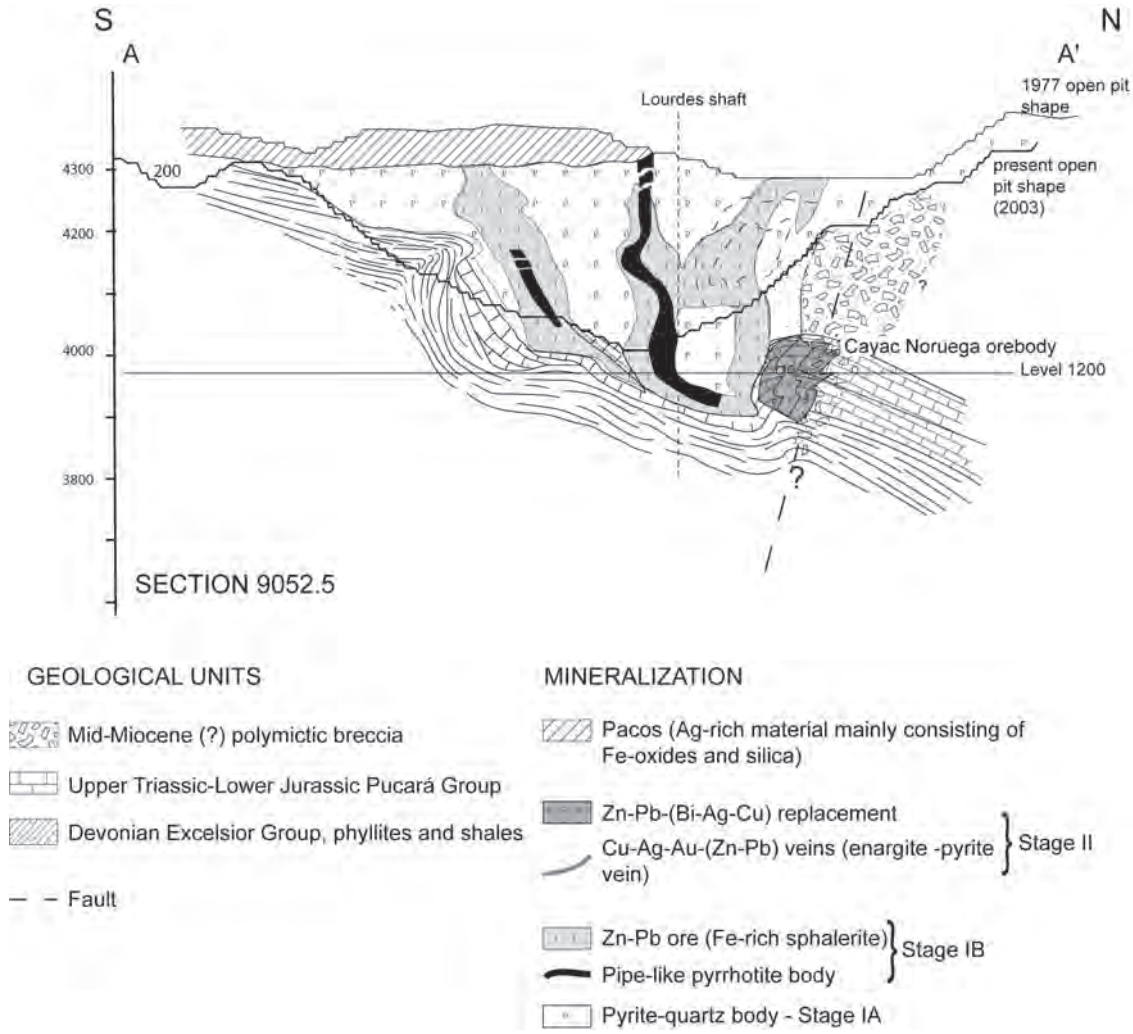

Fig. 4: *N-S cross section (A-A' in Fig. 3) showing pipe-like pyrrhotite bodies and related Zn-Pb ores from the first mineralization stage emplaced in the pyrite-quartz body and in the Triassic-Jurassic Pucará carbonate rocks, modified from Einaudi (1977). The second mineralization stage is also shown based on underground workings (contours absent in the section).*

alteration. The first type of occurrence corresponds to advanced-argillic-altered domes with alunite, quartz, and small amounts of zunyite, diaspore and pyrite while the second type corresponds to alteration halos from oxidized veins. These alteration halos consist of alunite, quartz, zunyite, and diaspore. The Venencocha oxidized veins contain massive goethite-jarosite and minor hematite and are similar to the enargite-pyrite veins on the western part of the open pit and were thus considered to be part of the second mineralization stage. In contrast, the advanced argillic alteration in the domes may either correspond to the alteration related to the enargite-pyrite veins or a previous hydrothermal pulse.

Approach and analytical techniques

Analytical techniques and minerals used in this study are summarized in Table 1. The sample locations are reported in Figure 3 and Appendix 1. Microthermometric measurements were made mainly on fluid inclusions in quartz from the first mineralization stage as well as in quartz and sphalerite from the second mineralization stage. Stable isotope compositions have been measured on sulfide and quartz from the first mineralization stage and on silicate, sulfate, sulfide, and carbonate from the second stage (Table 1). In addition, a detailed cathodoluminescence (CL) survey on quartz from both mineralization stages was done to identify different quartz generations within a single grain and to correlate them with fluid inclusion assemblages located using transmitted light microscopy.

A fluid inclusion study of quartz crystals from the first mineralization stage pyrite-quartz body was conducted on samples located more than 10m from

Table 1: Summary of analytical techniques and mineral used in this study.

	First mineralization stage			Second mineralization stage		Venencocha	
	Pyrite-quartz body	Pipe-like pyrrhotite bodies	Zn-Pb ore	Enargite veins	Carbonate replacement bodies	Domes	Oxidized veins
Fluid inclusions							
Mineral	Quartz	Quartz	Quartz	Quartz Enargite	Quartz Sphalerite		Quartz
Isotope compositions							
$\delta^{18}O$	Quartz			Quartz Barite Alunite (Santa Rosa)	Quartz Kaolinite Barite Fe-Mn-Zn carbonates (+ late calcite)	Alunite	Quartz Alunite
δD				Alunite (Santa Rosa)	Kaolinite	Alunite	Alunite
$\delta^{34}S$		Pyrite Sphalerite Galena		Barite Pyrite Enargite Alunite (Santa Rosa)	Barite Pyrite Sphalerite Galena	Alunite	Alunite
$\delta^{13}C$					Fe-Mn-Zn carbonates (+ late calcite)		

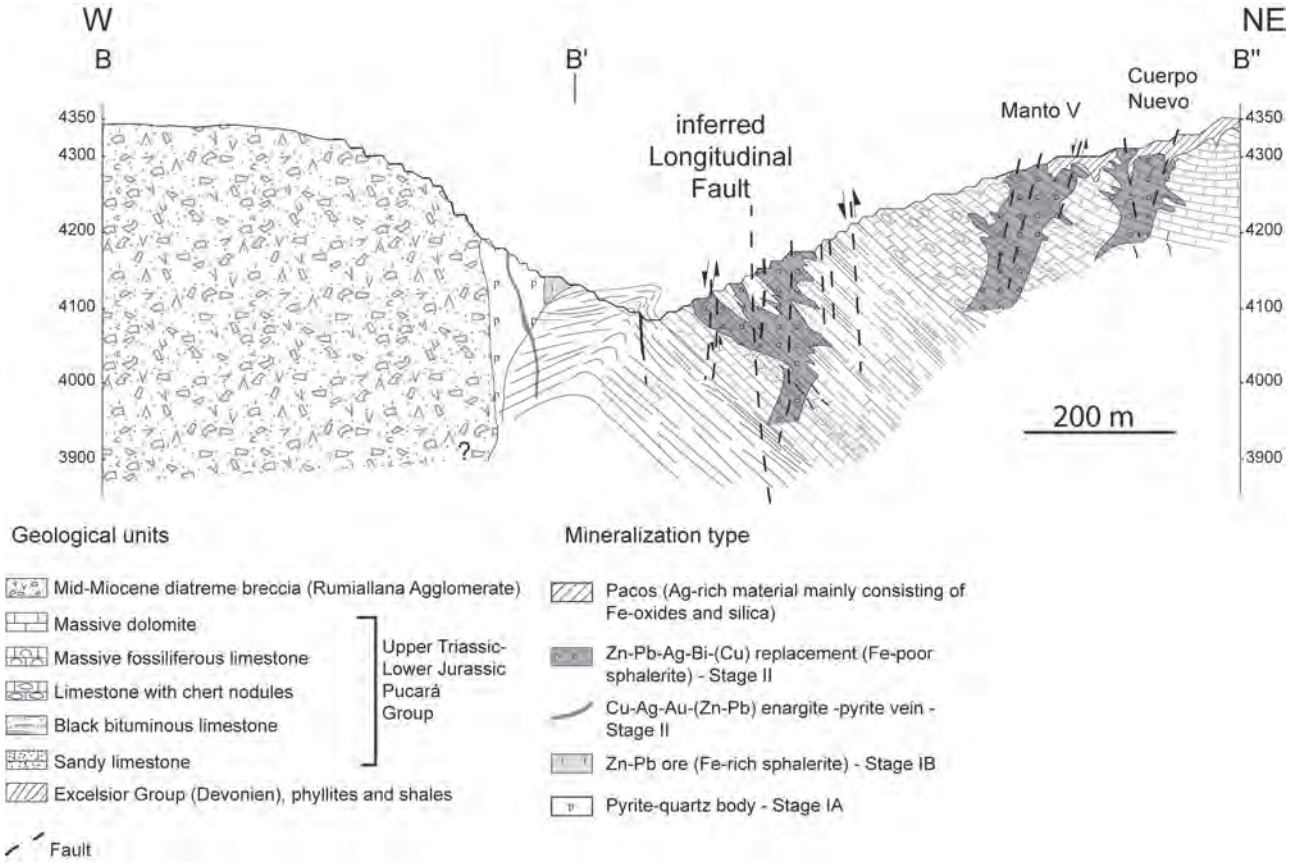

Fig. 5: *B-B'B" cross section (in Fig. 3) through the diatreme and the first mineralization stage (including the pyrite-quartz body and the Zn-Pb ores) and the second stage enargite-pyrite veins in the diatreme breccia as well as replacement bodies hosted in Pucará carbonate rocks. Note that the second mineralization stages orebodies are controlled by faults.*

enargite-pyrite veins in order to avoid overprint by the later generations. Generally, the quartz is cryptocrystalline and occasionally single idiomorphic quartz grains are present in open spaces within massive pyrite and locally, pyrite coats quartz. In the first mineralization stage pyrrhotite pipes, selected quartz grains occur in association with pyrrhotite, quartz, and pyrite. In the related Zn-Pb ores, selected quartz occurs within Fe-rich sphalerite as small idiomorphic grains in association with pyrite, sphalerite, and arsenopyrite. For the second mineralization stage of the western enargite-pyrite veins, single quartz grains occurring with enargite and pyrite in the core zone were selected for analysis. These quartz crystals occur in vuggy quartz within veins or with enargite that precipitated in open spaces. Enargite crystals from the assemblage enargite-pyrite-quartz in the core zone have also been analyzed. In the carbonate hosted replacement bodies, single quartz grains from the famatinite-pyrite core zone and sphalerite from the outer zone were selected for measurements. In the Venencocha area, quartz crystals from the alteration halos of oxidized veins have been sampled. They occur in the assemblage alunite-quartz-zunyite in open spaces of dissolved clasts.

All single quartz grains were coated with resin and fixed onto a glass slide, after which they were doubly polished to a thickness of 100-150 μm thick and subsequently released from the resin (Fig. 6A, D, G and J). Other samples were doubly polished to 100-150 μm thick wafers.

The scanning electron microscope (SEM)-CL images on quartz were obtained on a CamScan CS44LB instrument at ETH Hönggerberg, Zürich, Switzerland. Backscatter electron (BSE) and cathodoluminescence (CL) images were taken immediately one after each other under the same instrumental conditions (accelerating voltage of 15 kV, beam current of 10-15 nA and the sample was untilted and adjusted in height to the lower edge of the ellipsoidal mirror). The SEM is equipped with a 4 quadrant semiconductor backscattered electron (BSE) gun and a mirror focuses the CL signal onto a standard photomultiplier detector.

Single quartz grains as well as sphalerite used for heating and freezing measurements were selected on the basis of (Roedder, 1984) criteria. Inclusions that experienced necking down were avoided. Temperatures of homogenization to the liquid and final melting of ice were measured on a Linkam heating-freezing stage (THMSG 600) mounted on a DMLB Leica microscope, calibrated using synthetic fluid inclusions (SYN FLINC) to ±0.2°C for the melting point of CO_2 (–56.6°C), and the melting point of H_2O (0.01°C), and to ± 1 °C for the critical point of pure H_2O (374.1°C). The errors on freezing runs are ± 0.1°C and ± 2°C on heating runs. The apparent salinity of fluid inclusions, expressed in weight percent NaCl equivalent (wt % NaCl equiv) was determined from final melting of ice (Bodnar, 2003). The terminology used for the fluid inclusion study is reported in Table 2. The homogenization temperatures and salinities for fluid inclusions in enargite obtained by Jobin (2004) were measured under infrared light on a USGS heating-freezing stage mounted on an Olympus-BHMS infrared microscope equipped with long working distance, high magnification infrared objectives, and an infrared-sensitive Hamamatsu type C2400-03D camera. The errors on freezing runs are ± 0.1°C and ± 1°C on heating runs.

The O, H, C, and S stable isotope analyses were measured in the Stable Isotope Laboratory at the University of Lausanne, Switzerland. The stable isotope compositions of minerals from Cerro de Pasco were measured on handpicked monomineralic concentrates of quartz, kaolinite, carbonate, sulfides, and sulfates from the first and second mineralization stages (Table 1). All isotope compositions are reported as δ-values in permil using the conventional formula where R_s is the respective isotope ratio of the standard, R_x is the isotope ratio of the sample, and δ is the deviation (δ in ‰) of the isotope ratio in the sample relative to the standard:

Table 2: Terminology used for microthermometry in this study

Abbreviation	Explanation	Purpose
wt % NaCl equiv	Salinity in wt percent NaCl equivalent	Apparent salinity of fluid inclusions
Tm (ice)	Last ice melting temperature	Calculation of the apparent salinity of fluid inclusions (Bodnar, 2003)
Tm (hydrohalite)	Last hydrohalite melting temperature.	If hydrohalite disappears after ice, the apparent salinity is known to be between 23.2 and 26.3 wt-% NaCl eq.
Th V+L →L	Homogenization temperature to liquid	Estimation of a minimum P-T condition of entrapment, unless pressure corrections are applied

$$\delta^{18}O, \delta D, \delta^{34}S, \delta^{13}C = \left(\frac{R_x}{R_s} - 1\right) \bullet 1000$$

, where R = $^{18}O/^{16}O$, D/H, $^{34}S/^{32}S$, or $^{13}C/^{12}C$, respectively. The values are reported relative to Vienna Standard Mean Ocean Water (VSMOW) for O and H, Cañon Diablo Troilite (CDT) for S, and Vienna Peedee Belemnite (VPDB) for C.

Sulfur isotope compositions from pyrite, sphalerite, galena, enargite, barite, and alunite were analyzed using a Carlo Erba 1108 elemental analyzer connected to a Finnigan MAT Delta-S mass spectrometer, following the technique described by Giesemann et al.(1994). Sample powders (150-200 µg for sulfide samples and ~250 µg for sulfate) were wrapped in tin capsules. Vanadium oxide was not added as a catalyst/reactant for the combustion as tests at the University of Lausanne have shown that for the present system this is not necessary. The samples were combusted at 1020°C and all gases produced during the combustion transported in a stream of helium to the reduction furnace (at 650°C). Subsequently, water was removed in a water trap. SO_2 was separated from other gases (CO_2 and NO_2) in a gas chromatography column (heated at 50°C) and analyzed in the mass spectrometer. Reference gas SO_2 for isotopic calibration was introduced into the carrier gas stream via a CONFLO III. $\delta^{34}S$ standards used during runs of sulfides included NBS 123 sphalerite ($\delta^{34}S$ = +17.3 ‰); Py-E pyrite ($\delta^{34}S$ = -7 ‰), and IAEA-S1 silver sulfide ($\delta^{34}S$ = -0.3 ‰) and NBS 127 barium sulfate ($\delta^{34}S$ = 20.3 ‰) for sulfates. External precision for the isotopic compositions was better than 0.2 permil.

Oxygen isotope composition of kaolinite and quartz were analyzed using a CO_2 laser fluorination system similar to that described by Sharp (1990) and Rumble and Hoering (1994) and that is described in more detail in Kasemann et al (2001). Between 1 to 2 mg of sample was loaded on a Pt-sample holder and pumped out to a vacuum of better than 10^{-6} mbar. After prefluorination overnight, the samples were heated using a CO_2 laser in the presence of about 50 mbars of pure F_2, the latter generated by a potassium nickel fluoride salt when heated at >250°C. The heated mineral reacts quickly with F_2, releasing O_2 from silicate or oxide minerals. Excess F_2 is separated from O_2 produced by the conversion to Cl_2 using KCl held at 150°C. The extracted O_2 is collected on a molecular sieve (13x) and subsequently expanded into the inlet of a Finnigan MAT 253 isotope mass ratio spectrometer. In-house standards used during the run were Kaolinite #17 (mean $\delta^{18}O$ = 8.24 ‰ ± 0.12, n=4) and LS1 (quartz, mean $\delta^{18}O$= 18.1 ‰ ± 0.15, n=26) for quartz. Replicate oxygen isotope analyses generally have an average precision of ± 0.2 permil.

In order to measure $\delta^{18}O(SO_4)$ in alunite ($KA1_3(SO_4)_2(OH)_6$), a chemical treatment to separate oxygen present in (SO_4) and (OH) sites is applied by reprecipitating it as barite according to procedures described by Wasserman et al. (1992). 20 to 80 mg of alunite was dissolved in a 0.5N NaOH solution and heated to 80°C (±10°C) for 3 hours. The filtered solution is titrated by adding a 10N HCl solution, which acidifies the solution to a low pH, avoiding the precipitation of $Al(OH)_3$ at intermediate pH. To precipitate $BaSO_4$, 5 ml of 0.5N $BaCl_2$ is added to the solution. The $BaSO_4$ precipitate can subsequently be analyzed for its oxygen isotope composition. 500-600 µg of $BaSO_4$ precipitate (from alunite) as well as 250 µg of natural barite were analyzed using He-carrier gas with a High Temperature Conversion Elemental Analyzer (TC-EA) coupled to a Delta^{Plus} XL mass spectrometer from ThermoFinnigan according to a method similar to that described in Vennemann and O'Neil (1993). This method is based on reduction in the presence of graphite and a buffer of glassy carbon at temperatures higher than 1450°C. The standard used was NBS 127 (barium sulfate, mean $\delta^{18}O$ = 9.3 ‰ ± 0.39, n=9). $\delta^{18}O$ values are precise within 0.3 permil.

Hydrogen isotope compositions were measured on 500 to 560 µg alunite and kaolinite using a TC-EA continuous flow reactor linked to a ThernoFinnigan Delta^{Plus} XL mass spectrometer according to a method adapted after Sharp et al. (2001). An in-house kaolinite standard (Kaol #17, mean δD = –125 ‰, n=12) and biotite standard (G1 mean δD = –66 ‰, n=18) were used for the normalization and these have been calibrated against NBS-30 biotite (δD = –65‰, VSMOW). δD values are precise to within 2 permil.

Carbon and oxygen isotopic compositions on Fe-Mn-Zn carbonates, late calcite, and whole rocks were analyzed on a Gas Bench (continuous flow) coupled to a ThernoFinnigan Delta^{Plus} XL mass spectrometer according to methods adapted after Spoetl and Vennemann (2003). Carbonates are reacted with H_3PO_4 to form, amongst others, CO_2. This gas is transported with He carrier gas via a water trap to remove any H_2O produced and passed through a gas chromatograph, followed by another water trap, and finally into the mass spectrometer for C and O isotope analysis. Samples are normalized to an in-house calcite standard (CMSTD; $\delta^{13}C$ = 2.5‰ ± 0.12, n=6; $\delta^{18}O$ VPDB = –1.70 ‰ ± 0.14, n=6), which has been calibrated relative to NBS-19 ($\delta^{13}C$ = 1.95‰, VPDB; $\delta^{18}O$ = –2.20‰, VPDB). Precision for the analyses is better than 0.1 or 0.15‰ for $\delta^{13}C$ and $\delta^{18}O$ values, respectively.

Cathodoluminescence, fluid inclusion petrography and microthermometry results

The fluid inclusions measured in this study are all two-phase (liquid + vapor) aqueous inclusions and results are summarized in Table 3. Microthermometric measurements have been conducted on fluid inclusions belonging to a same assemblage which, according to Goldstein and Reynolds (1994) is defined as primary inclusions in a single and distinguishable growth zone or inclusions defining a single healed microfracture. The fluid inclusions measured in this study were classified into types and subtypes. The first mineralization stage fluid inclusions are termed type I (Table 3). Fluid

Table 3: Summary of fluid inclusion types, morphology, and characteristics at Cerro de Pasco (data in Appendix 2, Fig. 9 and 10).

Fluid inclusions							phases at 25°C					
Type	Subtype	Mineral	Mineralization stage	Inclusion shape	Size (µm)	Number	Type	Homogenization temperature min to max (°C)	Homogenization temperature median (°C)	Salinity min to max (wt-% NaCl equiv)	Salinity median (wt-% NaCl eq.)	Remarks
I	A1	quartz	Pyrite-quartz body (first stage)	Negative crystals or rounded	5-30	43	Liquid + vapor	200 - 275a	251	0.2 - 6.8	2.4	In growth zones
I	B1	quartz	Pyrrhotite bodies (first stage)	rounded or irregular	5-15	12	Liquid + vapor	192-250	210	1.1- 4.3	3.4	Occurs with pyrrhotite
	B2	quartz	Fe-rich sphalerite bearing Zn-Pb ore (first stage)	rounded or irregular	5-15	6	Liquid + vapor	183 - 212	200	3.2 - 4.0	3.48	Occurs with Fe-rich sphalerite
II	A1	quartz	? (pre- or syn-second stage)	Negative crystals or rounded,	15-45	28	Liquid + vapor	220 - 280	239	0.7 - 22.3 (if hydrohalite is present, up to 23.2 - 26.3	11.9	Appear in cracks within magmatic quartz core. Presence of vapor-rich inclusions.
	A2	quartz	Second stage enargite veins	rounded or irregular	10-25	89	Liquid + vapor	187 - 293	227	0.2 - 5.2	1.1	In groth zones in quartz surrounding magmatic quartz
	A3	enargite	Second stage enargite veins	elongated or irregular	15-40	21	Liquid + vapor	195 - 270°C	239b	3.5 - 9.3*	6.4*	Data from Jobin (2004)
II	B1	quartz	Replacement bodies (second stage)	rounded or irregular	10-30	34	Liquid + vapor	178 - 265	234	0.2 - 7.5	4.2	In growth zones
	B2	sphalerite		rouned or irregular	10-20	14	Liquid + vapor	168 - 222	196	3 - 11.8	7.1	isolated inclusions along growth zones
II	C	quartz	Veins at Venencocha	rouned or irregular	15-25	9	Liquid + vapor	245 - 261	260	3.23 - 7.7	5.7	In growth zones

a Two fluid inclusion assemblages with a total of 5 measures yielding homogenization temperatures between 340 and 375°C and salinites ranging from 0.8 to 5.71 wt percent NaCl equiv have not been considered. They occur in a part of a growth zone (in sample CPR 23a) which could correspond to a relic of former quartz or these high temperatures are due to necking down because several inclusions in the same zone show necking down.

b To be used with caution. Homogenization temperature values are probably underestimated and salinity values overestimated, see text.

inclusions measured in quartz occurring in the assemblage quartz-pyrite from the pyrite-quartz body are designated subtype IA1. Fluid inclusions measured in quartz occurring in the association quartz, pyrrhotite, pyrite in the pyrrhotite bodies correspond to subtype IB1, while subtype IB2 corresponds to those measured in quartz from the association quartz, pyrite, sphalerite, arsenopyrite from Zn-Pb sphalerite-bearing ores (Table 3). The second mineralization stage fluid inclusions are termed type II. Western enargite-pyrite veins single quartz crystals occurring with pyrite and enargite contain magmatic quartz cores within hydrothermal quartz. These magmatic cores enclose cracks containing fluid inclusions designated as subtype IIA1. The hydrothermal rims of these grains contain fluid inclusions, which are termed subtype IIA2. Fluid inclusions measured in enargite from core zones (Jobin, 2004) in western veins are designated as subtype IIA3. In carbonate replacement bodies hosted in Pucará carbonate rocks, fluid inclusions in quartz from the pyrite-famatinite core zone are designated as subtype IIB1 while those in sphalerite from the outer zone are termed subtype IIB2. Finally, fluid inclusions in quartz from the mineral association quartz, alunite, zunyite, and diaspore in the oxidized veins halos at Venencocha are subtype IIC.

Raman spectroscopy on selected samples failed to detect CO_2 or other gases. In addition, no clathrate formed during freezing, indicating that CO_2, if present, must be in undetectable amounts (less than 1000 ppm). Because the hydrothermal system formed close to the present surface (Baumgartner and Fontboté, Part I), no pressure corrections have been applied.

Pyrite-quartz body (1st mineralization stage)

Cathodoluminescence (CL) imaging in quartz grains from the pyrite-quartz body shows one dull-luminescing quartz generation with occasionally bright-luminescing oscillating growth zones (Fig. 6B). Locally, irregularly shaped bright-luminescent areas also occur. The quartz growth zones contain primary fluid inclusions of subtype IA1 occurring in assemblages (Table 3 and Fig. 6C and 7A) and have sizes between 10 and 30 µm, rarely up to 60 µm. Isolated fluid inclusions also occur in single quartz grains. Measured homogenization temperatures (T_h V+ L → L) and salinities range between 200 and 275 °C and between 0.2 and 11 wt percent NaCl equiv (Fig. 8 and 9), respectively. They show in general narrow variations within single assemblages however, some wide variations in salinity are observed (see Appendix 2). The highest salinities (from 9 to 11 wt% NaCl equiv.) are part of fluid inclusion assemblages (see Appendix 2) which contains also low-salinity inclusions. Two explanations can be given for this wide salinity variation within an assemblage. Either what is defined as an assemblage is none and fluids were trapped at different times, or the assemblage is real but the variability of data shows that the inclusions have been opened after their trapping and have partly been reequilibrated with another fluid. We therefore will consider only assemblages where narrow salinity variations are observed and they are generally below 7 wt% NaCl eq. The salinities thus vary from 0.2 to 7.5 wt% NaCl equiv. Two fluid inclusion assemblages with a total of 5 measurements yield homogenization temperatures between 340 and 375°C and salinities ranging from 0.8 to 5.7 wt percent NaCl equiv. They occur in a part of a growth zone (in sample CPR 23a) where numerous fluid inclusions show features of necking down and therefore are not considered further. Minimum pressures were estimated using L-V isochores calculated with Flincor applying the equation of Brown and Lamb (1989). They range from 10 to 55 bars corresponding to minimum depths of approximately 100 to 600 meters below the water table.

Pipe-like pyrrhotite bodies and related Zn-Pb ore (1st mineralization stage)

Cathodoluminescence (CL) has not been done on the tiny quartz grains (500 µm) within pyrrhotite from the pyrrhotite bodies and within sphalerite from related Zn-Pb ores, the only material available for the fluid inclusion survey. These quartz grains contain subtype IB1 (pyrrhotite bodies) and IB2 fluid inclusions (Zn-Pb ores) ranging between 10 and 15 µm in size (Table 3, Fig. 7B). Fluid inclusion assemblages and isolated inclusions measured in growth zones in quartz (subtype IB1) within pyrrhotite give T_h V+ L → L between 192 and 250°C and salinities between 3.7 and 12 wt% NaCl equiv. Again, the higher salinities are probably the result of reopened inclusions. The considered salinities range from 1.1 to 4.3. Measurements on subtype IIB2 fluid inclusion assemblages in quartz within Fe-rich sphalerite yield T_h V+ L → L between 183 to 212°C and salinities ranging from 3.2 to 7.5 wt% NaCl equiv. The minimal

Fig. 6: *Transmitted light, cathodoluminescence, and growth zones pictures from quartz grains used for the microthermometric measurements in the fluid inclusion study from the pyrite-quartz body (A and B, sample CPR 23c, C sample 23a, first mineralization stage), from the Venencocha area (D, E, and F, sample CPR 365, second mineralization stage), from quartz grains from the enargite-pyrite veins in the western part of the open pit (G, H, and I, CPR 439b, second mineralization stage), and from the carbonate replacement bodies in the Matagente area (J. K, and L, sample CPR 480c, second mineralization stage). Note that in the image H, CL imaging reveals a magmatic quartz core (1) which shows dissolution borders and overgrown by a CL-texturally irregular hydrothermal quartz (2), also showing dissolution textures. This quartz is in part overgrown by CL- oscillating growth zones hydrothermal quartz (3).*

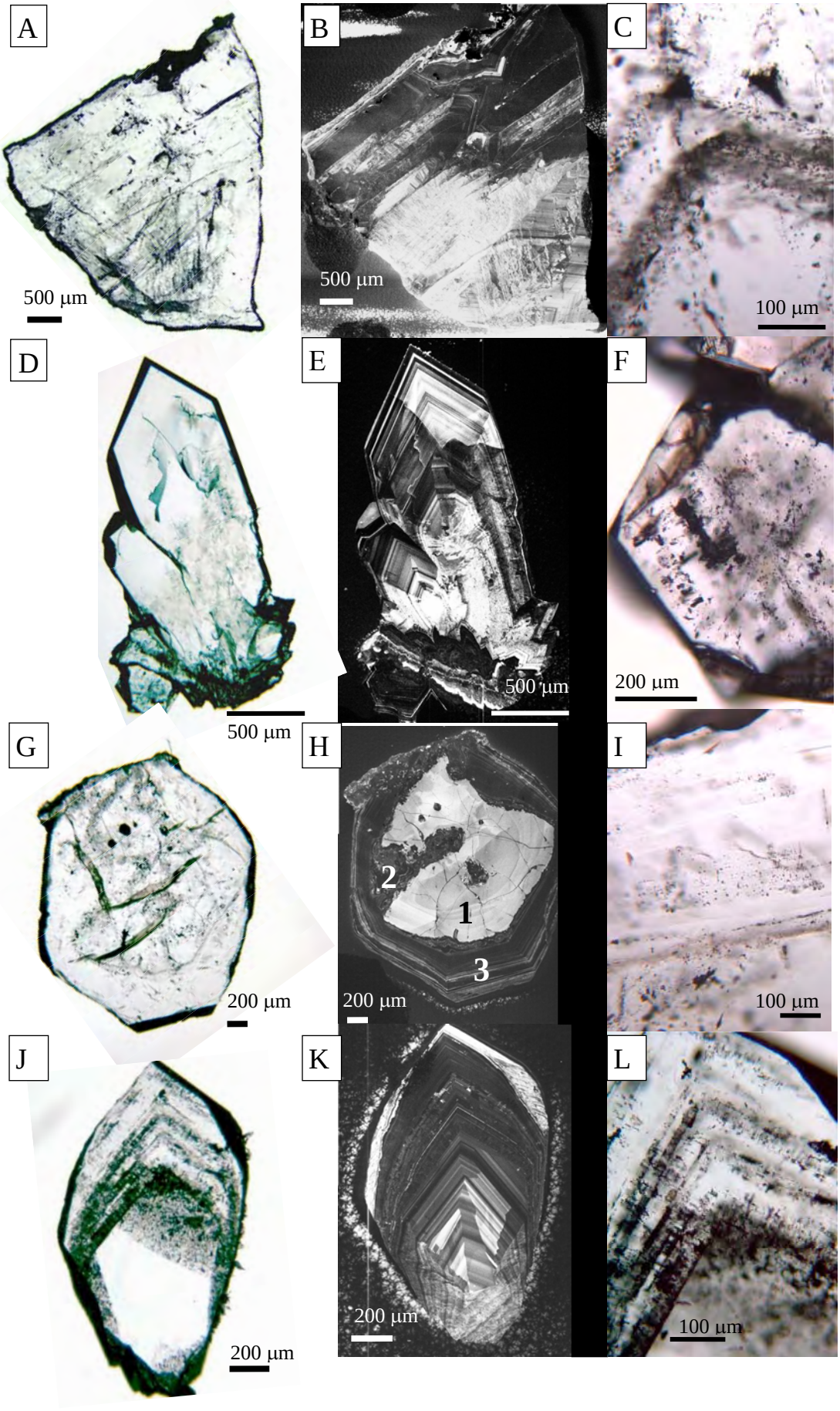
A
500 µm
B
500 µm
C
100 µm
D
500 µm
E
500 µm
F
200 µm
G
200 µm
H
2
1
3
200 µm
I
100 µm
J
200 µm
K
200 µm
L
100 µm

estimated pressure, calculated with Flincor applying the equation of Brown and Lamb (1989), range between 10 and 60 bars and correspond to minimal depths of 100 to 600 m, which is in agreement with the minimal estimates for the pyrite-quartz body.

Western enargite pyrite veins (2nd mineralization stage)

Cathodoluminescence (CL) imaging on single quartz grains from the western veins indicates multiple quartz generations. All analyzed euhedral quartz grains associated with enargite in the core of the veins show a CL-bright luminescing core with complex oscillatory growth zones typical of magmatic quartz and irregular margins indicating dissolution (1 in Fig. 6H). These magmatic cores contain magmatic inclusions (~50 μm glass inclusion with a shrinkage bubble) and two-phase aqueous as well as vapor inclusions (subtype IIA1) along cracks. The magmatic quartz cores are all surrounded by hydrothermal quartz characterized by marked oscillation with predominantly CL-dull to CL-dark luminescence and rare bright-luminescing growth zones (3 in Fig. 6H). This hydrothermal quartz contains abundant measurable aqueous inclusions in growth zones (subtype IIA2, Fig. 6I and 7I). Healed fractures are present in the hydrothermal quartz but fluid inclusions present in those fractures have not been measured because of their small size. In one sample (CPR 439), between the magmatic quartz core and the hydrothermal quartz showing growth zones, a CL-texturally irregular hydrothermal quartz occurs. It contains minute inclusions of pyrite and anatase grains and the CL-irregular texture is characterized by dark and -bright luminescent areas. The external borders of this "irregular" quartz show dissolution borders (Fig. 6H). It contains aqueous inclusions of various shapes and sizes consistently showing necking down and therefore, were not selected for microthermometric measurements.

The two-phase aqueous inclusions coexisting with vapor inclusions along cracks within the magmatic quartz core in diatreme-hosted veins (subtype IIA1, between 15 and 45 μm is size, Table 3, Fig. 7C and D) show T_h V+ L → L between 220 and 280°C and highly variable salinities, from 1 up to 22.3 wt% NaCl equiv (Fig. 8 and 9). These cracks do not extend within the hydrothermal quartz suggesting that the associated, in part moderately saline (up to 21 wt% NaCl equiv) aqueous inclusions record a previous hydrothermal pulse. Rare IIA1 fluid inclusions contain hydrohalite which disappears after ice melting, indicating that the apparent salinity is between 23.2 and 26.3 wt% NaCl equiv (Goldstein and Reynolds, 1994). Vapor-dominated inclusions (>80% in volume) contain no detectable CO_2 and freezing temperatures were not obtained due to unobservable phase changes.

The aqueous fluid inclusion assemblages of subtype IIA2 in growth zones from hydrothermal quartz yield T_h V+ L → L from 187 to 293°C and salinities between 0.2 and 5.2 wt% NaCl equiv. In one sample (CPR 439b), fluid inclusions within a growth zone were observed to coexist with a small number of vapor inclusions. Homogenization or freezing temperature measurements were not possible on the vapor-rich inclusions. Subtype IIA2 fluid inclusions range in size from 10 to 25 μm. The minimum pressure estimates from subtype IIA2 fluid inclusions, calculated with Flincor using the equation of Brown and Lamb (1989), range from 20 to 70 bars and correspond to depth of 200 to 700 m below the water table at hydrostatic pressures.

The fluid inclusions (15-40 μm in size) in single enargite grains from the second mineralization stage enargite-pyrite veins (subtype IIA3, Table 3, Fig. 7F) measured under infrared light gave T_h V+ L → L between 195 and 270°C with wide variations of salinities (3.5 – 9.3 wt % NaCl equiv, Jobin, 2004). The above results may need re-interpretation because according to Moritz (2006), homogenization and melting temperatures obtained by infrared light depend on the light intensity, resulting in the overestimation of fluid salinities and the underestimation of homogenization temperatures. According to the tests done on enargite by Moritz (2006), the homogenization temperatures may be underestimated by 15 – 25°C (i.e. 220 – 295°C instead of 195 – 270°C). Taking into account the temperature uncertainty, the obtained homogenization temperatures are in agreement with the measured temperatures obtained in quartz (220 to 290°C) from the quartz-enargite assemblage. The real salinities are difficult to evaluate because the light intensity may dramatically affect the final ice melting temperatures Moritz (2006), resulting in overestimated salinities.

Fig. 7: *Selected images of typical fluid inclusion occurrences from the Cerro de Pasco district. A) Fluid inclusions along a growth zone in quartz from the pyrite-quartz body (subtype IA1, CPR 23a). B) Isolated fluid inclusion in quartz within pyrrhotite from the first mineralization stage (subtype IB1, fpe 131-1). C) Saline fluid inclusion along a fracture within magmatic quartz core (subtype IIA1, CPR 439b). D) Vapor-rich fluid inclusions along cracks within magmatic quartz core (subtype IIA1, CPR 439b). E) Fluid inclusions in a growth zone in quartz from the enargite veins, second mineralization stage (subtype IIA2, CPR 439b). F) Infrared picture of a fluid inclusion along a growth zone in enargite (subtype IIA3, photo by Jobin, 2004). G) Fluid inclusions in growth zone of a quartz crystal from the carbonate replacement bodies (subtype IIB1, CPR 608a3). H) Fluid inclusions along growth zones in sphalerite from carbonate replacement bodies from the second stage (subtype IIB1, CPR 480). I) Isolated fluid inclusion in a growth zone in quartz from carbonate replacement bodies (subtype IIB2, CPR 325).*

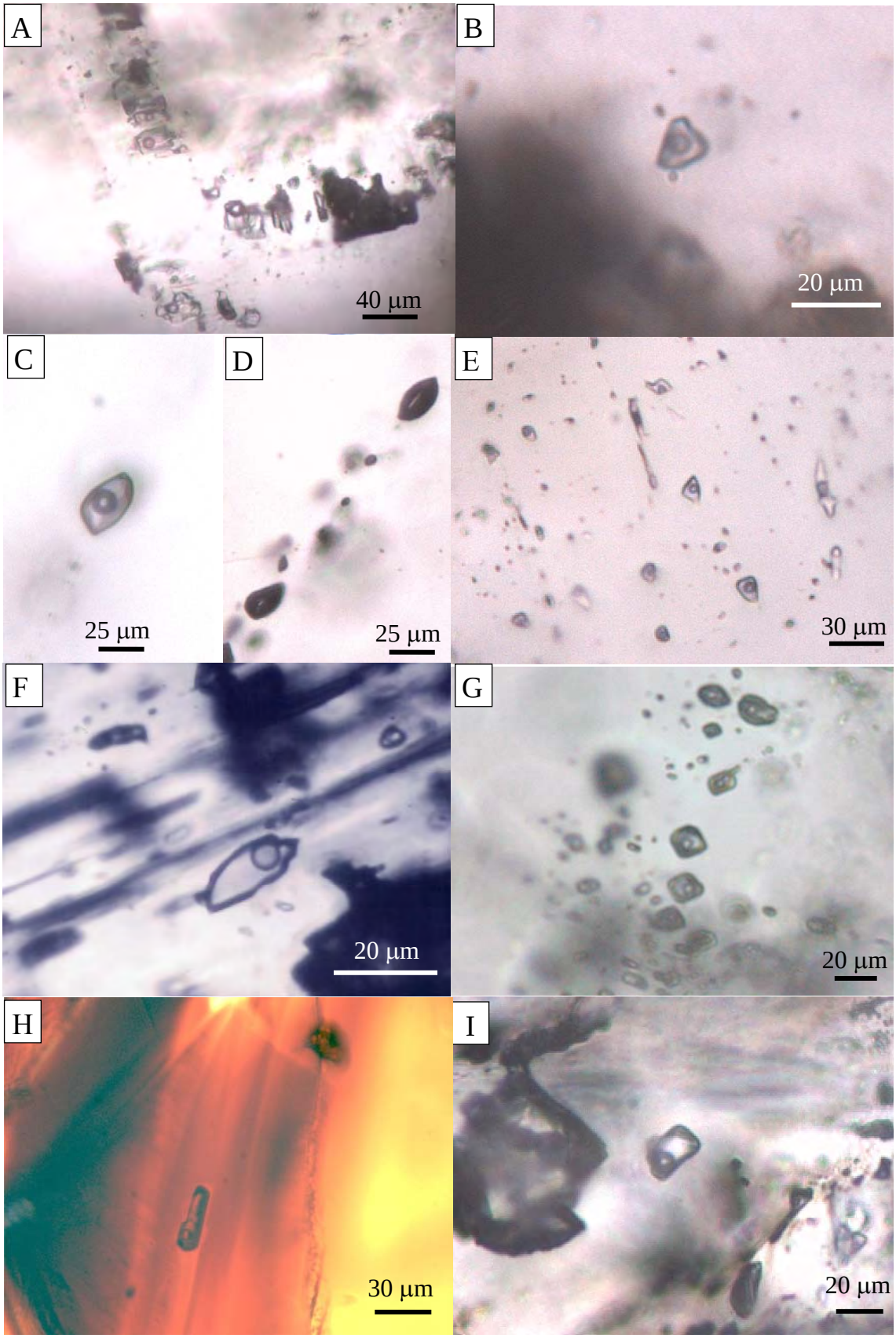
A
40 µm
B
20 µm
C
25 µm
D
25 µm
E
30 µm
F
20 µm
G
20 µm
H
30 µm
I
20 µm

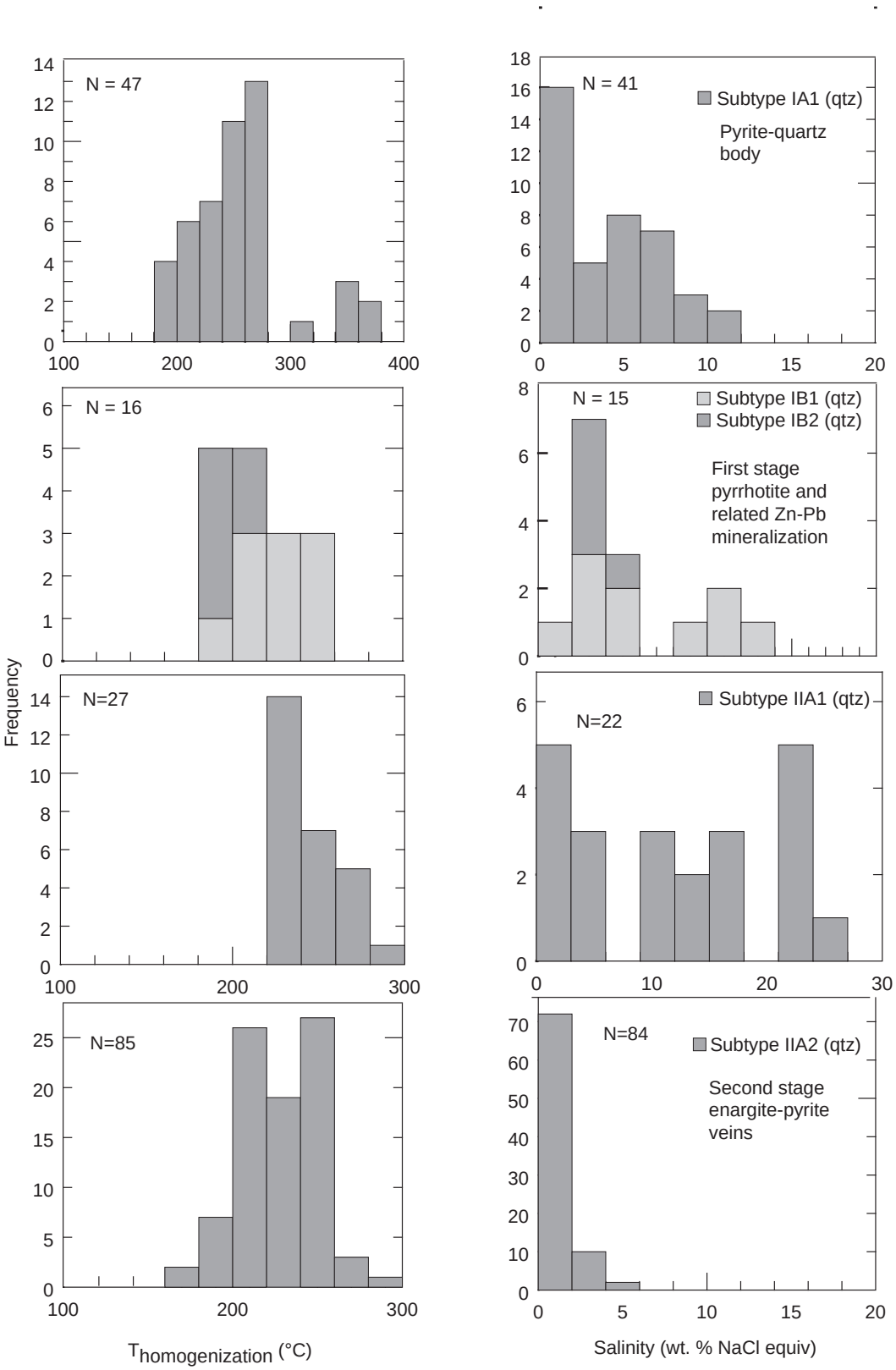

Fig. 8: *Frequency diagram showing the homogenization temperatures (diagrams on the left) and salinities (diagrams on the right) from the different types of fluid inclusions in quartz from the first (type I) and second mineralization stages (type II). The type I includes fluid inclusions in quartz from the pyrite-quartz body (subtype IA1), from quartz within pyrrhotite (subtype IB1) and within Fe-rich sphalerite from the Zn-Pb ores (subtype IB2). The type II includes fluid inclusions in quartz from magmatic quartz core in enargite-pyrite veins (subtype IIA1), in hydrothermal quartz from the enargite-pyrite veins (subtype IIA2), in enargite from enargite-pyrite veins (subtype IIA3), in quartz from carbonate replacement bodies (subtype IIB1), in sphalerite from carbonate replacement bodies (subtype IIB2), and in quartz from the oxidized veins in Venencocha area (subtype IIC).*

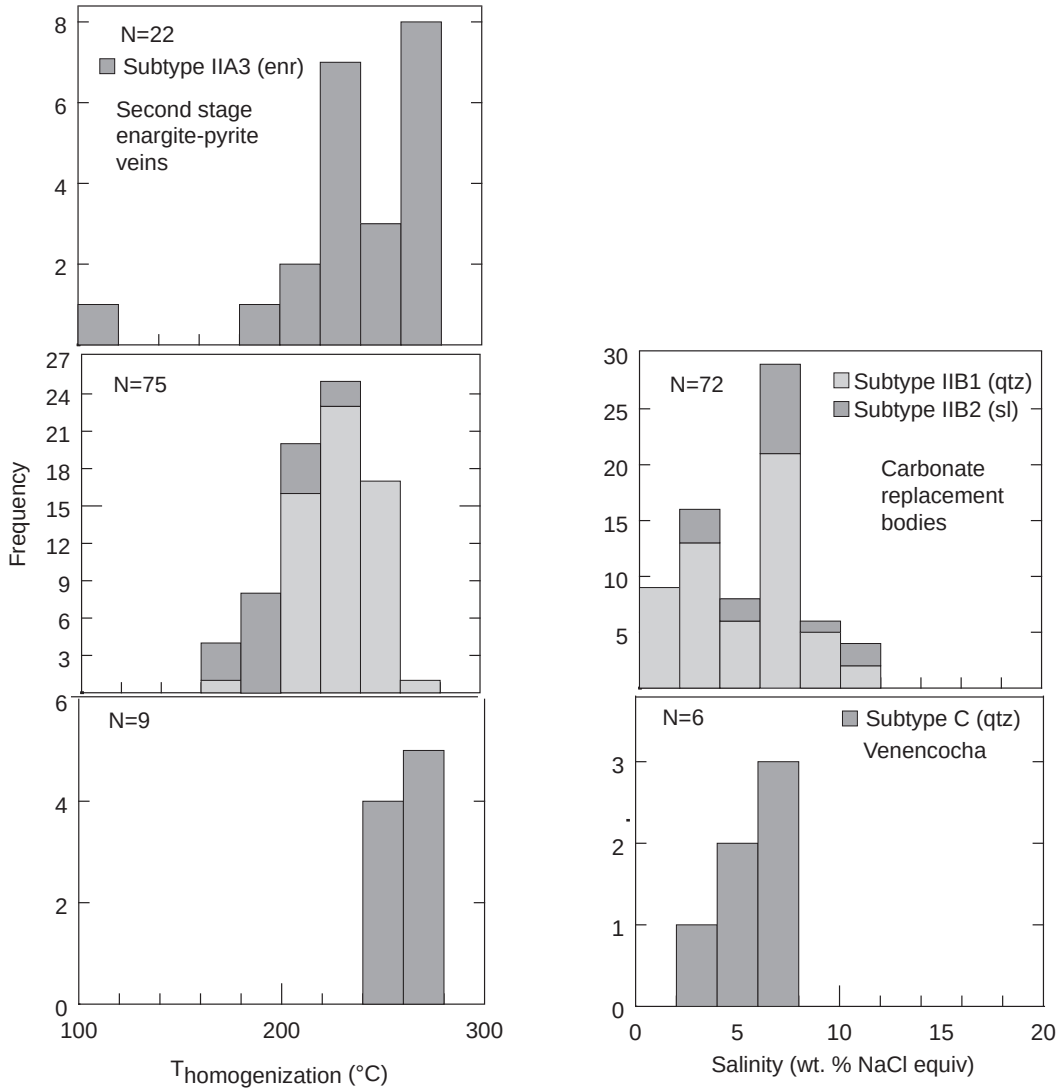

Fig. 8: *(cont.)*

Carbonate replacement bodies (2nd mineralization stage)

Several quartz crystals from the center of carbonate replacement bodies show only one generation of hydrothermal quartz using CL imaging, characterized by bright-CL oscillatory luminescence in the center of the crystal that becomes CL-darker toward the borders (Fig. 6K). Some bands contain pyrite inclusions. The abundant sub-type IIB1 fluid inclusions contained in this quartz are present in growth zones (Fig. 6L and 7G) and are considered to be primary in origin. They are two-phase, between 10 and 30 μm in size (Table 3, Fig. 7G), and yield T_h V+ L → L between 178 and 265°C and salinities from 0.2 to 10.6 wt% NaCl equiv. (Fig. 8 and 9). As it is the case for the first mineralization stage, the inclusions with a medium salinity coexist in the same assemblage with low salinity inclusions. For the same reasons explained above, the measurements obtained on fluid inclusion assemblages yielding high salinity variations are discarded. Thus, the salinities vary from 0.2 to 7.5. Pressure estimates using L-V isochor calculated after Brown and Lamb (1989) in Flincor vary between 20 and 50 bars, corresponding to a minimum depth of 200 to 500 m below water table at hydrostatic pressure.

Two-phase subtype IIB2 fluid inclusions in sphalerite (subtype IIB2) from the outer zone of carbonate replacement bodies are 10-20 μm in size (Table 3, Fig. 7H), and give T_h V+ L → L between 168 and 222°C and salinities between 3 and 11.8 wt% NaCl equiv. These microthermometric results on sphalerite containing 1-2 mole percent FeS, although measured on a Linkam stage equipped with an infra-red filter, could also be affected by the method-induced limitations described for enargite by Moritz (2006).

Venencocha

One single quartz crystal from oxidized veins in the Venencocha area (northwestern margin of the diatreme-dome complex) has been studied and shows on CL imaging bright-CL oscillatory luminescence in the center and darker in the external part (Fig. 6E). Two-phase fluid inclusions (subtype IIC) are 15-25 μm in

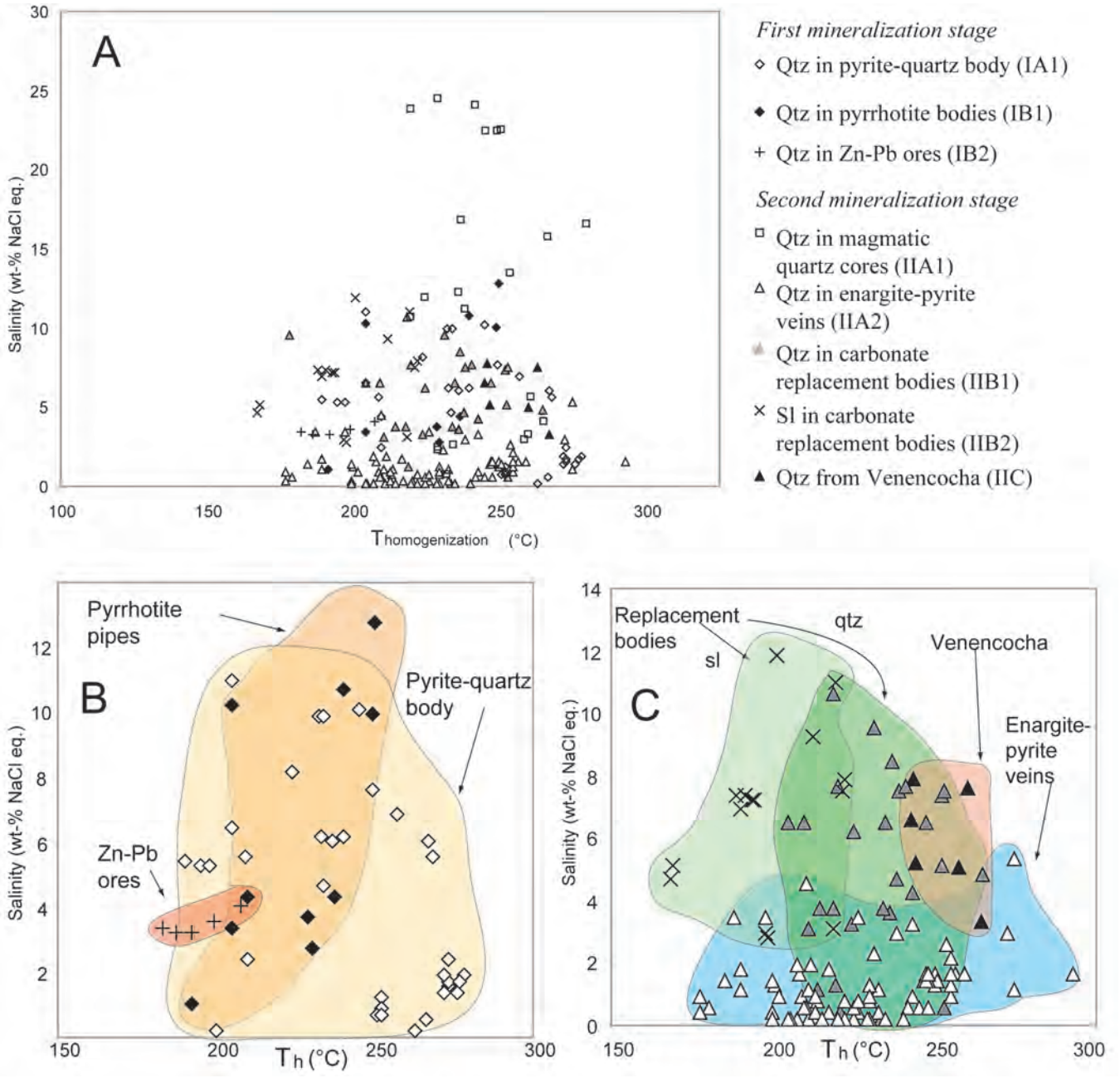

Fig 9: *A) Homogenization temperature (Th) vs. salinity (wt % NaCl equivalent) diagram of single fluid inclusions mainly in quartz from the first and second mineralization stages and in sphalerite from the carbonate replacement bodies (second stage). B) Detail of A, Th vs. salinity of single inclusions in quartz from the first mineralization stage including the pyrite-quartz body, the pyrrhotite bodies, and the related Zn-Pb ores. C) Idem as B) but from fluid inclusions in quartz from the second mineralization stage including the enargite-pyrite veins, the carbonate replacement bodies (also sphalerite), and the oxidized veins at Venencocha.*

size (Table 3, Fig. 7B) and yield a narrow range of T_h V+ L → L between 245 and 265 °C and salinities between 3.2 and 7.4 wt% NaCl equiv. Minimum hydrostatic pressures have been estimated between 30 and 45 bars which is equivalent to depths of 300 to 450 m.

Stable isotope results

Pyrite-quartz body (1st mineralization stage)

Oxygen and sulfur isotope compositions of three quartz samples (CPR 4 and 23, FPE-130-13) and two pyrite samples (CPR 15 and 38) from the pyrite-quartz body were analyzed. $\delta^{18}O$ values range from 13.3 to 16.5 permil and $\delta^{34}S$ values are around 0.4 permil (Table 4 and 5).

Sulfur isotope compositions of two pyrite (CPR 319 and 464) and 7 sphalerite samples (CPR 319, 461, 464, 76, 77a, 77b, and 405) from the first stage Zn-Pb mineralization fall in a narrow range from 2.8 to 3.3 ‰

and 1.9 to 2.1 ‰, respectively (Table 5). In addition, Austria (1975, in Einaudi, 1977) provided sulfur isotope analyses on pyrite, sphalerite, and galena from the Zn-Pb ores in underground levels from the mine (Table 5). $\delta^{34}S$ values for pyrite range from 0 to 1.5 permil, between –1.6 to –0.2 permil for galena, and from 0.8 to 3.5 permil for Fe-rich sphalerite.

Western enargite-pyrite veins (2nd mineralization stage)

Oxygen isotope compositions of three quartz grains from the enargite- pyrite core zone (CPR 19, 440) and isolated in vuggy quartz vugs (CPR 439) have values of $\delta^{18}O$ between 10.8 and 13.3 permil (Table 4). Enargite and pyrite from the core zone, both in the assemblage pyrite-enargite-quartz, have $\delta^{34}S$ values of 0 and 2.5 permil, respectively. Barite from the intermediate zone of western veins hosted by the diatreme breccia has a $\delta^{34}S$ value of 31.2 ‰ (Fig. 10 and Table 5).

Carbonate replacement bodies (2nd mineralization stage)

Oxygen isotope compositions of 6 quartz samples (CPR 25, 58, 395, 480, 309, and 471) from the core zone of carbonate replacement bodies, occurring with pyrite, have a $\delta^{18}O$ range from 10.1 to 17.8 permil (Table 4). Oxygen isotope compositions of 8 barite samples (CPR 10, 11, 25, 48, 58, 59, 459, and 475) have values between -1 and 10.4 permil (Table 4).

Hydrogen and oxygen isotope compositions have been measured on 14 kaolinite samples from the carbonate replacement bodies at Cuerpo Nuevo and the Colas area (Fig. 3). From the Cuerpo Nuevo orebody (4320 and 4310 bench), four kaolinite samples (CPR 27, 30, 44, 47) have been collected in the intermediate zone where kaolinite occurs with hinsdalite, tetrahedrite, and pyrite. In the outer zone of the Cuerpo Nuevo orebody (bench 4320 and 4310), four samples (CPR 10, 11, 26, 54) where kaolinite is intergrown with sphalerite and galena have been collected. In the Colas orebodies, five samples have been studied, two of them (CPR 82, 311) are from the intermediate zone where kaolinite occurs with tetrahedrite and pyrite and the three remaining kaolinite (CPR 309, 417, 422) from the outer zone, intergrown with sphalerite and galena (Table 4). $\delta^{18}O$ and δD values of kaolinite, plotted in a $\delta^{18}O$ versus δD diagram (Fig. 11), show two populations ranging from $\delta D = –85$ to –97 and $\delta^{18}O = 5.3$ to 10.5 ‰ for the first population and between $\delta D = –114$ to –106 ‰ and $\delta^{18}O = 9.2$ to 10.8 ‰ for the second population (Table 4).

Sulfur isotope compositions of pyrite, sphalerite, and galena as well as barite have been measured in orebodies at Cuerpo Nuevo, Colas, and San Alberto (Table 5). The small veins in the northeastern part of the open pit have also been sampled (Fig. 3). $\delta^{34}S$ values for pyrite (Table 5) from the intermediate and outer zones of the bodies vary from –0.1 to 1.6 permil. $\delta^{34}S$ values for sphalerite from the outer zone range between –3.7 and 4.2 permil and those for galena range from –0.7 to 3.1 ‰. Barite $\delta^{34}S$ values show two groups. The first group comprises barite with high $\delta^{34}S$ values (18.1 to 31.2 ‰), including five of six samples from Cuerpo Nuevo (19.3 to 24.4 ‰), one sample from San Alberto (18.1 ‰), and the only available sample for the western enargite-pyrite veins (31.2 ‰). The second group (4.2 to 10.5 ‰) includes the single analyzed sample from the uneconomic small veins in the northeastern part of the open pit (5.5 ‰), a sample from Cuerpo Nuevo (4.2 ‰), as well as one from San Alberto (10.5 ‰).

Carbon and oxygen isotopes were measured from the outermost zone Fe-Mn-Zn carbonates, from late calcite veins close to the orebodies in slightly altered Pucará limestone, and from unaltered Pucará Group rock. The measured Fe-Mn-Zn carbonates include grains encrusting sphalerite and/or galena, and idiomorphic grains as void fillings. $\delta^{13}C$ values for unaltered Pucará Group carbonate rocks range from 1.36 to 2.74 ‰ and $\delta^{18}O$ from 19.16 to 25.3 ‰. Late calcite veins have $\delta^{13}C$ values ranging from 0.73 to 0.98 ‰ and $\delta^{18}O$ from 18.8 to 21.3 ‰. Fe-Mn-Zn carbonates have a wide $\delta^{13}C$ variation from –8.07 to 1.03 ‰ and $\delta^{18}O$ from 9.5 to 19.5 ‰. The results are shown in a $\delta^{13}C$ - $\delta^{18}O$ diagram (Fig. 12).

Venencocha and Santa Rosa

Oxygen isotope compositions of two quartz samples from advanced argillic halos from oxidized veins in Venencocha have $\delta^{18}O$ values of 14.5 and 17.5 ‰. Four alunite samples occurring in the association alunite, quartz, zunyite, and diaspore from advanced altered halos in oxidized veins at Venencocha have been analyzed for their $\delta^{18}O_{SO4}$, δD, and $\delta^{34}S_{SO4}$ values (Table 4 and 5). Alunite from sample CPR 365 occurs in residual sugary silica with euhedral quartz crystals. Sample CPR 347 was sampled from a dome located on the northwestern margin of the diatreme-dome complex and sample CPR 380 comes from a dome, located 400 m from the above mentioned dome; both domes are altered to an assemblage quartz-alunite, which in part fills leached feldspar phenocrysts. Sample CPR 381 is located a few meters from the CPR 380 and alunite occurs in large crystals (up to 2 mm in size) in a vein crosscutting the Excelsior Group phyllites. $\delta^{18}O_{SO4}$ was measured because the sulfate is more reliable than the hydroxyl site for the retention of primary oxygen-isotope compositions in alunite (Bethke et al., 2005). The $\delta^{18}O_{SO4}$ values range from 2.5 to 6.9‰, the δD values from –55.8 to –69.3 permil (Table 4), and the $\delta^{34}S_{SO4}$ values from 21.1 to 24.2 permil (Table 4).

In the Santa Rosa area, alunite (CPR 351) filling leached feldspar phenocrysts in advanced argillic altered intrusive rock, probably a quartz-monzonite porphyry dyke yield $\delta^{18}O_{SO4}$ values of 1.9 ‰, δD of –72.5 ‰, and $\delta^{34}S_{SO4}$ of 21.5 permil.

The Venencocha alunite sample (CPR 347) and that from Santa Rosa (CPR 351) have distinctly younger ages (12.3 Ma) than the other analyzed alunite samples

Table 4: Hydrogen, Oxygen and Carbon isotope compositions of ore and gangue minerals. For sample locations, see Appendix 2

Location	Sample	Zone	Mineral	$\delta^{18}O$	$\delta^{18}O_{H2O}$	δD	δD_{H2O}	$\delta^{34}C$
First mineralization stage								
Pyrite-quartz body								
4210 m western pit	CPR 4		Quartz	17.2	8.7			
4250 northern pit	CPR 23		Quartz	16.0	7.5			
Southwestern pit	FPE-130-13		Quartz	16.6	8.1			
Second mineralization stage								
Enargite-pyrite veins								
4280 m, northen pit	CPR 19	core	Quartz	13.3	3.9			
4200 m, western pit	CPR 439a	core	Quartz	12.2	2.8			
	CPR 439b	core	Quartz	11.0	1.6			
4190 m, western pit	CPR 440	core	Quartz	10.8	1.5			
4190 m, western pit	CPR 440	core	Barite	10.0				
Matagente area (including Cuerpo Nuevo and Manto V								
4310 m, Cuerpo N.	CPR 10	outer	Kaolinite	9.2	4.6	-107	-90	
4310 m, Cuerpo N.	CPR 11	outer	Kaolinite	9.6	5.0	-107	-90	
4310 m, Cuerpo N.	CPR 26	outer	Kaolinite	10.9	6.3	-106	-89	
4310 m, Cuerpo N.	CPR 27	intermediate	Kaolinite	10.5	7.2	-89	-73	
4320 m, Cuerpo N.	CPR 30	intermediate	Kaolinite	9.3	6.0	-88	-72	
4310 m, Cuerpo N.	CPR 44	intermediate	Kaolinite	10.0	6.7	-87	-71	
4310 m, Cuerpo N.	CPR 47	intermediate	Kaolinite	8.0	4.7	-85	-69	
4320 m, Manto V	CPR 54	outer	Kaolinite	9.7	5.2	-100	-83	
4310 m, Cuerpo N.	CPR 25a		Quartz	17.2	6.3			
	CPR 25b		Quartz	17.9	7.0			
4310 m, Cuerpo N.	CPR 10	outer	Barite	10.6				
4310 m, Cuerpo N.	CPR 11	outer	Barite	10.2				
4310 m, Cuerpo N.	CPR 25	outer	Barite	9.3				
4320 m, Cuerpo N.	CPR 56	outer	Barite	9.6				
4320 m, Cuerpo N.	CPR 150	intermediate	Barite	10.3				
4310 m, Cupero N.	CPR 7	outermost	Fe-Mn-Zn carbonate	15.9				-2.0
4310 m, Cuerpo N.	CPR 11	outermost	Fe-Mn-Zn carbonate	15.9				-2.0
4310 m, Cuerpo N.	CPR 12	outermost	Fe-Mn-Zn carbonate	16.4				-4.5
4310 m, Cuerpo N.	CPR 47	outermost	Fe-Mn-Zn carbonate	18.0				-1.0
San Alberto								
4330 m, San Alberto	CPR 58a	outer	Quartz	9.1	-1.8			
	CPR 58b		Quartz	10.1	-0.8			
4300 m, San Alberto	CPR 395		Quartz	10.4	-0.5			
4330 m, San Alberto	CPR 48	outer	Barite	10.2				
4330 m, San Alberto	CPR 59	outer	Barite	9.5				
Colas area								
4300 m, southern pit	CPR 57.2	intermediate	Kaolinite	10.6	7.3	-89	-73	
southern open pit	CPR 480a	core	Quartz	16.8	7.4			
	CPR 480b	core	Quartz	17.1	7.7			
4200 m	CPR 417	outer	Kaolinite	10.8	6.2	-106	-88	
4200 m	CPR 422	outer	Kaolinite	9.9	5.3	-112	-95	

Table 4: (cont.)

Location	Sample	Zone	Mineral	d18O	d18OH2O	dD	dDH2O	d34C
4170 m	CPR 309	outer	Kaolinite	10.0	5.4	-114	-97	
4170 m	CPR 311	intermediate	Kaolinite	5.3	2.0	-95	-79	
4180 m	CPR 309		Quartz	15.0	5.6			
3180 m	CPR 471a		Quartz	15.7	4.8			
	CPR 471b		Quartz	16.0	5.1			
below 4320 m	CPR 475	intermediate	Barite	-1.5				
4200 m	CPR 429	outermost	Fe-Mn-Zn carbonate	16.2				-7.0
4200 m	CPR 431	outermost	Fe-Mn-Zn carbonate	15.8				-4.3
3180 m	CPR 471	outermost	Fe-Mn-Zn carbonate	16.4				-8.1
Cayac Noruega orebody								
4186 m, DDH CP-00-108	CPR 82	intermediate	Kaolinite-dickite	11.6	8.3	-82	-66	
Northeastern open pitsmall veins								
4300 m, northen pit	CPR 58	outermost	Fe-Mn-Zn carbonate	9.5				-5.1
4300 m, northen pit	CPR 59	outermost	Fe-Mn-Zn carbonate	12.4				-6.1
4290 m, northen pit	CPR 407	outermost	Fe-Mn-Zn carbonate	18.1				-6.6
4290 m, northen pit	CPR 413	outermost	Fe-Mn-Zn carbonate	17.9				-6.5
4290 m, northen pit	CPR 432	outermost	Fe-Mn-Zn carbonate	19.5				-6.1
4290 m, northen pit	CPR 433	outermost	Fe-Mn-Zn carbonate	19.0				-5.7
4290 m, northen pit	CPR 459	outermost	Fe-Mn-Zn carbonate	17.6				-5.9
4290 m, northen pit	CPR 459	outer	Barite	4.5				
Underground mine								
4040 m, 9020E, 9890N	CPR 319a		Quartz	15.3	4.7			
	CPR 319b		Quartz	15.8	5.1			
Venencocha								
Venencocha area	CPR 365		Quartz	14.6	5.2			
	CPR 376a		Quartz	17.7	8.3			
	CPR 376b		Quartz	17.6	8.2			
	CPR 347		alunite	2.5	-5.9	-66	-73	
	CPR 365		alunite	3.5	-4.9	-69	-76	
	CPR 380		alunite	6.7	-1.7	-60	-67	
	CPR 381		alunite	6.9	-1.4	-56	-62	
Santa Rosa								
Santa Rosa pit	CPR 351		alunite	1.9	-6.4	-73	-79	
Late calcite veins								
4300 m, Cuerpo N.	CPR 399a	outermost	Calcite	18.8				0.7
4300 m, Cuerpo N.	CPR 399b	outermost	Calcite	20.1				0.9
4200 m, Colas	CPR 424a	outermost	Calcite	21.0				1.0
Unaltered Pucará carbonate rocks								
	RB 5		Whole rock	19.2				2.4
	RB 4		Whole rock	23.1				1.4
	RB 3		Whole rock	24.7				2.9
	RB 1		Whole rock	25.3				2.7

Note: a and b are replicates

Table 5: Sulfur Isotope Compositions of sulfides and sulfates. For sample location, see Appendix 2

			d^{34} S (‰ CDT)						
Location	Sample	Zone	Barite	Galena	Pyrite	Enargite	Sphalerite	Alunite	Temperature (°C)[1]
First mineralization stage									
Pyrite-quartz body									
western 4070 bench	CPR 15				0.4				
southern 4240 bench	CPR 38				0.4				
Zn-Pb related to pipe-like pyrrhotite bodies									
CN-C	CPR 319				2.8		2.0		*340?*
CN-A	CPR 461						2.1		
CN-A	CPR 464				3.3		1.9		*197*
M-309	6_18[2]			-0.2	1.1		2.6		260
CN-A	10_19[2]			-1.6	2.0		0.8		304?, *280*, *227*
CN-A	12_4[2]			-0.7	0.0		2.4		234
CN-A	14_28[2]			-0.6	0.1		2.9		205
CN-A	16_41[2]			-0.7	1.5		1.4		344?
Cayac Noruega	CPR 76	outer w/ kaol					2.6		
Cayac Noruega	CPR 77a	intermediate to outer					2.8		
Cayac Noruega	CPR 77 b	intermediate to outer					3.5		
2nd ramp NW	CPR 405						0.0		
Second mineralization stage									
Western enargite-pyrite veins									
en veins	CPR 439	core				-0.0			
en veins 2nd ramp	CPR 440	interm	31.2						
Plan J norte, W pit	FPE-130-7	in volc rock diss			2.5				
Cuerpo Nuevo (Matagente area)									
Matagente 4310	CPR 7	outer		2.3					
Matagente 4310	CPR 10	outer	22.0						
Matagente 4310	CPR 11	outer	22.9						
Matagente 4310	CPR 25	outer	24.4		1.6				**264**
Matagente 4310	CPR 26	outer		3.1			2.2		
Matagente	CPR 30	outer, sulf rock					-0.5		
Matagente 4310	CPR 47	outer		0.7			4.2		204
Matagente 4310	CPR 56	outer	19.3						
Matagente 4320	CPR 150	interm	22.3		-0.1				**271**
Matagente 4320	CPR 394	outer, sulf rock		-0.1			-3.7		
Matagente below 4320	CPR 475	outer	4.2						
Matagente below 4320	CPR 477	outer, sulf rock					-0.3		
Colas area									
bench E	CPR 309	outer, sulf rock				1.3			
tajo E	CPR 398	outer		0.8	1.0	-0.4			*195*
colas	CPR 417	outer, sulf rock				1.3			
colas	CPR 422	outer				1.6			
colas	CPR 428	outer w/carb				2.4			
colas	CPR 429	outer w/carb				0.2			
tajo E	CPR 431	outer w/ carb		-0.5		0.4			
NE open pit small veins									
NE pit	CPR 407	outer w/ carb		0.4		0.6			
NE pit	CPR 456	outer, sulf rock		-0.7		1.4			290
NE pit	CPR 459	outer	5.5						
San Alberto									
San Alberto	CPR 48	outer	18.1						
San Alberto	CPR 59	outer	10.5						

Table 5: (Cont)

San Alberto	CPR 395	outer				-0.5	
San Alberto	CPR 486	outer	0.9	0.6			
San Alberto	CPR 486	outer				0.8	
Venencocha							
Venencocha area	CPR 347						21.8
Venencocha area	CPR 365						23.3
Venencocha area	CPR 380						21.1
Venencocha area	CPR 381						24.2
Santa Rosa							
Santa Rosa pit	CPR 351						21.6

[1] Temperatures calculated for mineral pairs.

[2] Isotope data from Austria (1975) in Einaudi (1977)

Notes: Temperatures followed by an interrogation mark (?) are rejected (see text). Pairs without temperatures have not been calculated because of lack of equilibrium. Temperatures in bold are calculated on the mineral pair ba-py, temperatures in italic are calculated on the pair py-sl, temperatures in regular font are calculated on the pair ga-sl, and temperatures in italic underlined are calculated on the pair gn-py.

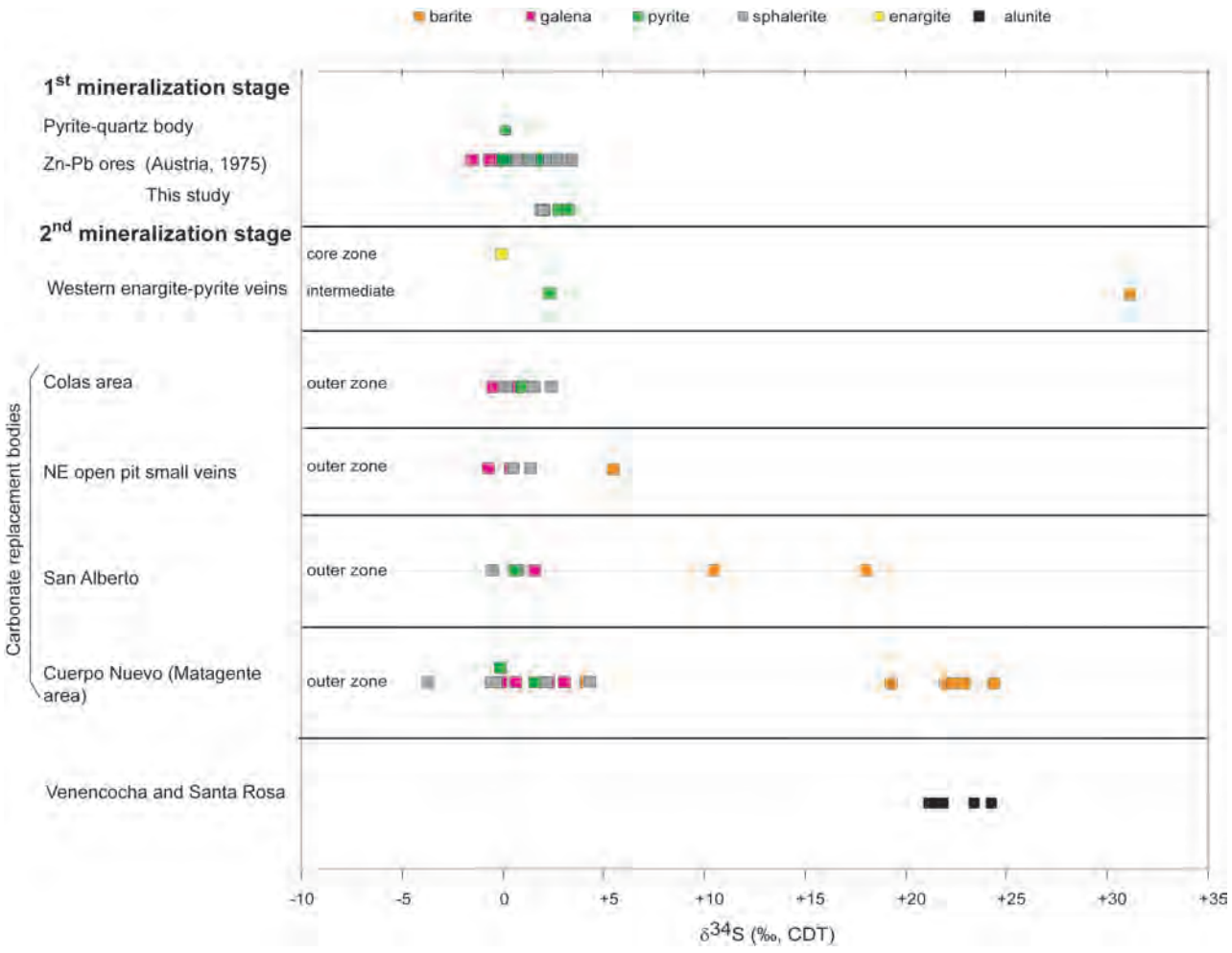

Fig. 10: *δ ^{34}S values of sulfides and sulfates from the first and second mineralization stages at Cerro de Pasco.*

(14.5 Ma) and the assumed mineralization age (14.5 to 14.4 Ma, Baumgartner et al. Part II). The younger ages are interpreted to be disturbed by late circulating fluids and therefore, it is probable that the two younger alunite samples experienced post-depositional isotopic exchange.

Discussion-Fluid inclusions

Fluid inclusions from the first mineralization stage

Results of the fluid inclusion study in quartz (subtpye IA1) from the first mineralization stage pyrite-quartz body support the presence of low to moderately saline fluids (0.2 to 6.8 wt % NaCl equiv.) at temperatures ranging from 200 to 275°C. These temperatures are compatible with the formation of the quartz-sericite alteration halo adjacent to the pyrite-quartz body. The relatively large dispersion of the salinity values (0.2 to 6.8 wt % NaCl equiv) and the absence of evidence for boiling is best explained by different mixing ratios of a saline fluid with a non-saline fluid. Since the microthermometric data do not show any correlation between salinity and homogenization temperature (Fig. 9), the non-saline fluid could be meteoric water, which has circulated deep enough and long enough to attain the same temperature as the saline fluids (170-200°C).

The fluid inclusion results obtained in the pipe-like pyrrhotite bodies (192 to 250°C, 1.1 to 4.3 wt % NaCl equiv.) zoned to Zn-Pb mineralization (183 to 212°C, 3.2 to 4 wt % NaCl equiv.) show a slight temperature decrease with salinity (Fig. 9). This suggests a mixing between a hot and saline fluid (at least 7 wt % NaCl equiv) with a slightly cooler non-saline fluid. Again, the non-saline fluid could be meteoric water circulating at a significant depths to attain at least 180°C, which is the lowest homogenization temperature observed in pyrrhotite bodies and related Zn-Pb ores.

Fluid inclusions from the second mineralization stage

From paragenetic observations, the fluid precipitating enargite in the second stage enargite-pyrite veins on the western part of the open pit may be represented by the fluid inclusions in growth zones from hydrothermal quartz (subtype IIA2) yielding homogenization temperatures from 187 to 293°C and salinities from 0.2 to 5.2 wt % NaCl equiv. (Table 3, Figs. 8 and 9). Taking into account the limitations of the method described above, the fluid inclusions in enargite are compatible with these values. The slightly higher homogenization temperatures and salinities obtained in fluid inclusions in quartz (subtype IIC) from the Venencocha area (245 to 261°C, 3.2 to 7.7 wt % NaCl equiv) are in agreement with temperature estimates using mineralogical assemblages such as quartz-diaspore and quartz-zunyite also characteristic of advanced argillic alteration. They constrain the temperature between 220 and 300°C for diaspore and 250 to 300°C for zunyite (Reyes, 1990).

In carbonate replacement bodies, a temperature decrease between the fluid inclusion data of quartz from the core zone (178-265°C, 0.2-7.5 wt % NaCl equiv) and sphalerite from the outer zone 168-222°C, 3-11.8 wt % NaCl equiv, these salinity values may be overestimated as discussed above for fluid inclusions in enargite (Fig. 9) is observed. The temperatures correspond to those expected for dickite and kaolinite stability fields, minerals present in the intermediate zone. According to Watanabe and Hedenquist (2001), the upper temperature limit of dickite stability is 270°C.

In summary, all studied fluid inclusions of the second mineralization stage, except those in the cracks within magmatic quartz cores, are characterized by moderate salinities (maximum of 7.5 and 5 wt % NaCl equiv for the carbonate replacement bodies and enargite-pyrite veins, respectively). Owing to the very restricted amount of vapor inclusions, the dispersion of the salinity values can result from different mixing ratios of a saline fluid (at least 7 wt % NaCl equiv) with meteoric water. The numerous aqueous inclusions in quartz from the enargite-pyrite veins and subordinately in the carbonate replacement bodies showing salinity values close to zero (17 analyses of subtype IIA2 and 3 of subtype IIB1 below 0.3 % NaCl equiv, with temperatures between 200 and 250°C, Fig. 9), could represent the non saline end-member consisting of heated meteoric water.

The much higher salinities encountered in the subtype IIA1 fluid inclusions observed along cracks within a magmatic quartz core (subtype IIA1, 1 to 22.3 wt % NaCl equiv and 220 to 280°C) may be due to boiling and probably do not represent a fluid that originally had higher salinities. The presence of numerous vapor inclusions favors this hypothesis, which is also compatible with the observed salinity variations without temperature change. It can be speculated that the formation of subtype IIA1 fluid inclusions along the cracks was related to the deposition of the CL texturally irregular hydrothermal quartz (2 in Fig. 6H) deposited between the magmatic quartz core (1 in Fig. 6H) and the CL oscillation-rich growth zones of hydrothermal quartz (3 in Fig. 6H). Boiling can take place when the pressure decreases abruptly and cracks within the magmatic quartz core could be the result of this pressure decrease.

Minimal pressures and fluid origin

The present study shows that salinity and temperature of the first and second mineralization stages are similar. Ore formation depths using calculated minimal pressures with L-V isochores in the pyrite-quartz body (10-55 bars), the pyrrhotite bodies and the Zn-Pb ores (10 and 60 bars) of the first mineralization stage, and from the second mineralization stage enargite-pyrite veins (20-70 bars), carbonate replacement bodies (20-50 bars) as well in the Venencocha area (30-45 bars), suggest that the Cerro de Pasco deposit formed at depths of at least 400-500 m below the water table. More precise pressure estimations could not be made because of the

lack of boiling assemblages. The obtained depths are consistent with estimates of erosion based on geological evidence.

The different ores of the first mineralization stage all show similarly moderate salinities (pyrite-quartz body = 0.2 – 6.8 wt % NaCl equiv, pyrrhotite bodies = 1.1 – 4.3 wt % NaCl equiv, and Zn-Pb ores = 3.2 – 4.0 wt % NaCl equiv). These values are in the same range as those obtained for the second stage ores (enargite-pyrite veins = 0.2 – 5.2 wt % NaCl equiv, carbonate replacement bodies = 0.2 – 7.5 wt % NaCl equiv, and Venencocha = 3.2 – 7.7 wt % NaCl equiv). The median temperatures show a decrease from the pyrite quartz body and the pyrrhotite pipes (pyrite-quartz body = 247°C and pyrrhotite bodies = 230°C) to the related Zn-Pb ores outwards (196 °C). The carbonate replacement bodies and the western enargite-pyrite veins show similar temperatures (235 and 227°C, respectively in median temperatures). Fluids with the above mentioned characteristics can result from a diluted brine, a single-phase magmatic fluid in the sense of Hedenquist et al. (1998), or from a contracted vapor in the sense of Heinrich (2005). It should be noted that a contracted magmatic vapor may have salinities close to those of a single phase fluid (~7 wt % NaCl equiv) if the phase separation occurs sufficiently deep.

Discussion - Stable isotopes

The most detailed isotopic analyses have been made for the carbonate replacement bodies (O, H, C, S), the enargite-pyrite veins (S, O), and alunite from Venencocha and Santa Rosa (S, O, H). For the pyrite-quartz body, only oxygen and sulfur isotope data are available. Therefore, the first part of the discussion is mainly based on the results of the second mineralization stage. In the second part of the discussion, owing to similar fluid inclusion data of both mineralization stages, an appraisal of the entire mineralization system is attempted.

Ore-forming fluids

Oxygen and hydrogen isotope compositions obtained on alunite at Venencocha and Santa Rosa areas provide an estimate of the composition of meteoric water, which is one of the end-members identified in the ore-forming fluids of several Cordilleran base metal deposits including Colquijirca, Bendezú (2007), Julcani (Deen et al., 1994), San Cristobal (Campbell et al, 1984; Beuchat et al. 2004), Main Tintic (Hildreth and Hannah, 1996, Table 6). Another ore-fluid end-member identified in these deposits is magmatic water. These two end-member fluids have also been observed in high sulfidation precious metal deposits (e.g. Arribas et al., 1995; Hedenquist et al. 1998). The isotopic composition of magmatic and meteoric end-member fluids can evolve through time by reaction with wall rocks and/or by mixing and it is therefore important to evaluate their original isotopic composition (e.g. Bethke et al., 2005).

In contrast to other mineralized districts where unaltered silicates allow the O and H isotope composition of aqueous fluids generated during crystallization of a magma body to be estimated, this is not possible at Cerro de Pasco because all quartz-monzonite porphyritic dykes are altered, with biotite altered to chlorite and plagioclase to calcite. Conventional references for primary magmatic water (PMW of Taylor, 1979) and for felsic magmatic water (FMW of Taylor, 1992) have been plotted in Figure 11, as well as the meteoric water (Craig, 1961) and kaolinite (Savin and Epstein, 1970) lines. Exsolved fluids often undergo isotopic exchange with a crystallizing magma Bethke et al., 2005) when they migrate upward to the plastic subsolidus region of the intrusion's carapace, remaining there until release (Fournier, 1999). Deen et al. (1994) calculated the isotopic exchange track of primary magmatic fluids as calculated in Ohmoto (1974) with felsic rocks having compositions compatible with those of biotite in the glassy rocks at Julcani. The resulting "exchanged" magmatic water field at 400°C has been plotted in a $\delta D - \delta^{18}O$ diagram (Fig. 11). The use of the Julcani data is appropriate because of the geographic proximity and the similar geological situation, including the presence of felsic rocks that are similar in composition to those of the diatreme-dome complex at Cerro de Pasco.

Values of δD and $\delta^{18}O$ for fluids in equilibrium with alunite were calculated using the fractionation factors determined experimentally by Stoffregen et al. (1994) at a temperature of 250°C, estimated from the mineral assemblages as well as from the microthermometric data on quartz occurring with alunite (subtype IIC). These are given in Table 4 and shown in Figure 11.

The isotopic composition of meteoric water at Cerro de Pasco can be evaluated by linearly extrapolating the trend obtained for fluids in equilibrium with alunite at Venencocha and Santa Rosa, hence representing mixtures of magmatic and unexchanged meteoric fluids. The two alunite samples, which probably experienced post-depositional isotopic exchange have not been considered for the mixing regression line (Fig. 11). Linear extrapolation suggests Mid-Miocene local meteoric water at Cerro de Pasco at a $\delta D = -95 \pm 10$ ‰ and $\delta^{18}O$ close to -13 ± 1 ‰ (Fig. 11), somewhat higher in δD and $\delta^{18}O$ than the isotopic composition of local meteoric waters at Julcani during the Mid-Miocene ($\delta D = -120$ to -138 ‰ and $\delta^{18}O = -17.5$ to -18.8 ‰, Deen et al., 1994), values based on a mixing regression line represented by fluids extracted from inclusions in late stage barite, siderite, and pyrite. The inferred values are also higher than those proposed by Bendezú (2007) at Colquijirca ($\delta D = -140 \pm 10$ ‰ and $\delta^{18}O = -18 \pm 1$ ‰) obtained by projecting the regression mixing line representing the entire population of alunite fluids. These deposits are today located at a similar altitude (4000 – 4300 m) but are of slightly younger age (10 – 12 Ma) compared to Cerro de Pasco. Lower values for meteoric waters are also used by Strusievicz et al. (1998) and Fifarek and Rye (2005) at Pierina (δD between -130

Table 6: Fluid inclusion and stable isotope data from Cordilleran base metal deposits

Location	Age	Host rock	First stage main ore minerals described	Second stage main ore minerals	Fluid inclusion data[1]	Stable isotope data	Interpretation
Cerro de Pasco, Peru	15-11 Ma	Mainly carbonate rocks (Pucará Grp.) but also diatreme breccia and siliciclastic rocks (Excelsior Fm.)			1st stage: 185-275°C and 0.5-12 wt-% NaCl eq. 2nd stage: 170-290°C and		This study
Colquijirca, Peru	10.6-12.4 Ma	Mainly carbonate Pocobamba Fm. but also in diatreme breccia and dacitic volcanic rocks		enr, cpy, tn-tt, bn, sl, gn	165-300°C and 0.2-7 wt-% NaCl eq.	$\delta^{18}O$ and δD values from 1.9 to 12.8 ‰ and from -97 to -142 ‰ (kaol)	Mixing of magmatic brine and meteoric water (Bendezú, 2006)
Huanzala, Peru	7.7 ± 0.4 Ma	Santa Formation limestone	po, asp, sl	tn, enr	Early stage: 200-330°C Late stage: 250-330°C	No data	Imai et al. (1985), Imai (1986)
Hualgayoc, Peru	~11 Ma	Limestones from the Chulec Fm. and sandstone from the Goyllarisquizga Group and the Inca Fm.		replacement bodies: po, asp, sl, veins: enr, tn, cp, pyrg, sl, gn	170-300°C and 1.2-12.0 wt-% NaCl eq.	$\delta^{18}O$ and $\delta^{13}C$ (cal and rdc) from 9.1 to 13.8 ‰ and from -3.6 to -9.8 ‰	Macfarlane et al (1994)
Julcani, Peru	10.1-7.0 Ma	Dacite-rhyolite domes		enr, cp, sl, gn	180-330°C and 2.7-11.2 wt-% NaCl eq.	$\delta^{18}O$-δD: -8.7 to 3.7 ‰ and -112 to -60 ‰ (fluids from fluid inclusions)	Magmatic brine mixing with isotopically exchanged meteoric water. (Deen et al., 1994):
San Cristobal, Peru	~5-6 Ma	Pucará Group limestone, Mitu Group volcanics	py-qtz body, py, wf, tt, sl-gn asp, sl		Early stage: 205-260 °C and 2.9 to 5.1 wt-% NaCl eq (Beuchat, 2003). 230-330 °C and 1 to 6.3 wt-% NaCl eq. (Campbell, 1984) Late stage: 150-320 °C and 0.2 to 7 wt-% NaCl eq. (Campbell, 1984)	Early stage $\delta^{18}O$-δD in qtz and wf: 1.4 to 7.3 ‰ and -58 to -148 ‰ (Campbell ,1984) Late stage: 5 to 7 ‰ and -90 to -140 ‰ (Beuchat, 2003)	Mixing of magmatic brine with isotopically exchanged meteoric water (Campbell ,1984 and Beuchat et al. 2004)
Pasto Buena, Peru	~9 Ma	Quartz-monzonite Consuzo stock	wf, po, asp, mo,	late stage: enr, tt, sl, gn	175-290°C and 2-17 wt-% NaCl eq.	$\delta^{34}S$ sulfide: -6.0 to 3.0 ‰ $\delta^{18}O$-δD: -0.2 to 6 ‰ and -50 to-110 ‰	Meteoric water influx in magmatic brine (Landis and Rye, 1974)
Main and East Tintic, Utah, USA	Late Eocene	Paleozoic limestones (Ophir Fm.)		enr, tn-tt, Ag-gn, sl	160-360°C and 0.2-8.8 wt-% NaCl eq. (Hildreth & Hannah, 1996) 150°-200°C (Batchelder, 1978)	$\delta^{18}O$-δD in FI in qtz: -5.1 to 0.0 ‰ and 121 to -118 ‰ $\delta^{18}O$-δD in FI in py: similar $\delta^{18}O$ and -118 to -101 and -89 to -84 (Batchelder 1978): $\delta^{34}S$: -2.0 ‰ (Hildreth & Hannah, 1996)	Early fluids represent early aliquots of exsolved magmatic fluids (formation of early quartz) and late high salinities fluids forming main ore (Hildreth & Hannah, 1996)
Butte Main stage, Montana, USA	66-63 Ma	Butte quartz-monzonite		enr, cc, bn, cv, dg, tn, cp, sl, gn	Main stage:	Main stage: $\delta^{34}S$ sulfides: -3.7 to 4.8 ‰	Field et al (2005)
Bisbee, Arizona, USA	Late Jurassic	Argillaceous limestone		enr, bn	300-340°C		Friehauf (1998)
Collahuasi, Rosario vein, Chile	32.9 Ma (porphyry stage)	Porphyry stock and volcano-sedimentary rocks		py-cp-(tn), py-bn-(enr), cc-dg-cv	220-320°C and 0.7 to 6.8 wt-% NaCl eq.	no data	Masterman et al. (2005)

[1]all fluid inclusions reported were measured in quartz

Mineral abbreviations: asp = arsenopyrite; bn = bornite; cc = chalcocite; cp = chalcopyrite; cst = cassiterite, cv = covellite; dg = digenite; enr = enargite; fm = famatinite; gn = galena; lz = luzonite; mt = magnetite; mo = molybdenite; po = pyrrhotite; pyrg = pyrargyrite; py = pyrite; sl = sphalerite; tn = tennantite; tt = tetrahedrite; wf = wolframite

and -150‰ and $\delta^{18}O$ between -20 to -17 ‰), which is located at an elevation of 4000 m and dated at 14.5 Ma. The different isotopic composition of meteoric water at Cerro de Pasco may be due to somewhat lower altitude at around 14.5 to 15 Ma and the fact that at that time, global temperatures were still somewhat warmer. The period between 16 and 14 Ma represents a period of significant global change in climatic conditions, in particular the onset of large-scale cooling and the growth of the bulk of the Antarctic ice sheets (Zachos et al., 2001).

The alunite-fluid mixing line projects to the field of magmatic fluids exchanged at 400°C of Deen et al., (1994) so that the magmatic fluid end-member is assumed to have a composition around $\delta D = -30$ ‰ and $\delta^{18}O = 7$ ‰. In high sulfidation deposits where a magmatic-hydrothermal genetic model is proposed (Bendezú, 2007; Arribas et al., 1995; Bethke et al., 2005; Deyell et al., 2005; Fifarek and Rye, 2005) two end-member fluids have also been identified, whereby magmatic-hydrothermal alunite forms subsequent to disproportionation of a SO_2 vapor plume into H_2S and HSO_4^- by condensation into meteoric water (Arribas et al., 1995; Rye et al., 1992).

Kaolinite samples present in the carbonate replacement bodies are considered to be of hypogene origin because they do not fall close the kaolinite line (Fig. 11) of Sheppard et al. (1969), which represents supergene kaolinite and/or kaolinite that experienced significant post-depositional exchange with meteoric water at supergene conditions. Therefore, fluids in equilibrium with kaolinite should constitute a good approximation to the ore-forming fluids for the intermediate and outer zones of the carbonate replacement bodies. Oxygen and hydrogen isotope compositions of fluids in equilibrium with kaolinite were calculated at 220°C for the intermediate zone and at 200°C for the outer zone using equations of Sheppard and Gilg (1996) for $\delta^{18}O$ and of Gilg and Sheppard (1996) for δD. Temperatures used are based on microthermometric measurements obtained in quartz from the core zone (subtype IIB1) and sphalerite from the outer zones (subtype IIB2). The intermediate zone values are characterized by higher δD values (–71 to –79‰) and therefore lie closer to the magmatic end-member than those from the outer zone (–83 to –97 ‰). The $\delta^{18}O$ values for both zones are similar ($\delta^{18}O = 2.0$ to 7.3 ‰ and 4.6 to 6.3 ‰, respectively). The isotope compositions of all fluids in equilibrium with kaolinite do not fall on the alunite mixing line since they have distinctly lower δD and higher $\delta^{18}O$ values compared to fluids in equilibrium with alunite (Fig. 11). It has to be mentioned that the variations in δD from the fluid in equilibrium with kaolinite may also be the result of pressure effects which have not been taken into account in the fractionation equation of Gilg and Sheppard (1996), as reported by Driesner (1997).

The interaction of hot fluids (around 300°C) in an open, convecting system with wall rocks can lead to a pronounced shift in the isotopic compositions of the fluid and hence the alteration minerals precipitating in equilibrium with these exchanged fluids (Taylor, 1974) may well have compositions different from those minerals precipitating from unexchanged fluids. According to Fournier (1999), meteoric-derived fluids have been found in deep geothermal exploration wells at temperatures up to around 350°C. Models for isotopic exchange of meteoric water with (1) volcanic, (2) Excelsior Group rocks, and (3) Pucará carbonate rocks over a range of temperature from 25 to 400°C have been calculated following the equation of Ohmoto and Rye (1974) and are plotted in Figure 11. Estimates of the δD and $\delta^{18}O$ values of volcanic rocks (-92 and 8.5 ‰, respectively) have been taken from Deen et al. (1994) and those from sedimentary rocks (close to Excelsior Group rocks in composition, -60 and 16 ‰) containing siliciclastic components from Field and Fifarek (1985). For carbonate rocks, $\delta^{18}O$ was measured in Pucará Group rocks not affected by possible ore-mineralizing fluids at 15 ‰, this value is in agreement with the field of Pucará carbonate rocks of Moritz et al. (1996). Using the equation of Ohmoto and Rye (1974), original meteoric water isotopic compositions at Cerro de Pasco, and water/rock weight ratios of 1.8 for isotopic exchange with Excelsior Group rocks at around 200°C, results in values for the exchanged fluids that would be similar to those in equilibrium with kaolinite. A similar result is obtained by isotopic exchange of meteoric water with the Pucará carbonate rocks. In that case, there is only a significant $\delta^{18}O$ shift of the meteoric water isotopic composition and virtually none in the δD value. Isotopic exchange with exclusively volcanic rocks is considered unlikely because, according to the model used, exchanged meteoric water would have appropriate compositions in equilibrium with kaolinite only at around 400 °C. These temperatures prevail near the brittle-ductile transition and it is improbable that meteoric water circulates that deep in a porphyry related geological context (Fournier, 1999). In addition, the volume of volcanic rocks present at Cerro de Pasco is relatively small compared to that of the Excelsior Group rocks. Therefore, it is believed that Excelsior Group phyllite and shale played a major role in the isotopic exchange process, whereby a subordinate participation of magmatic rocks. According to the geological situation and assumed fluid path (Fig. 4), fluid interaction with the Pucará carbonate rocks is considered to be minor compared to that with the Excelsior Group rocks.

The curve modeled for isotopic exchange with Excelsior Group rocks shows realistic temperatures (around 200°C), which are sufficient to obtain isotope values similar to those required to form kaolinite fluids by mixing exchanged meteoric waters with magmatic water. The water/rock weight ratios used (for Excelsior Group, volcanic, and carbonate rocks) are in agreement with those estimated for many epithermal districts and those observed in active geothermal systems (Field and Fifarek, 1985; Taylor, 1974). The end-member of isotopically exchanged meteoric water necessary to explain the kaolinite $\delta^{18}O$ and δD values, could correspond to a non-saline, hot end-member of the ore-forming fluids

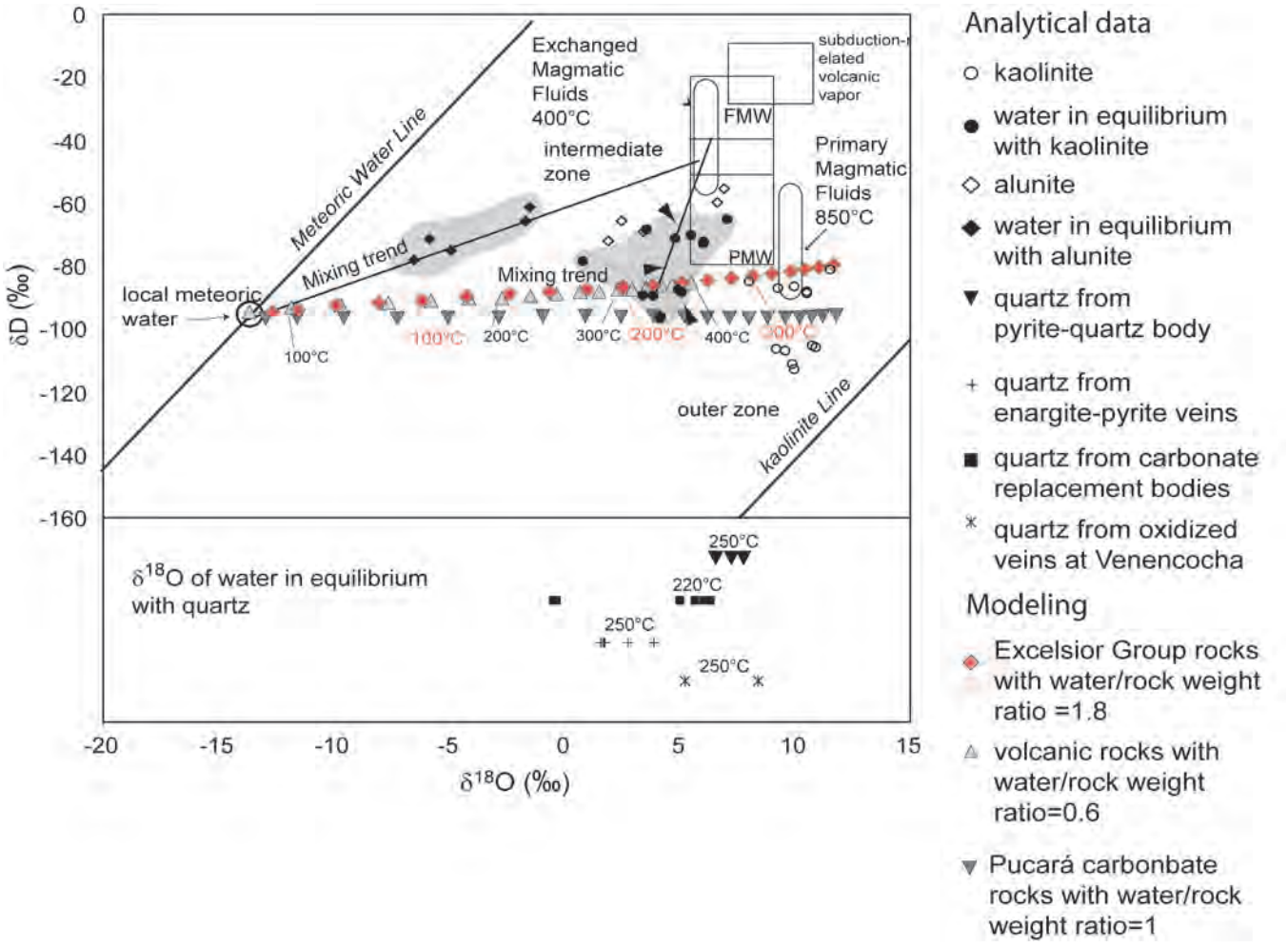

Fig. 11: *δD and $\delta^{18}O$ plot of alunite and kaolinite with corresponding fluids in equilibrium with those minerals. The δD and $\delta^{18}O$ values of fluid in equilibrium with alunite (from oxidized veins at Venencocha and Santa Rosa) were calculated using equation of Stoffregen et al. (1994) at 250°C. A mixing trend line shows the two fluid end-members forming the alunite fluids. This mixing trend intersects the meteoric water line of Craig (1961) at the δD and $\delta^{18}O$ values estimated for Mid-Miocene meteoric water at Cerro de Pasco (δD = 95 ± 10 ‰ and $\delta^{18}O$ close to 13 ± 1 ‰). The δD and $\delta^{18}O$ values of fluids in equilibrium with kaolinite were calculated using Sheppard and Gilg (1996) for O and Gilg and Sheppard (1996) for H, at 220°C for kaolinite from the intermediate zone and at 200°C for kaolinite from the outer zone of carbonate replacement bodies. The kaolinite fluids lie on a mixing trend between the exchanged magmatic fluid end-member of Deen et al. (1994) and an end-member composed of isotopically exchanged meteoric water at around 200-250°C. δD and $\delta^{18}O$ values of meteoric water exchanged with typical volcanic and Excelsior Group rocks have been modeled. The model shows that the end-member composed of isotopically exchanged meteoric water mainly exchanged with Excelsior Group rocks at depths and at a temperature of 200 to 250°C. In the lower part of the diagram, $\delta^{18}O$ values of fluids in equilibrium with quartz are presented, calculated using equation of Zhang et al. (1989) at 250°C for quartz in the pyrite-quartz body, 220°C for quartz occurring in the cores of carbonate replacement bodies, 250°C for quartz in the enargite-pyrite veins, and 250°C for quartz in oxidized veins at Venencocha. Other field and lines are the kaolinite line after Sheppard et al. (1969), primary magmatic fluids after Deen et al. (1994), felsic magmatic water (FMW) after Taylor (1992), primary magmatic water (PMW) after Taylor (1979), and subduction-related volcanic vapor after Giggenbach (1997).*

(at least 180°C) postulated by the fluid inclusion study. According to the isotopic results, the more saline fluid (at least 7 wt % NaCl eq.) identified in the fluid inclusion study is closest to the magmatic fluid end-member. The mixing proportions of these two end-members are variable, as shown by the vertical part of the trend depicted by the fluids in equilibrium with the kaolinite (Fig. 11).

An alternative interpretation to explain the fluids in equilibrium with kaolinite would be mixing between unexchanged meteoric water and magmatic water. On the basis of isotopic compositions for meteoric water similar to those estimated for other deposits in this region (Deen et al., 1994; Bendezu, 2007), this would require either unrealistically low temperatures (100-130°C) of kaolinite formation or an unrealistically high component of magmatic water, even higher than that for alunite for the fluids of the more distal kaolinite. As has been shown by Cooke and Simmons (2000), waters precipitating hypogene clays, silica and ore minerals in high sulfidation deposits such as Nansatsu (Japan), Rodalquilar (Spain) or la Mejicana (Mexico) have consistently shown to have a greater component of meteoric water than those precipitating alunite. However, yet another possibility could be that the meteoric water at the time of mineralization at Cerro de Pasco was marginally higher in ^{18}O and D than at Colquijirca, Julcani or Pierina, as a result of either earlier formation of this deposit and climatically different conditions prior to about 14.5 Ma (Zhang et al., 1989) and/or as a result of slightly lower altitudes at that time. If that is the case, then the fluids in equilibrium with the kaolinite may represent exchanged and wall-rock buffered fluids, not requiring a larger magmatic fluid component compared to fluids in equilibrium with alunite.

The $\delta^{18}O$ values of kaolinite precipitating fluids are corroborated by the oxygen isotope compositions of fluids in equilibrium with quartz. Calculated isotopic compositions of water in equilibrium with quartz from the core zone of carbonate replacement bodies and enargite pyrite veins, using equations of Zhang et al. (1989) at 250°C, are presented in Figure 11. Most quartz values of the carbonate replacement bodies (–1.78 to –0.80 ‰) and enargite-pyrite veins (1.5 to 3.8 ‰), with both mineralization types containing a core and an intermediate zone, agree with the $\delta^{18}O$ values estimated for fluids in equilibrium with kaolinite. At the San Alberto carbonate replacement bodies, where only the outer zone is present, the $\delta^{18}O$ value of quartz precipitating fluids is much lower, perhaps due to a larger proportion of unexchanged meteoric water in the fluid or a smaller contribution of carbonate rocks in the isotopic exchange process with meteoric water. Values of fluids in equilibrium with quartz from enargite-pyrite veins must be interpreted with caution because the analyzed quartz crystals contain magmatic cores, as discussed above. Although no hydrogen isotope composition is available for the fluids forming the enargite-pyrite veins, the similar $\delta^{18}O$ values of fluids in equilibrium with quartz of enargite-pyrite veins and of the carbonate replacement bodies, together with the similar microthermometric results obtained for both second stage mineralization types, allow for the hypothesis that the enargite-pyrite veins were also formed from mixed magmatic- isotopically exchanged meteoric fluids. It should be also considered that the microthermometric results on quartz from the enargite-pyrite veins demand a hot and non-saline fluid, which could be the isotopically exchanged meteoric water end-member.

A similar reasoning can be applied for the pyrite-quartz body. The $\delta^{18}O$ values calculated for fluids in equilibrium with quartz from the pyrite-quartz body at 250°C range from 6.6 to 7.8‰ and are slightly higher than those from the second mineralization stage (Fig. 11), but still compatible with the $\delta^{18}O$ values of the kaolinite precipitating fluids.

Marine carbonates, the host rocks of the replacement bodies, have $\delta^{13}C$ values between 1.3 and 2.8 permil and $\delta^{18}O$ values between 19.1 and 24.7 permil, which are compatible with the compositions of Pucará limestone reported by Moritz et al. (1996, Fig. 12). The $\delta^{13}C$ values between -6.6 and -4.5 ‰ and $\delta^{18}O$ values between 9.51 and 19.5 ‰ of hydrothermal Fe-Mn-Zn carbonates differ from the $\delta^{13}C$ and $\delta^{18}O$ values of Pucará limestone, as would be expected for hydrothermal Fe-Mn-Zn carbonates. The lower $\delta^{13}C$ values indicate a contribution of ^{13}C-depleted carbon from organic matter in sedimentary rocks (Bowman, 1998). Bituminous horizons from the Pucará limestone or shale from the Excelsior Group would be viable sources for this ^{13}C-depleted carbon. A magmatic source for the lower $\delta^{13}C$ values is also possible. Since the ^{13}C depletion is in general small, the organic carbon source contribution would constitute only a small part of the total carbon. Oxygen isotope fractionation equations available in the literature for fluids in equilibrium with siderite, magnesite and smithsonite (Zheng, 1999) are similar. Applying the isotope fractionation equation for siderite of Zheng (1999), $\delta^{18}O$ values of water in equilibrium with Fe-Mn-Zn carbonates in the range of –1.0 to 8.0 permil at 200°C are obtained, which are similar to the $\delta^{18}O$ values of the quartz and kaolinite fluids (2.0 to 7.3 ‰). The late vein calcite samples ($\delta^{13}C$ = 0.7 to 0.9 ‰ and $\delta^{18}O$ = 18.8 to 21.0 ‰) lie close to the field of marine limestone, suggesting that the late calcite veins recycled carbonate from the Pucará Group rocks and/or formed at much lower temperatures from fluids buffered to be in equilibrium with the wall rocks.

Sulfur source

Sulfur isotope compositions measured in sulfides from the first and second mineralization stage are compatible with a magmatic source for sulfur (-3.7 to 4.2‰, Table 5; e.g., Ohmotho, 1986). Sulfur isotopic temperature estimates from pyrite-sphalerite, pyrite-galena, and galena-sphalerite pairs from the first mineralization stage pyrrhotite bodies and related Zn-Pb ores using the fractionation equations of Kajiwra and Krouse (1971),

range between 197 and 260°C (Table 3). These temperatures are in agreement with those obtained from fluid inclusions in quartz from the pyrrhotite pipes and related Zn-Pb ores (192 to 250°C). Three other mineral pairs yield unrealistically high temperatures marked with a question mark in Table 5, suggesting that isotopic equilibrium was not achieved and/or that these pairs are not co-genetic. The sulfur isotope temperature estimates of the second mineralization stage carbonate replacement bodies mineral pairs pyrite-sphalerite, and galena-sphalerite and barite-pyrite using equations of Kajiwra and Krouse (1971) indicate temperatures between 195 and 271°C (Table 5), in the same range to those obtained by microthermometric measurements (178 – 265°C). The $\delta^{34}S_{SO4}$ and $\delta^{18}O_{SO4}$ values of alunite from Venencocha and Santa Rosa and of barite from the enargite-pyrite veins and carbonate replacement bodies are summarized in Figure 13. All the alunite samples have high $\delta^{34}S$ values, characteristic for magmatic-hydrothermal alunite samples as defined by Rye et al. (1992). In Fig. 13, the wide range in $\delta^{18}O$ values of the alunite with values extending towards ^{18}O-depleted compositions suggests that SO_2 condensed in meteoric water. Barite samples show a concave-down J-shaped variation trend ($\delta^{34}S_{SO4}$ = 4 to 24‰ and $\delta^{18}O_{SO4}$ = –1.5 to 10.5‰). The isotopically heavy end-member sulfate in barite is likely to have a strong magmatic-hydrothermal sulfur source, whereas the isotopically light end-member sulfate most likely formed from SO_4^{2-} generated by a large contribution of magmatic H_2S oxidized in a meteoric-water dominant environment near the surface (steam-heated). The barite samples from this isotopically light end-member sulfate are those which were described as late in the paragenetic sequence. The obtained sulfur isotope systematics for alunite and barite at Cerro de Pasco are similar to those recognized in other deposits, such as Summitville, USA (Rye et al., 1990; Bethke et al., 2005) and Julcani, Peru (Rye, 2005) and in many other magmatic hydrothermal acid sulfate systems associated with high sulfidation mineralization (Rye et al., 1992; Cooke and Simmons, 2000; Rye et al., 2005; Fifarek and Rye, 2005). The systematics is an expression of the fact that magmatic vapor condenses and interacts with oxidized meteoric water. Such a mixing process is an efficient depositional mechanism for barite (Holland and Malinin, 1979).

In summary, for the hydrothermal system at Cerro de Pasco two different mixing trends have been recognized on the basis of microthermometric and stable isotope data. The results for the second mineralization stage fluids essentially suggest mixing of magmatic and isotopically exchanged meteoric waters. The results point to an important contribution of isotopically exchanged meteoric fluids, around 50 % for the intermediate zone and around 80 % for the outer zone. The similarity in fluid inclusion characteristics of both mineralization stages might indicate that this interpretation is also valid for the first mineralization stage. A different mixing trend is defined by alunite present in oxidized polymetallic veins at Venencocha and at Santa Rosa, which is interpreted to result from mixing of a magmatic fluid and isotopically unexchanged meteoric waters. The proportion can be evaluated between 70 and 40 % of magmatic water.

Nature of the magmatic saline end-member

The above discussion points to the existence of a saline magmatic end-member of the mineralizing fluid. It could be derived from a diluted brine, a magmatic fluid in the sense of Hedenquist et al. (1998), or from a contracted magmatic vapor in the sense of Heinrich (2005). If the more saline fluid inclusions in quartz of the first mineralization stage (up to 6.8 wt % NaCl equiv) and second mineralization stage carbonate replacement bodies (up to 7.7 wt % NaCl equiv) are representative of the ore fluid, only dilution of a brine could explain the obtained results. Considering a dilution of 50 to 80 %, as indicated by the stable isotope results of kaolinite of the carbonate replacement bodies, magmatic fluids with salinities over 15 wt% NaCl equiv. are necessary to explain the salinities. The more saline fluid inclusions in quartz from the enargite-pyrite veins reach up to 5 wt% NaCl equiv. (max. 5.26 wt % NaCl equiv) and could also be explained in terms of mixing of a contracted vapor separated at great depths (which would be similar to a single-phase fluid). The different metal budget of the enargite-pyrite veins and the Zn-Pb carbonate replacement bodies could be a hint for different fluids forming both mineralization types during the second stage. In this perspective, the magmatic end-member of the enargite-pyrite veins could be a contracted vapor enriched in Cu and Au (Heinrich, 2005). However, even if this explanation is very suggestive, it should be underlined that it is highly speculative. On the basis of the available data, it is equally possible that the magmatic end-member in the enargite-pyrite veins is also a diluted magmatic brine. The relatively higher salinities of the quartz in the Venencocha polymetallic oxidized veins, which are thought to be equivalent to the enargite-pyrite veins, would favor the last explanation. Fluids with similar characteristics to those found at Cerro de Pasco have been described in other Cordilleran base metal deposits. Table 6 summarizes the fluid inclusion and stable isotope data for Colquijirca, Huanzala, Hualgayoc, Julcani, San Cristobal, and Pasto Buena (Peru) Main and East Tintic, Bisbee, and Butte (USA), and Collahuasi (Chile). Fluid inclusion studies in quartz from these deposits indicate homogenization temperatures between 170 and 350°C and salinities ranging from 0.2 to 8 wt% NaCl equiv. (one generation at Tintic up to 17 wt %), which are in agreement with those obtained at Cerro de Pasco. $\delta^{18}O$ and δD values are variable from one deposit to another but for all, a magmatic and a meteoric end-member are recognized and are both involved in the mineralization. At Julcani (Deen, 1994), San Cristobal (Campbell et al., 1984; Beuchat et al., 2004) , and Colquijirca (Bendezú, 2007), a contribution of meteoric water isotopically ex-

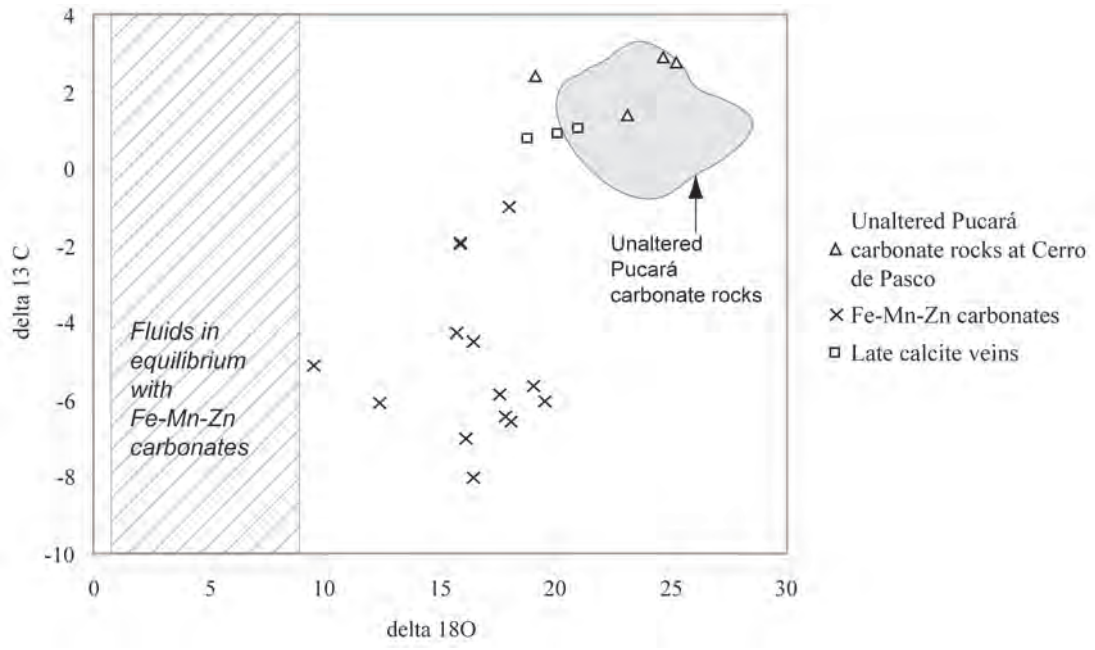

Fig. 12: *Plot of δ ^{13}C versus $\delta^{18}O$ values of Fe-Mn-Zn carbonates and late calcite veins from the carbonate replacement bodies (second mineralization stage). Grey field representing δ ^{13}C versus $\delta^{18}O$ of unaltered Pucará carbonate rocks after Moritz et al.(1996). The hatched field represents $\delta^{18}O$ values of fluids calculated in equilibrium with Fe-Mn-Zn carbonates using the equation of Zheng (1999) for siderite at 200°C.*

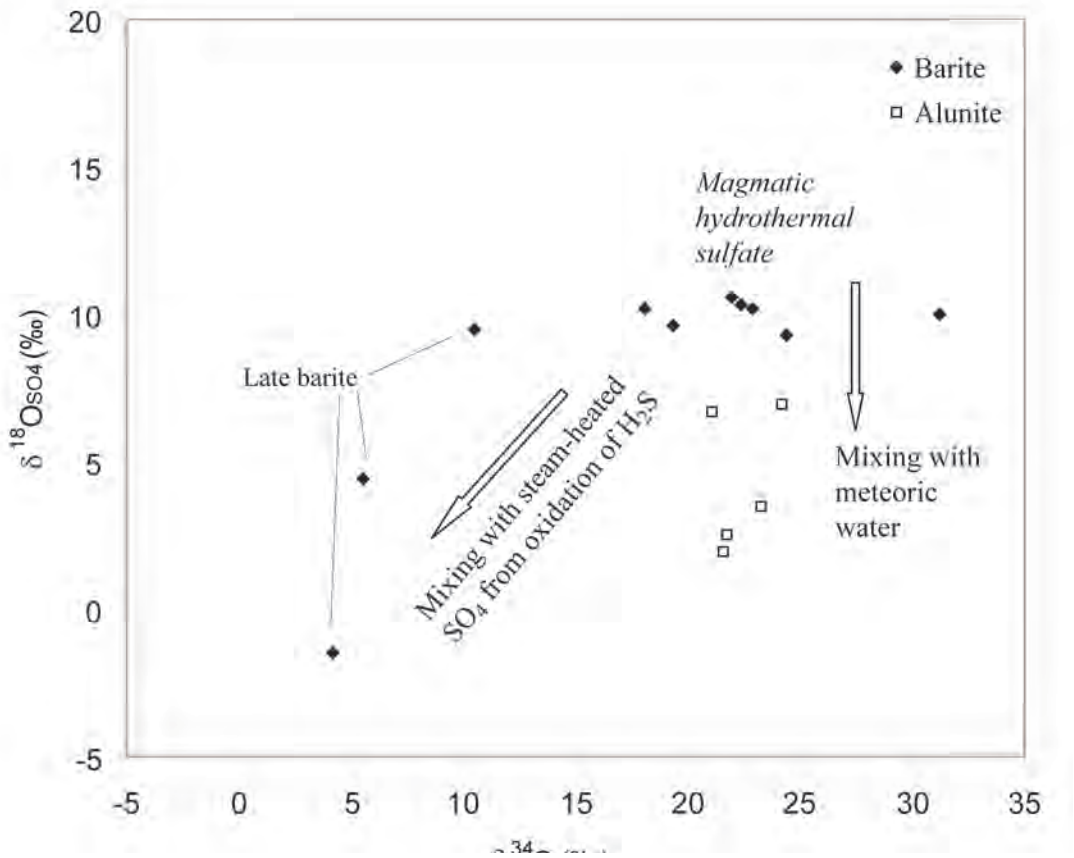

Fig. 13: *Summary of $\delta^{34}S$ and $\delta^{18}O_{(SO4)}$ values on alunite (from oxidized veins at Venencocha) and barite (from carbonate replacement bodies and enargite-pyrite veins) at Cerro de Pasco, with arrows showing mixing of magmatic-hydrothermal sulfate with meteoric water in alunite and with steam-heated sulfate from oxidation of magmatic H_2S in barite.*

changed with the country rocks has been proposed.

Evolution of the hydrothermal system at Cerro de Pasco

A geological scenario that is consistent with the available geochronological results (Baumgartner et al., Part II) as well as with the microthermometric and isotopic results discussed above is shown in Figure 14. This scenario takes into account the existence of two different fluid mixing trends.

At Cerro de Pasco, explosive volcanism took place in the Mid-Miocene and a diatreme-dome complex of more than 2 km in diameter was emplaced along a longitudinal fault (Figs. 14A and B). According to current models for the evolution of porphyry copper systems (e.g. Fournier, 1999; Einaudi et al., 2003), exsolving magmatic fluids accumulate in apophyses, in the brittle-ductile subsolidus transition zone at around 450°C. Following a pressure decrease near the brittle-ductile transition, phase separation into a coexisting dense brine phase and a low density vapor phase could have occurred (Ulrich et al., 1999; Harris et al., 2003). At Cerro de Pasco, the dense brine phase remained at depth, while the less dense vapor would have ascended to higher levels. This buoyant SO_2 vapor plume rose rapidly along fractures and condensed into unexchanged meteoric water forming H_2S and HSO_4^- generating acidic fluids that strongly leached the diatreme-dome complex rocks during the second mineralization stage, as shown by the presence of vuggy quartz and barren advanced argillic altered domes and dykes at Venencocha and Santa Rosa. The input of low density magmatic vapors is traced by the alunite isotope composition, which points to mixing with unexchanged meteoric waters. No evidence for the presence of a low density vapor or related alteration associated to the first mineralization stage has been found, but it cannot be excluded that the vapors altered the upper parts of the diatreme, now eroded (Fig. 14C).

The microthermometric and stable isotope data suggest that saline magmatic fluids mixed with isotopically exchanged, hot meteoric water, a process that enabled fluid ascent due to a density decrease. The microthermometric results of all but one studied ore type from both mineralization stages can be interpreted as that the saline magmatic fluids were issued from hypersaline magmatic fluids (Fig. 14C and D). The fluid inclusion results of the enargite-pyrite veins could also allow that the magmatic saline fluids represented contracted magmatic vapor separated at great depth in the sense of Heinrich (2005) or a magmatic fluid in the sense of Hedenquist et al. (1998).

The fact that the first mineralization stage contains low sulfidation state mineral assemblages could indicate that, en route to the deposition site, the magmatic-derived ore-forming fluids probably were reduced by Excelsior Group shale and phyllite host rocks. Fluids forming the second mineralization stage, which are characterized by high to intermediate sulfidation state mineral assemblages, would have encountered rocks that had already lost their buffering capacity.

In the core zones of the second mineralization stage, alunite deposited from fluids derived from a SO_2 volcanic plume and quartz and ore minerals derived from a magmatic saline fluid spatially coincide (Fig. 14D). The paragenetic relationships cannot distinguish between a vapor plume that preceded the ore forming fluids or if sporadic vapor plume incursions took place during the ascent of a more steady flow of moderately saline fluids, as suggested in Colquijirca by Bendezú (2007).

The microthermometric and stable isotope results suggest that the first and the second mineralization stages were formed by similar fluids at similar temperatures. This implies that the large pyrite-quartz body was formed during an early pulse of the same hydrothermal system that formed the rest of the Cerro de Pasco deposit. Taking into account the existence of early W and /or Sn-bearing pyrite/pyrrhotite-quartz stages also in several other Cordilleran deposits (Table 6), it is proposed that both mineralization stages are linked and constitute subsequent stages of Cordilleran base metal deposits. The large size of the pyrite-quartz body at Cerro de Pasco probably reflects a substantial hydrothermal system providing fluids rich in sulfur (Baumgartner and Fontboté, Part I).

The hydrothermal fluids identified at Cerro de Pasco are those that could be expected in the upper part of a porphyry copper system. In Butte, Morococha, Yauricocha, among other districts, Cordilleran base metal deposits are superimposed on sizeable porphyry copper deposits. The question can be posed if at Cerro de Pasco a concealed porphyry deposit exists. Evidence to answer this question is lacking. However, it can be noted that the existence of a large diatreme preceding the Cordilleran mineralization could have favored a dramatic pressure decrease, inhibiting the formation of a large porphyry deposit. In addition, mineralized diatreme clasts are absent suggesting that prior to the diatreme formation, porphyry mineralization was not initiated.

Conclusions

The fluids forming the first and second mineralization stages at Cerro de Pasco had similar temperatures (between 290 down to 170°C) as well as comparable salinities (ranging from 0.1 to 7.5 wt % NaCl equiv). The stable isotope results coupled with the microthermometric data support the existence of two mixing fluids. A first trend reflects mixing of a saline magmatic end-member and an isotopically exchanged hot meteoric water end-member. The ore-forming fluids result from variable mixing ratios between the two end-members. According to the available data, of all ore types except for the enargite-pyrite veins from the western part of the open pit, the saline end-member is a hypersaline magmatic fluid. For the enargite-pyrite veins, the saline magmatic end-member could also correspond to a contracted vapor separated at great depth

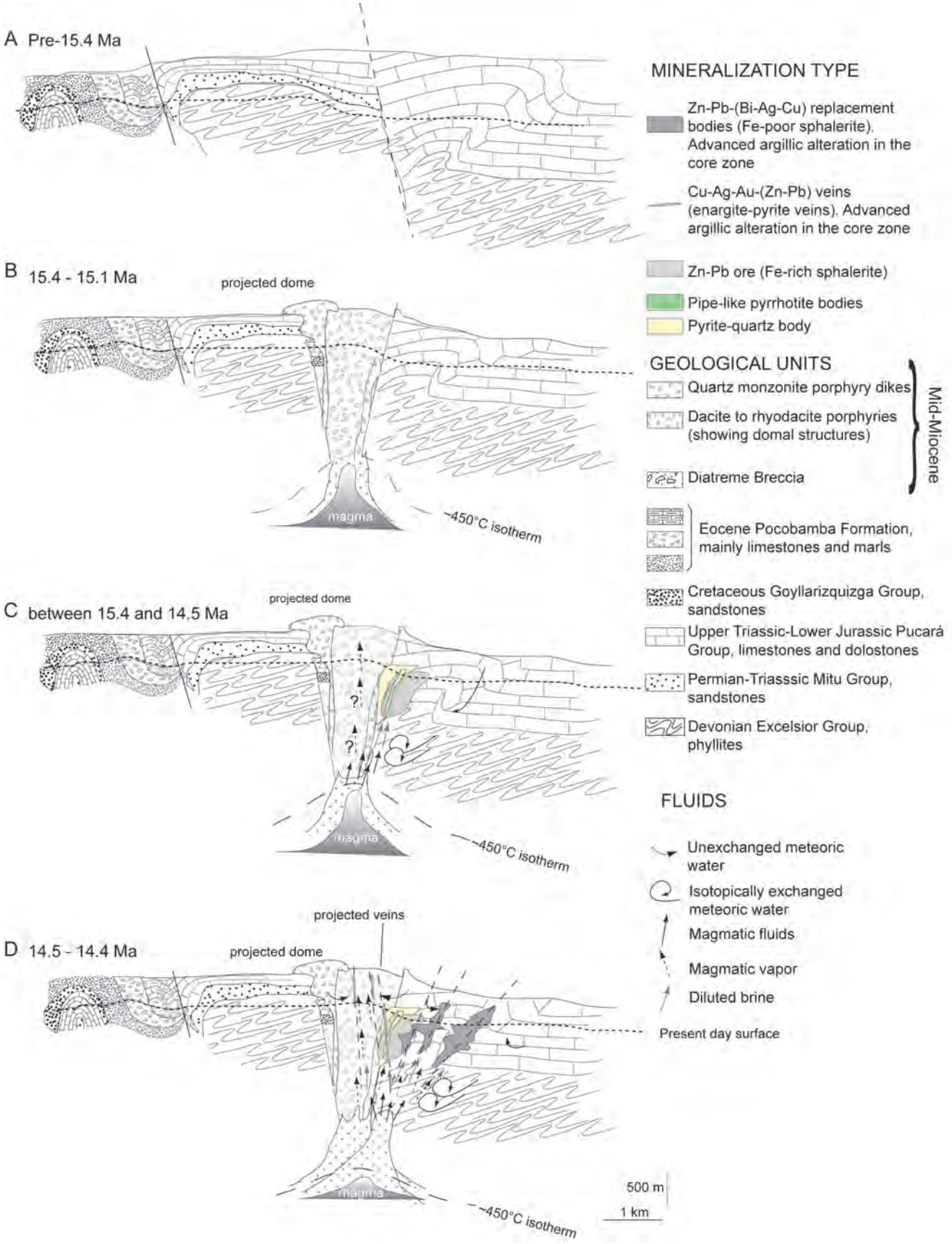
A Pre-15.4 Ma
B 15.4 - 15.1 Ma
projected dome
magma
~450°C isotherm
C between 15.4 and 14.5 Ma
projected dome
?
?
magma
~450°C isotherm
D 14.5 - 14.4 Ma
projected veins
projected dome
magma
~450°C isotherm
500 m
1 km
MINERALIZATION TYPE
Zn-Pb-(Bi-Ag-Cu) replacement bodies (Fe-poor sphalerite). Advanced argillic alteration in the core zone
Cu-Ag-Au-(Zn-Pb) veins (enargite-pyrite veins). Advanced argillic alteration in the core zone
Zn-Pb ore (Fe-rich sphalerite)
Pipe-like pyrrhotite bodies
Pyrite-quartz body
GEOLOGICAL UNITS
Quartz monzonite porphyry dikes
Dacite to rhyodacite porphyries (showing domal structures)
Diatreme Breccia
Mid-Miocene
Eocene Pocobamba Formation, mainly limestones and marls
Cretaceous Goyllarizquizga Group, sandstones
Upper Triassic-Lower Jurassic Pucará Group, limestones and dolostones
Permian-Triasssic Mitu Group, sandstones
Devonian Excelsior Group, phyllites
FLUIDS
Unexchanged meteoric water
Isotopically exchanged meteoric water
Magmatic fluids
Magmatic vapor
Diluted brine
Present day surface

Figure 14: *Time and space evolution of the geologic and mineralization setting at Cerro de Pasco. Geology based on Jenks (1953) and Angeles (1999). A) geological setting before the magmatic activity (before 15.4 Ma, Baumgartner, 2007). B) Magmatic activity forming between 15.4 and 15.1 Ma, chronologically the diatreme, dacitic domes and quartz-monzonite dykes (Baumgartner, 2007). C) Hydrothermal activity forms the first mineralization stage (including the pyrite-quartz body and pyrrhotite pipes zoned to Zn-Pb ores). This stage is formed by diluted brines (grey arrows) issued from mixing between a non-saline end-member (probably isotopically exchanged meteoric waters, curled arrows) with a saline end-member (probably magmatic brines, plain arrows). Magmatic vapors (dashed arrows) were probably present in the systems prior and/or during the first mineralization stage although any related alteration has not been observed, suggesting that it was eroded. D) Formation of the second mineralization stage (between 15.5 and 14.4 Ma, Baumgartner, 2007). The carbonate replacement bodies in the eastern part of the open pit were formed by diluted brines issued from mixing between a saline end-member (probably magmatic brines, grey arrow) and a hot, non-saline fluid represented by isotopically exchanged meteoric water (curled arrow). The saline end-member in the enargite-pyrite veins could be represented by contracted vapors (in the sense of Heinrich, 2005) which separated at sufficient depth, or a single phase fluid in the sense of Hedenquist et al. (1998). The alunite occurring in the advanced argillic altered halos of oxidized veins at Venencocha and Santa Rosa (second mineralization stage) are formed by a mixing between a magmatic fluid end-member (likely magmatic SO_2 vapor plumes, dashed arrow) and an isotopically unexchanged meteoric water end-member (curved arrow).*

in the sense of Heinrich (2005) or a single phase fluid in the sense of Hedenquist (1998). A second trend, indicated by the stable isotope results of alunite present in alteration assemblages related to second mineralization stage oxidized veins in the Venencocha and Santa Rosa areas, points to mixing of volcanic SO_2 vapor plumes with unexchanged meteoric water.

The relatively shallow emplacement of the hydrothermal system at Cerro de Pasco, predicted from erosion estimates, is consistent with the microthermometric results that indicate minimal depths in the range of 200 to 500 m. This epithermal system corresponds to the upper parts of a porphyry environment, although porphyry copper mineralization, economic or not, remains undiscovered.

The similar temperatures and salinities obtained for the first (pyrite-quartz body, pyrrhotite pipes and related Zn-Pb ores) and second mineralization stages (enargite-pyrite veins and carbonate replacement bodies) coupled with the stable isotope study has permitted to conclude that they are linked and represent successive mineralizing stages of Cordilleran base metal deposits.

Acknowledgments

This work was conducted as part of the senior author's PhD. dissertation at the University of Geneva. The present investigation was carried out with the support of the Swiss National Science Foundation (FN 200020-108026). The authors would like to thank Jacob Timmers and Victor Gobitz from the Vólcan Compañía Minera S.A. for providing financial and logistical support. Special thanks to Hugo Alvarez, Romulo Sunny, Enrique Lopez, Luis Fuentes, and Carlos Vera from the Cerro de Pasco Geology staff. We gratefully acknowledge Ronner Bendezú for fruitful discussions as well as Kalin Kouzmanov for the CL images. Jorge Spangenberg is thanked for the sulfur isotope measurements, while Benita Putlitz kindly helped with the analyses of the silicates. A special thank to M. Einaudi and R. Moritz for reviewing this manuscript.

References

Angeles, C., 1999, Los sedimentos Cenozoicos de Cerro de Pasco; estratigrafia, sedimentacion y tectonica, *in* Machare, J., Benavides-Caceres, V., and Rosas, S., eds., Sociedad Geológica del Perú, Volúmen Jubilar, 5, p. 103-118.

Arribas, A., Cunningham, C. G., Rytuba, J. J., Rye, R. O., Kelly, W. C., Podwysocki, M. H., McKee, E. H., and Tosdal, R. M., 1995, Geology, geochronology, fluid inclusions, and isotope geochemistry of the Rodalquilar gold alunite deposit, Spain: Economic Geology, v. 90, p. 795-822.

Austria, B. S., 1975, Geochemical implications of iron in sphalerite, Unpulished PhD Thesis, Harvard University.

Baumgartner, R., Fontboté, L., and Bendezú, R., 2003, Low temperature, late Zn-Pb-(Bi-Ag-Cu) mineralization and related acid alteration replacing carbonate rocks at Cerro de Pasco, Central Peru: Mineral Exploration and Sustainable Development, Athen, 2003, p. 441-444.

Baumgartner, R., Fontboté, L., Ovtcharova, M., Spikings, R., and Page, L., 2006, 5 My of magmatic and hydrothermal activity at Cerro de Pasco, Central Peru: A $^{40}Ar/^{39}Ar$ and U/Pb geochronological study: SEG Conference, Keystone, 2006.

Bendezú, R., 2007, Shallow polymetallic and precious metal mineralization associated to a Miocene diatreme-dome complex of the Peruvian Andes. The Colquijirca District., Terre & Environnement, p. 221.

Bendezú, R., Fontboté, L., and Cosca, M., 2003, Relative age of Cordilleran base metal lode and replacement deposits, and high sulfidation Au-(Ag) epithermal mineralization in the Colquijirca mining district, central Peru: Mineralium Deposita, v. 38, p. 683-694.

Bethke, P. M., Rye, R. O., Stoffregen, R. E., and Vikre, P. G., 2005, Evolution of the magmatic-hydrothermal acid-sulfate system at Summitville, Colorado: integration of geological, stable-isotope, and fluid-inclusion evidence: Chemical Geology, v. 215, p. 281-315.

Beuchat, S., Moritz, R., and Pettke, T., 2004, Fluid evolution in the W-Cu-Zn-Pb San Cristobal vein, Peru: fluid inclusion and stable isotope evidence: Chemical Geology, v. 210, p. 201-224.

Bodnar, R. J., 2003, Reequilibration of fluid inclusions. , *in* Samson, I., Anderson, A., and Marshall, D., eds., Fluid Inclusions: Analysis and Interpretation. , 32, Mineralogical Association of Canada, Short Course p. 213-230.

Bowditch, S. I., 1935, The geology and ore deposits of Cerro de Pasco, Peru, Unpublished PhD thesis, Harvard University, 160 p.

Bowman, J. R., 1998, Stable-isotope systematics of skarns, *in* Lentz, D. R., ed., Mineralized intrusion-related skarn systems. Short Course Series, p. 99-145.

Brown, P. E., and Lamb, W. M., 1989, P-V-T properties of fluids in the system H2O±CO2±NaCl: New graphical presentations and implications for fluid inclusion studies: Geochimica et Cosmochimica Acta, v. 53 p. 1209-1221.

Campbell, A. R., Rye, D., and Petersen, U., 1984, A hydrogen and oxygen isotope study of the San Cristobal Mine, Peru; implications of the role of water to rock ratio for the genesis of wolframite deposits: Economic Geology, v. 79, p. 1818-1832.

Cooke, D. R., and Simmons, S. F., 2000, Characteristics and genesis of epithermal gold deposits, *in* Hagemann, S. G., and Brown, P. E., eds., Gold in 2000, 13, Reviews in Economic Geology, p. 221-244.

Craig, H., 1961, Isotopic variations in meteoric waters: Science, v. 133, p. 1702-1703.

Deen, J. A., Rye, R. O., Munoz, J. L., and Drexler, J. W., 1994, The magmatic hydrothermal system at Julcani, Peru; evidence from fluid inclusions and hydrogen and oxygen isotopes: Economic Geology, v. 89, p. 1924-1938.

Deyell, C. L., Leonardson, R., Rye, R. O., Thompson, J. F. H., Bissig, T., and Cooke, D. R., 2005, Alunite in the Pascua-Lama High-Sulfidation Deposit: Constraints on Alteration and Ore Deposition Using Stable Isotope Geochemistry: Economic Geology, v. 100, p. 131-148.

Driesner, T., 1997, The Effect of Pressure on Deuterium-Hydrogen Fractionation in High-Temperature Water: Science, v. 277, p. 791-794.

Einaudi, M. T., 1968, Pyrrhotite-pyrite-sphalerite relations at Cerro de Pasco, Peru, Unpublished PhD Thesis, Harvard University, 381 p.

Einaudi, M. T., 1977, Environment of ore deposition at Cerro de Pasco, Peru: Economic Geology, v. 72, p. 893-924.

Einaudi, M. T., Hedenquist, J. W., and Inan, E. E., 2003, Sulfidation state of hydrothermal fluids: The porphyry-epithermal transition and beyond: Society of Economic Geologists Special Publication, p. 285-313.

Field, C. W., and Fifarek, R. H., 1985, Light stable-isotopes systematics in the epithermal environment. In: Geology and geochemistry of epithermal systems, Society of Economic Geology, 99-128 p.

Fifarek, R. H., and Rye, R. O., 2005, Stable-isotope geochemistry of the Pierina high-sulfidation Au-Ag deposit, Peru: influence of hydrodynamics on SO42--H2S sulfur isotopic exchange in magmatic-steam and steam-heated environments: Chemical Geology, v. 215, p. 253-279.

Fischer, J., 1977, Silver mines and silver miners in colonial Peru 1776-1824. Centre for Latin-American studies: University of Liverpool, Monograph 7, p. 150p.

Fournier, R. O., 1999, Hydrothermal processes related to movement of fluid from plastic into brittle rock in the magmatic-epithermal environment: Economic Geology, v. 94, p. 1193-1211.

Geological staff of Cerro de Pasco Corporation, 1950, Lead and zinc deposits of the Cerro de Pasco Corporation in Central Peru: 18th International Geological Congress, Great Britain 1948, 1950, p. 154-186.

Giesemann, A., Jager, H.-J., Norman, A. L., Krouse, H. R., and Brand, W. A., 1994, On-line sulfur-isotope determination using an elemental analyzer coupled to a mass spectrometer: Analytical Chemistry, v. 66, p. 2816–2819.

Giggenbach, W. F., 1997, The origin and evolution of fluids in magmatic-hydrothermal systems, *in* Barnes, H. L., ed., Geochemistry of Hydrothermal Ore Deposits: N. Y., Wiley and Sons, Inc., p. 737-796.

Gilg, H. A., and Sheppard, S. M. F., 1996, Hydrogen isotope fractionation between kaolinite and water revisited: Geochimica et Cosmochimica Acta, v. 60, p. 529-533.

Goldstein, R. H., and Reynolds, T. J., 1994, Systematics of fluid inclusions in diagenetic minerals, SEPM (Society for Sedimentary Geology), Short Course Notes, 31, p. 199.

Graton, L. C., and Bowditch, S. I., 1936, Alkaline and acid solutions in hypogene zoning at Cerro de Pasco, Peru: Economic Geology, v. 31, p. 651-698.

Harris, A. C., Kamenetsky, V. S., Van-Achterbergh, E., White, N. C., and Ryan, C. G., 2003, Melt inclusions in veins; linking magmas and porphyry Cu deposits: Science, v. 302, p. 2109-2111.

Hedenquist, J. W., Arribas, A., and Reynolds, T. J., 1998, Evolution of an intrusion-centered

hydrothermal system; Far Southeast-Lepanto porphyry and epithermal Cu-Au deposits, Philippines: Economic Geology, v. 93, p. 373-404.

Heinrich, C. A., 2005, The physical and chemical evolution of low-salinity magmatic fluids at the porphyry to epithermal transition: a thermodynamic study: Mineralium Deposita, v. 39, p. 864-889.

Hildreth, S. C., and Hannah, J. L., 1996, Fluid inclusion and sulfur isotope studies of the Tintic mining district, Utah; implications for targeting fluid sources: Economic Geology, v. 91, p. 1270-1281.

Holland, H. D., and Malinin, S. D., 1979, Oxygen and hydrogen isotope relationships in hydrothermal mineral deposits, *in* Barnes, H. L., ed., Geochemistry of Hydrothermal Ore Deposits, 2nd ed., Wiley, New York, p. 461-508.

Huanqui, F., 1994, Ocurrencias de mineralización en la chimenea volcanica de Cerro de Pasco, Unpublished internal memorandum to A. Alvarez, Empresa Minera del Centro del Perú, p. 15.

Inan, E. E., and Einaudi, M. T., 2002, Nukundamite (Cu3.38Fe0.62S4)-Bearing Copper Ore in the Bingham Porphyry Deposit, Utah: Result of Upflow through Quartzite: Economic Geology, v. 97, p. 499-515.

Jenks, W. F., 1951, Triassic to Tertiary stratigraphy near Cerro de Pasco, Peru: The Geological Society of America Bulletin, v. 62, p. 203-219.

Jiménez, C., 1924, Síntesis de la minería peruana en el centenario de Ayacucho, Ministerio de fomento, Minas y Petróleo, p. 3-71.

Jobin, Y., 2004, High sulfidation enargite-pyrite veins at Cerro de Pasco, Peru. A mineralogical study of ore and alteration minerals and an infra-red fluid inclusion study on enargite, Unpublished MSc thesis, University of Geneva, Switzerland, 139 p.

Kajiwra, Y., and Krouse, H. R., 1971, Sulfur isotope partitioning in metallic sulfide systems: Canadian Journal of Earth Sciences, v. 8, p. 1397-1408.

Kasemann, S., Meixner, A., Rocholl, A., Vennemann, T., Rosner, M., Schmitt, A. K., and Wiedenbeck, M., 2001, Boron and oxygen isotope composition of certified reference materials NIST SRM 610/612 and reference materials JB-2 and JR-2.: Geostandards Newsletter, v. 12, p. 405–416.

Lacy, W. C., 1949, Types of pyrite and their relations to mineralization at Cerro de Pasco, Peru, Unpublished PhD Thesis, Harvard University, 193 p.

McLaughlin, D. H., 1924, Geology and physiography of the Peruvian Cordillera, Department of Junin and Lima: Geological Society of America Bulletin, v. 35, p. 591-632.

Mégard, F., 1978, Etude géologique des Andes du Pérou central-Contribution à l'étude écologique des Andes, Mémoire ORSTOM no. 86, Office de la Recherche Scientifique et Technique Outre-Mer, Paris,, 310 p.

Moritz, R., 2006, Fluid salinities obtained by infrared microthermometry of opaque minerals: Implications for ore deposit modeling -- A note of caution: Journal of Geochemical Exploration, v. 89, p. 284-287.

Moritz, R., Fontboté, L., Spangenberg, J., Rosas, S., Z., S., and Fontignie, D., 1996, Sr, C and O isotope systematics in the Pucará Basin, central Peru Comparison between Mississippi Valley-type deposits and barren areas: Mineralium Deposita, v. 31, p. 147-162.

Ohmoto, H., 1986 Stable isotope geochemistry of ore deposits, *in* Valley, J. W., Taylor, H. P., and O'Neil, J. R., eds., In Stable Isotopes in High Temperature Geological Processes . Reviews in Mineralogy, 16, Mineralogical Society of America, Washington, D.C, p. 491-559.

Ohmoto, H., and Rye, D., 1979, Isotopes of sulfur and carbon, *in* Barnes, H. L., ed., Geochemistry of hydrothermal deposits, p. 509-567.

Ohmoto, H., and Rye, R. O., 1974, Hydrogen and Oxygen Isotopic Compositions of Fluid Inclusions in the Kuroko Deposits, Japan: Economic Geology, v. 69, p. 947-953.

Petersen, U., 1965, Regional geology and major ore deposits of central Peru: Economic Geology, v. 60, p. 407-476.

Reyes, A. G., 1990, Petrology of Philippine geothermal systems and the application of alteration mineralogy to their assessment: Journal of Volcanology and Geothermal Research, v. 43, p. 279-309.

Rivera, N., 1997, The Pasco belt and the metallogenesis of the Cerro de Pasco mineral district: IX Congreso Geológico del Perú, 1997, p. 167-173.

Roedder, E., 1984, Fluid inclusions: Reviews in Mineralogy, v. 12, p. 644.

Rumble, D., and Hoering, T. C., 1994, Analysis of oxygen and sulfur isotope ratios in oxide and sulfide minerals by spot heating with a carbon dioxide laser in a fluorine atmosphere: Accounts of Chemical Research,, v. 27, p. 237-241.

Rye, R., Bethke, B. R., and Stoffregen, R. E., 1990, Stable isotope systematics and magmatic hydrothermal processes in the Summitville, Colorado, gold deposit: U.S. Geol. Survey. Open-File, p. 90-626.

Rye, R. O., 2005, A review of the stable-isotope geochemistry of sulfate minerals in selected igneous environments and related hydrothermal systems: Chemical Geology, v. 215, p. 5-36.

Rye, R. O., Bethke, P. M., and Wasserman, M. D., 1992, The stable isotope geochemistry of acid sulfate alteration: Economic Geology, v. 87, p. 225-262.

Savin, S. M., and Epstein, S., 1970, The oxygen and hydrogen isotope geochemistry of clay minerals: Geochimica et Cosmochimica Acta, v. 34, p. 25-42.

Sharp, Z. D., Atudorei, V., and Durakiewicz, T., 2001, A rapid method for determination of hydrogen and oxygen isotope ratios from water and hydrous minerals: Chemical Geology, v. 178, p. 197-210.

Sharp, Z. D., 1990, A laser-based microanalytical method for the in situ determination of oxygen isotope ratios of silicates and oxides: Geochimica et Cosmochimica Acta, v. 54, p. 1353-1357.

Sheppard, S. M. F., and Gilg, H. A., 1996, Stable isotope geochemistry of clay minerals; The story of sloppy, sticky, lumpy and tough, Cairns-Smith (1971): Clay Minerals, v. 31, p. 1-24.

Sheppard, S. M. F., Nielsen, R. L., and Taylor, H. P., 1969, Oxygen and hydrogen isotope ratios of clay minerals from porphyry copper deposits: Economic Geology, v. 64, p. 755-777.

Silberman, M. L., and Noble, D. C., 1977, Age of igneous activity and mineralization, Cerro de Pasco, central Peru: Economic Geology, v. 72, p. 925-930.

Spoetl, C., and Vennemann, T. W., 2003, Continuous-flow IRMS analysis of carbonate minerals: Rapid Communications in Mass Spectrometry, v. 17, p. 1004-1006.

Stoffregen, R. E., Rye, R. O., and Wasserman, M. D., 1994, Experimental studies of alunite: I. 18O-16O and D-H fractionation factors between alunite and water at 250-450°C: Geochimica et Cosmochimica Acta, v. 58, p. 903-916.

Strusievicz, R. O., Clark, A. H., Lee, J. K. L., and Farrar, E., 1998, Laer-probe $^{40}Ar/^{39}Ar$ age data for hydrothermal systems in the Callejón de Huaylas district, Ancash, northen Peru: Part II. Alunite and illite from the Pierina deposit. Ancash., *in* Unpublished report for Minera ABX Exploraciones, S. A., ed., p. 1-6.

Taylor, H. P., 1974, The Application of Oxygen and Hydrogen Isotope Studies to Problems of Hydrothermal Alteration and Ore Deposition: Economic Geology, v. 69, p. 843-883.

Taylor, H. P., 1979, Oxygen and hydrogen isotope relationships in hydrothermal deposits, *in* Barnes, H. L., ed., Geochemistry of hydrothermal ore deposits, Wiley and Sons, p. 236-277.

Taylor, H. P., 1992, Degassing of H2O from rhyolitic magma during eruption and shallow intrusion, and isotopic composition of magmatic water in hydrothermal systems, Rep. 279, Geological Survey Japan, p. 190-194.

Ulrich, T., Günther, D., and Heinrich, C. A., 1999, Gold concentrations of magmatic brines and the metal budget of porphyry copper deposits: Nature (London), v. 399, p. 676-679.

Vennemann, T. W., and O'Neil, J. R., 1993, A simple and inexpensive method of hydrogen isotope and water analyses of minerals and rocks based on zinc reagent: Chemical Geology, v. 103, p. 227-234.

Ward, H. J., 1961, The pyrite body and copper orebodies, Cerro de Pasco Mine, central Peru: Economic Geology, v. 56, p. 402-422.

Watanabe, Y., and Hedenquist, J. W., 2001, Mineralogic and Stable Isotope Zonation at the Surface over the El Salvador Porphyry Copper Deposit, Chile: Economic Geology, v. 96, p. 1775-1797.

Wasserman, M. D., Rye, R. O., Bethke, P. M., and Arribas Jr, A., 1992, Methods for separation and total stable isotope analysis of alunite.: Open-File Rep. 92-9. U.S. Geol. Survey, Reston, VA.

Zachos, J., Pagani, M., Sloan, L., Thomas, E., and Billups, K., 2001, Trends, Rhythms, and Aberrations in Global Climate 65 Ma to Present: Science, v. 292, p. 686-693.

Zhang, X., Nesbitt, B. E., and Muehlenbachs, K., 1989, Gold mineralization in the Okanagan Valley, southern British Columbia; fluid inclusion and stable isotope studies: Economic Geology, v. 84, p. 410-424.

Zheng, Y. F., 1999, Oxygen isotope fractionation in carbonate and sulfate minerals: Geochemical Journal, v. 33, p. 109-126.

Appendix 1: Location of samples used for the stable isotope study (for legend, see Fig. 3)

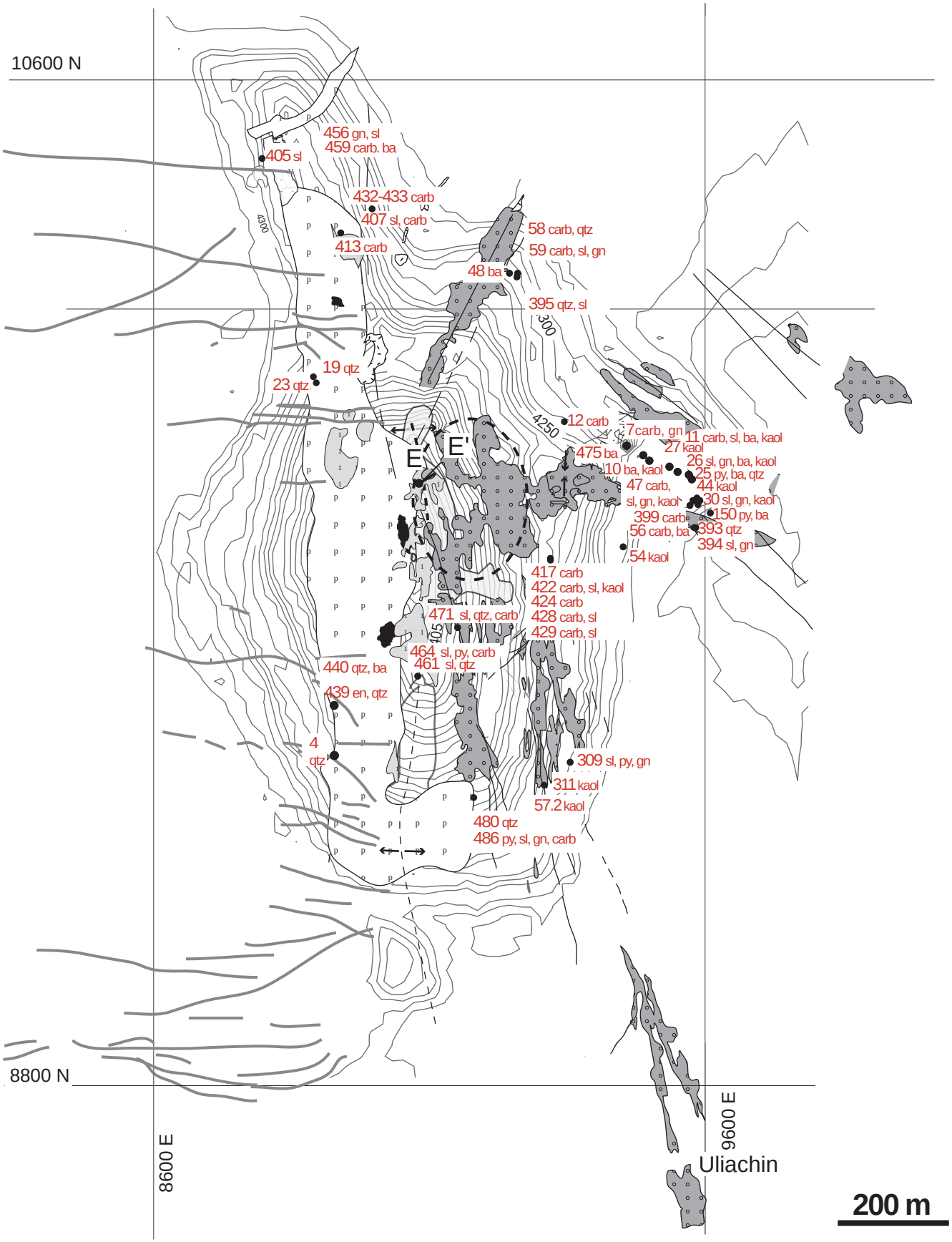

Appendix 2: Microthermometric data for fluid inclusions at Cerro de Pasco

Sample n°	Chip n°	Assemblage n°	FI n°	Type	Filling	Degree of fill	Size (µm)	Th final(°C)	$T_{m\ ice}$ (°C)	Salinity[1] (wt. % NaCl eq)
First mineralization stage										
Pyrite-quartz body										
CPR 38	CPR 38a	A	1					195	-3.2	5.26
			2					198	-3.2	5.26
			3					209	-3.4	5.56
			4					233.9	-2.8	4.65
			5					205	-4	6.45
		B	1					233	-3.8	6.16
			2					249.5	-4.8	7.59
			3					245		
		C	1					190	-3.3	5.41
			2					245	-6.7	10.11
			3					224	-5.2	8.14
			4					236.5	-3.7	6.01
			5					205	-7.4	10.98
			6					180	-10.1	
CPR 23	CPR 23a	A	1	G	L-V		60	267	-3.7	6.01
		A	2	G	L-V		20	257	-4.3	6.88
		A	3	G	L-V		30	240	-3.8	6.16
		A	4	G	L-V		20	250		
		A	5	G	L-V		10	245		
		A	6	G	L-V		30	260		
		A	8	G	L-V		15	268	-3.4	5.56
		C	2	G	L-V				-1.8	3.06
		C	3	pseudio-sec (	L-V			210	-1.4	2.41
		C	4	pseudio-sec (	L-V			214		
		C	5	pseudio-sec (	L-V			232.5	-6.5	9.86
		C	6	pseudio-sec (	L-V			234	-6.5	9.86
		C	7	pseudio-sec (	L-V					
		G	11	isolated	L-V			200	-0.1	0.18
		G	12	G	L-V			263	-0.1	0.18
		G	13	G	L-V			273	-1.4	2.41
Fpe 130-13b	Fpe-130-13b	A	1					252	-0.7	1.22
		A	2					266.5	-0.3	0.53
		A	3					252	-0.5	0.88
		A	4					251	-0.4	0.70
		A	5					252	-0.4	0.70
		B	1					273	-0.9	1.57
		B	2					273	-1	1.74
		B	4					278	-1.1	1.91
		C	1					272	-1.1	1.91
		C	2					277	-1	1.74
		C	3					276	-0.8	1.40
		C	4					272	-0.8	1.40
CPR 23	CPR 23a	C	8	primary	L-V			346	-1.3	2.24
		C	9	?	L-V			234.5	-0.7	1.22
		G	1	G	L-V			365	-1.7	2.90
		G	2	G	L-V			351	-0.5	0.88
		G	9	G	L-V			375	-2.5	4.18
		G	10	G	L-V			340.2	-3.5	5.71

Appendix 2 *(cont.)*

Sample n°	Chip n°	Assemblage n°	FI n°	Type	Filling	Degree of fill	Size (µm)	Th final(°C)	$T_{m\ ice}$ (°C)	Salinity* (wt. % NaCl eq)
median								251		2.41
average								243		3.3
Pyrrhotite pipes (quartz)										
FPE 131-1	chip 1	A	1					229	-2.2	3.71
		A	2							
		A	3							
		B	1					230	-1.6	2.74
		C	1					192	-0.6	1.05
		C	2					205	-2	3.39
		C	3					205	-6.8	10.24
		C	4					237	-2.6	4.34
		C	5					210	-2.6	4.34
	chip 2	A	1					240	-7.2	10.73
		B	1					250	-8.9	12.73
		C	1					249	-6.6	9.98
median								230		3.4
average								225		3.2
Zn-Pb ores (quartz)										
CPR 461	CPR 461a	A	1					208	-2.4	4.03
		A	2					212.5		
	CPR 461b	A	1					199.5	-2.1	3.55
			2					187	-1.9	3.23
			3					183	-2	3.39
median								199.5		3.39
average										
			4					192.5	-1.9	3.23
median								200		3.4
average								197		3.5
Second mineralization stage										
Carbonate replacement bodies (quartz)										
CPR 480	CPR 480d	A	1	G	L-V		18	220	-4.8	7.59
		A	2	G	L-V		18	241.5		
		A	3	G	L-V		18	205	-4	6.45
		A	4	G	L-V		30	209.7	-4	6.45
		A	5	G	L-V		25	252.5	-3.1	5.11
		A	6	G	L-V		15	235	-4	6.45
		B	1	G	L-V		18	247.5	-4	6.45
		B	2	G	L-V		25	238.7	-4.7	7.45
		B	3	G	L-V		10	237	-5.4	8.41
		B	4	G	L-V		15	241	-4.8	7.59
CPR 480	CPR 480c		1	G	L-V		35	231.6	-6.2	9.47
			2	G	L-V			218.8	-7.1	10.61
			3	G	L-V			252.3	-4.6	7.31
			4	G	L-V			253.1	-4.7	7.45
			5	G	L-V		60	214.7	-2.2	3.71
			6	G	L-V			218.5	-2.2	3.71
			7	G	L-V			219.4	-0.7	1.22
			8	G	L-V		15	214.0	-0.6	1.05
			9	G	L-V		15	225.0	-3.8	6.16

Appendix 2 *(cont.)*

Sample n°	Chip n°	Assemblage n°	FI n°	Type	Filling	Degree of fill	Size (µm)	Th final(°C)	$T_{m\ ice}$ (°C)	Salinity* (wt. % NaCl eq)
			10	G	L-V		16			
			11	G	L-V		15	236.2	-2.1	3.55
			12	G	L-V			234.2	-2.2	3.71
			13	G	L-V			220.8	-0.2	0.35
			14	G	L-V			224.3	-1.9	3.23
			15	G	L-V			253.2	-0.3	0.53
			16	G	L-V			243.0	-2.5	4.18
			17	G	L-V			211.0	-1.8	3.06
CPR 480	CPR 480e		1	G	L-V		15	233.6	-0.1	0.18
			2	G	L-V			236.3		
			3	G	L-V		20	243.7		
			4	G	L-V		12	265.0	-2.9	4.80
			5	G	L-V		12		-1.9	3.23
			6	G	L-V		25	238.0	-2.8	4.65
			7	G	L-V		40	178.9	-6.2	9.47
median								235		4.9
average								231		5.1
Carbonate replacement bodies (sphalerite)										
CPR 76	CPR 76 Z1							222.3	-5.0	7.86
CPR 76								218.8	-1.8	3.06
CPR 76								198.1	-1.6	2.74
CPR 325	CPR 325 Va							168.9	-3.1	5.11
CPR 74	CPR 74 Wf							221.7	-4.7	7.45
	CPR 74 Wg							168.0	-2.8	4.65
CPR 427	CPR 427 Ya							197.4	-1.7	2.90
	CPR 427 Yb							191.4	-4.6	7.31
								188.5	-4.6	7.31
								193.5	-4.5	7.17
								194.2	-4.5	7.17
								190.0	-4.3	6.88
	CPR 427 Za							174.0	n.d.	
CPR 76								201.2	-8.1	11.81
CPR 74								219.7	-7.4	10.98
CPR 76 Ya								212.1	-6.0	9.21
median								196		7.1
average								197		6.8
Enargite-pyrite veins (quartz)										
cpr 608	cpr 608a2	A’	1	G	L-V	15	35	233	-0.6	1.05
		A’	2	G	L-V	15	18	255	-0.5	0.88
		A’	3	G	L-V		20	209	-0.5	0.88
		A’	4	G	L-V		35	233	-0.2	0.35
		B	1	G	L-V		10	243	-1.9	3.23
		B	2	G	L-V		15	230	-0.7	1.22
		B	3	G	L-V		10	243	-0.5	0.88
		B	4	G	L-V		10	230	-0.4	0.70
		B	5	G	L-V		10	255	-0.7	1.22
		B	6	G	L-V		10	200.5	-0.7	1.22
		C	1	G	L-V	20	25	226.5	-0.2	0.35
		C	2	G	L-V	15	25	217	-1	1.74

Appendix 2 *(cont.)*

Sample n°	Chip n°	Assemblage n°	FI n°	Type	Filling	Degree of fill	Size (µm)	Th final(°C)	$T_{m\ ice}$ (°C)	Salinity* (wt. % NaCl eq)
		C	3	G	L-V	20	15	200	-0.8	1.40
		C	4	G	L-V	15	15	200	-0.2	0.35
		C	5	G	L-V	15	18	190	-1	1.74
		C	6	G	L-V	15	20	185	-0.8	1.40
		C	7	G	L-V	15	25	226.5	-2	3.39
		E	1	G	L-V	10	30	210	-2.7	4.49
		E	2	G	L-V	15	15	207.5	-0.1	0.18
		E	3	G	L-V	15	25	208.5	-0.9	1.57
		E	4	G	L-V	15	20	207.5	-1.1	1.91
		E	5	G	L-V	15	20	212	-1.1	1.91
		F	1	G	L-V	10	25	211	-0.6	1.05
		F	2	G	L-V	10	25	180	-0.3	0.53
		F	3	G	L-V	10	25	177.5	-0.2	0.35
		F	4	G	L-V	10	20	202	-0.5	0.88
		F	5	G	L-V	13	20	213.5	-0.4	0.70
		F	6	G	L-V	10	15	177.5	-0.5	0.88
		F	7	G	L-V	10	30	190	-0.6	1.05
		F	8	G	L-V	10	18	210	-0.3	0.53
cpr 608	cpr 608a3	A	1	G	L-V	20	20	230	-0.5	0.88
		A	2	G	L-V	15	15	242	-0.3	0.53
		A	3	G	L-V	15	10	225	-0.1	0.18
		A	4	G	L-V	15	18	235	-0.1	0.18
		A	5	G	L-V	15	10	222.2	-0.1	0.18
		C	1	G	L-V	15	25	240.3	-0.1	0.18
		C	2	G	L-V	15	25	211.3	-0.1	0.18
		C	3	G	L-V	15	18	230	-0.1	0.18
		C	4	G	L-V	15	25	207.5	-0.1	0.18
		C	5	G	L-V	15	20	200	-0.1	0.18
		C	5’	G	L-V	15	18	205.1	-0.1	0.18
		C	6	G	L-V	15	18	217.5	-0.2	0.35
		C	7	G	L-V	15	18	229	-0.1	0.18
		C	8	G	L-V	15	20	213	-0.2	0.35
		C	9	G	L-V	15	18	213	-0.5	0.88
		C	11	G	L-V	15	28	222.5	-0.1	0.18
		C		G	L-V					
		C	13	G	L-V	15	30	220	-0.1	0.18
		C	14	G	L-V	15	25	225	-0.3	0.53
		C		G	L-V					
		C	16	G	L-V	15	40	213	0	0.00
		C	17	G	L-V	15	30	222.5	-0.4	0.70
		C	18	G	L-V	15	18	226.5	-0.4	0.70
		C	19	G	L-V	15	20	205	-0.1	0.18
		C	12	G	L-V	15	20	215	-0.1	0.18
		C	15	G	L-V	15	33	200	-0.1	0.18
cpr 439	cpr 439b	A	1	G	L-V		12	256.5	-0.9	1.57
		A	2	G	L-V		12	275	-0.6	1.05
		A	3	G	L-V		15	251	-0.8	1.40
		B	1	G	L-V		30	293	-0.9	1.57
		B	2	G	L-V		24	247	-0.8	1.40
		B	3	G	L-V		24	247.5	-0.9	1.57

Appendix 2 *(cont.)*

Sample n°	Chip n°	Assemblage n°	FI n°	Type	Filling	Degree of fill	Size (µm)	Th final(°C)	$T_{m\ ice}$ (°C)	Salinity* (wt. % NaCl eq)
		B	4	G	L-V		12	250	-0.9	1.57
		C	1	G	L-V		18	250	-0.7	1.22
		C	2	G	L-V		12	245.1	-0.3	0.53
		C	3	G	L-V		10	250	-0.9	1.57
		C	4	G	L-V		15	209.6	-0.3	0.53
		D	1	G	L-V		12	248	-0.9	1.57
		D	2	G	L-V		10	255	-1.2	2.07
		D	3	G	L-V		18	255	-0.9	1.57
		D	4	G	L-V		12	255	-0.9	1.57
		D	5	G	L-V		18	255	-0.9	1.57
		D	6	G	L-V		10	255	-0.9	1.57
		E	1	G	L-V		25	251	-0.8	1.40
		E	2	G	L-V		25	248	-0.8	1.40
		E	3	G	L-V		20	259	-0.9	1.57
		E	4	G	L-V		20	247.5	-0.8	1.40
		j	1	G	L-V	15-20	30	248	-0.3	0.53
cpr 439	cpr 439a	A	1	G	L-V		10	272.5	-1.7	2.90
		A	2	G	L-V		25	238.6	-1.7	2.90
		A	3	G	L-V		15	254	-1.5	2.57
		A	4	G	L-V		25	275	-3.2	5.26
		B	1	G	L-V		15	248	-0.9	1.57
		B	2	G	L-V		20	231.1	-1.3	2.24
		B	3	G	L-V		15	187.9	-2	3.39
		B	5	G	L-V		20	197.6	-2	3.39
		B	6	G	L-V		20	187.9	-2	3.39
median								227		1.1
average								227		1.2
cpr 439	cpr 439b	M	1	P1	L-V	15-20	30	254	-9.5	13.40
		M	2	P1	L-V	15-20	15	242	-22.3	23.89
		M	1	P1	L-V	15-20	24	275.5		
		M	2	P1	L-V	15-20	20	237.1	-12.75	16.66
		M	3	P1	L-V	15-20	30	220	-7.1	10.61
		M	4	P1	L-V	15-20	22	238.6	-7.5	11.10
		M	1	P1	L-V	20	25	235		
		M	2	P1	L-V	20	35	236.5	-8.4	12.16
		M	3	P1	L-V	20	30	233		
		M	4	P1	L-V	20	25	225	-8.1	11.81
		M	5	P1	L-V	20	35	260	-1.9	3.23
		M	6	P1	L-V	15-20	20	223		
		M	7	P1	L-V	20	25	240		
		F	1	P1	L-V		25	229.5	-1.4	2.41
		F	2	P1	L-V		18	232.5	-0.4	0.70
		F	3	P1	L-V		25	265.5	-2.4	4.03
		F	4	P1	L-V		30	234.7	-1.5	2.57
		G	1	P1	L-V		25	229.5	-1.3	2.24
		G	2	P1	L-V		45	229.5	-23	24.34
		G	3	P1	L-V		30	220	-22	23.70
		H	1	P1	L-V		15	261	-3.4	5.56
		H	2	P1	L-V		30	251	-20	22.38

Appendix 2 *(cont.)*

Sample n°	Chip n°	Assemblage n°	FI n°	Type	Filling	Degree of fill	Size (µm)	Th final(°C)	$T_{m\ ice}$ (°C)	Salinity* (wt. % NaCl eq)
		H	3	P1	L-V		15	280	-12.5	16.43
		H	4	P1	L-V		45	266.8	-11.7	15.67
		I	1	P1	L-V		45	245.8	-19.9	22.31
		I	2	P1	L-V		20	249.5	-19.9	22.31
		I	3	P1	L-V		25	258.8	-1.7	2.90
Venencocha (quartz)										
cpr 365	cpr 365b	A	1		L-V			261		
		A	2		L-V			260	-3	4.96
		A	3		L-V			267	-1.9	3.23
		A	4		L-V			248		
		A	5		L-V			260		
		A	6		L-V			245	-4	6.45
		A verso	1		L-V			246	-4.9	7.73
		A verso	2		L-V			263	-4.7	7.45
		A verso	3		L-V			247	-3.1	5.11
median					L-V			260		5.7
average					L-V			255		5.7

[1] Salinity = 0,00 + 1,78q - 0,0442q2 + 0,000557q3, Bodnar (1993)

P1 = FI in fractures within magmatic quartz; G = growth zone, L-V (liquid-vapor)

Appendix

List of samples

Sample	Localisation	Deposit	Description	XRF	XRD	LM	SP	ICP-MS/INAA	Ar Ar	U-Pb	Hf	C	H, O	S	F. I.	Rb-Sr	N° labo
CPR2	3rd bench W	Tajo Raul Rojas	Pb-Zn (marmatite) ore with pyrite, quartz, and pyrrhotite. 1st min. stage.														9498
CPR3	2nd bench W	Tajo Raul Rojas	quartz-sericite-pyrite alteration of diatreme breccia													ser, py	
CPR4	2nd bench W	Tajo Raul Rojas	Zb-Pb ore (1st mineralization stage)														
CPR6	2nd bench W	Tajo Raul Rojas	enargite-pyrite vein with contact halo in diatreme breccia. Chalcopyrite, tennantite, covelline. Vein 43														8853-8854
CPR7	bench 4310	Tajo Matagente	oxydized rock with sphalerite, galena, hematite, pyrite. 2nd min. stage, outer most zone.										carb	gn			9499
CPR8	bench 4310	Tajo Matagente	galena in carbonate rocks with siderite in open space. Contains Fe-poor sphalerite														10271
CPR10	bench 4310	Tajo Matagente	Pb-Zn ore with galena and idiomorphic barite and kaolinite										kaol, ba	ba			
CPR11	bench 4310	Tajo Matagente	Pb-Zn ore with Fe-poor sphalerite, galena and barite. 2nd min. stage, outer zone.										kaol, ba, carb	ba			8423
CPR12	bench 4300	Tajo Matagente	rodochrosite associated with a dark metallique mineral														
CPR13	bench 4300	Tajo Matagente	Zn-Pb-Bi vein in carbonates from Matagente with coarse grained argile. After XRD: quartz-muscovite-sphalerite-siderite-oligonite														?
CPR15	4th bench W	Tajo Raul Rojas	quartz-pyrite body with abundant alunite near enargite vein			LP	LP							py			9406-9402
CPR16	bench 4300	Tajo Matagente	carbonate rock with sphalerite, galena, quartz, oligonite, muscovite														9492-8856-8867
CPR19	N 1st bench	Tajo Raul Rojas	coarse grained alunite and quartz with enargite veins in silicified carbonates with pyrite. Vein 28			LP							qtz				12220
CPR21	N 1st bench	Tajo Raul Rojas	quartz- monzonite dyke with phyllic alteration with sericite replacing feldspars. pyrite and quartz also present													ser	9526
CPR23	N 1st bench	Tajo Raul Rojas	pyrite-quartz body with idiomorph quartz grains										qtz		qtz		
CPR24	bench 4310	Tajo Matagente CN	Zn-Pb ore with galena														10274
CPR25	bench 4310	Tajo Matagente CN	barite vein with pyrite , kaolinite and quartz										qtz, ba	ba, py			10276
CPR26	bench 4310	Tajo Matagente CN	Zn-Pb ore with galena, sphalerite, and kaolinite										kaol	gn, sl			9720
CPR27	bench 4310	Tajo Matagente CN	light sulfide rock with kaolinite and pyrite. After XRD: svanbergite-kao-hinsdalite-angesitel-sphalerite. intermediate zone because hinsd-svanb.										kaol				9143
CPR28	bench 4320	Tajo Matagente CN	dark sulfide rock with pyrite and galena and barite grains. Sphalerite also present with white clay (kaol?). 2nd min. stage, outer zone.														9500
CPR29	bench 4320	Tajo Matagente CN	sulfide rock with quartz-galena-marcasite-pyrite-kaolinite-sphalerite. 2nd min. stage, outer zone														10273
CPR30	bench 4320	Tajo Matagente CN	sulfide rock with galena-sphalerite-kaolinite and dickite. 2nd min. stage, outer zone.										kaol	gn, sl			
CPR31	bench 4320	Tajo Matagente CN	Fe-poor sphalerite, galena and pyrite														10275
CPR32	bench 4320	Tajo Matagente CN	Fe-poor sphalerite, galena and pyrite			LP	LP										10286
CPR36	bench 4310	Tajo Matagente CN	sulfide rock rich in organic material with sulfates. Ith quartz and hinsdalite														10281

Sample	Localisation	Deposit	Description	XRF	XRD	LM	SP	ICP-MS/INAA	Ar Ar	U-Pb	Hf	C	H, O	S	F. I.	Rb-Sr	N° labo
CPR37	bench 4310	Tajo Matagente CN	Zn-Pb ore with pyrite-galena-sphalerite-kaolinite-quartz-hinsdalite. 2nd min. stage, outer zone														8845-8859
CPR38	S 1st bench	Tajo Raul Rojas	alunite (?) in pyrite-quartz body (southern part of the pit) near enargite vein. Vein 73											py	qtz		
CPR40	bench 4310	Tajo Matagente CN	barite from zonation of sulfide rock			LP	LP										9496
CPR41	bench 4310	Tajo Matagente CN	sulfide rock in a vein. After XRD: kaolinite-sphalerite-galena.														
CPR44	bench 4310	Tajo Matagente CN	Dickite/Kaolinite in massiv Zn-Pb ore with pyrite, kaolinite, svanbergite, barite. 2nd min. stage, outer zone										kaol				10284
CPR45	bench 4310	Tajo Matagente CN	botroydal pyrite adjacent to Cu veins. 2nd min. stage, outer zone.														8855
CPR46	bench 4310	Tajo Matagente CN	sulfide rock with kaolinite, hinsdalite, pyrite, quartz														9142
CPR47	bench 4310	Tajo Matagente CN	Zn-Pb ore with interesting structure										kaol, carb	gn, sl			
CPR48	cuerpo San Alberto	Tajo Raul Rojas N	sulfide rock with sphalerite, barite, galena										qtz	ba			10272
CPR49	macchu picchu bench (1st E)	Tajo Raul Rojas E	sulfide rock with quartz-muscovite-svanbergite-sphalerite-galena. 2nd min. sateg, outer zone.														8848-9145
CPR50	bench 4320	Tajo Matagente CN	sulfide rock with dickite, quartz, galena, sphalerite.														
CPR51	bench 4320	Tajo Matagente CN	sulfide rock with galena, kaolinite and pyrite, qtz, hinsdalite, florencite, gibbsite														9144-8858
CPR53	bench 4330	Tajo Matagente CN	massive quartz and pyrite. 2nd min. stage, outer zone														8868-8862-8863
CPR54	bench 4320	Matagente Manto V	sulfide rock with kaolinite-quartz-pyrite-sphalerite-galena										kaol				8847, 8865
CPR56	bench 4320	Matagente Manto V	karstique carbonate with ankerite-siderite, barite										ba	ba			
CPR57	bench 4320	Matagente Manto V	sulfide rock														10282
CPR57.1	2nd bench E	Tajo Raul Rojas E	magnetite veins with E-W direction with sphalerite. 2nd min. stage, outermost zone			LP	LP										9497
CPR57.2	2nd bench S	Tajo Raul Rojas E	near tunnel, sulfide rock with green/blue argile. Halloysite (Al2Si2O5(OH)4										kaol				
CPR58	cuerpo San Alberto	Tajo Raul Rojas N	quartz with siderite										qtz, carb				
CPR59	cuerpo San Alberto	Tajo Raul Rojas N	sphalerite from a vein (N95°E) with barite, Fe-Mn-Zn carbobate and kaolinite.										ba, carb	ba			
CPR60	DDH SR-00-03 (17.00m)	Santa Rosa	sericite-pyrite-quartz alteration			LP	LP										10284
CPR61	DDH SR-00-03 (24.60m)	Santa Rosa	sericite-pyrite-quartz alteration			LP	LP										10293
CPR62	DDH SR-00-03 (24.50m)	Santa Rosa	sericite-pyrite-quartz alteration			LP	LP										10288
CPR63	DDH SR-00-03 (32.00m)	Santa Rosa	kaolinite + quartz			LP	LP										10292
CPR64	DDH SR-00-03 (44.10m)	Santa Rosa	Vuggy quartz			LP	LP										10290
CPR65	DDH SR-00-03 (64.00m)	Santa Rosa	advanced argillic alteration with fine grained alunite			LP	LP										10289
CPR66	DDH SR-00-03 (71.60m)	Santa Rosa	advanced argillic alteration with alunite			LP	LP										10295
CPR67	DDH SR-00-03 (92.80m)	Santa Rosa	alunite in enargite-pyrite veins														9070,10278
CPR68	DDH SR-00-03 (91.20m)	Santa Rosa	Cu-min with pyrite and quartz														9071,10277
CPR69	DDH SR-00-03 (97.70m)	Santa Rosa	Excelsior phyllite with pyrite-kaolinite veinlets														
CPR70	DDH SR-00-04 (94.50m)	Santa Rosa	alunite in enargite-pyrite vein														10285
CPR71	DDH SR-00-04 (94.70m)	Santa Rosa	sulfures in pyrite-quartz														9672, 10279

Sample	Localisation	Deposit	Description	XRF	XRD	LM	SP	ICP-MS/INAA	Ar Ar	U-Pb	Hf	C	H, O	S	F. I.	Rb-Sr	N° labo
CPR72	DDH SR-00-04 (100.60m)	Santa Rosa	Excelsior phyllite with sericite and quartz, with sulfur veinlets			LP	LP										9075
CPR73	DDH SR-00-03 (76.20m)	Santa Rosa	vuggy quartz rich in Ag (>10 oz/t)			LP	LP										10291
CPR74	DDH CP-00-108 (5.00m)	Tajo Raul Rojas E	massive sphalerite and galena with pyrite and kaolinite. 2n min. stage outer zone												sl		9075
CPR75	DDH CP-00-108 (8.50m)	Tajo Raul Rojas E	mixing zone with Fe-poor and rich sphalerite and galena-pyrite-kaolinite. 2nd min. stage, outer zone														9493, 8421
CPR76	DDH CP-00-108 (9.70m)	Tajo Raul Rojas E	sphalerite with galena and kaolinite and proustite-jordanite. 2nd min. stage, outer zone			LP								sl	sl		9501, 8420
CPR77	DDH CP-00-108 (13.00m)	Tajo Raul Rojas E	marmatite-blende-kaolinite and pyrite, sphalerite, galena, anglesite											sl			9078
CPR78	DDH CP-00-108 (17.00m)	Tajo Raul Rojas E	pyrite-rich rock bismutinite-stibnite solid solution, covellite. 2nd min. stage, intermediate zone.														9077
CPR79	DDH CP-00-108 (18.00m)	Tajo Raul Rojas E	pyrite-rich rock with sphalerite-galena and carb. 2nd min. stage, outer zone														9079
CPR80	DDH CP-00-108 (26.50m)	Tajo Raul Rojas E	py rich rock with kaolinite and Bi min. 2nd min. stage, intermediate zone														8429
CPR81	DDH CP-00-108 (23.50m)	Tajo Raul Rojas E	Bi rich rock with py and darker parts. 2nd min. stage, intermediate zone														8428
CPR82	DDH CP-00-108 (34.00m)	Tajo Raul Rojas E	rock with tetrahedrite, atimonpearcite, matildite, and chalcopyrite. 2nd min. stage, intermediate zone.										kaol				9083, 9085
CPR83	DDH CP-00-108 (36.40m)	Tajo Raul Rojas E	sulfide rock with pyrite and kaolinite. 2nd min. stage, outer zone														9082
CPR84	DDH CP-00-108 (51.80m)	Tajo Raul Rojas E	kaolinite-rich sulfide rock with pyrite, tetrahdrite, famatinite and colusite. 2nd min. stage, intermediate zone														9080
CPR85	DDH CP-00-108 (58.20m)	Tajo Raul Rojas E	sulfide rock with pyrite, tetrahedrite, chalcopyrite, and kaolinite. 2nd min. stage, intermediate zone														9084
CPR86	DDH CP-00-108 (61.30m)	Tajo Raul Rojas E	sulfide rock with pyrite galena, and kaolinite . 2nd min. stage, outer zone														9081
CPR87	DDH CP-00-108 (68.10m)	Tajo Raul Rojas E	pyrite-rich rock with galena, pyrite, sphalerite, and hinsdalite, kaolinite. 2nd min. stage, intermediate zone														8425
CPR88	DDH CP-00-108 (73.80m)	Tajo Raul Rojas E	sulfide rock with pyrite, sphalerite, galena, and hematite. 2nd min. stage, outer zone														9076
CPR89	DDH CP-00-108 (74.70m)	Tajo Raul Rojas E	Massive rock with hematite, magnetite and sphalerite. 2nd min. stage, outermost zone														8427
CPR90	DDH CP-00-108 (84.50m)	Tajo Raul Rojas E	silicified limestone with Fe-Mn-Zn carbonates, magnetite, hematite, and galena, sphalerite. 2nd min. stage, outermost zone.														9074
CPR91	DDH SR-00-04 (93.70m)	Tajo Raul Rojas E	Pyrite-quartz with silicified clastes.														10280
CPR96	2nd bench center	Tajo Raul Rojas W	Sericite from alteration halo from quartz-pyrite body														
CPR97	2nd bench N (curve)	Tajo Raul Rojas N	heavy white rock with Zn-Mg carbonates.														
CPR 100	DDH CP-00-139 (19.70m)	Tajo Raul Rojas E	2nd stage intermediate-outer zone with pyrite, covellite, galena and hinsdalite, svanbergite														8659
CPR 101	DDH CP-00-139 (42.00m)	Tajo Raul Rojas E	2nd stage intermediate-outer zone with pyrite, covellite, galena and sphalerite. Presence of alunite (?)														9010
CPR 102	DDH CP-00-150 (41.50m)	Tajo Raul Rojas E	2nd min. stage outer zone with sphalerite, galena, hinsdalite.														8672
CPR 103	DDH CP-00-150 (50m)	Tajo Raul Rojas E	2nd min. stage outer zone with sphalerite, galena, and Fe-Mn-Zn carbonates														8660

Sample	Localisation	Deposit	Description	XRF	XRD	LM	SP	ICP-MS/INAA	Ar Ar	U-Pb	Hf	C	H, O	S	F. I.	Rb-Sr	N° labo
CPR 104	DDH CP-00-146 (283m)	Tajo Raul Rojas E	2nd min. stage outer zone with sphalerite, galena, and Fe-Mn-Zn carbonates														9012
CPR 105	DDH CP-00-146 (283m)	Tajo Raul Rojas E	2nd min. stage outer zone with sphalerite, galena, and Fe-Mn-Zn carbonates														9013
CPR 106	DDH CP-00-146 (291.30m)	Tajo Raul Rojas E	2nd min. stage outer zone with sphalerite, galena, and Fe-Mn-Zn carbonates														8661
CPR 107	DDH CP-00-146 (276.20m)	Tajo Raul Rojas E	sulfide rock from the 2nd min. stage interemdiate zone.														8662
CPR 145	bench 4320 Matagente	Tajo Raul Rojas E, CN	carbonate rock with pyrite vein containing sphalerite														8871
CPR 147	bench 4320 Matagente	Tajo Raul Rojas E, CN	carbonate rock with galena, sphalerite, and pyrite														9011
CPR 149	bench 4320 Matagente	Tajo Raul Rojas E, CN	Sulfide rocks with famatinite. 2nd min. stage, core zone														9016
CPR 150	bench 4320 Matagente	Tajo Raul Rojas E, CN	Sulfide rocks with famatinite and tetrahedrite. 2nd min. stage, core zone														8872
CPR 151	bench 4320 Matagente	Tajo Raul Rojas E, CN	Sulfide rocks with famatinite, chalcopyrite tetrahedrite. 2nd min. stage, intermediate zone														9694
CPR 155	bench 4320 Matagente	Tajo Raul Rojas E, CN	Massive galena with sphalerite. 2nd min. stage, outer zone														8873
CPR300	2nd bench N (curve)	Tajo Raul Rojas N	sulfide rock from a vein with pyrite and kaolinite														8846-8866
CPR302	2nd bench N (curve)	Tajo Raul Rojas N	sulfide rock with sphalerite and pyrite														8857
CPR304	2nd bench N (curve)	Tajo Raul Rojas N	heavy carbonate rock with Fe-Mn-Zn carbonates														
CPR305	3rd bench S	Tajo Raul Rojas S	carbonate rock with sphalerite and galena.														
CPR306	3rd bench S	Tajo Raul Rojas S	massive marmatite with pyrite, arsenopyrite, magnetite, galena and quartz, anglesite.														8426
CPR307.1	3rd bench S	Tajo Raul Rojas S	sulfide rock with sphalerite, pyrite, and galena and quartz-muscovite-hinsdalite														8840
CPR307.2	3rd bench S	Tajo Raul Rojas S	90% pyrite with sphalerite + galena and anlgesite, kaolinite, dickite, montmorillonite														8841
CPR307.3	3rd bench S	Tajo Raul Rojas S	60% pyrite, sphalerite, galena, and kaolinite, anglesite, dickite														8842
CPR307.4	3rd bench S	Tajo Raul Rojas S	breccified pyrite-quartz with galena,														8843
CPR307.5	3rd bench S	Tajo Raul Rojas S	quartz-pyrite body with galena, pyrite														8844
CPR309	3nd bench E	Tajo Raul Rojas	sulfide rock with sphalerite										kaol, qtz	sl			
CPR311	3nd bench E	Tajo Raul Rojas	sulfide rock next to tunnel										kaol				
CPR312	3nd bench s	Tajo Raul Rojas	sulfide rock below the pyrite-quartz body, with pyrite														
CPR314			veins with magnetite near 4160 E, siderite, sphalerite														
CPR315	Level 1200, 8920E-9860N, piso 19	underground mine	sulfide rock with kaolinite and blende and pyrite-quartz-gunningite (?)														8849
CPR316	Level 1200, 8920E-9860N	underground mine	sulfide rock with alunite, pyrite, quartz, halloysite														
CPR318	Level 1200, 12889E	underground mine	kaolinite with sphalerite and pyrite. Transition zone between Fe-rich and Fe-poor sphalerite											py			8861
CPR319	Level 1200, 9020E, 9890	underground mine	Massive 1st stage ore with galena and marmatite. 1st min. stage										qtz	sl, py			8860
CPR322	Level 1200, 8902E, 10395	underground mine	Massive 1st stage ore with galena , pyrrhotite, arsenopyrite, and marmatite														9495
CPR323	DDH CP-00-146 (323m)		unaltered mitu Group rock														
CPR324	DDH CP-00-146 (328m)		breccia with sphalerite and galena														8424
CPR325	DDH CP-00-146 (337.30m)		Zn-Pb ore with abundant zoned sphalerite and galena												sl		9494

Sample	Localisation	Deposit	Description	XRF	XRD	LM	SP	ICP-MS/INAA	Ar Ar	U-Pb	Hf	C	H, O	S	F. I.	Rb-Sr	N° labo
CPR326	Uliachin 5	Uliachin	sulfide rock with kaolinite, dickite, quartz-crandallite														8850
CPR327	Uliachin 6	Uliachin	black sulfide rockwith dickite, quartz, hinsdalite														
CPR328	Uliachin 7	Uliachin	black sulfide rock with kaolinite, quartz, hinsdalite														
CPR330			quartz and muscovite bearing rock														
CPR331			sulfide rock with quartz, hinsdalite, and marcasite														
CPR332			dickite, woodhouseite, quartz and minrecordite														
CPR333	Uliachin 8	Uliachin	sulfide rock														
CPR335	Uliachin	Uliachin	sulfide rock with quartz, kaolinite, florencite														
CPR336	Yanacancha	Yanacancha	kaolinite with pyrite, glaena hinsdalite, kaolinite, and anglesite														
CPR337	Yanacancha	Yanacancha	rock from Pilar open pit with anglesite, pyrite, galena, chalcopyrite														
CPR338	Venencocha A	Venencocha	sulfide rock														9734
CPR339	Venencocha B	Venencocha	sulfide rock														
CPR340	Venencocha C	Venencocha	sulfide rock														9529
CPR341	Venencocha D	Venencocha	sulfide rock														
CPR343	Venencocha F	Venencocha	sulfide rock														9414
CPR344	Venencocha G	Venencocha	tuff within diatreme with magmatic biotite														9412
CPR347	Venencocha J	Venencocha	porphyry dome showing vuggy quartz with alunite and zunyite. Qz eyes.			LP							al	al			9413
CPR349	Venencocha K-L	Venencocha															9811
CPR350	Venencocha L	Venencocha	porphyry dome with alunite														
CPR351	Tajo Santa Rosa	Tajo Santa Rosa	alunite in vuggy quartz from the diatreme breccia			Lp							al	al			12223
CPR352.1	3rd bench, near entrance tunnel W	Tajo Raul Rojas	massive pyrite, pyrrhotite and marmatite. 1st min. stage														8851
CPR352.2	3rd bench, entrance tunnel W	Tajo Raul Rojas	massive pyrite with arsenopyrite and marmatite and dolomite. 1st min. stage														8852
CPR360	Venencocha	Venencocha	breccia-tuf. Fine matrix composed of alunite and qtz. Clasts are resorbed quartz, volcanic glass, pucara silicified. Pervasive advanced argillic alteration. Well developed alunite			LP											12219
CPR361	Venencocha	Venencocha	Breccia-tuf, with clasts having different dimensions (<1cm). Pervasive advanced argillic alteration and filling by alunite in dissolved clasts. Matrix is residual quartz. Sample contains some vugs			LP											9394
CPR365	Venencocha	Venencocha	Vuggy quartz with alunite. Rock is very porous			LP							qtz, al	al	qtz		12221
CPR366	Venencocha	Venencocha	Breccia with angular to rounded clasts. Grey matrix. Clasts are altered to dissolved, and replaced by alunite and quartz. Some clasts are silicified														9398
CPR367	Venencocha	Venencocha	volcanic rock with fine matrix with pyrite fantoms. Open space filling alunite. Resorbed quartz eyes. Pervasive advanced argillic alteration with diaspore, woodhouseite, pyrophillite, quartz			LP											9400
CPR369	Venencocha	Venencocha	Oxidized vein in Excelsior Fm. Heavy sample. quartz, goetite, jarosite, muscovite														
CPR372	Venencocha	Venencocha	Altered porphyry rock with a fine grey-greenish matrix containing disseminated pyrite. Minerals are altered, book biotite => chlorite. Presence of calcite, eyes of quartz. Propyllitic alteration. Presence of zicon														9403

Sample	Localisation	Deposit	Description	XRF	XRD	LM	SP	ICP-MS/INAA	Ar Ar	U-Pb	Hf	C	H, O	S	F. I.	Rb-Sr	N° labo
CPR374	Venencocha	Venencocha	Mitú polymictic breccia with rounded clasts of phyllites and milky quartz from Excelsior Fm. Sandy matrix.														9405
CPR375	0361168E, 8821701N	Venencocha	Altered Rumiallana diatreme breccia.														9396
CPR376	Venencocha	Venencocha	well cristallized hydrothermal quartz in a vein in Excelsior Fm.										qtz				
CPR377	0361412E, 8821849N	Venencocha	Relatively heavy sample with “banded” texture” containing hematiteand goetite and qtz, pyrophyllite, greigite.														
CPR378	Venencocha	Venencocha	Oxidized vein near dacitic dome, with Fe oxides (goetite, jarosite) and alunite, quartz, zunyite.														
CPR379	Venencocha	Venencocha	alunite as open space filling in porphyritic dome. Resorbed quartz eyes. Pervasive advanced argillic alteration														
CPR380	Venencocha	Venencocha	Pervalsively advanced argillic altered dome with quartz and pink alunite filling open spaces. Rock contains phantoms of pyrite. Qtz is resorbed.										al	al			9397
CPR381	Venencocha	Venencocha	Giant alunite from an altered vein cutting the Excelsior.			LP							al	al			12218
CPR383	Venencocha	Venencocha	Altered breccia with alunite and hydrothermal quartz.														9530
CPR384	Venencocha	Venencocha	zunyite and alunite from a vein in Excelsior.			LP											9810
CPR385	Venencocha	Venencocha	Altered Mitú with qtz-sericite aleration														9411
CPR386	Venencocha	Venencocha	altered Mitú with kaol and dickite														9408
CPR388	0361095E, 8821841N	Venencocha	Fresh porphyritic dome with biotite and feldspars														9409
CPR389	Venencocha	Venencocha	Altered porphyritic dome. Biotite => chlorite. Resorbed quartz. Perasive propyllitic alteration. Transparent mineral with an elongated shape														9410
CPR390	Venencocha	Venencocha	Fresh phyllite from Excelsior formation.														9401
CPR391	Venencocha	Venencocha	Oxydized vein with Fe-oxides with goetite and alunite														
CPR392	0361273E, 8821907N	Venencocha	Dacitic dome with biotite, feldspar, quartz, plagioclase and disseminated pyrite														9399
CPR393	matagente	cuerpo nuevo-mantoV	heavy carbonate rock, with Fe-Mn-Zn carbonates. Rock presents breccia texture, but only monomictic.														
CPR394	matagente	cuerpo nuevo	massive sulfide rock with pyrite, galena, sphalerite, kaloinite. 2nd min. stage, outer zone											gn, sl			9713
CPR395	san alberto	san alberto	silicified carbonate rock with shalerite, galena, kaolinite, Fe-Mn-Zn carbonate.										qtz	sl			
CPR398	2nd ramp E	Tajo Raul Rojas E	massive pyrite- sphalerite-galena and Fe-oxydes. 2nd min. stage, outer zone.											gn, py, sl			9718
CPR399	matagente, 4300	cuerpo nuevo	brechified carbonate rock distal to the ore with a) white sample with dolomite and b) dark carbonate rock, silicified with other carbonate min. C) brechified rock distal to ore, but heavy										ca				
CPR401a	matagente	cuerpo nuevo-mantoV	sulfide rock with pyrite, galeny, and clays														9532
CPR401b			sulfide rock with pyrite, galeny, and clays														9533
CPR402a	matagente	cuerpo nuevo	sulfide rock with Bi-minerla, pyrite, galena														9534
CPR402b			sulfide rock with Bi-minerla, pyrite, galena														9535
CPR403	matagente	cuerpo nuevo	sulfide rock in Ag-Bi rich zone. 2nd min. stage, intermediate zone														9719
CPR404	2nd ramp NW	Tajo Raul Rojas NW	enargite well developed														13553
CPR405	2nd ramp NW	Tajo Raul Rojas NW	Fe-poor sphalerite on pyrite											sl			

Sample	Localisation	Deposit	Description	XRF	XRD	LM	SP	ICP-MS/INAA	Ar Ar	U-Pb	Hf	C	H, O	S	F. I.	Rb-Sr	N° labo
CPR406	2nd ramp NE	Tajo Raul Rojas NE	N100° vein with siderite-galena-kaolinite-pyrite- Fe-poor sphalerite and quartz														9536
CPR407	2nd ramp NE	Tajo Raul Rojas NE	massive gn vein with siderite/ankerite-pyrite-sphalerite									carb		gn, sl			
CPR408	2nd ramp NE	Tajo Raul Rojas NE	banded texture with galena-sphalerite from the N100° vein (id as cpr 406)														9537
CPR412	2nd ramp NE	Tajo Raul Rojas NE	sulfide rock with pyrite-Fe-poor sphalerite-galena-carbonate-kaolinite														10283
CPR413	2nd ramp NE	Tajo Raul Rojas NE	rock with 50% carbonates and Fe-poor sphalerite-pyrite-quartz									carb					9538
CPR414	Venencocha	Venencocha	heavy oxidized vein														
CPR415	0361'181E, 8821'705N	Venencocha	oxidized (goetite) vein with alunite-svanbergite-quartz halo on border of vein.														
CPR416	Diamante, 4200	Tajo Raul Rojas E	border on an oxidized vein with heavy carbonate rock														
CPR417	Diamante, 4200	Tajo Raul Rojas E	Zn-Pb ore with Fe.poor sphalerite, galena, pyrite, and kaolinite. 2nd min. stage, outer zone.									kaol		sl			9715
CPR420	Diamante, 4200	Tajo Raul Rojas E	oxidized vein, very heavy														9721
CPR421	Diamante, 4200	Tajo Raul Rojas E	heavy carbonate rock with sphalerite														9731
CPR422	Diamante, 4200	Tajo Raul Rojas E	banded vein with sphalerite-pyrite-carbonates-magnetite-hematite and kaolinite. 2nd min. stage, outer most zone.									kaol		sl			9716
CPR423	Diamante, 4200	Tajo Raul Rojas E	heavy carbonate rock with hematite and relics of magnetite			LP	LP										9525
CPR424	Diamante, 4200	Tajo Raul Rojas E	nearly unaltered Pucara limestone with dolomite vein									carb					
CPR427	Diamante, 4200	Tajo Raul Rojas E	Fe-Mn-Zn carbonates and other sulfures from the zonation of vein			lp									sl		9723
CPR428	Diamante, 4200	Tajo Raul Rojas E	magnetite and hematite with Fe-Mn-Zn carbonates (outermost zone)											sl			9712
CPR429	Diamante, 4200	Tajo Raul Rojas E	Heavy rock with Fe-Mn-Zn carbonates (outer zone)									carb		sl			?
CPR430	Diamante, 4200	Tajo Raul Rojas E	sulfide rock														9732
CPR431	Diamante, 4200	Tajo Raul Rojas E	Fe-poor sphalerite from a galena-rich vein.									carb		gn, sl			
CPR432	2nd ramp NE	Tajo Raul Rojas NE	vein with Fe-Mn-Zn carbonates-pyrite-sulfures														
CPR433	2nd ramp NE	Tajo Raul Rojas NE	N100° oxidized vein with pyrite, sphalerite. 2nd min. stage, outer most zone.														9714
CPR436	Diamante, 4200	Tajo Raul Rojas E	Carbonate rock with Fe-Mn-Zn carbonates and magnetite. 2nd min. stage, outermost zone.														9717
CPR439	2nd ramp W	Tajo Raul Rojas W	enargite vein with well formed quartz			lp						qtz		enr	qtz		9726
CPR440	2nd ramp W	Tajo Raul Rojas W	enargite-pyrite vein with quartz									qtz, ba		ba			
CPR442	Venencocha	Venencocha	center of an oxidized vein														
CPR443	Venencocha	Venencocha	alteration 20m from the center of a vein with quartz-alunite-diaspore.														9393
CPR444	Venencocha	Venencocha	Advanced argillic alteration ahlo from a vein														9531
CPR445	Venencocha	Venencocha	alteration halo of oxidized vein														9527
CPR446	Venencocha	Venencocha	oxidized vein in diatrem breccia														
CPR449	Venencocha	Venencocha	N100° oxidized vein														
CPR452	Venencocha	Rica Cerrena	altered pyroclastic breccia near an oxidized vein with zunyite														9528
CPR456	2nd ramp NE	Tajo Raul Rojas NE	Fe-poor and Fe-rich sphalerite. 2nd min. stage, outer zone.											gn, sl			9722

Sample	Localisation	Deposit	Description	XRF	XRD	LM	SP	ICP-MS/INAA	Ar Ar	U-Pb	Hf	C	H, O	S	F. I.	Rb-Sr	N° labo
CPR457	2nd ramp NE	Tajo Raul Rojas NE	zonation of a vein rich in siderite and hematite														9539
CPR458	2nd ramp NE	Tajo Raul Rojas NE	zonation of a vein rich in siderite and hematite, 2nd min. stage, outer most zone.														9711
CPR459	2nd ramp NE	Tajo Raul Rojas NE	zonation of a vein rich in siderite and hematite,. 2nd min. stage, outer most zone.									ba, carb		ba			
CPR460	2nd ramp NE	Tajo Raul Rojas NE	zonation of a vein rich in siderite and hematite. 2nd min. stage, outer most zone.			lp											9727
CPR461	4nd ramp W, bottom open pit	Tajo Raul Rojas W	marmatite-rich sample. 1st min. stage.			lp								sl	sl, qtz		9733
CPR462	4nd ramp W, bottom open pit	Tajo Raul Rojas W	marmatite with Fe-poor sphalerite			lp											9729
CPR463	4nd ramp W, bottom open pit	Tajo Raul Rojas W	marmatite near 2nd po pipe			lp											97??
CPR464	4nd ramp W, bottom open pit	Tajo Raul Rojas W	Fe-poor and Fe-rich sphalerite			lp								py, sl			9725
CPR465	4nd ramp W, bottom open pit	Tajo Raul Rojas W	altered diatreme breccia with some sericite and some alunite (?)														9730
CPR470	3nd ramp W, bottom open pit	Tajo Raul Rojas W	alunite from enargite vein in py-qtz body			lp											9728
CPR471	3180 ramp under Diamante	Tajo Raul Rojas E	Fe-Mn-Zn carbonte and quartz (outermost zone)									qtz, carb					
CPR472	2nd ramp E,	Tajo Raul Rojas E	Quartz-monzonite porphyric dyke a in open pit.														9407-9395
CPR 473		Tajo Raul Rojas W	Quartz-sericite alteration from quartz-pyrite body														9540
CPR 475	below bench 4320 matagente	Tajo Matagente, CN	barite-rich sample from the outer zone									ba		ba			
CPR 476		Tajo Matagente, CN	sulfide rock with alunite-group minerals			LP											10572
CPR 477	below bench 4320 matagente	Tajo Matagente, CN	sulfide rock with muscovite, quartz amd pyrite			LP								sl			10571
CPR 478	below bench 4320 matagente	Tajo Matagente, CN	sulfide rock with alunite-group minerals			LP											10579
CPR 480	s open pit	Tajo Raul Rojas south	center of an enargite-pyrite vein									qtz			qtz		10575
CPR 481	S open pit	Tajo Raul Rojas	Intermediate zone (adjacent to sample cpr 480)														10570
CPR 482	S open pit	Tajo Raul Rojas	Intermediate zone (adjacent to sample cpr 480)			LP											10574
CPR 483	San alberto	Tajo Raul Rojas	sulfide rock from the intermediate zone														10569
CPR 486	San alberto	Tajo Raul Rojas	Zn-Pb ore from the outer zone with sphalerite											gn, py, sl			
CPR 490	qtz py body	tajo raul rojas	Pyrite-quartz body 2 types of pyrite are present. Octahedral and pyritohedral														
CPR 492	matagente bench 4320 CN	tajo raul rojas	Fe-Mn-Zn carbonates														
CPR 496	DDH Rd-EX-12-01-02 (302.15m)	underground mine	Intermediate zone														12791
CPR 497	DDH Rd-EX-12-01-02 (302.65m)	underground mine	Intermediate zone														12790
CPR 498	2nd ramp W, bench 4190m	tajo raul rojas	Sericite-pyrite halo in diatreme breccia													ser	
CPR 499	3rd ramp W, bench 4190m	tajo raul rojas	Sericite-pyrite halo in diatreme breccia						py, ser							ser, py	
CPR **600**	bench 4170, (near po pipes)	tajo raul rojas	enargite-pyrite veins with alunite														
cpr 602	360806 E, 8821005N, 4395m	diatreme	acretionnary lappili tuff														
cpr 603	360255E, 8820377N, 4404m	SW margin of Cerro diatreme	dactitic to rhyodacitic porphyry dome			LP											12207, 12206
cpr 604	360838E, 8820315 N, 4401m	S of Cerro diatreme	quartz-monzonite porphyry dyke.														
cpr 605	Yanamate, 361524E, 8810913 N	Yanamate	porphyry dacitic dome from Yanamate			LP											12209
cpr 606	Huacchuacaja, 358522E, 8808330N	Colquijirca district	Porphyry dacitic dome from Huacchuacaja near Colquijirca			LP											12210
pr 607a	enargite-pyrite veins	tajo raul rojas	bornite with chalcopyrite and pyrite														12794
cpr 607	underground mine	Cerro de Pasco	diatreme breccia with pyrite, showing weak alteration			LP											13728
cpr 608	venencocha														qtz		
cpr 608 (a)	level 1400, gallery 1484-E	underground mine	albitized quartz-monzonite dyke			LP											3729
cpr 609	underground mine	underground mine	altered diatreme breccia			LP											13730

REMERCIEMENTS

Après toutes ces années passées comme étudiante de doctorat, je voudrais remercier toutes les personnes qui ont contribués à l'achèvement de ce travail de thèse.

J'aimerai remercier le Prof. L. Fontboté qui m'a proposé le sujet. Il a su prendre le temps de discuter, lire, corriger pendant de longues heures aussi bien les rapports pour la compagnie minière que le manuscrit final. Les quelques mois qui ont précédé la défense ont été importants et toutes les heures passées dans son bureau à discuter de la thèse mais aussi d'autres choses en ont fait un mentor pour moi. Ses conseils furent toujours avisés et justes. Merci infiniment.

J'aimerai également remercier le Prof. M.T. Einaudi, Dr. R. Moritz, Prof. Urs Schaltegger ainsi que le Prof. T. Vennemann pour avoir accepté de faire partie de mon jury de thèse ainsi que pour leurs excellentes corrections et commentaires qui ont permis d'améliorer le travail final.

Cette thèse a été possible grâce au soutient logistique de de Volcán Compánia Minera S.A particulièrement je remercie V. Gobitz, J. Timmers ainsi que toute l'équipe de géologie incluant H. Alvarez, R. Sunny, E. Lopez, L. Fuentes et C. Vera. Tous ont contribué au bon déroulement des différentes campagnes de terrain.

Concernant l'analytique, j'aimerai remercier le Prof. T. Vennemann qui m'a accueilli dans son laboratoire à l'Université de Lausanne pour l'analyse des isotopes stable de H, O et C. Je remercie aussi le Dr. J. Spangenberg pour l'analyse des isotopes de S. Un énorme merci à Dr. M. Ovcharova pour les analyses U-Pb et les longues discussions que nous avons eu. Merci également au Prof. Schaltegger pour avoir répondu à mes questions. Les analyses de microsonde électronique ont été possibles grâce à l'aide du Dr. G. Morris, Dr. C. Ginibre ainsi que Dr. K. Kouzmanov. Je remercie le Dr. J. Schneider pour les analyses de Rb-Sr et de Pb et les nombreux échanges d'e-mail. P. Voldet est remerciée pour les analyses de terres rares, ainsi que Jean-Marie Boccard pour les lames minces et sections polies, défiant toujours l'impossible et Fabio Capponi pour les analyses XRF. Tous mes remerciements vont aussi au Dr. Richard Spikings pour les analyses Ar/Ar et pour m'avoir toujours aidée lors des difficultés relative au laboratoire. Je tiens à remercier tout particulièrement le Dr. Kalin Kouzmanov pour sa patience aussi bien à la microsonde qu'aux MEB et envers mes questions ainsi que sa rigueur scientifique. Je remercie également le Dr. Robert Moritz pour ses conseils et son humour sarcastique qui me fait toujours bien rire.

Je tiens à remercier du fond du cœur mes collègues du Département de Minéralogie pour leur amitié et leur disponibilité lors des «up» et «down», en particulier Isabelle Chambefort, ma fidèle collègue et amie du bureau 701, Antoine de Haller, Carol Dolorier, Carolina Rodriguez, Daniel Selles, Cédric Rapaille &Co, Yves Jobin (mon compagnon de terrain), le bureau 700, Mélisse Henry, Jean Vallance, Vincent Badoux, Benjamin Sallier, Agnès Markowski (tout deux anciens locataires du bureau 701), Sébastien Beuchat, le bureau 703, Massimo Chiaradia &Co, Diego Villagomez, Julie Bourquin et tous les autres que j'aurai pu oublier! Merci encore à Jacqueline Berthoud pour son sourire, sa bonne humeur, sa patience et pour son aide.

J'aimerai remercier mes amis dont Katia Valenza, Monique Adamer, Sabrina Pozzi, Laurent Langhi, Anne Girardet, Hélène Bourdy et Fabien Desponds, Laurie Cortesi, Agathe Weber, Isabelle, Stéphanie et Caroline Geissbühler, Adiela Martinez, Elizabeth Martley…

Merci à mes parents qui ont toujours eu confiance en moi et qui m'ont soutenu tout au long de mes études, Sabine et Maya mes sœurs ainsi que Steven qui a toujours montré beaucoup d'intérêts pour la géologie.

Je dédie cette thèse à Ronner, ma douce moitié, sans qui cette thèse n'aurait été possible. Merci pour ta patience, ton amour, tes conseils et tes encouragements à distance. Merci de tout cœur et pour toujours (∞).

Ce projet a été subventionné par le Fond National Suisse de la Recherche Scientifique (projet 2000-02 108026, Prof. L. Fontboté) ainsi que Volcán Compánia minera SA. Le fond Marc Bikigt ainsi que le Fond Lombard m'ont permis de participer à divers congrès et excursions et je les en remercie.

Déjà paru /already published :

Vol. 44 (2004) D. Vignati: Trace metal partitioning in freshwater as a function of environmental variables and its implications for metal bioavailability. (272 pages). ISBN 2-940153-43-4
Commande à : Institut F.-A. Forel, 10 route de Suisse, 1290 Versoix (Suisse); 30.- CHF

Vol. 45 (2004) C.-A. Hasler: Geometry and internal discontinuities of an Ypresian carbonate reservoir (SIT field, Tunisia). (230 pages). ISBN 2-940153-44-2
Commande à : Département de Géologie, 13 rue des Maraîchers, 1205 Genève; 30.- CHF

Vol. 46 (2004) J. Poté: Devenir de l'ADN d'origine végétale dans les compartiments environnementaux : analyse systémique, rémanence et transport de l'ADN transgénique dans le sol. (200 pages). ISBN 2-940153-45-0
Commande à : Institut F.-A. Forel, 10 route de Suisse, 1290 Versoix (Suisse); 30.- CHF

Vol. 47 (2004) J.-L. Malfère: Panache mantellique et recyclage de matériel lithosphérique: Etude des isotopes de Hf, Pb, Sr et Nd et des éléments en trace des basaltes néovolcaniques islandais. (148 pages). ISBN 2-940153-46-9
Commande à : Département de Minéralogie, 13 rue des Maraîchers, 1205 Genève; 50.- CHF

Vol. 48 (2004) S. Jorry: The Eocene nummulite carbonates (central Tunisia and NE Libya): sedimentology, depositional environments, and application to oil reservoirs. (206 pages).
ISBN 2-940153-47-7
Commande à : Département de Géologie, 13 rue des Maraîchers, 1205 Genève; 30.- CHF

Vol. 49 (2004) A. Piuz: Micropaléontologie d'une plate-forme bioclastique échinodermique: Les calcaires à entroques du Bajocien du Jura méridional et de Bourgogne. (267 pages).
ISBN 2-940153-48-5
Commande à : Département de Géologie, 13 rue des Maraîchers, 1205 Genève; 30.- CHF

Vol. 50 (2005) J. Dominik, D. Chapman and J.-L. Loizeau (eds.): NEAR curriculum in natural environmental science. (192 pages). ISBN 2-940153-49-3
Commande à : Institut F.-A. Forel, 10 route de Suisse, 1290 Versoix (Suisse); 30.- CHF

Vol. 51 (2005) P. Le Guern: Caractérisation pétrographique et pétrotexturale des éolianites holocènes et pléistocènes. (219 pages). ISBN 2-940153-50-7
Commande à : Département de Géologie, 13 rue des Maraîchers, 1205 Genève; 30.- CHF

Vol. 52 (2005) I. Chambefort: The Cu-Au Chelopech deposit, Panagyurishte District, Bulgaria: Volcanic setting, hydrothermal evolution and tectonic overprint of a Late Cretaceous high-sulfidation epithermal deposit. (173 pages). ISBN 2-940153-51-5
Commande à : Département de Minéralogie, 13 rue des Maraîchers, 1205 Genève; 50.- CHF

Vol. 53 (2005) G. Gong: Physical properties of Alpine rocks: A laboratory investigation. (142 pages). ISBN 2-940153-52-3
Commande à : Département de Minéralogie, 13 rue des Maraîchers, 1205 Genève; 50.- CHF

Vol. 54 (2005) P. Rossé: Le " Single Particle Counter" un instrument pour l'étude des colloïdes dans les eaux de surface. (136pages). ISBN 2-940153-53-1
Commande à : Institut F.-A. Forel, 10 route de Suisse, 1290 Versoix (Suisse); 30.- CHF

Vol. 55 (2005) B. Koukal: Influence des colloïdes sur la toxicité des métaux (Cd, Cu, Pb, Zn) chez l'algue verte *Pseudokirchneriella subcapitata*. (242pages). ISBN 2-940153-54-X
Commande à : Institut F.-A. Forel, 10 route de Suisse, 1290 Versoix (Suisse); 30.- CHF

Vol. 56 (2005) C. Clerc: Les Miliolina (Foraminifères porcelanés) du Dogger du Jura méridional (France): Systématique, stratigraphie et paléoenvironnement. (250 pages). ISBN 2-940153-55-8
Commande à : Département de Géologie, 13 rue des Maraîchers, 1205 Genève; 30.- CHF

Vol. 57 (2006) B. Sallier: Carbonates microporeux: influence de l'architecture du milieu poreux et la mouillabilité sur les écoulements diphasiques dans les réservoirs pétroliers. (230 pages). ISBN 2-940153-56-6
Commande à : Département de Géologie, 13 rue des Maraîchers, 1205 Genève; 30.- CHF

Déjà paru /already published :

Vol. 58 (2006) A. de Haller: The Raúl-Condestable iron oxide copper-gold deposit, Central coast of Peru. (123 pages). ISBN 2-940153-57-4
Commande à : Département de Minéralogie, 13 rue des Maraîchers, 1205 Genève; 50.- CHF

Vol. 59 (2006) A. C. Rodriguez Soto: Intra-crustal origin of Holocene adakitic magmas at Nevado de Longavi Volcano (Chilean Andes, 36.2°S). (120 pages). ISBN 2-940153-58-2
Commande à : Département de Minéralogie, 13 rue des Maraîchers, 1205 Genève; 50.- CHF

Vol. 60 (2006) M. Polliand: Evolution, and tectonic setting of the Upper Cretaceous Perubar Ba-Pb-Zn volcanic-hosted massive sulfide deposit, Central Peru. (141 pages). ISBN 2-940153-59-0
Commande à : Département de Minéralogie, 13 rue des Maraîchers, 1205 Genève; 50.- CHF

Vol. 61 (2006) D. F. Sellés Mathieu: Stratigraphy, petrology, and geochemistry of Nevado de Longaví Volcano, Chilean Andes (36.2°S). (103 pages). ISBN 2-940153-60-4
Commande à : Département de Minéralogie, 13 rue des Maraîchers, 1205 Genève; 50.- CHF

Vol. 62 (2006) M.-H. Pereira de Abreu: Spéciation et mobilité du chrome dans les environnements aquatiques pollués par les effluents de tanneries. Etude par couplage HPLC-ICP-MS. (273 pages + CD-Rom pour les annexes). ISBN 2-940153-61-2
Commande à : Institut F.-A. Forel, 10 route de Suisse, 1290 Versoix (Suisse); 30.- CHF

Vol. 63 (2006) C. Ruchonnet: Climatic and oceanographic evolution of the Mediterranean basin during the Late Serravallian/Early Tortonian (Middle/Late Miocene): the record from the Ragusa platform (SE Sicily, Italy). (103 pages). ISBN 2-940153-62-0
Commande à : Département de Géologie, 13 rue des Maraîchers, 1205 Genève; 30.- CHF

Vol. 64 (2007) R. Bendezú Juarez: Shallow polymetallic and precious metal mineralization associated with a Miocene diatreme-dome complex: the Colquijirca district in the Peruvian Andes. (221 pages). ISBN 2-940153-63-9
Commande à : Département de Minéralogie, 13 rue des Maraîchers, 1205 Genève; 50.- CHF

Vol. 65 (2007) N. Roduit: JMicroVision: un logiciel d'analyse d'images pétrographiques polyvalent. (116 pages). ISBN 2-940153-64-7
Commande à : Département de Géologie, 13 rue des Maraîchers, 1205 Genève; 30.- CHF

Vol. 66 (2007) R. Baumgartner: Sources and evolution in space and time of hydrothermal fluids at the Cerro de Pasco Cordilleran base metal deposit, Central Peru.(167 pages). ISBN 2-940153-65-5
Commande à : Département de Minéralogie, 13 rue des Maraîchers, 1205 Genève; 50.- CHF

ISBN 2 - 940153 - 65 - 5